8-2024

Filter Incidence Narrowband Infrared Spectrometer for Space-Based Methane Measurement and Plume Detection

Bruno Mattos
Utah State University

Recommended Citation

Mattos, Bruno, "Filter Incidence Narrowband Infrared Spectrometer for Space-Based Methane Measurement and Plume Detection" (2024). *All Graduate Theses and Dissertations, Fall 2023 to Present*. 272.
https://digitalcommons.usu.edu/etd2023/272

FILTER INCIDENCE NARROWBAND INFRARED SPECTROMETER FOR SPACE-BASED METHANE MEASUREMENT AND PLUME DETECTION

by

Bruno Mattos

A dissertation submitted in partial fulfillment
of the requirements for the degree

of

DOCTOR OF PHILOSOPHY

in

Electrical Engineering

Approved:

Charles Swenson, Ph.D. Major Professor	Jacob Gunther, Ph.D. Committee Member
Todd Moon, Ph.D. Committee Member	Bela Fejer, Ph.D. Committee Member
David Geller, Ph.D. Committee Member	Allan Marchant, Ph.D. Committee Member

D. Richard Cutler, Ph.D.
Vice Provost of Graduate Studies

UTAH STATE UNIVERSITY
Logan, Utah

2024

ABSTRACT

Filter Incidence Narrowband Infrared Spectrometer for space-based methane measurement and plume detection

by

Bruno Mattos, Doctor of Philosophy

Utah State University, 2024

Major Professor: Charles Swenson, Ph.D.
Department: Electrical and Computer Engineering

Monitoring methane emissions from space is crucial for reducing global warming in the near term. Despite recent advancements in space sensor technology for greenhouse gas monitoring, a technological gap remains for a compact, lightweight instrument capable of accurately measuring methane emissions onboard nanosatellites. This dissertation addresses this need by detailing the concept and development of the Filter Incidence Narrowband Infrared Spectrometer (FINIS), a compact and light-efficient infrared imaging spectrometer designed for methane emission measurements.

FINIS innovates by employing two optically efficient filtering imaging spectrometers that share the same field of view. Both imagers measure the Earth's reflected spectral radiance around the strongest methane absorption feature centered at 1666 nm with 1.5 nm (FWHM) spectral resolution. Light filtering is performed by two identical narrow-band interference filters placed at the aperture of each imager with a tilt angle of 10 degrees.

Each imager captures the light spectrum across the image plane by exploiting the interference filter's bandpass dependency on the angle of incidence of incoming light, which varies across the field. By tilting the interference filters in opposite directions in each imager, the methane absorption feature appears at mirrored positions across the field of view (FOV).

Full spectrum acquisition is performed by taking a sequence of overlapping pairs of frames over the area of interest using a method known as windowing. By combining the pair of images and registering the stack of frames, a relative spectral radiance measurement vector for each ground sample is assembled and used to estimate the methane vertical column concentration relative to the background.

This dissertation details FINIS's technological advancements from its prototype version to its space flight version, scheduled to fly as a student project onboard the ACMES (Active Cooling for Multispectral Earth Sensors) mission, a 16U CubeSat planned for launch in late 2025. Significant improvements include implementing lower noise cameras with a wider focal plane array (FPA) and transitioning the optical design from a single folded telescope to a binocular optical system with an embedded onboard calibration unit. The new design enables relative radiance measurements independent of surface reflectance functions and resolves the parallax problem of the original design.

The modeling and methods sections describe how FINIS captures spectral information across its two cameras' FPA. The spectrum response model shows how the tilted interference filter distributes the center wavelength across each FPA based on the target's location in the field of view. Radiometric analysis under various lighting conditions demonstrates that FINIS achieves a high signal-to-noise ratio. Under low light conditions (surface albedo of 0.1, solar zenith angle (SZA) of 60 degrees), FINIS achieves a single measurement SNR exceeding 70 for each camera. Under high light conditions (surface albedo of 0.6, SZA of 20 degrees), the SNR can peak at 280.

Subsequent retrieval noise analysis used these radiometric performance outcomes to compute the relative measurement noise for targets across the field of view. Slight performance variations were observed across the track, with better performance at the edges compared to the center. Assuming an albedo of 0.2 and a data acquisition rate of 5 frames per second, the methane retrieval noise relative to the background is anticipated to be less than 3.5% for an SZA of 60 degrees and under 3% for an SZA of 30 degrees. Given the estimated pixel size of 150×200 meters for its 550 km orbital altitude operation onboard

ACMES, this precision is adequate for detecting plumes from leak rates exceeding 1 ton per hour at 60 degrees SZA and 500 kilograms per hour at 30 degrees SZA under low wind conditions.

A plume detection simulation demonstrated FINIS's data acquisition and processing methods, generating methane map products. The simulation involved generating images by simulating ground scanning, considering factors such as field of view, orbital altitude, inclination, and integration time. Processing the simulated images using the fast retrieval method confirmed the detection of all simulated plumes with varying leak rates, meeting performance requirements.

Preliminary tests and calibration results are also presented, including focus, stereo camera, dark frame, flat frame, and onboard flat field calibrations. Additionally, a methane cell calibration, where images are taken through a gas cell filled with low-pressure methane, confirmed the filter's spectral response model accuracy.

Future work includes the final integration of FINIS into the ACMES bus, and post-launch operations and data processing for validating FINIS performance and plume detection capability. Its successful deployment and operation onboard ACMES will significantly contribute to global efforts to reduce greenhouse gas emissions, thereby aiding in the fight against global warming.

(211 pages)

PUBLIC ABSTRACT

Filter Incidence Narrowband Infrared Spectrometer for space-based methane measurement and plume detection

Bruno Mattos

Monitoring methane emissions from space is essential for reducing global warming. This dissertation introduces the Filter Incidence Narrowband Infrared Spectrometer (FINIS), a compact, lightweight instrument designed for nanosatellites to accurately measure methane emissions. FINIS uses two innovative imaging spectrometers to capture the Earth's reflected light, focusing on the strongest methane absorption feature at 1666 nm. By using tilted interference filters, each imager collects detailed spectral data, allowing precise methane detection. FINIS has been significantly improved from its prototype to its space-ready version, set to launch on the ACMES CubeSat in late 2025. The new design includes a binocular optical system and an onboard calibration unit, enabling accurate measurements independent of surface reflectance. Radiometric analysis shows that FINIS can achieve a high signal-to-noise ratio under various lighting conditions, ensuring reliable methane measurements. Simulations confirmed FINIS's ability to detect methane plumes, demonstrating its data acquisition and processing methods. Preliminary tests and calibrations, including focus, stereo camera, and methane cell calibrations, verified the instrument's performance. Future work will focus on integrating FINIS into the ACMES bus and validating its performance post-launch. FINIS's successful deployment will enhance global methane monitoring efforts, contributing to the fight against climate change.

I would like to dedicate this dissertation to my beloved daughter, Manoela A. Mattos, who has been my source of strength, inspiration, and joy.

ACKNOWLEDGMENTS

I would like to express my deepest gratitude to my advisor, Dr. Charles Swenson, for his unwavering support, guidance, and mentorship throughout my PhD journey. His insightful feedback and encouragement have been invaluable to my research and personal growth.

I am also grateful to the members of my dissertation committee. Special thanks to Dr. Allan Marchant, who led the previous FINIS team during the initial development phases. His leadership demonstrated the instrument concept and paved the way for this work. I appreciate his valuable guidance during the optical redesign and his thorough review of my analyses. To Dr. Bela Fejer, for his friendship, mentorship, and guidance.

Special thanks to the other students of the Center for Space Engineering who contributed to the FINIS project, particularly Michael Kirk, who conducted extensive work on FINIS' mechanical design, procured parts, assembled them, and prepared our Clean Room facility, which was extensively used during the FINIS calibration campaign.

I would like to extend my heartfelt gratitude to the Brazilian Air Force for sponsoring my PhD program. In particular, I thank Dr. Luis Loures, who enabled and strengthened the relationship between ITA and USU by leading work on important US-Brazil space projects. I return to my home country committed to applying the knowledge gained through this research, as well as from my classes and other academic activities, to educate the next generation of space engineers and to advance strategic space capabilities in Brazil.

I am profoundly grateful to my family. To my parents, Ademar and Deuza, thank you for your unconditional love, patience, and belief in me. To my cousin José Barbosa and his family, who welcomed me into their home during the first year of my preparation for ITA's national exam in 2008. Their generous act completely changed the course of my life, ultimately leading to this accomplishment in 2024.

I am also thankful for the ASSERT program, an autism support service run by USU, which provided invaluable support for Manoela's education and development during our time in Logan.

Last but not least, I am grateful to my wife, Monique, for accompanying me on this journey and facing all the challenges involved in moving to another country with a different culture and language, far from family. Your support and understanding have been my anchor during challenging times. And to my daughter, Manoela, who brings me joy and teaches me how to be a better person every day.

Bruno Mattos

CONTENTS

LIST OF TABLES

Table Page

LIST OF FIGURES

Acronyms

AFM Area Flux Mapper

AGC Automatic Gain Control

AOI Angle of Incidence

AR Assessment Report

COP Conference of the Parties

COTS Commercial-off-the-shelf

CSE Center of Space Engineering

CWL Center wavelength

DF Dark Frame

DN Digital Number

EFL Effective Focal Length

EMIT Earth surface Mineral dust source InvesTigation

FF Flat Frame

FINIS Filter Incidence Narrowband Infrared Spectrometer

FOV Field of View

FPA Focal Plane Array

FPS Frames per second

FTS Fourier Transform Spectrometer

GSD Ground Sample Distance

GWP Global warming potential

IF Interference Filter

IFOV Instantaneous Field of View

InGaAs Indium Gallium Arsenide

IPCC Intergovernmental Panel on Climate Change

ISR Instrument Spectral Response

ISRF Instrument Spectral Response Function

ISS International Space Station

JPL Jet Propulsion Lab

MAP Maximum a Posterior Solution

MCT Mercury Cadmium Telluride

NASA National Aeronautics and Space Administration

NB Narrowband

NEI Noise Equivalent Irradiance

NEP Noise Equivalent Power

PSI Point Source Imager

RMS Root mean square

SNR Signal-to-Noise ratio

SSO Sun-synchronous orbit

SWIR Shortwave Infrared

SZA Solar Zenith Angle

TCCON The Total Carbon Column Observing Network

TEC Thermal Electric Cooler

TIR Thermal Infrared

TOA Top of Atmosphere

TRL Technology Readiness Level

USRA Universities Space Research Association

USU Utah State University

WF Weighting Function

CHAPTER 1

INTRODUCTION

1.1 The importance of measuring methane

Climate change stands as one of the most pressing challenges of our time, with its potential to disrupt ecosystems, jeopardize human livelihoods, and reshape the world as we know it. While carbon dioxide (CO_2) is widely recognized as a prominent contributor to this problem, methane (CH_4), a greenhouse gas with significantly higher heat-trapping potential, has gained substantial attention in recent years. Accurately measuring atmospheric methane concentrations is of paramount importance in addressing this concern, and space-based sensors have emerged as an invaluable tool in this endeavor.

Although natural sources like wetlands, mud volcanoes, seeps, and wildlife collectively account for approximately 39% of global methane emissions, the majority, amounting to 61%, stems from human activities. Among anthropogenic sources, the agriculture, energy, and waste sectors contribute 31%, 28%, and 15% of the global anthropogenic emissions, respectively [2]. With industrialization, the increasing human-related methane emissions have increased the atmospheric methane concentration by more than 150% since 1750, peaking at 1934 parts per billion (ppb) by November of 2023 [3].

Although carbon dioxide is much more abundant in the atmosphere, with an average atmospheric concentration currently exceeding 422 ppm by January of 2024 [3], methane demonstrates approximately 85 times greater global warming potential (GWP) over a 20-year timeframe and about 32 times greater GWP over a 100-year period, considering climate feedbacks (IPCC AR5; [4]). In practical terms, reducing 1 ton of methane emissions is equivalent to mitigating the impact of 85 tonnes of CO_2 emissions over the next two decades in terms of global warming. The relatively short lifetime of methane in the atmosphere, approximately a decade [5], is primarily attributed to its oxidation with hydroxyl (OH).

However, this oxidation process also contributes to the formation of ground-level ozone, which poses harm to both humans and ecosystems, besides functioning as another potent greenhouse gas. The reduction of methane emissions, therefore, signifies one of the greatest, and perhaps one of the last, opportunities for humankind to extend its existence on this planet.

All these facts led 150 countries to sign the Global Methane Pledge, launched at COP 26 in November 2021, by which they committed to working together to collectively reduce global anthropogenic methane emissions by at least 30% from the 2020 level by 2030, which could eliminate over 0.2 °C warming by 2050 and help to achieve the Paris Agreement's goal of limiting the total warming to 1.5–2 °C.

To correctly measure the progress of such policy, participant countries also committed to enhancing the accuracy, transparency, consistency, comparability, and completeness of the national greenhouse gas inventory by following the methodologies and guidelines issued by the Intergovernmental Panel on Climate Change (IPCC).

Traditionally, monitoring methane concentrations relied on a network of ground-based measurement stations, aircraft observations, and in-situ measurements. While these methods have provided valuable insights, their spatial and temporal coverage limitations hinder the comprehensive understanding of global methane dynamics. Furthermore, ground-based monitoring faces geographical constraints and access limitations, particularly in remote or politically sensitive regions.

In light of these challenges, satellite technology has transformed our capacity to observe and quantify methane concentrations in the atmosphere. Satellite-based monitoring offers several compelling advantages. It provides global coverage, enabling the continuous observation of methane concentrations over extensive regions, including those challenging to access through alternative means. Additionally, satellites offer the potential for real-time or near-real-time data collection, facilitating swift responses to unforeseen events, such as large-scale methane emissions or natural releases. Moreover, satellites can assist in source identification, emission quantification, and trend tracking, all of which are vital for climate science and environmental policymaking.

While invaluable in advancing our understanding of atmospheric methane dynamics, the current generation of space-based greenhouse gas sensors faces several limitations. First and foremost, these sensors tend to be large and costly, which restricts their deployment on a wide scale. These limitations stem from the design complexity of the used spectrometers, which are designed to measure various trace gases beyond methane, which naturally requires a broad spectrum coverage with high spectrum resolution. Additionally, existing sensors often exhibit limitations in terms of spatial and temporal resolution, making it challenging to capture fine-scale methane emission sources and fluctuations.

To address these shortcomings and enhance the accessibility of methane monitoring, there is a growing imperative to develop more compact and cost-effective methane sensors. These sensors are expected to leverage advancements in miniaturization and innovative technologies to provide reliable and high-resolution methane data. By overcoming the limitations of their predecessors, such sensors have the potential to revolutionize our ability to comprehensively monitor and understand the distribution of methane in the Earth's atmosphere while making these measurements more accessible for a wider range of applications, from climate research to environmental monitoring and policy development.

This dissertation seeks to explore an innovative design for a space-based methane sensor, evaluating its viability in measuring emissions from both extended regions and discrete point sources (methane plumes). The proposed design employs a tilted narrowband interference filter, capturing the spectrum as the sensor traverses the area of interest. Distinguished by a high transmission coefficient within the pass-band, the filter allows unrestricted aperture, thereby achieving superior throughput compared to similarly sized dispersive imaging spectrometers utilizing slit apertures and less efficient grating or prism devices. The consequential advantage in throughput, coupled with its streamlined design, facilitates the creation of a compact and economically viable methane sensor, referred to herein as the **Filter Incidence Narrowband Infrared Spectrometer (FINIS)**.

The work discussed in this dissertation covers the technological advancement of FINIS from its ground-tested prototype version to its space version. This development includes aspects of redesigning, modeling, building, and testing an optical instrument, in addition to developing the data processing algorithms and planning for its upcoming space flight. This advancement could not have been achieved without the previous work done by graduate and undergraduate students and professors of the Department that conceptualized the instrument, built and proved its operation concept as a viable solution for a space-based methane sensor. The next section, therefore, summarizes the major milestones of the previous development that provided the foundation for this work.

1.2 Previous development on FINIS

Sponsored by the Universities Space Research Association (USRA), the Center for Space Engineering (CSE) at Utah State University (USU) started the development of FINIS towards the end of 2017, as shown in the timeline displayed in Fig. 1.1. The instrument concept was invented by Dr. Alan Marchant and Dr. Charles Swenson, with its patent published in 2022, US 2022/0003665 A1 [6]. As a precursor of FINIS, in 2013, the CSE worked on the development of the Conjugate Etalon Spectral Imager (CESI), a project funded by NASA's Small Business Innovation Research / Small Business Technology Transfer (SBIR/STTR) program to enable the miniaturization of hyperspectral and SWIR-band imaging instrumentation compatible with nanosatellite platforms.

Led by Dr. Marchant and Dr. Swenson, the team of USU undergraduate students conducted the initial development of FINIS in a two-phase program, where the first phase focused on instrument laboratory development and analysis, and the second phase focused on assembly and testing of FINIS from an airplane platform. In the first phase, benchtop testing demonstrated the viability of the FINIS concept and raised its Technology Readiness Level (TRL) to 3. In phase two, the team developed an airborne version of the instrument, which was flown onboard a Cessna aircraft.

The ground testing campaign, which included methane cell imaging, showed the viability of the sensor's innovative design for capturing the main methane absorption feature at around 1666nm wavelength. On the other hand, the data acquired in the flight test indicated that the ground illuminance pattern sometimes could change significantly across the frames acquired during the overpass. This problem was identified as parallax since it is related to the change in the viewing geometry during acquisition. The new FINIS design discussed here addressed this issue by using a binocular system, where the pair cameras acquire a sequence of pairs of images during the overpass. Since the pair of images are acquired with the same viewing geometry, the surface reflectance function can be normalized across the spectrum.

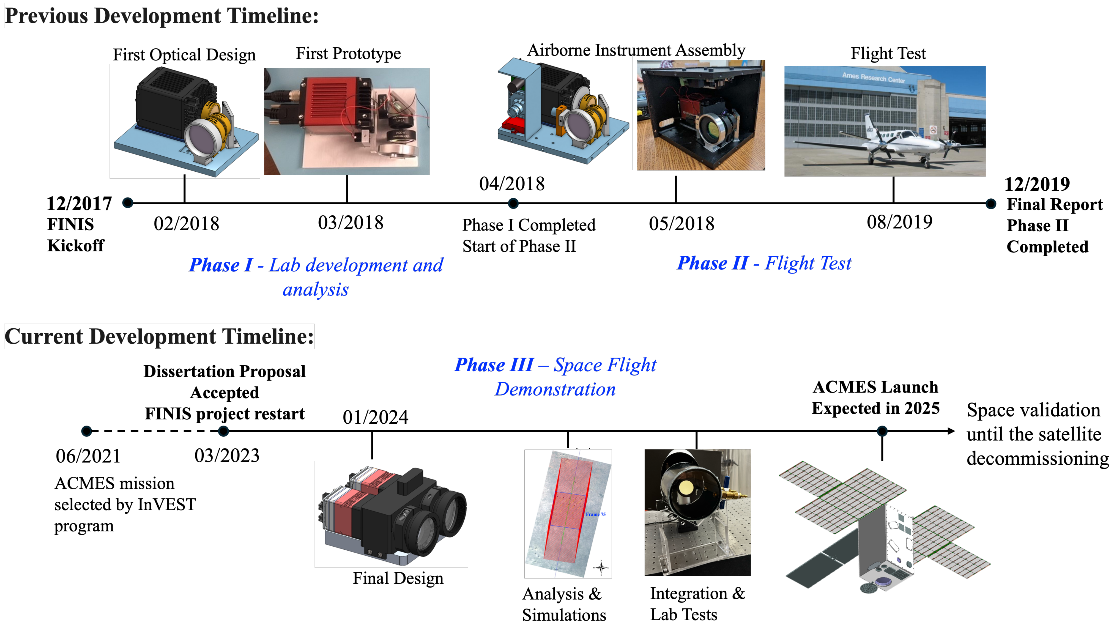

Fig. 1.1: FINIS project timeline highlighting the previous development milestones and the current ongoing development in phase III as it is being prepared for its spaceflight demonstration.

The initial optical design of FINIS used in the airborne test is depicted in Fig. 1.2. As detailed in this dissertation, the new design of FINIS (space version) differs from the original, incorporating different camera and optics configurations along with an integrated onboard calibration unit. Nevertheless, the fundamental operational concept of the instrument persists. This endeavor stands as a testament to the remarkable groundwork laid by the preceding team, whose tireless efforts paved the way for advancing FINIS's TRL for eventual space testing.

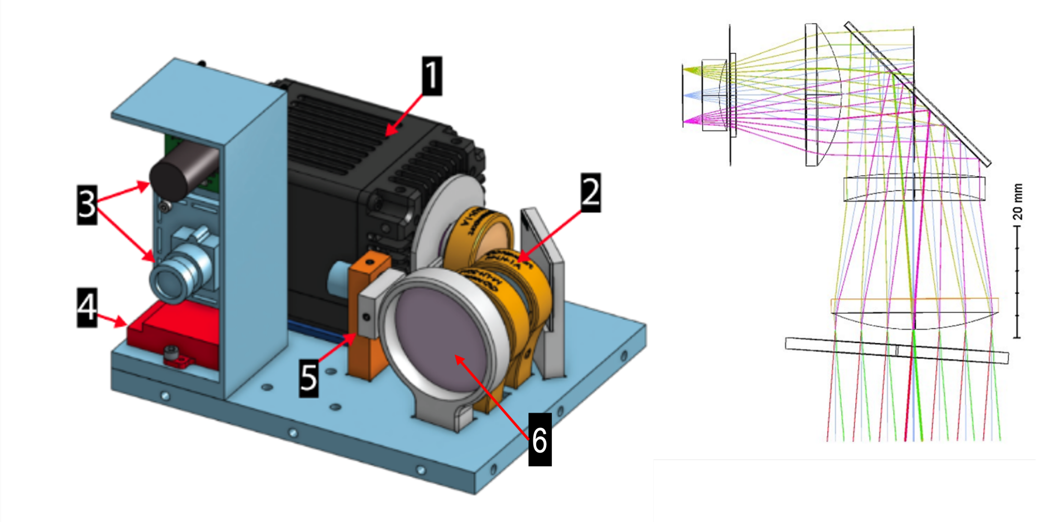

Fig. 1.2: Left: Original FINIS CAD model: (1) SWIR camera (2) Optics (3) Context cameras (4) IMU (5) Shutter (6) Tilted narrowband interference filter. Right: Ray tracing for the original FINIS optics.

1.3 The ACMES mission

FINIS is planned to be tested and validated in space onboard the Active Cooling for Multispectral Earth Sensors (ACMES), a 16U CubeSat mission planned to be launched by the end of 2025 or early 2026. ACMES was selected by the In-space Validation of Earth Science Technologies (InVEST) program in support of NASA Science Mission Directorate [7]. Besides FINIS, three other payload technologies will be tested in space: the Active Thermal Architecture (ATA), the Hyperspectral Thermal Imager (HyTI), and the Planer Langmuir/Impedance Diagnostic (PLAID) sensor, as depicted in Fig. 1.3.

The advanced ACMES bus is equipped with 230 W high-powered sun-tracking solar arrays and an onboard propulsion system. Initially designed for a one-year technology validation mission, it can extend up to three additional years for scientific research. The propulsion system is designed to maintain its orbital altitude above 400km altitude during the four-year lifetime, in addition to collision avoidance and deorbit.

The high power demand is mainly from the HyTi 2.0 instrument operation, which uses a cryocooler to cool its thermal detector and a powerful onboard computer for data processing [8]. The intense thermal load on this 16U CubeSat is managed by the ATA [9], which extracts the heat from HyTi heat source components and transports it via a closed fluid loop system to be rejected on the two-fold deployable and rotative radiator. ATA's control system adjusts the circulating fluid speed by controlling the pump, ensuring that the temperature of the HyTi remains within its operational optimal range.

Similar to FINIS, PLAID is another student-led research project to be validated onboard ACMES. PLAID is a surface-mounted impedance probe designed for ionospheric studies. Current PLAID is an enhanced version of the previously deployed probe in the joint Brazil-US 6U CubeSat SPORT mission, launched in 2022 from the ISS [10].

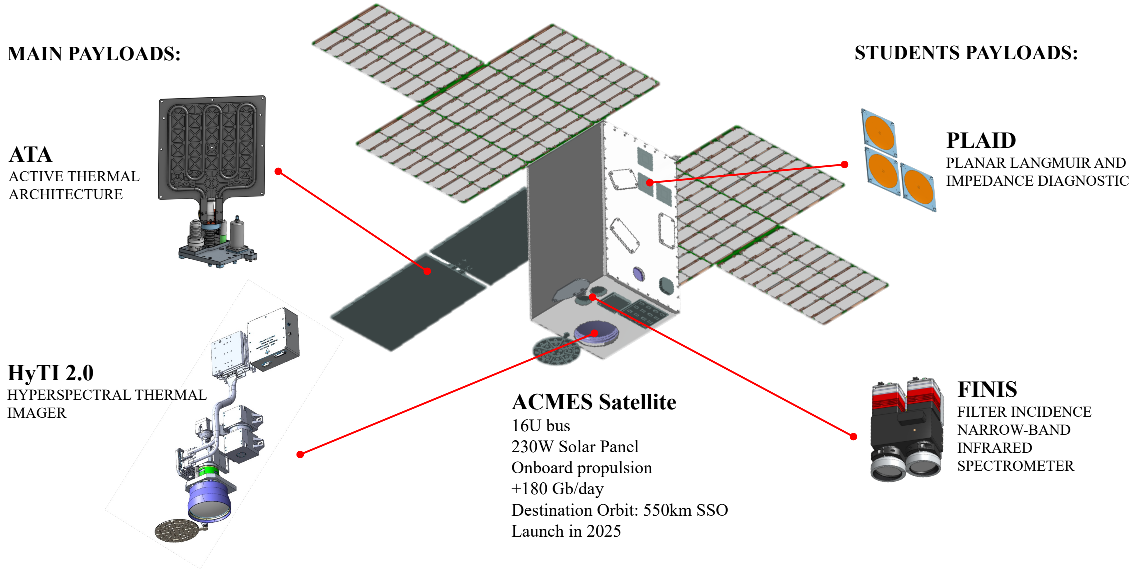

Fig. 1.3: Main payloads and students lead research projects on upcoming ACMES mission

ACMES will be placed in a sun-synchronous orbit at 550 km altitude. The orbital local time of the ascending node (LTAN) will be between 10 am and 12 pm during its lifetime (∼4 yrs), which ensures an imagery acquisition configuration in nadir-pointing with low solar zenith angle (SZA) for a wide latitude range. As discussed later, FINIS benefits from low

SZA ($< 60°$) since it collects more surface-reflected radiation and reduces the uncertainty of the measurements.

1.4 Significance and contribution

The importance of this research lies in its potential to address critical challenges in methane monitoring and contribute significant advancements to the field of environmental sensing. Here are key points that emphasize the importance of this research:

Increased Throughput and Efficiency: The utilization of a high-transmission coefficient interference filter without a restrictive slit aperture results in higher throughput compared to traditional dispersive imaging spectrometers. This increased throughput, combined with the elimination of slit-related efficiency limitations, signifies a substantial advancement in the efficiency of methane detection. This innovation directly addresses limitations observed in similar-sized instruments.

Compact Design and Low Complexity: The compact and low-complexity design of FINIS is a noteworthy feature. This aspect is crucial for space-based applications where size, weight, and power constraints are significant considerations. The ability to develop a compact methane sensor with reduced complexity has broader implications for the feasibility of space missions, enabling cost-effective solutions without compromising performance.

Cost-Effectiveness: The combination of increased throughput, low design complexity, and a compact form factor positions FINIS as a cost-effective solution for methane monitoring from space. This economic efficiency is particularly relevant in the context of environmental monitoring programs where the deployment of multiple sensors is often necessary to achieve comprehensive coverage.

Applicability to Extended Areas and Point Sources: The primary focus on measuring methane emissions from extended areas and point sources addresses a critical need in environmental monitoring. Understanding methane sources and their distribution is essential for effective climate change mitigation and resource management. FINIS's capabilities in this regard make it a valuable tool for gaining insights into both localized and widespread methane emissions.

Contributions to Environmental Policy and Mitigation Strategies: By providing a tool that enhances our ability to monitor methane emissions cost-effectively from space, this research contributes directly to environmental policy and mitigation strategies. Accurate and efficient monitoring is essential for implementing evidence-based policies to reduce greenhouse gas emissions and combat climate change.

In summary, this research on the design and implementation of FINIS represents a significant contribution to the field of space-based methane sensing. The innovative features of the sensor have the potential to address existing limitations, making it a valuable tool for environmental monitoring, policy development, and climate change mitigation efforts.

1.5 Dissertation outline

This dissertation is structured into eight chapters, each focusing on distinct aspects of the design, development, analysis, testing, and integration of FINIS into the ACMES mission. The following provides a concise overview of the content covered in each subsequent chapter:

Chapter 2: Background

This chapter provides a comprehensive literature review of space-based spectrometers used to measure greenhouse gases. It examines existing technologies, methods, and the challenges inherent in current approaches.

Chapter 3: Design and Development

Chapter 3 delves into the details of the sensor development. It begins by defining the mission objectives and requirements for FINIS in the context of its first space flight demonstration. The chapter then presents the instrument's concept of operation. It discusses the optimization process to determine the spectral fitting window that provides the most accurate methane retrieval using the sequence of image pairs. Following this, it explores the optical and mechanical design considerations of FINIS and details the implementation of an onboard calibration unit.

Chapter 4: Models and Methods

The fourth chapter elucidates the main models employed in the analysis and simulation processes. These include the sensor model, instrument spectral response model, radiative transfer model, and retrieval methods crucial for estimating the methane concentrations and detect plumes.

Chapter 5: Analysis and Simulation

Chapter 5 presents in-depth analyses of the radiometric and retrieval performance, shedding light on FINIS's capability to provide high signal-to-noise ratio measurements for different illumination conditions. Additionally, it discusses simulations conducted to evaluate plume detection capabilities.

Chapter 6: Testing and Calibration

This chapter outlines the rigorous testing and calibration procedures undergone by FINIS. It encompasses various calibration techniques such as dark frame calibration, flat fielding, methane cell calibration, and stereo calibration to ensure optimal performance.

Chapter 7: Mission Integration

Chapter 7 focuses on FINIS's integration into the ACMES mission. It details the definitions of mechanical and electrical interfaces, operational plans, and data formats necessary for image processing routines.

Chapter 8: Summary and Future Work

The final chapter summarizes the key findings of the dissertation, highlighting its contributions to space-based methane measurement. It also offers insights into the research's implications and provides recommendations for future endeavors.

CHAPTER 2

BACKGROUND

2.1 Introduction to Space-Based Imaging Spectrometers

Remote sensing of the atmosphere primarily involves measuring the effects of the interactions between molecules, particles, and electromagnetic radiation. Passive methods encompass sensing thermal emissions in the infrared and microwave spectra, scattered solar radiation in the visible and ultraviolet ranges, and solar radiation absorption across all wavelengths from microwave to ultraviolet. Active techniques include radio occultation and lidar.

In the context of methane detection, prevailing methodologies primarily revolve around sensing thermal emissions or solar absorption using thermal infrared (TIR) and short-wave infrared (SWIR) imaging spectrometers, respectively. However, it's noteworthy that a promising space-based Lidar instrument, the Methane Remote Sensing LIDAR Mission (MERLIN), is currently under development through a joint French-German cooperation [11].

TIR spectrometers offer the advantage of not relying on reflected solar radiance but instead leveraging the contrast between target gas emissions and background radiation. This characteristic enables robust measurements over surfaces with low albedo, such as seawater and snow, as well as in high-latitude regions where SWIR spectrometer applications are limited. Notably, TIR spectrometers can operate during nighttime, further enhancing their utility.

However, TIR spectrometers demonstrate reduced sensitivity to methane concentrations in the lower atmosphere compared to SWIR spectrometers, which maintain uniform sensitivity across all atmospheric layers [12]. Furthermore, the design of TIR spectrometers requires more complex detectors with stringent cooling systems, leading to increased power demands and costs. Consequently, SWIR spectrometers are more commonly employed in satellites dedicated to trace gas measurements. The following section describes the different classes of imaging spectrometers based on how they acquire spatial and spectra information.

2.1.1 Imaging Spectrometer Classifications

Imaging spectrometers, used in remote sensing applications, are instruments capable of measuring the radiance as a function of the spatial and frequency domain. The data collected by those instruments are usually formatted as a 3-D dataset, also referred to as a data cube. If the radiance measurement is provided as absolute values through a process of absolute radiometric calibration, then the instrument might also be called an imaging spectroradiometer.

R. G. Sellar and G. D. Boreman [13] proposed a classification of imaging spectrometers based on the methods by which they acquire spatial and spectral information. The spatial information is acquired by scanning the area of interest, and the methods include whiskbroom, pushbroom, framing, and windowing. Methods of acquiring spectral information include interferometric, dispersive, and filtering techniques.

Scanning Methods

Fig. 2.1 lists the different types of spatial information acquisition methods commonly seen in remote sensing applications.

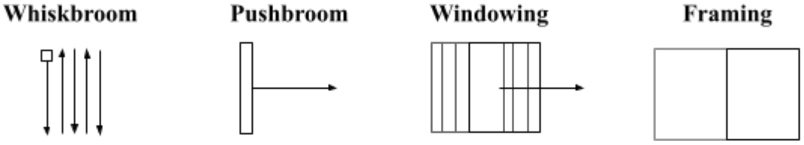

Fig. 2.1: Scanning Methods

Whiskbroom: In the whiskbroom scanning method, the instrument FOV forms a spot on the ground (0-D FOV). Typically using a rotating mirror, the spot scans the area in the cross-track directions, while it moves in the along-track direction using the platform motion. In this approach, the instrument scans the scene point by point along a curvilinear path, and all components of the spectrum are recorded simultaneously.

Pushbroom: In the pushbroom method, the instrument FOV is obtained by a slit aperture that translates to a line projected on the ground (1-D FOV), and the scan only happens in one direction, usually along-track, using the platform motion. Similarly to the whiskbroom, components of the spectrum are recorded simultaneously. This is a very common approach seen in a variety of imaging spectrometers.

Windowing: In the windowing method, the instrument employs a 2-D FOV, which captures the entire spatial information of the scene, but only a component of the spectrum on each exposure. To form the full spectrum, the instrument takes a sequence of overlapping images by moving the FOV along-track, where each image records a different component of the spectrum for each pixel. Those images are then stacked in a process known as registering. Differently from the last two scanning methods, in the windowing strategy, the components of the spectrum are not recorded simultaneously, which implies a different viewing geometry.

Framing: In the framing method, also known as the staring, the instrument employs a 2-D FOV, which remains locked over the target during the entire spectral acquisition. In this method, multiple frames can be concatenated along-track to extend the coverage.

Spectrum Acquisition Methods

Dispersive Spectrometers: Dispersive spectrometers use a prism or grating to disperse the incoming light spatially as a function of the wavelength. They are commonly associated with the whiskbroom and pushbroom scanning methods, where a line of detectors records the dispersed light coming from the ground samples.

Interferometric Spectrometers: Fourier-transform spectrometers (FTS), are typically based on two-beam interferometry using a Michelson interferometer, which splits the incoming beam into two beams and then recombines them after applying a time-varying optical path difference, creating an interferogram.

Filtering Spectrometers: Fabry-Perot and Interference filters are considered multi-beam interferometers but are classified in the filtering class since they operate as narrow bandpass filters given a certain light incidence geometry. [13]

2.2 Methane Absorption Spectrum

An imaging spectrometer can be designed to detect methane in the atmosphere by measuring the earth surface reflected solar radiance in a spectral region with distinguishable methane absorption lines. There are two regions within the SWIR band where intense methane absorption lines are present: one near the 1.6 μm wavelength and the other around the 2.3 μm wavelength. However, imaging spectrometers with high spectral resolution have limited bandwidth, so the instrument designer must choose between these two regions to operate the instrument, considering a series of potential trade-offs.

The first difference between the two spectrum regions can be seen by comparing the plots (a) and (d) in Fig. 2.5. In 1.6 μm band, the reflected solar radiance is almost four times higher than at 2.3 μm. This higher radiance level favors the 1.6 μm band for providing a higher signal-to-noise ratio, assuming the same surface albedo. In contrast, by comparing plots (b) and (e), which show the relative drop in radiance caused by doubling the CH_4 concentration across all layers of the atmosphere, we can see that the absorption features in the 2.3 μm band are much stronger and prominent over a wider range, making the 2.3 μm band more methane sensitive. Moreover, due to the presence of denser absorption lines, the 2.3 μm band requires lower spectrum resolution instruments to properly resolve the methane absorption features when compared to the 1.6 μm band.

It's crucial to be able to differentiate between radiance absorption caused by methane from other absorbers present in the atmosphere, such as water (H_2O). The plots (c) and (f) in Fig. 2.5 illustrates the radiance change as the effect of doubling the water concentration in the atmosphere. In the 1.6 μm band, the strongest methane absorption feature centered at 1666 nm is not significantly affected by water absorption, making it a distinguishable methane signature. On the other hand, in the 2.3 μm band, strong water absorption is present along with methane absorption features, particularly above 2340 nm wavelength.

However, the uncorrelated shapes of their absorption profiles make it possible to differentiate between CH_4 and H_2O.

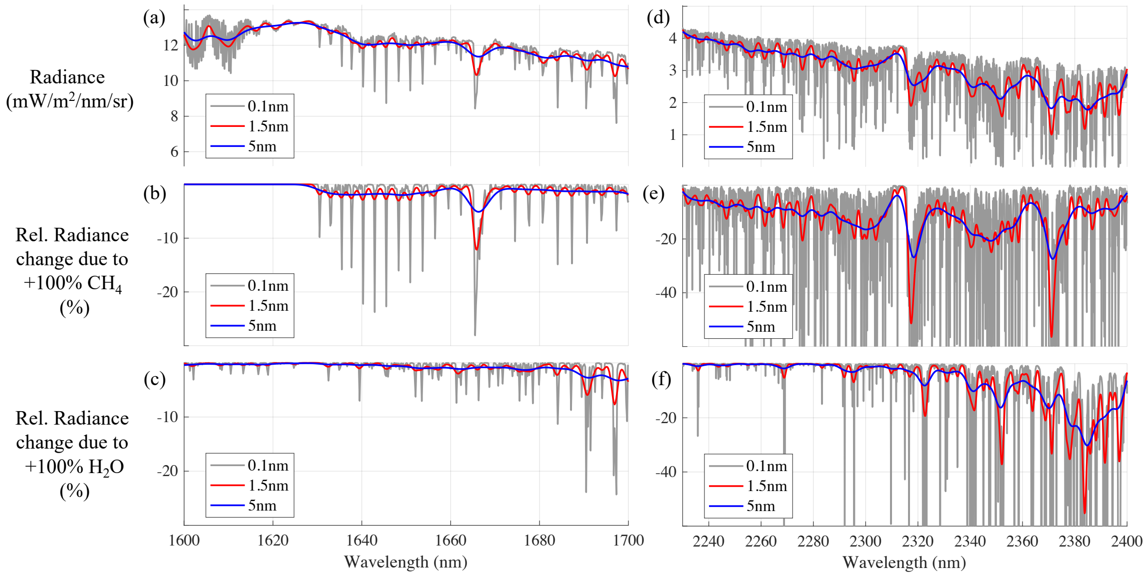

Fig. 2.2: Simulated top of atmosphere solar radiance for a standard profile atmosphere and 0.2 albedo surface for fitting windows around 1.6μm (a-c) and 2.3μm (d-f), and different spectral resolutions. The relative radiance change due to the increase of CH_4 (b,e) and H_2O (c,f) were simulated considered the same relative concentration increase throughout all layers.

Jongaramrungruang in [14] offers a comprehensive analysis comparing the two spectrum regions for CH_4 concentration retrieval. Among the findings, the 2.3 μm band is shown to provide consistently better performance in terms of methane retrieval precision when compared to the 1.6 μm band across different spectral resolutions. The only exception for that is when the surface has a much higher albedo at 1.6 μm compared to at 2.3 μm, which is not a highly representative situation since most of the surfaces present similar albedo for both bands. This result suggests that the more intense solar irradiance in 1.6 μm has a less dominant role in the methane retrieval performance compared to the stronger and broader absorption of CH_4 in the 2.3 μm region.

Besides the methane retrieval performance, another important practical aspect when choosing between the two bands is the detector technology and its temperature control requirements. For the 1.6 μm band, there are plenty of options for commercial-off-the-shelf (COTS) cameras with Indium Gallium Arsenide (InGaAs) detectors with cutoff wavelengths at 1.7 μm and integrated cooling systems, whereas for the 2.3 μm band, the detector is usually custom-built based on Mercury Cadmium Telluride (HgCdTe) technology and its cooling system needs to be also developed to meet stricter temperature ranges.

2.3 Current and planned space methane sensors

Significant advancements have been achieved over the past two decades in the development of space-based instruments capable of detecting and quantifying methane emissions across global, regional, and local scales. As illustrated in Fig. 2.3, a compilation of current and forthcoming space-based hyperspectral imaging spectrometers dedicated to trace gas measurements, including methane, underscores the strides made in this domain.

Moreover, recent studies have demonstrated the potential of multispectral data from general-purpose remote sensing satellites, such as Landsat-8/9 [15], Sentinel-2A/2B [16], and WorldView-3 [17], in methane monitoring, albeit with certain performance limitations attributed to lower spectral resolution.

Even with such a fleet of spacecraft, data acquisition is still insufficient to reduce the uncertainties over emission levels attributed to countries and sectors. The aggregated emission values reported by countries to the UN Framework Convention on Climate Change (UNFCCC) are roughly half of the estimated emissions attributed to the O&G sector [18]. Of particular significance is the status of numerous spacecraft currently operating in extended missions within the dedicated atmospheric monitoring satellite fleet, necessitating imminent consideration for their replacement.

Methane sensors deployed in space can be categorized according to their primary function. An Area Flux Mapper (AFM) is designed to measure methane concentrations dispersed over large areas, while a Point Source Imager (PSI) specializes in detecting localized methane enhancements originating from facilities or point source emissions. This classification primarily hinges on spatial resolution and measurement precision. [19]

AFM sensors typically exhibit coarse spatial resolution (pixel size > 1 km), offering global or regional coverage, coupled with high measurement precision (< 1%). In contrast, PSI sensors generally feature lower measurement precision (> 1.5%), limited to local coverage, but boast high spatial resolution (pixel size < 100 m), enabling the detection of plumes from small leaks. Some sensors possess intermediate capabilities, with pixel sizes in the order of hundreds of meters, serving as a compromise solution capable of functioning as both Area Flux Mappers with regional coverage and Point Source Imagers adept at detecting intermediate-sized plumes.

For further reference, Table 2.1 presents a comprehensive list of current and planned space-based methane sensors categorized by their application. Additionally, Fig. 2.4 presents the current and planned methane detection capability plotted in terms of coverage and the detection limit in terms of methane leak rate, measured in metric tonnes per hour.

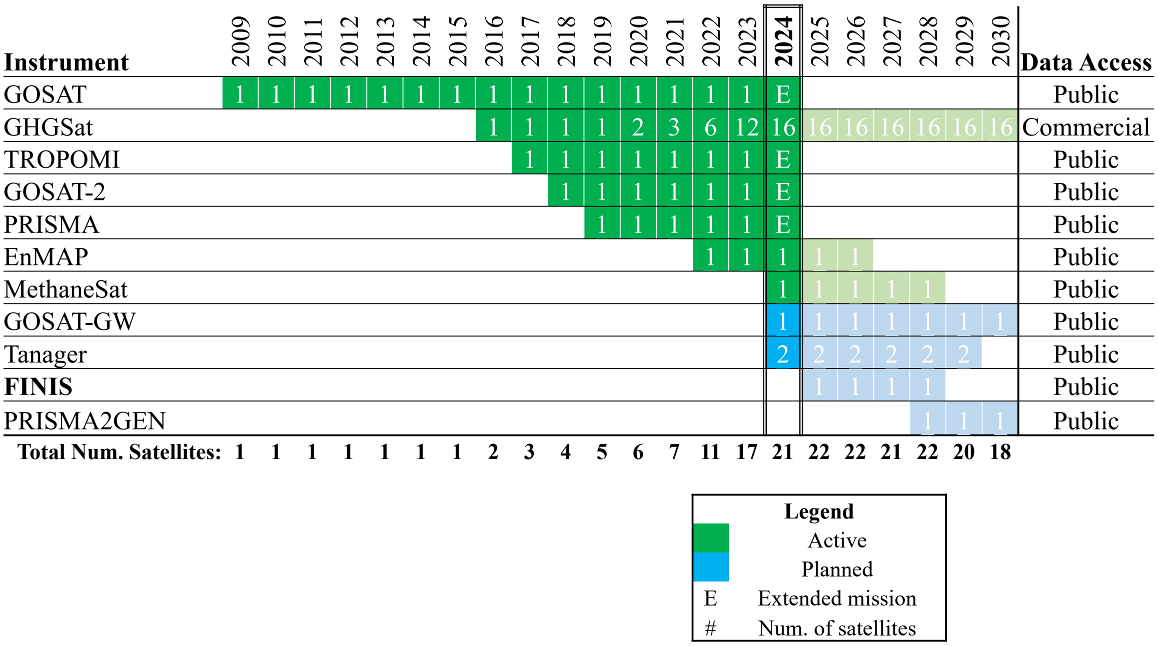

Instrument	2009	2010	2011	2012	2013	2014	2015	2016	2017	2018	2019	2020	2021	2022	2023	**2024**	2025	2026	2027	2028	2029	2030	**Data Access**
GOSAT	1	1	1	1	1	1	1	1	1	1	1	1	1	1	1	E							Public
GHGSat								1	1	1	1	2	3	6	12	16	16	16	16	16	16	16	Commercial
TROPOMI									1	1	1	1	1	1	1	E							Public
GOSAT-2										1	1	1	1	1	1	E							Public
PRISMA											1	1	1	1	1	E							Public
EnMAP														1	1	1	1	1					Public
MethaneSat																1	1	1	1	1			Public
GOSAT-GW																1	1	1	1	1	1	1	Public
Tanager																2	2	2	2	2	2		Public
FINIS																	1	1	1	1			Public
PRISMA2GEN																				1	1	1	Public
Total Num. Satellites:	**1**	**1**	**1**	**1**	**1**	**1**	**1**	**2**	**3**	**4**	**5**	**6**	**7**	**11**	**17**	**21**	**22**	**22**	**21**	**22**	**20**	**18**	

Legend

🟩	Active
🟦	Planned
E	Extended mission
#	Num. of satellites

Fig. 2.3: Current and planned dedicated space-based greenhouse gas monitoring sensors

The TROPOMI instrument, onboard the Sentinel-5P, operational since 2017, is an example of an AFM with a pixel size of 7 km x 5.5 km that has been used for measuring emissions at a regional scale (e.g., Permian basin in the US; [29]) and country scale (e.g.,

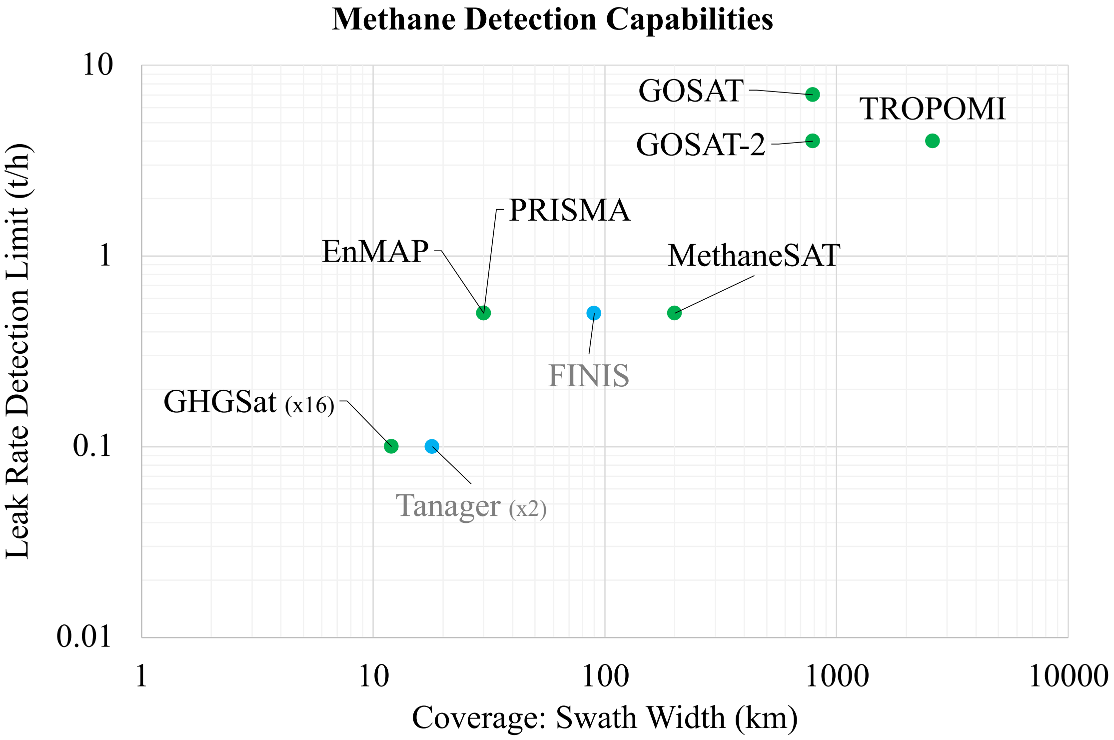

Fig. 2.4: Methane detection capabilities in terms of minimum detectable leak rate and coverage. The green dot indicates active instruments, and the blue dot indicates planned instruments.

Mexico; [30]). In contrast, PSI are designed to have narrower coverage in exchange for high spatial resolution (25-50m), which enables them to detect and quantify plumes from individual emitters on the ground. Governmental satellites such as PRISMA (Italy, launched in 2019) and EnMAP (Germany, launched in 2022), as well as the commercial satellites from GHGSat company, are in this category.

Hybrid space methane sensors are designed to fill the gap between AFM and PSI. They provide intermediate spatial resolution and coverage, enabling them to map area flux and detect point source emissions. MethaneSAT, recently launched in 2024, is an example of this category.

Table 2.1: Current and planned space-based methane sensors

Instrument	Number of Satellites	Nadir Pixel	Precision**	Swath (km)	Application	Ref.
Active sensors:						
GOSAT	2	10 km^a	0.7%	750	AFM	[20]
TROPOMI	1	5.5x7 km^2	0.8%	2600	AFM	[21]
GHGSat	16	25x25 m^2	1.5%	12	PSI	[22]
PRISMA	1	30x30 m^2	3-9%	30	PSI	[23]
EnMAP	1	30x30 m^2	3-9%	30	PSI	[24]
EMIT (ISS)	1	60x60 m^2	2-5%	75	PSI	[25]
Planned sensors:						
GOSAT-GW	1	1x1,10x10 km^2	0.6%	90 - 911	AFM	[26]
MethaneSAT	1	130x400 m^2	0.1-0.2%	200	AFM/PSI	[27]
Tanager	2	30x30 m^2	1.2-1.5%	18	SPI	[28]

** Precision is reported as a percentage of the retrieved dry column methane mixing ratio.
[a] Circular pixel diameter

2.4 Spectrometer technologies

Spaceborne imaging spectrometers used for atmospheric sounding exhibit considerable diversity in terms of complexity, volume, power consumption, and mass. These instruments can be classified based on the method used to collect spatial and spectral information, as discussed in Section 2.1.1. Additionally, they can be categorized according to their primary application: Area Flux Mapper or Point Source Imager, as explained in Section 2.3. It's noteworthy that each spectrometer design offers a unique set of capabilities, and its suitability for a particular mission is contingent upon specific mission requirements. Fig. 2.5 illustrates the classification of the current and planned space-based imaging spectrometers in terms of their scanning and spectrum acquisition methods. Subsequent sections delve deeper into the operational principles of each spectrometer class, elucidating their strengths and limitations in greater detail.

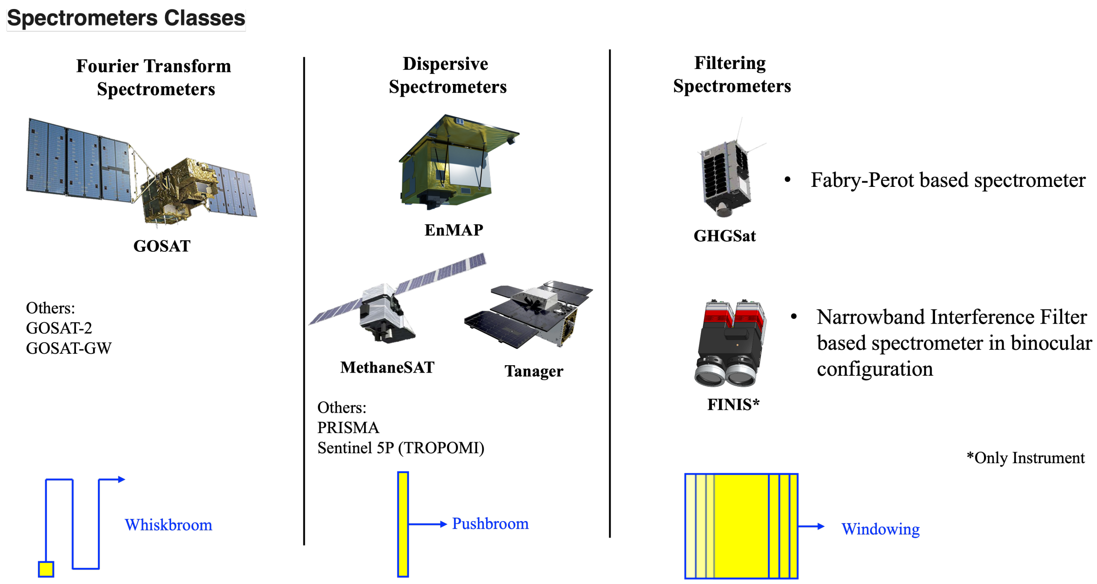

Fig. 2.5: Imaging spectrometer classes of current space-based methane sensors, including FINIS.

2.4.1 Fourier Transform Spectrometers

The JAXA's Greenhouse Gases Observing Satellite (GOSAT) series are equipped with Fourier Transform Spectrometers (FTS), named TANSO-FTS. In those spectrometers, the collected light is directed onto a beamsplitter, which divides the light into two beams. Using a rotary mechanism attached to a double pendulum with two cube-corner reflectors, the TANSO-FTS creates an variable optical path difference between the two beams, which are then recombined at the beamsplitter and interfere with each other. This interference pattern, known as an interferogram, is detected by multiple photodetectors, one for each band. The interferogram contains information about the spectrum of the light, encoded in the form of fringes. By applying Fourier transform mathematics to the interferogram, the spectrum of the light can be reconstructed. Fourier transform converts the time-domain interferogram into the frequency-domain spectrum. This process allows for high-resolution spectral measurements across a wide range of wavelengths. Additionally, it's worth noting that FTS spectrometers are typically configured as whiskbroom systems, where a single detector sweeps across the scene perpendicular to the satellite's motion. [31]

Launched in 2018 onboard GOSAT-2, a 1750kg spacecraft, the TANSO-FTS-2 spectrometer has four bands, one more than the previous TANSO-FTS. For methane emission quantification, band 2 is used, covering wavelength from 1.56μm to 1.72μm with spectral resolution lower than 0.27cm^{-1} ($\sim$0.08nm, FWHM). Moreover, to ensure optimal data quality, TANSO-FTS-2 incorporates intelligent pointing, utilizing a dedicated monitor camera and onboard cloud detection algorithms to avoid cloud-obscured data acquisition. [31]

However, despite the remarkable spectral capabilities, TANSO-FTS spectrometers grapple with inherent limitations. Their coarse spatial resolution, around 10.5km of round pixel size, renders them inadequate for pinpoint methane leak detection. Furthermore, the intricacies of their design pose significant challenges for widespread utilization. Weighing in at 225kg and with an average power consumption of 270W, these spectrometers prove impractical for deployment in small satellite applications, underscoring the need for alternative solutions in certain contexts.

2.4.2 Dispersive Spectrometers

Dispersive spectrometers, the most common class of spectrometers among greenhouse gas (GHG) satellites, are instruments used to measure the spectrum of light by dispersing it into its constituent wavelengths. This is typically achieved using a diffraction grating or prism, where light of different wavelengths is bent at different angles, allowing for the separation and analysis of the spectrum. In the context of methane detection, dispersive spectrometers offer certain strengths and limitations. One of their key strengths lies in their ability to provide high-resolution spectral measurements, allowing for precise identification and quantification of methane concentrations in the atmosphere. Additionally, dispersive spectrometers often offer a wide spectral range, enabling the detection of multiple gases simultaneously. However, they are typically limited by their size, weight, and power requirements, making them less suitable for deployment on small satellites or unmanned aerial vehicles. Furthermore, their mechanical moving parts may introduce complexities and potential points of failure, necessitating careful calibration and maintenance to ensure accurate measurements over time. These spectrometers are usually configured as pushbroom systems, where a linear array of detectors sweeps across the scene to collect spectral data, offering efficient coverage and high spatial resolution.

TROPOMI is an example of an advanced 200kg dispersive spectrometer (grating-based) onboard a 1-ton class spacecraft, Sentinel-5P (launched in 2017). It was designed to observe a long list of atmospheric constituents such as ozone (O_3), nitrogen dioxide (NO_2), carbon monoxide (CO), sulfur dioxide (SO_2), methane (CH_4), and others [32]. To enable this broad usage, it covers the ultraviolet-visible (270-495 nm), near-infrared (675-775 nm), and shortwave infrared (SWIR, 2305-2385 nm) bands, with a spectral resolution of 0.25 nm in the SWIR band [33]. It features specialized freeform mirrors in its telescope [21], a folding mirror mechanism, a polarization scrambler, a complete calibration unit, and a dedicated radiant cooler [32,34]. A similar level of design complexity also tracks back to its predecessors, such as the Global Ozone Monitoring Experiment (GOME, 50 kg, launched in 1995, [35]), the SCIAMACHY (198kg, launched in 2003; [36]), and the Ozone Monitoring Instrument (OMI, 65 kg, launched in 2004; [37]).

Additionally, PRISMA (launched in 2019) and EnMAP (launched in 2022) represent further instances of dispersive spectrometers employing prism technology [23, 24]. Both instruments boast comparable acquisition capabilities: ground sample distance (GSD) of approximately 30 meters, swath widths spanning 30km, and spectral resolutions in the SWIR band of around 10nm. While PRISMA and EnMAP serve as versatile hyperspectral imagers catering to diverse environmental monitoring tasks, their broader design mandates necessitated spectrometers capable of broader spectral coverage and additional onboard calibration functionalities. Consequently, this expanded functionality significantly impacted their system complexity, physical dimensions, and mass. With launch masses of 830kg and 980kg for PRISMA and EnMAP, respectively, the prospect of assembling them into a satellite constellation to enhance temporal resolution becomes economically unviable.

The recently launched MethaneSAT is classified as a grating-based dispersive spectrometer. Weighing approximately 350 kilograms, MethaneSAT incorporates two grating spectrometers: one targeting the methane weak band (1605-1683 nm) and another spanning the 1249-1305 nm range to measure O_2 concentration, thereby constraining the optical path in the atmosphere. Both spectrometers deliver a spectral resolution of 0.3 nanometers with a spectral sampling of 0.1 nanometers. In comparison to point source imagers, MethaneSAT offers a moderate spatial resolution (approximately 100m×400m) but boasts a significantly wider field-of-view (FOV) of 21 degrees, translating to about 200km at nadir, considering its orbital altitude design of 526 km. To optimize detection performance, each spectrometer employs custom-built HgCdTe detectors featuring 2048x2048 pixels, necessitating maintenance at or below 190 Kelvin. However, a notable downside is that MethaneSAT requires a separate and dedicated cryogenic thermal system for focal plane cooling. [27]

2.4.3 Filtering Spectrometers

Filtering spectrometers operate by selectively allowing specific wavelengths of light to pass through a filter while blocking others. This methodology facilitates the isolation of spectral bands relevant to methane detection and analysis. In the context of methane detection, filtering spectrometers exhibit distinctive strengths and limitations. One notable advantage is their simplicity and robustness, often resulting in reduced size, weight, and power consumption compared to dispersive counterparts. This makes them more suitable for deployment on smaller platforms such as CubeSats or unmanned aerial vehicles, expanding the accessibility of methane monitoring capabilities. Additionally, filtering spectrometers can offer excellent spectral resolution within targeted methane absorption bands, enhancing sensitivity to methane concentrations in the atmosphere. However, their spectral range may be limited compared to dispersive spectrometers, potentially constraining their ability to detect additional gases simultaneously. Furthermore, precise calibration and characterization are crucial to ensure accurate measurements, particularly due to potential spectral overlap and calibration drift over time.

In 2016, the Canadian firm GHGSat launched its inaugural methane-focused satellite, GHGSat-D [22]. Weighing a mere 15 kilograms at launch, GHGSat-D showcased the prowess of its innovative compact filtering spectrometer in measuring surface-level methane emissions with high spatial resolution (30–50 m GSD), ideal for monitoring methane emissions at the facility scale. Diverging from conventional grating or prism spectrometers, GHGSat devised and patented its spectrometer employing a wide-angle fixed-cavity Fabry-Pérot (FP) as its primary filtering element [38]. Operating on a distinctive measurement concept called windowing, the spectrum is captured as the satellite traverses the target area, capturing a sequence of overlapping images at a high rate (approximately 200fps). Because the FP pass-band depends on the angle of incidence (AOI) of the incoming light from the target, each image in the observation sequence records a different segment of the methane weak band (1630-1675 nm), later assembled through post-processing image registration. Despite its restricted measurement domain (12×12 km^2; [39]) and inherent technical challenges, GHGSat-D successfully showcased the potential of its filtering spectrometer to generate valuable and commercially viable data, paving the way for the company to augment its fleet with an enhanced iteration of its initial FP spectrometer.

As elaborated upon in this dissertation, FINIS also falls within this category of spectrometers. However, it diverges from GHGSat's spectrometers, which employ fixed-cavity Fabry-Pérot (FP) technology. Instead, FINIS leverages the wavelength bandpass dependency with the AOI of its narrowband interference filters positioned at the telescope aperture. Both methodologies yield significantly higher optical transmittance for instruments compared to the more prevalent dispersive push-broom spectrometers. Whereas the optical transmittance of a typical diffraction grating-based spectrometer typically falls below 40% [40, 41], FINIS achieves over 85% optical transmittance in each imager. This remarkable performance is attributable to its streamlined optical design, comprising just one high-transmission narrowband interference filter at the entrance, three anti-reflective coated lenses, and one blocking filter in each telescope. Consequently, FINIS enjoys a substantial light throughput advantage, enabling it to deliver comparable signal-to-noise ratio (SNR) performance while retaining a compact form factor.

2.5 Expanding Methane Monitoring Capabilities

As previously assessed, the current landscape of space-based greenhouse gas sensors, with the exception of commercial GHGSats, predominantly relies on large and intricate satellite platforms weighing over 100 kilograms to sustain their operations. With medium-to-high spatial resolution, these sensors encounter limitations in revisit rates, primarily due to the prohibitive costs associated with launching multiple units. This restricted revisit frequency over a given area hampers the ability to capture potential emissions variability and impacts the application of mass balance and atmospheric models essential for estimating the methane budget using the top-down approach. A significant airborne campaign over the Permian Basin in 2019 revealed that 74% of the 1100 detected sources were intermittent, underscoring the necessity for enhanced monitoring capabilities [42]. Furthermore, persistent cloud cover, particularly in wet tropical regions, poses challenges for obtaining valid measurements. A constellation of nanosatellites, such as CubeSats, outfitted with greenhouse gas sensors, offers a cost-effective remedy to these challenges by enabling more frequent revisits to the same targets at various times of the day.

Previous endeavors to develop lightweight instruments for CubeSat applications include the Argus 1000 and 2000 series of SWIR micro-spectrometers [43]. Due to their compact size (4.5 x 8 x 8 cm) and minimal mass (approximately 280 grams), both versions of Argus have been successfully deployed in various nanosatellite missions. However, the Argus 2000, utilizing a grating to disperse light onto an array of 1x256 InGaAs detectors, offers a limited field-of-view (FOV) of 0.15 degrees or about 1.4 kilometers at a 550-kilometer orbital altitude. Although covering a wide spectral range from 1.0 to 1.65 micrometers, its coarse spectral resolution of 6 nanometers, coupled with high instrument noise (2.5% per pixel), renders it inadequate for accurately retrieving atmospheric methane concentrations.

While not directly suited for methane retrieval, the Nano-satellite Atmospheric Chemistry Hyperspectral Observation System (NACHOS) stands out as a noteworthy endeavor in developing a lightweight hyperspectral imager for greenhouse gas monitoring in CubeSat applications. Launched in 2022, NACHOS, a 3U CubeSat, is equipped with a compact grating-based spectrometer based on an Offner-type design [44]. Covering a wavelength range of 290-500 nanometers with a spectral resolution of 1.3 nm and sampling of 0.57 nm, NACHOS is particularly adept at measuring NO_2 and volcanic SO_2. With a swath width of approximately 130 kilometers and spatial resolution of 400 meters at an orbital altitude of roughly 485 kilometers, NACHOS showcases the potential for CubeSats in atmospheric monitoring.

As graphically represented in Fig. 2.6, this research endeavor seeks to bridge this technological gap and empower CubeSats to accurately monitor methane emissions. FINIS represents the next evolution in lightweight imaging spectrometer development, capable of delivering precise spectral radiance measurements over the methane absorption feature around 1666 nm wavelength. By harnessing advanced interference filter technology and methodologies, FINIS aims to unlock new frontiers in methane monitoring from space, revolutionizing our understanding and management of important greenhouse gas emissions.

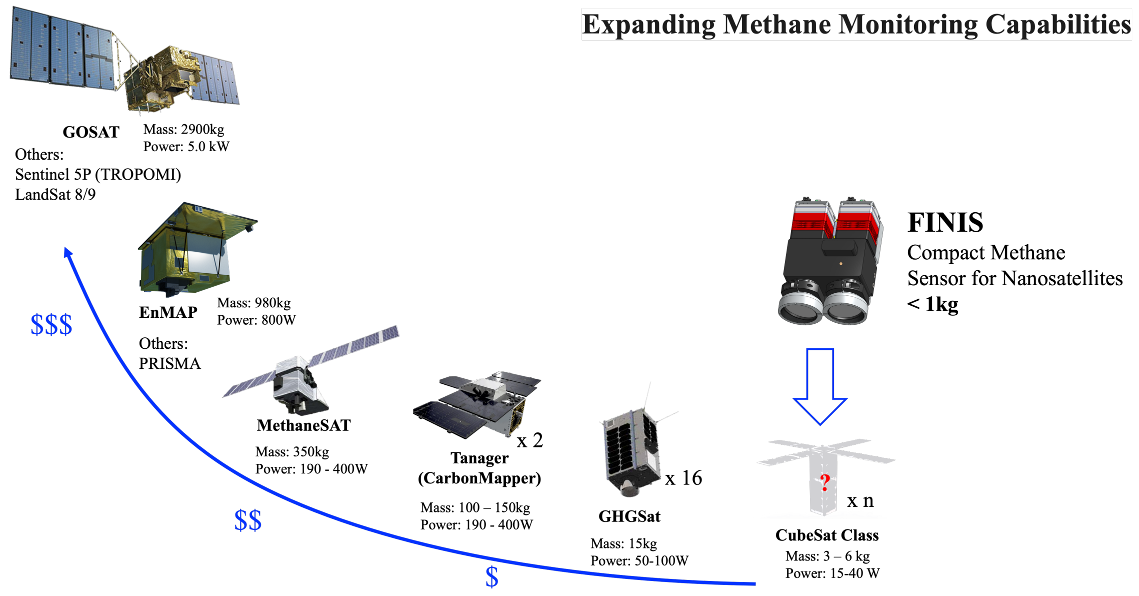

Fig. 2.6: FINIS as compact new IR spectrometer enables more cost-effective solutions for methane monitoring using nanosatellites

CHAPTER 3

INSTRUMENT DESIGN AND DEVELOPMENT

This chapter explores the process of designing and developing FINIS, an imaging spectrometer intended for a space flight demonstration. It begins by outlining the mission objectives, focusing on the instrument's goal of detecting methane plumes with precision. We then explain how the sensor collects data and delve into its optical design. Next, we present the finalized CAD models showcasing the instrument's mechanical structure and components. Finally, we discuss the onboard calibration design, emphasizing its importance in ensuring accurate measurements throughout the mission. This chapter offers a concise overview of the steps taken to create FINIS, a groundbreaking tool for methane monitoring from space using nanosatellites.

3.1 Mission Objectives and Requirements

As explored in Section 1.2, this study represents a technological advancement of FINIS informed by earlier developments. Consequently, the specifications for this upgraded spectrometer, intended for its space demonstration, were formulated under certain constraints. For instance, the Tau SWIR cameras were chosen based on their flight heritage and to leverage existing interfaces with the spacecraft's main computer. Opting for a different camera would inevitably escalate development costs and extend the schedule. Furthermore, considering FINIS received the opportunity to fly on the ACMES mission as a student-led research project rather than as the primary payload, it was imperative that any design modifications to FINIS adhered to its allocated resources within the bus.

The original optical design for FINIS featured a compact and optically fast telescope with an F-number of approximately 2, predominantly utilizing Commercial Off-The-Shelf (COTS) lenses. To maintain consistent image quality performance and adhere to the objective of a compact and simple design, the new instrument necessitated a similar telescope setup. Through considerations such as available COTS lenses, instrument total size considering the binocular configuration, and interference filter size constrained by manufacturing capabilities and costs, an aperture diameter of approximately 28 millimeters was determined to be optimal, providing a field of view (FOV) of around 10 degrees, which balances image quality, spatial resolution, and coverage. At an orbital altitude of 550 kilometers and leveraging the 512x640 detector size offered by the Tau SWIR cameras, this FOV equips the new FINIS with a swath of about 90 kilometers and a spatial resolution of roughly 140 meters GSD.

For its inaugural space flight test, the primary goal is to showcase FINIS's ability to detect point sources of methane, achieving performance on par with other methane sensors possessing similar spatial coverage and resolution. In terms of detection limit performance, this goal can be achieved if FINIS is shown to be able to meet the following objectives:

- detect methane plumes with leak rates equal to or higher than 1 ton/h, under slow wind speed (5 km/h), in low illumination conditions: solar zenith angle (SZA) of 60 degrees and surface albedo of 0.2; and
- detect methane plumes from leak rates equal to or higher than 500 kg/h, under slow wind speeds (5 km/h), in medium illumination conditions: SZA equals to 30 deg and surface albedo of 0.2.

Table 3.1 summarizes FINIS mission objectives in terms of point source detection capability.

Table 3.1: Detection capability objectives

	Illumination Condition	SZA (°)	Albedo	Wind Speed (km/h)	Detection Limit (t/h)
Objective 1	Low	60	0.2	5	1.0
Objective 2	Medium	30	0.2	5	0.5

Those detection objectives can now be used to derive the retrieval precision requirement for FINIS. To do so, we consider the relative mean methane concentration enhancement ΔX

caused by the presence of a plume relative to the upwind background concentration. The diagram in Fig. 3.1 depicts the main scenario parameters that drives the detection capability, such as wind speed U, leak rate Q, pixel size W, SZA, and surface albedo. As demonstrated in [39], ΔX can be estimated using the mass balance equation given by Eq. (3.1), where g is gravity acceleration, p is dry surface atmospheric pressure and $M_a = 0.029$ kg mol^{-1} and $M_{CH_4} = 0.016$ kg mol^{-1} are the molecular weights of dry air and methane, respectively.

$$\Delta X = \frac{M_a}{M_{CH_4}} \frac{Qg}{UWp} \tag{3.1}$$

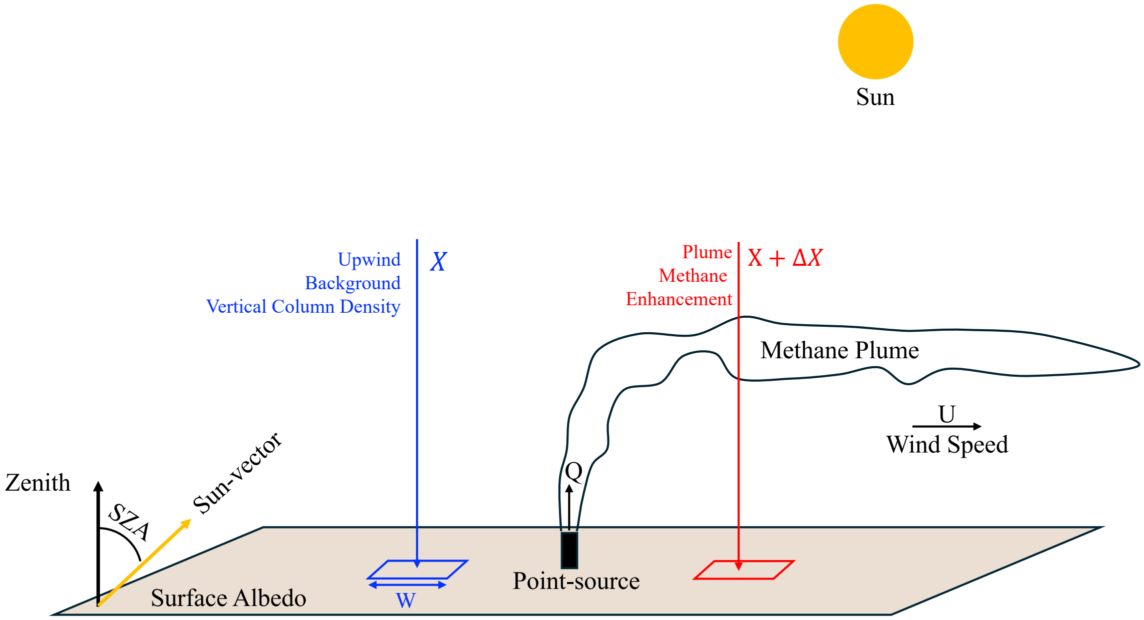

Fig. 3.1: Methane plume detection scenario definitions

Assuming $p = 1000$ hPa, $U = 5$ km/h, and $W = 140$m, a leak rate of 1 t/h results in a $\Delta X = 253$ parts per billion (ppb). Given a background concentration of 1800 ppb, this corresponds to a relative concentration enhancement of approximately 14%. For detection purposes, the retrieval precision must be at least half of this enhancement (a factor of two), equating to around 7% to fulfill Objective 1 (1th^{-1}) as outlined in Table 3.1. As this relationship is linear, Objective 2 (0.5th^{-1}) necessitates a retrieval precision of 3.5%

for the same pixel size. Fig. 3.2 illustrates the correlation between pixel size, leak rate, and measurement precision. Due to uncertainties regarding pixel size arising from factors such as orbital altitude, integration time, and optical performance, the plot depicts an interval for FINIS pixel size and, consequently, precision to satisfy each objective.

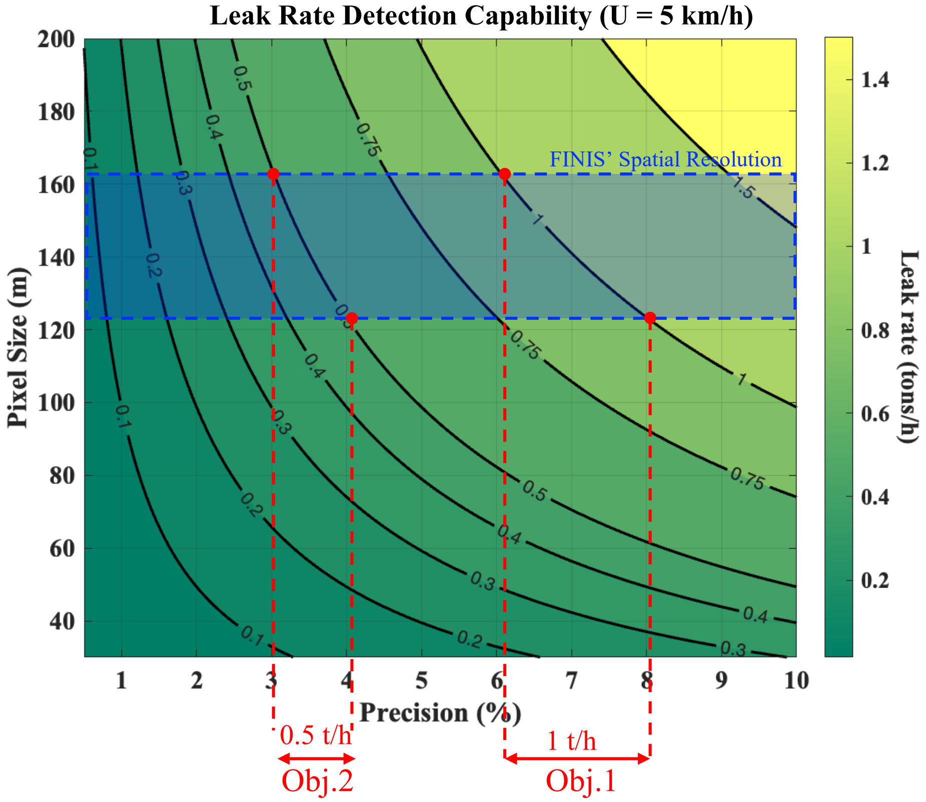

Fig. 3.2: Retrieval precision requirement as a function of single-pass detection limit and the sensor's spatial resolution. Wind speed: 5km/h, Surface Pressure: 1000hPa.

Table 3.2 summarizes the retrieval precision requirements to satisfy the detection objectives.

Table 3.2: Retrieval precision requirement to satisfy detection objectives

	Leak Rate (t/h)	Retrieval Precision Requirement σ_{CH_4}	Conditions
Obj. 1	1.0	6%	SZA = 60°, Alb = 0.2, U = 5km/h
Obj. 2	0.5	3%	SZA = 30°, Alb = 0.2, U = 5km/h

3.2 Concept of Operation

FINIS is a special type of infrared spectrometer that has two imagers, with a common 2D field of view. The instrument is designed to have a fixed nadir-pointing as the satellite passes over the target area. It collects both spatial and spectral information as it scans the target area in a method known as windowing [45]. The method of windowing involves moving the field of view across the target area in the along-track direction while acquiring a sequence of overlapping exposures as illustrated in Fig. 3.3.

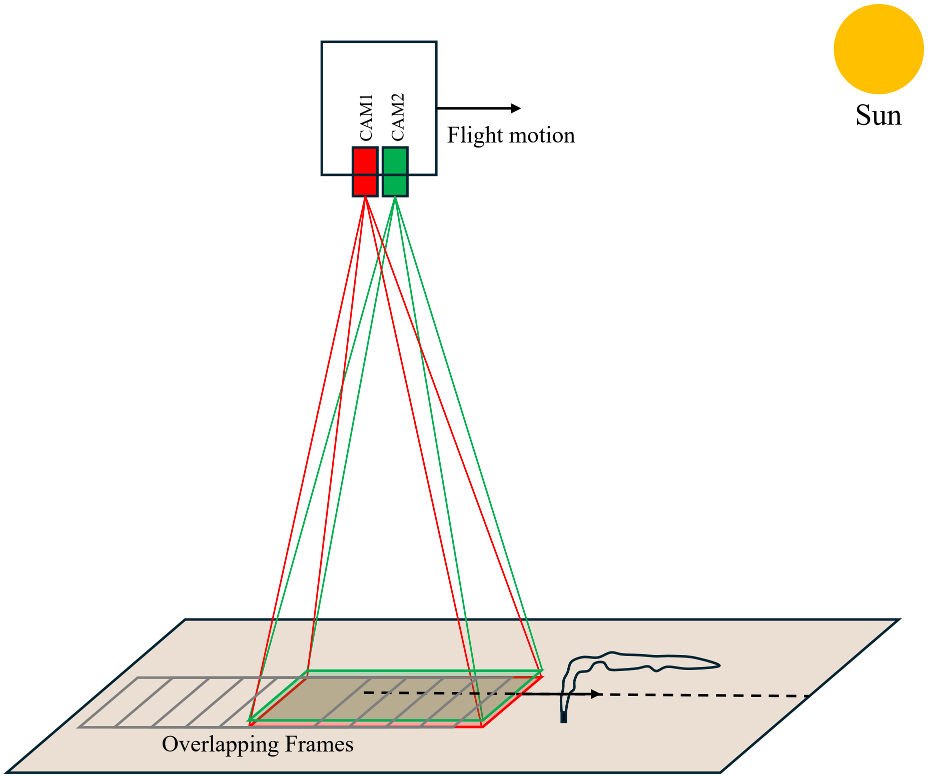

Fig. 3.3: FINIS ground scanning concept

A unique filtering approach is used to retrieve the spectral information. A narrowband interference filter (IF) is placed at the entrance of each imager, tilted relative to the imaging plane. Both IFs and optical assemblies are identical. This approach exploits the band-pass dependency of the IF on the angle of incidence (AOI) of the incoming light, which varies across the FOV. Consequently, the spectral information is imprinted across the image as a function of the AOI from ground sample light, depending on the viewing angle and the IF's relative orientation. As the target moves across the FOV, the images taken by both imagers capture different portions of the target spectrum. During the processing phase, the overlapping images are registered, and the full spectrum of all ground samples that crossed the FOV is reconstructed.

The tilted angles of the IFs on both imagers were tuned to cover the strongest methane absorption feature located in the 1.66μm wavelength region, taking into account the IF optical properties and the instrument F-number. The tilted angles of IF 1 and 2 are the same, but they are mirrored with respect to each other. This design choice was introduced to ensure that any target inside the FOV is simultaneously measured at two different wavelengths while observed with the same illumination (same viewing geometry). As will be discussed later, this feature enables rapid methane plume detection by comparing the pairs of images as they capture the approximated differential methane optical thickness. Regions with significantly higher than background differential methane optical thickness will be considered methane plume candidates.

3.3 Fitting Window Optimization

This section delves into the optimization of the spectral fitting window, which is essential for producing effective relative measurements with heightened methane sensitivity and minimal spectral correlation with water vapor. It specifically addresses the scenario where the spectra of both cameras are assumed to be mirrored, meaning that both imagers have identical interference filters (IFs), mounted with the same tilted angle but rotated in opposite directions along the same axis. FINIS exploits this spectrum symmetry in its methane retrieval algorithm, combining pairs of images to generate relative measurements.

The definition of the optimal spectral fitting window, which minimizes methane retrieval noise, dictates the IF requirements in terms of the center wavelength at normal incidence and the necessary tilt angle to create the desired spectral response.

The search for the optimum fitting window is depicted in Fig. 3.4, where the optimization variables include the start of the fitting window, denoted by λ_0, and the width of the fitting window, denoted by B. The search space is approximately centered around the strongest methane absorption feature, spanning from 1650nm to 1685nm. Within this spectrum range, no other atmospheric trace gas, besides methane and water vapor, exhibits significant absorption lines. The plot shows methane and water vapor's relative weighting functions (WF). The magnitude of the WF reflects the relative change in the measurement y with a 100% increase in the concentration of the respective gas. For the case shown in the plot, for example, where the measurement y is simply defined as the spectrum radiance L_1, a 100% increase in methane concentration induces a 12% decrease in radiance at 1666nm.

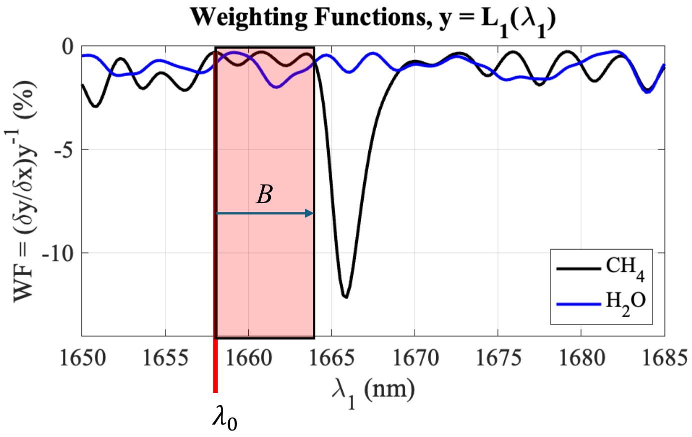

Fig. 3.4: Optimal fitting window search. Variables: Start wavelength (λ_0) and Bandwidth (B). Spectrum convolved considering 1.5nm FHWM.

To examine the performance of each fitting window, the retrieval precision is estimated by computing the covariance matrix of the optimum retrieval considering methane concentration, water vapor concentration, and albedo in the state vector with no prior information (unconstrained). A more in-depth explanation of the optimum retrieval method and how the covariance matrix is computed is provided in Section 4.5.1.

For each fitting window case, 50 radiance measurements with SNR=100 are considered. The sample wavelengths for both sensors are considered uniformly spaced, and the sequence of wavelengths for CAM2 is assumed to be identical to CAM1 in reverse order. Those assumptions simplify this analysis and are considered sufficient for the purpose of finding the optimal fitting windows; however, as will be seen in Section 4.2, the actual wavelength distribution in the image plane is not uniform, and the sample wavelengths vary across the FOV. In Section 5.2, the retrieval precision is re-evaluated considering the actual sensor performance and the correct wavelength samples for different crossing locations in the sensor's FOV.

As will be discussed in Section 4.5.1, both optimum and fast retrieval methods rely on the measurement vector y, computed by the natural log difference of each image pair, denoted as $y = ln(L_1/L_2)$ (unitless), where L_1 and L_2 represent the spectral radiance measured by the cameras CAM1 and CAM2, respectively. The wavelength λ_1 and λ_2 represent the wavelength samples of CAM1 and CAM2, respectively. The retrieval precision computed for each fitting window, therefore, is optimum when the water and methane weighting functions of the relative measurements are most uncorrelated, allowing us to distinguish between the contributions of the two gases.

The options of start wavelength λ_0 were explored within the range of 1650nm to 1670nm, while the bandwidth B varied from 5 nm to 15 nm. In Fig. 3.5, the retrieval precision figure of merit is depicted for all combinations of λ_0 and B. The regions with the lowest values, denoted by the darkest blue color, exhibit retrieval precision between 2–3%.

To gain further insight into the results, three specific points in the search space were examined: the first located near the left optimal region ($\lambda_0 = 1659$ nm, $B = 9$ nm), the second in middle of the right optimal region ($\lambda_0 = 1663$ nm, $B = 9$ nm), and the third in the sub-optimal region located between the two "lobes" ($\lambda_0 = 1661$ nm, $B = 10$ nm), where retrieval noise exceeded 10%.

In Fig. 3.6, the fitting window and weighting functions for the relative measurements at the first point near the left optimal region are displayed. The estimated retrieval noise for this point is 3.4%. As will be seen in Section 4.2, this corresponds to FINIS' fitting window.

Similarly, Fig. 3.7 showcases the measurement weighting functions for the second point in the right optimal region of the search space. For this point, the estimated retrieval noise

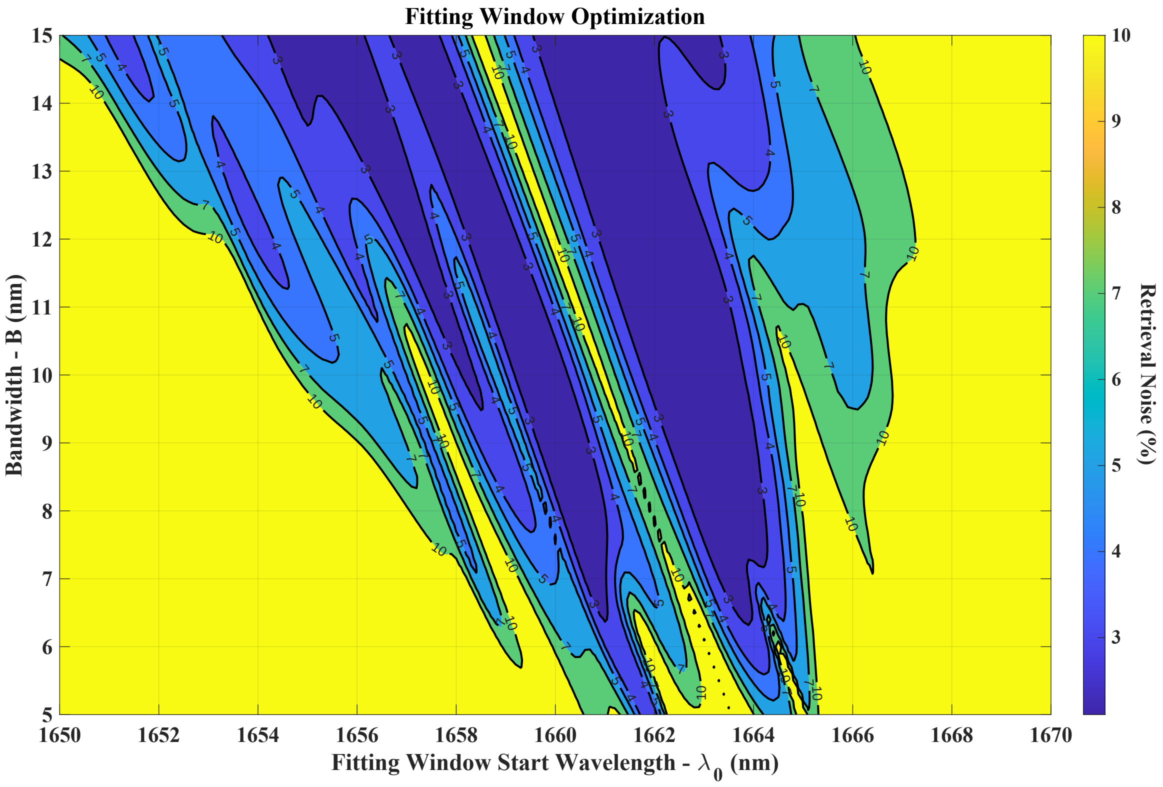

Fig. 3.5: Fitting window optimization

is 2.2%, indicating that this fitting window offers even higher retrieval precision than the first analyzed point. This improved performance is due to a more effective neutralization of water vapor absorption, as evidenced by the near-zero weighting function for water when the measurement is performed by the ratio.

Lastly, Fig. 3.8 illustrates the sub-optimal scenario where the methane absorption feature is centrally located within the fitting window. As depicted in the relative measurement's WF plot, the water and methane sensitivity curves exhibit a significantly higher correlation, while the methane sensitivity is notably lower compared to the optimal fitting windows described earlier. This disparity elucidates the diminished retrieval performance observed in this case.

As discussed in the forthcoming sensor model detailed in Section 4.1, the center wavelength (CWL) of the interference filter (IF) for normal incident light and the tilt angle were selected to closely approximate the fitting window outlined in Fig. 3.6. It's worth

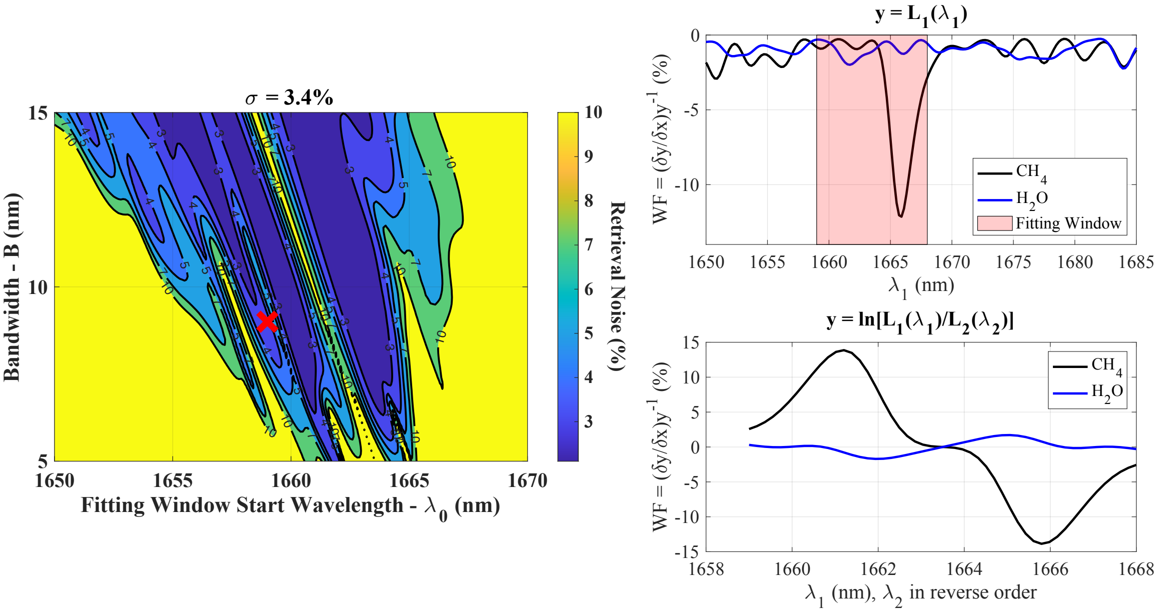

Fig. 3.6: Fitting window from 1659nm to 1668nm and respective measurement weighting functions for methane and water vapor. (left) Fitting window search space. (upper right) Methane and water WFs plots showing the fitting window region. (bottom right) Methane and water WFs plots for the relative measurement combining wavelength samples from CAM1 and CAM2.

noting that the CWL distribution across the image plane is non-linear, resulting in slight differences between the wavelengths sampled from CAM1 and CAM2 compared to those considered in the optimization analysis. However, as elucidated in Section 5.2, the retrieval precision outcomes incorporating the actual CWL distribution exhibit similar results.

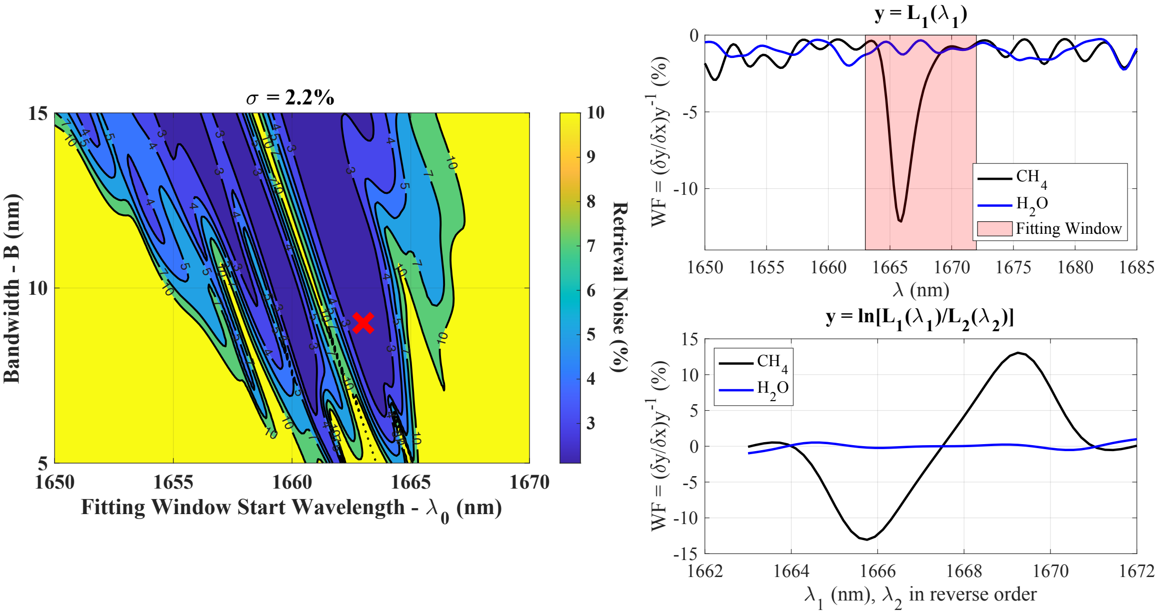

Fig. 3.7: Fitting window from 1663nm to 1672nm and respective measurement weighting functions for methane and water vapor. (upper right) Methane and water WFs plots showing the fitting window region. (bottom right) Methane and water WFs plots for the relative measurement combining wavelength samples from CAM1 and CAM2.

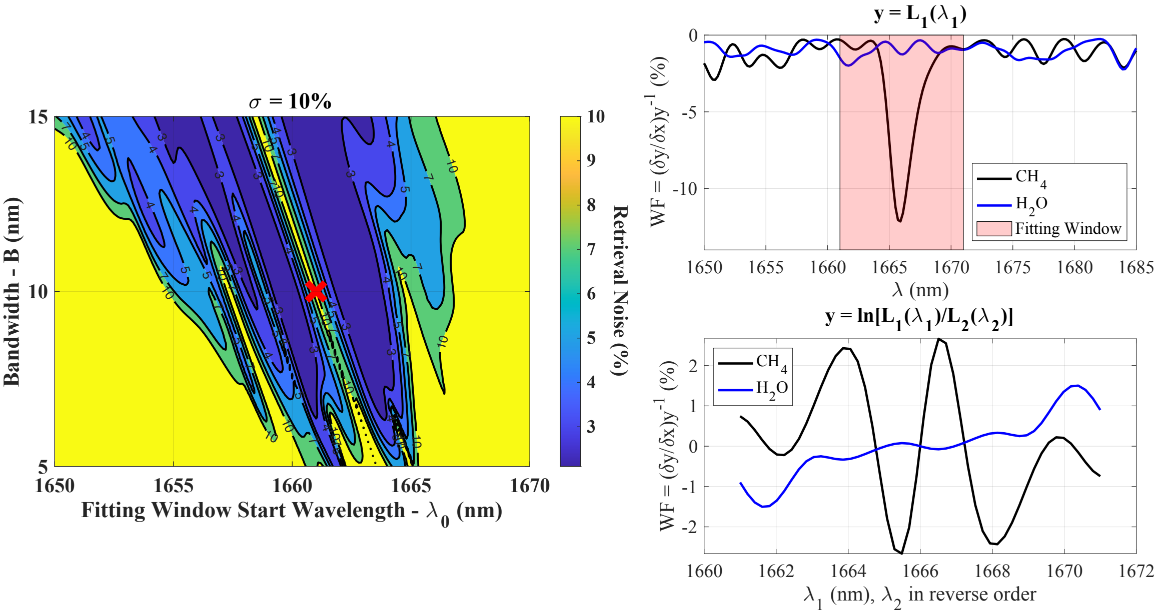

Fig. 3.8: Fitting window from 1661nm to 1671nm and respective measurement weighting functions for methane and water vapor. (upper right) Methane and water WFs plots showing the fitting window region. (bottom right) Methane and water WFs plots for the relative measurement combining wavelength samples from CAM1 and CAM2.

3.4 Optical Design

The optical design for FINIS went through a lot of iterations to accommodate all the changes from the original design show in Fig. 3.9. One of the most significant change was the replacement of the Goldeye cameras by the Tau SWIR cameras, which changed the size and spacing of the FPA.

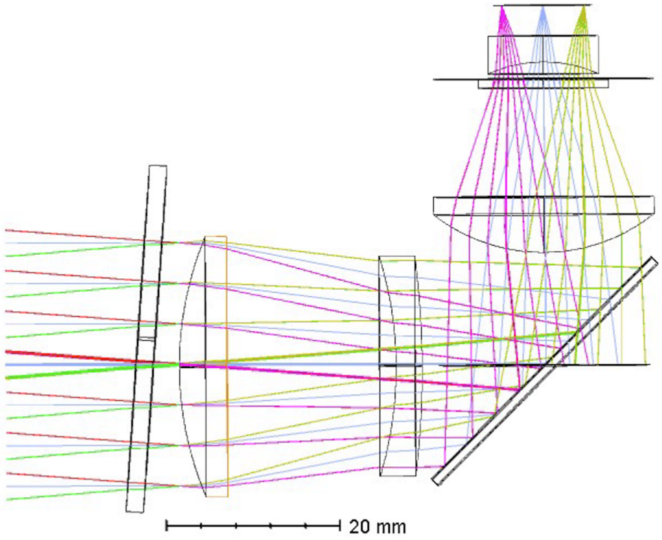

Fig. 3.9: Original optical design of FINIS

The new FINIS optical design were conducted using a ray-tracing software called OSLO from Lambda Research. The design had the following main requirements and constraints:

- The instrument's FOV shall be 10°;
- All lenses shall be COTS;
- The instrument's length, considering the camera, shall be less than 15 cm;
- The instrument shall use the previously selected Tau SWIR cameras;
- The instrument shall use the narrowband IF at its aperture;
- The instrument shall incorporate a blocking filter;

The optimum lenses' curvature radius and the spacing between all elements were found through an iterative optimization process, where the error function was set as such to minimize the spot size on the FPA, considering the different field points. The FOV of 10 degrees across the FPA's longest side (9.6 mm) was achieved by constraining the effective focal length to be around 55 mm. Several iterations were needed to ensure that all lenses could be acquired from vendors without the need for custom-making.

The resultant optimized optical layout with the ray tracing is presented in Fig. 3.10. During the optimization routine, the spacings between elements 1 to 3 were fixed as they are internal parts of the Tau SWIR cameras. The lenses' details are presented in Table 3.3.

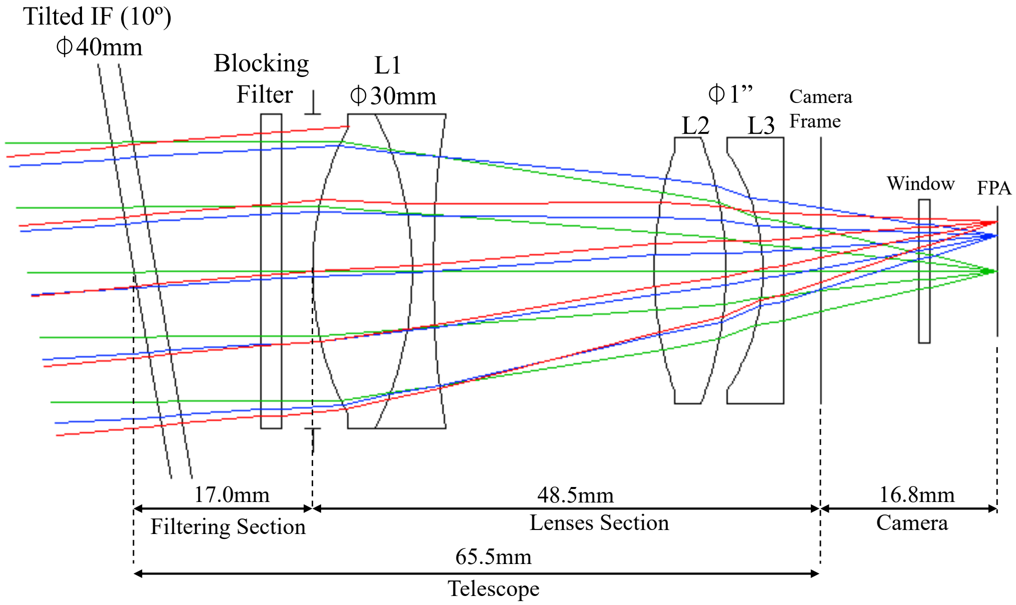

Fig. 3.10: New FINIS optical design showing the ray tracing and optical elements spacing

Table 3.3: FINIS lenses information

Element (Name)	Curvature radius (mm)	Central thickness (mm)	Diam. (mm)	EFL (mm)	Material
L1 (Doublet)	29.4, -33.9, 97.7	9.5, 2.0	30	30	N-BAF10/N-SF6
L2	34.9, -34.9	6.8	25.4	35	N-BK7
L3	-20.76, inf	2.0	25.4	-40	N-BK7

In Fig. 3.11, the modulation transfer function (MTF) derived from the optimized optical model is showcased. The system's spatial Nyquist rate, calculated based on the Focal Plane Array's (FPA) longest side (640 pixels/9.6 mm), amounts to 33 cycles/mm. At the 50% threshold, the system's cut-off frequency stands at approximately 23 cycles/mm at the edge of the field.

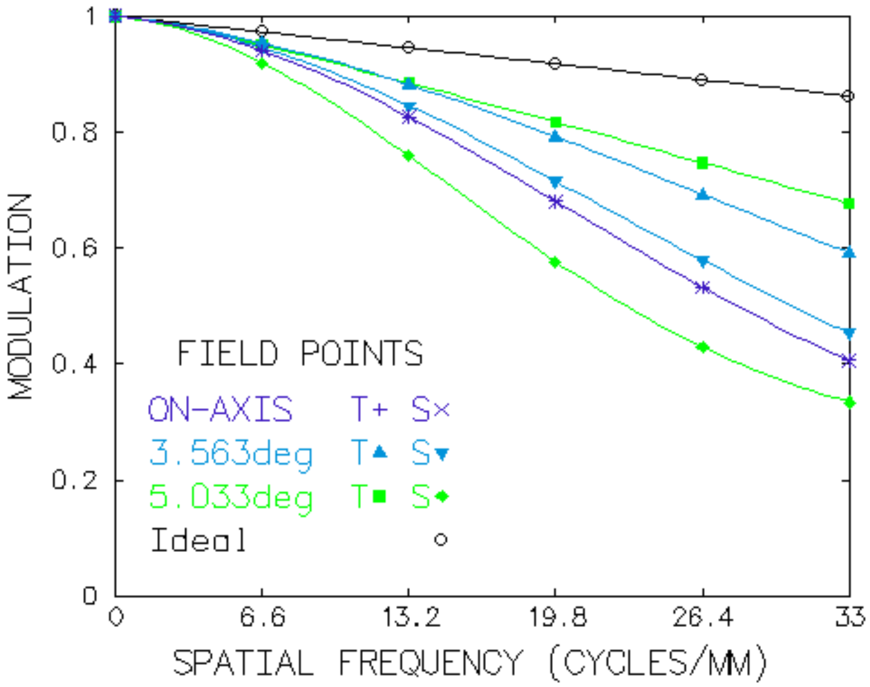

Fig. 3.11: Modulation Transfer Function

In Fig. 3.12, the Spot Size diagram is presented, showcasing various focus shifts. The reference scale of 0.2 mm corresponds to approximately 13 pixels in width. Overall, the systems presents good performance across the field, with minor astigmatism and coma aberrations closer to the field edge.

Meanwhile, Fig. 3.13 illustrates the Root Mean Square (RMS) of the spot size across the image field, alongside the Optical Path Distance (OPD). This parameter refers to the disparity in the optical path length experienced by light rays passing through an optical system in comparison to a reference path. Such discrepancies arise from deviations in the

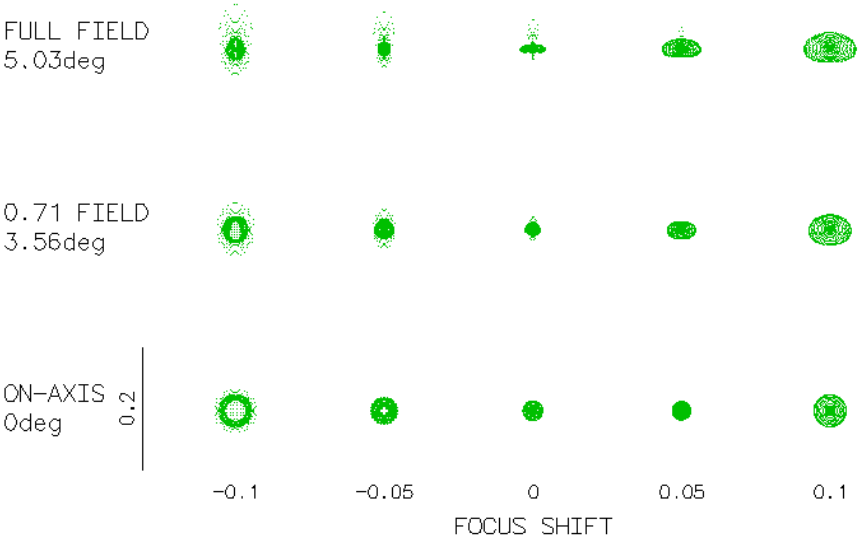

Fig. 3.12: Spot size diagram. Scale units: mm

shape or thickness of optical elements, inducing phase variations in the transmitted or reflected light. Given the detector size of 0.015 mm in the Tau SWIR camera, the spot size RMS is anticipated to remain below 80% of the pixel size, indicating a sufficiently sharp image quality for the system.

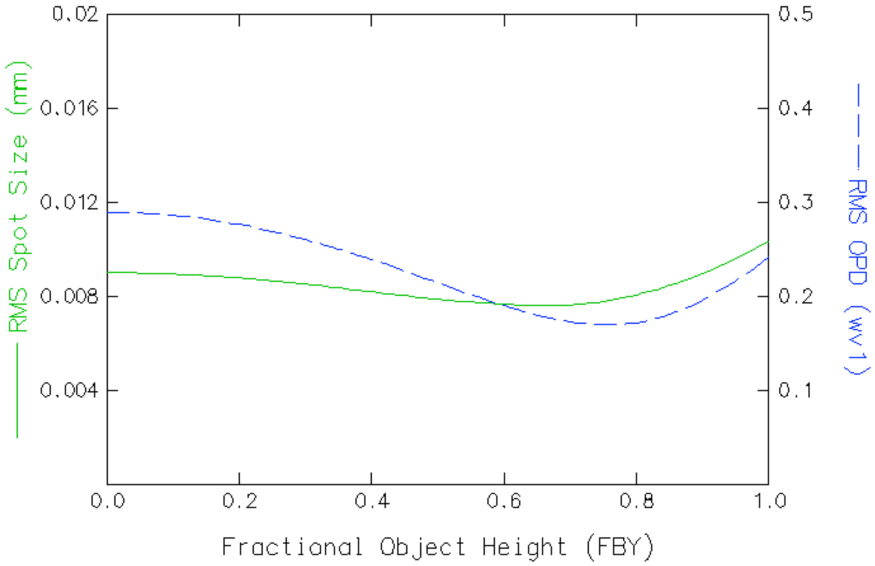

Fig. 3.13: Spot size RMS over field position

3.5 Mechanical Design

Following the completion of the optical design, which established the dimensions and spacing of the optical components, Michael Kirk undertook the mechanical design of the instrument. The mechanical design process involved careful consideration of various factors, as outlined below. For a comprehensive understanding of the design choices and iterative process, please refer to Michael Kirk's Master Thesis [46].

- The two telescopes shall maintain stable relative pointing with less than 1 degree of angular pointing separation;
- The IF shall be placed at the entrance of each telescope ensuring the correct tilt axis alignment with longest FPA's side;
- The instrument shall have an onboard calibration unit capable of dark and flat fielding calibration for both imagers;
- The shutter shall be mechanically held in the open position during launch;
- The base plate shall provide mechanical stability and thermal power dissipation;

Fig. 3.14 presents the final and complete CAD model of FINIS. Table 3.4 presents the instrument dimensions and estimated total mass.

Table 3.4: FINIS - Size and Design Mass

Parameter	Value	Unit
Instrument dimensions (H×W×L)	7.3×9.7×12.7	cm
Total mass	0.9	kg

Fig. 3.15 depicts a top-view cross-section of the instrument, illustrating the dense packing of components within the instrument to optimize both volume and mass utilization. The lenses were housed within threaded lens tubes and secured in place by retaining rings. The IFs placed at the aperture are also secured by retaining rings that are threaded with the same tilt angle.

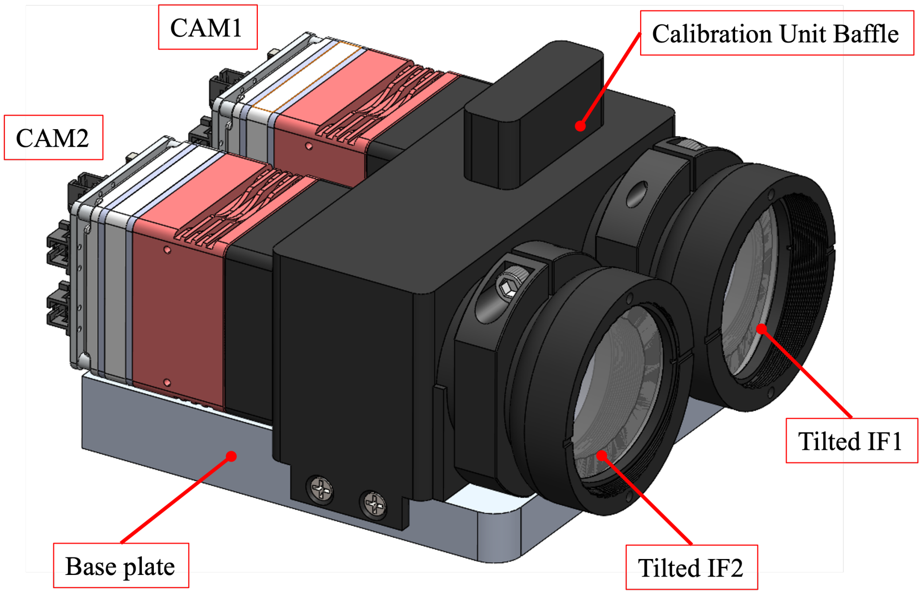

Fig. 3.14: FINIS - Complete CAD model in isometric view

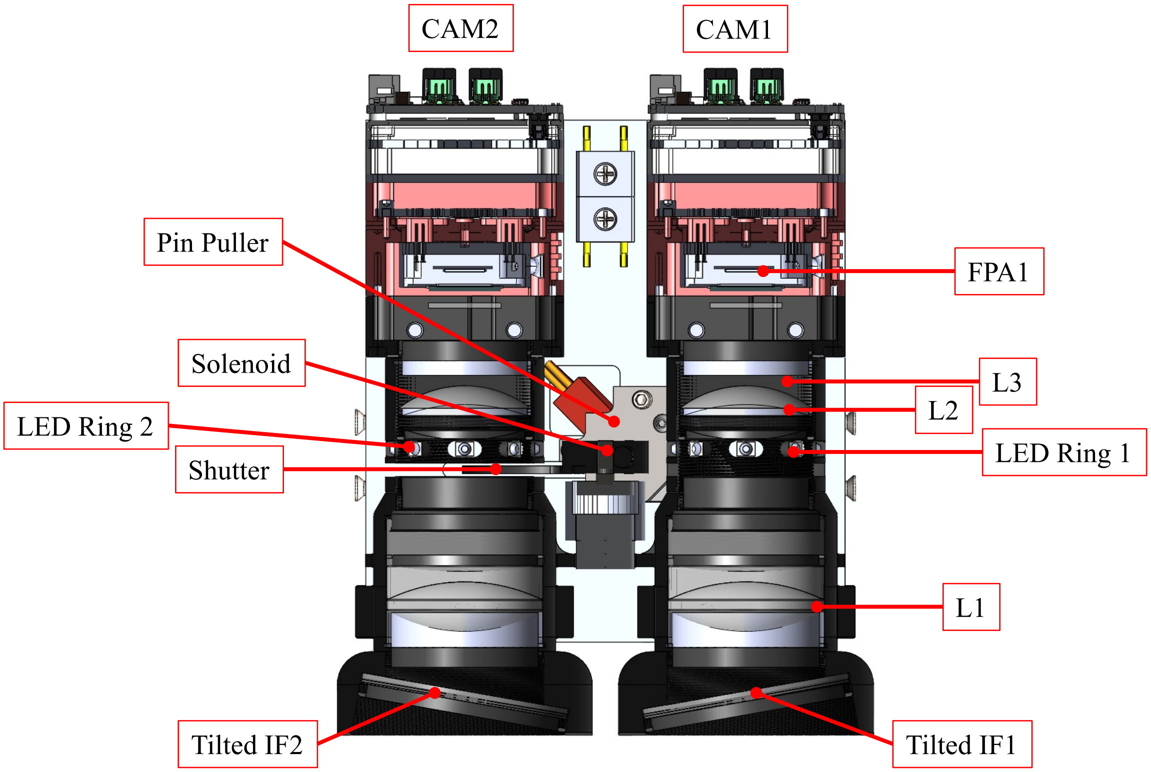

Fig. 3.15: FINIS - CAD model cross-section top view

3.6 Onboard Calibration Unit

FINIS design incorporates an onboard calibration unit capable of dark current and flat-fielding calibration to ensure measurement stability and accuracy. As show in Fig. 3.16, the unit consists of a rotating double shutter and a ring of LEDs. When activated, the double shutter entirely blocks the incoming light on both optical sets, allowing the acquisition of dark frames from both cameras. The shutter paddle is also covered with a diffusive reflecting film, so when illuminated by the LEDs, the shutter becomes a quasi-uniform target to perform the bright frames acquisition used in the flat-fielding calibration.

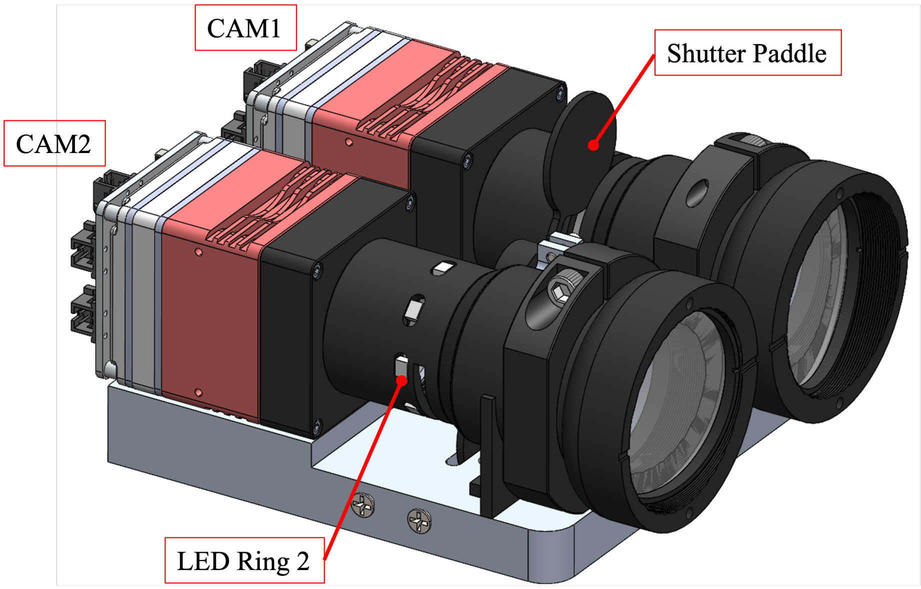

Fig. 3.16: FINIS CAD model showing the calibration unit uncovered by the baffle

The details of the diffusive film are presented in Fig. 3.17. A low-outgassing epoxy, FH-5313, was employed to adhere the film to the aluminum surface of the shutter.

The shutter rotation is performed by a self-restoring rotary solenoid, which magnetically latches the shutter in the open position until it is energized. This feature was selected to mitigate the risk of having the instrument blocked by the shutter in the case of a power loss or mechanical malfunction. During launch, a single-cycle pin-puller actuator will secure the shutter in its open position. Once deployed, the pin-puller retracts its pin, freeing the

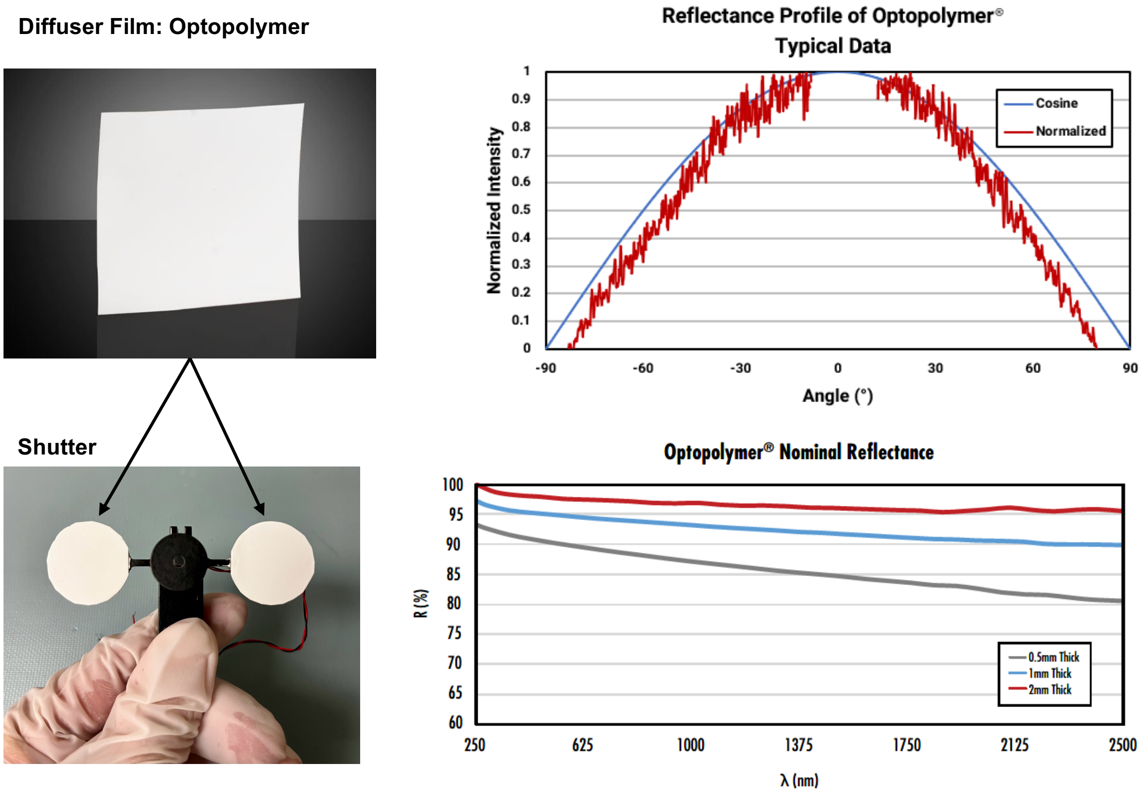

Fig. 3.17: Diffusive reflecting film used to cover the shutter surface: Optical PTFE Material with Lambertian Reflection. Showing the material's reflectance properties. Film thickness used: 1.0mm. Credits: Edmund Optics and Optopolymer.

shutter for movement.

Ideally, the shutter would be placed at the entrance of the instrument, covering all optics. However, that would require a shutter size of 40mm in diameter, a more powerful solenoid, and inevitably more volume to accommodate the shutter in its open position. Instead, the shutter was placed between the lenses L1 and L2 in the one-inch diameter section to keep the instrument under its available volume in the ACMES mission. The LED ring was placed right in front of the shutter, with all LEDs pointing towards the center of the tube.

The LED ring was designed to incorporate a total of eight IR LEDs. These LEDs are connected in parallel and mounted on a flexible PCB strip, as shown in Fig. 3.18. The strip is wrapped around the 1-inch lens tube section, which features eight machined through-holes to accommodate the LEDs. This design choice fully conceals the LEDs within the tube cross-section, effectively mitigating issues related to stray light. Additionally, the LED ring design incorporates a 10kΩ thermistor attached to the back of the strip to monitor the temperature of the ring. This allows for adjustments to the input signal based on temperature readings.

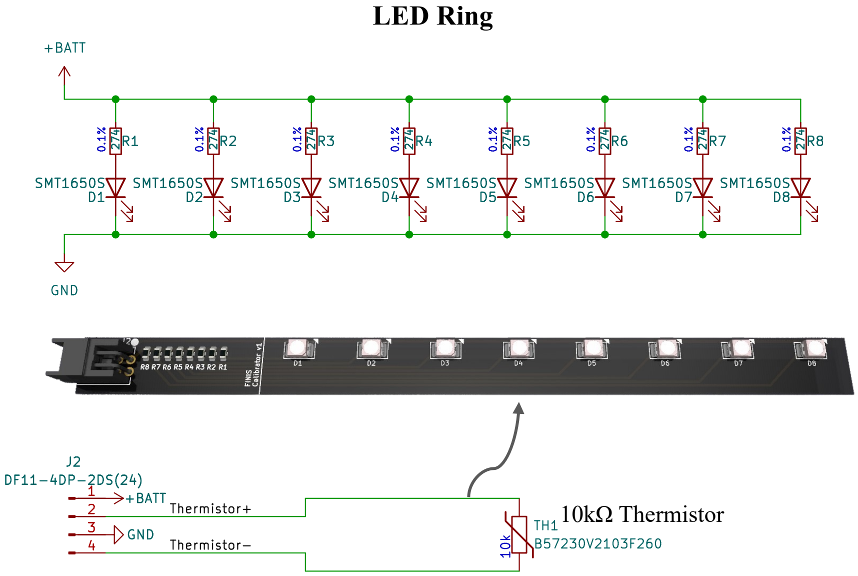

Fig. 3.18: LED Ring electronic and Flex PCB design. Credits: Rowan Antonuccio

A ray tracing analysis evaluating the illumination pattern over the shutter by the LED ring, as observed by the FPA, is detailed in Section 5.5.

CHAPTER 4

MODELS AND METHODS

This chapter delineates the sensor's modeling as an imaging system capable of capturing spectrum information across the FPA. It elucidates how the instrument's spectral response can be deduced from the scene-viewing geometry using the IF's properties and its bandpass dependency on the AOI. Additionally, the chapter presents the inputs and assumptions employed in the Radiative Transfer Model (RTM), crucial for simulating the spectrum radiance reaching the sensor in orbit. Furthermore, it outlines the plume model, essential for the subsequent Plume Detection Simulation as detailed in Section 5.4. Lastly, two methane retrieval approaches are discussed. Initially, the optical retrieval method is introduced to establish the groundwork for the inversion problem and to ascertain the rigorous estimation of retrieval noise using the Maximum Posterior Solution (MAP) approach. Subsequently, a fast retrieval method is proposed to capitalize on FINIS's relative measurements from both imagers, yielding less computationally intensive methane concentration maps suitable for detecting methane plume candidates.

4.1 Sensor Model

This section explains the sensor model employed to simulate FINIS measurements and estimate its operational performance. As illustrated in Fig. 4.1, FINIS is made up of two identical optical sensors that share the same field of view, creating a binocular system. Each sensor is modeled with a tilted narrowband interference filter (IF) at the entrance, an ideal imaging lens, and a focal plane. The ideal imaging lens acts as a circular aperture stop, while the focal plane array (FPA) functions as a rectangular field stop. Both FPAs have uniform characteristics in terms of responsivity and noise, and they have the same dimensions.

The telescope entrance has two narrowband interference filters identified as IF1 and

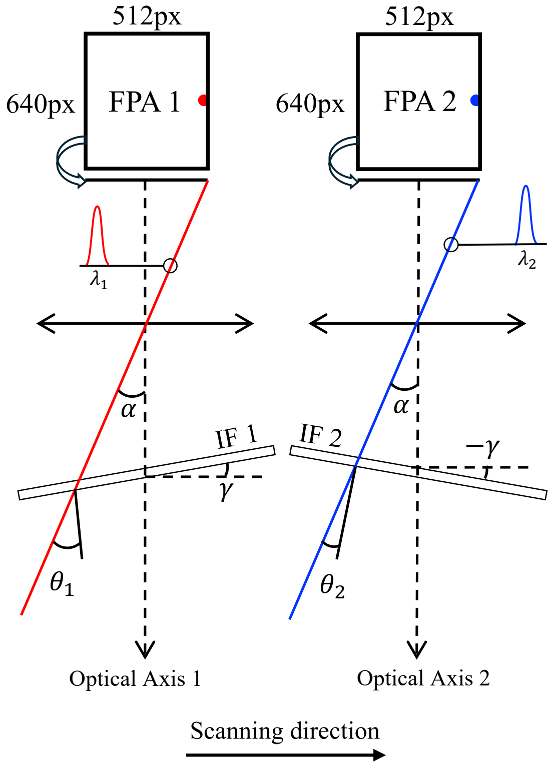

Fig. 4.1: FINIS simplified optical model

IF2. They have the same optical properties and are positioned with tilt angles γ and $-\gamma$ (listed in Table 4.1), respectively, in relation to the image plane as shown in Fig. 4.1. The angle at which the light from a given target point strikes the filter surface is known as the angle of incidence (AOI). The AOI in the IF1 and IF2 are indicated as θ_1 and θ_2, respectively. The angle α indicates the off-axis angle of a target centered at the cross-track direction but at the edge of the in-track FOV ($\alpha = FOV_i/2$). Since the scene distance, given by the orbital altitude, is infinity in comparison to the separation of the two sensors, the parallax is negligible.

As will be seen in Section 4.1.2, the center wavelength (CWL) of the IF's passband shifts toward a longer wavelength as the AOI (θ) increases. Since the tilt angle of both interference filters (IFs) has the same magnitude but is oriented in opposite directions along the same rotating axis, the center wavelength (CWL) distribution across FPA 1 is mirrored in FPA 2.

Table 4.1: FINIS optical parameters

Parameter (unit)	Symbol	Value
Focal length (mm)	f	55
Entrance aperture diameter (mm)	D	27
Entrance aperture area (mm^2)	A_c	572.55
F-number (-)	F	2.04
Optical efficiency (-)	τ_e	86.75%
Field of view cross-track (°)	FOV_c	9.97
Field of view in-track (°)	FOV_i	7.98
Instantaneous field of view ($mrad$)	$IFOV$	0.272
Tilt angle (°)	γ	10

The optical transmittance of each optical element is listed in Table 4.2. The details of the FPA are covered in the next subsection.

Table 4.2: Optical transmittance informed by the optical components' vendors

Element	Commercial Name	Vendor	Optical Transmittance (%)	Anti-Reflection Coating
Narrrowband IF	–	Alluxa	98	–
L1	AC300-080-C	Thorlabs	98	1050–1700 nm
Blocking Filter	BLP01-1550R	AVR Optics	99	–
L2	LB1811-C	Thorlabs	98	1050–1700 nm
L3	SLB-25-40N	OptoSigma	98	1650–1670 nm
Camera Window	–	FLIR	95	–
	System Optical Efficiency		**86.75%**	

4.1.1 Focal Plane Array

The FPAs are formed by the detector arrays of two identical Flir Tau SWIR cameras shown in Fig. 4.2. Those cameras were selected from a list of SWIR COTS cameras using a decision matrix, where the volume, detector array area, quantum efficiency (QE) and mass were the main decision drivers [46]. The detector array parameters provided by the cameras's manufacturer are listed in Table 4.3.

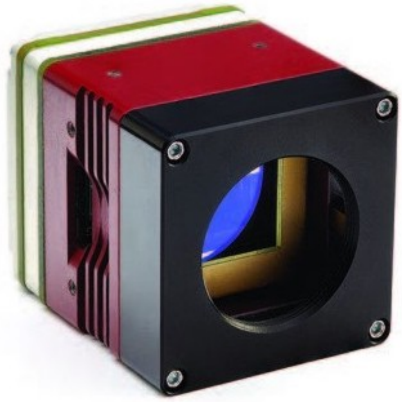

Fig. 4.2: Tau SWIR camera from FLIR

The Tau SWIR camera can operate in three gain modes: low, medium, and high. The camera documentation provides the Noise Equivalent Irradiance (NEI) only for the low and high gain, measured with the FPA at 20°C at a specific integration time (noise frequency bandwidth). The NEI is the irradiance value incident at the FPA that produces

Table 4.3: Tau SWIR camera - detector array parameters [1]

Parameter	Value
Manufacturer	FLIR
Model (Version)	Tau SWIR (Industrial)
Detector array size	640x512
FPA area	9.6 x 7.68 mm
Detector type	Indium Gallium Arsenide (InGaAs)
Detector size	15 μm
Detector area	2.25E-6 cm^2
Pixel depth	14 bits
Spectral range	0.9 - 1.7 μm (SWIR)
Quantum efficiency (QE)	60%

a unity SNR in the detector output, thus, it serves as an important figure of merit for the detector sensitivity. The NEI value for medium gain was interpolated from the low and high gain NEI values and reference integration times t_{ref} assuming a linear relationship between $NEI_{ref}\sqrt{t_d^{ref}}) \propto W_{e-}$, where t_d^{ref} is the reference integration time, and W_{e-} is well size, measured in terms of number of electrons. This assumption considers that the sensor's normalized detectitivy D* (D-star) increases linearly with the well size, thus the ratio of D* and the well size remains constant for all gains (same noise performance per electron).

The D* can be derived from the NEI values using Eq. (4.1). NEP is Noise Equivalent Power, which can be computed from NEI by multiplying it with the detector area A_d (2.25E-6 cm^2) and the photon energy E_λ = 1.24E-19J (λ=1.6μm), considered in the photon irradiance conversion. The noise bandwidth can be approximated by $\Delta F \approx 1/(2t_d^{ref})$. This metric is more practical figure of merit for comparing sensitivity across different detectors since it normalizes the detector area and noise bandwidth factors.

$$D^* = \frac{\sqrt{A_d \Delta f}}{NEP} = \sqrt{\frac{1}{2A_d t_d^{ref}}} \frac{1}{NEI_{ref}} \frac{1}{E_\lambda} \tag{4.1}$$

Table 4.4 lists the detector well size, dark current density, and sensitivity figure of merit previously described. Note that the dark current density is independent of the gain mode. [1]

By assuming the quantization error as uniformly distributed, Eq. (4.2) is used to derive the quantization noise (RMS) from the provided well sizes of each gain mode and the pixel depth N_D. The calculated values considering 14 bits of pixel depth are presented in Table 4.4.

$$\sigma_Q = \frac{W_{e-}}{(2^{N_D}\sqrt{12})} \tag{4.2}$$

Table 4.4: Tau SWIR camera - gain modes and noise characteristics (T_{ref}=20°C)

Gain:	Low	Medium	High	Ref
Well size (e^-)	1.35M	113k	38k	FLIR by e-mail
Camera Gain (e^-/count)	82.4	6.90	2.32	$W_{e-}/2^{14}$
NEI (photons/cm^2/s)	7.12e11	2.91e9[a]	1.78e9	[1]
Ref. integration time (ms)	1	33	33	[1]
D* (cm$\sqrt{Hz}W^{-1}$)	1.68E11	7.19E12	1.17E13	Derived using Eq. (4.1)
Read Noise (e-)	< 500	< 60	< 35	ISC1202
Quantization Noise (e-)	24	2	1	Derived using Eq. (4.2)
Dark current density (nA/cm^2)	<10	<10	<10	[1]

a. Interpolated value from low and high gain values.

4.1.2 Interference Filter Bandpass

FINIS uses a tilted narrowband interference filter (IF) at the entrance of each optical assembly as shown by Fig. 4.1. The IF spectral specifications for collimated light under normal AOI ($\theta = 0°$) are listed in Table 4.5.

Table 4.5: FINIS Narrowband Interference Filters' Specifications

Parameter	Spec
CWL (at 0° AOI)	1672±0.25 nm
FWHM	1.5±0.25 nm
Transmission	≥ 90%
Blocking	≥ OD4 avg, OD2.5min 1500-1800nm
Effective refractive index	1.87

The shifted bandpass's CWL λ_θ resulted from an AOI θ is estimated analytically using Eq. (4.3), valid for small angles. The filter is characterized by the CWL at normal incidence λ_0 and its effective refractive index n_{eff}. Since FINIS is designed to operate in the vacuum of space, the refractive index of the incident medium n_0 is always assumed to be unity.

$$\lambda_\theta = \lambda_0 \sqrt{1 - (\frac{n_0}{n_{eff}} sin\theta)^2} \tag{4.3}$$

As illustrated in Fig. 4.1, the AOI on the edge of the FOV is given by $\theta_1 = \alpha + \gamma$ for the IF1 and by $\theta_2 = \alpha - \gamma$ for IF2, where α is half FOV angle and γ is the IF's tilt angle. Due to the symmetry, the spectral range covered across both FPAs is given between λ_2 and λ_1. Where λ_1 and λ_2 are the CWL calculated at the AOI θ_1 and θ_2, respectively.

To illustrate the effect of the IF's tilt angle on the spectrum range imprinted across the FPA, consider a FOV of 10° ($\alpha = 5°$). If the IF is not tilted ($\gamma = 0°$), the AOIs inside the FOV only range from 0° to 5°, which results in a narrow spectrum window from approximately 1670nm to 1672nm. On the other hand, if the IF has a 10° tilt angle, for example, the AOIs inside the FOV range from 5° to 15°, resulting in a much broader spectrum window from 1656nm to 1670nm.

Besides the bandpass CWL, another important design aspect is the filter transmission curve, which will be later used to compute the Instrument Spectral Response Function (ISRF). The ISRF is needed for wavelength calibration and for the convolution of trace gas absorption spectrum to the instrument spectrum resolution [47].

In the case of FINIS, the narrowband IF's transmission curve is modeled using the super-Gaussian function S, described by Eq. (4.4). As shown in Fig. 4.3, the "classical" Gaussian shape (achieved by setting k=2) satisfactorily fits the filter transmission measurement data, which was provided by the IF's manufacturer.

$$S(\lambda) = \frac{k}{2\omega\Gamma(1/k)} exp(-\frac{|\lambda - \lambda_{CWL}|}{\omega})^k \tag{4.4}$$

Where $\omega = \frac{FWHM}{2\sqrt[k]{ln(2)}}$ defines the width of the curve, k defines the shape of the curve

($k = 2$ for gaussian shape), and Γ is the gamma function. For $k > 2$, S becomes more flat-topped, and for $k < 2$, S becomes sharper with long tails on both sides.

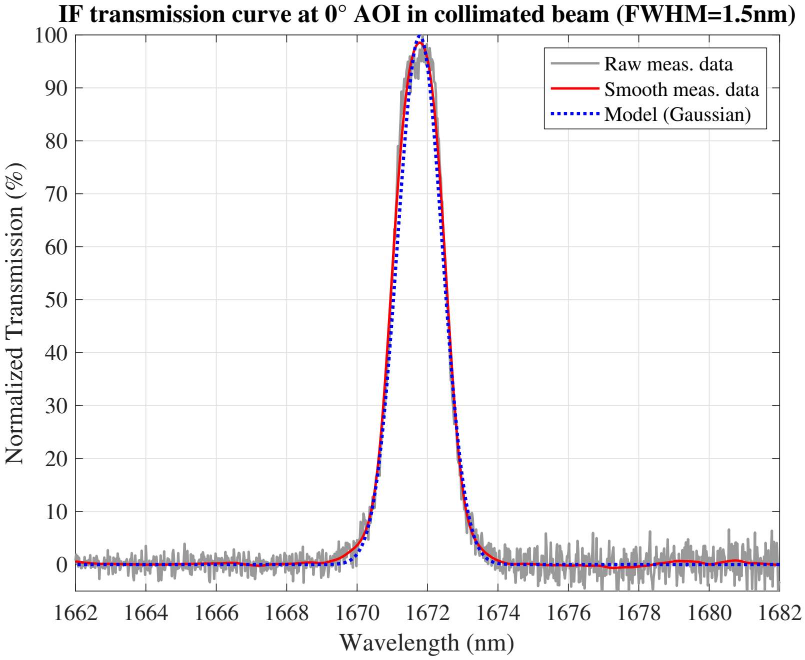

Fig. 4.3: Transmission curve for a narrowband interference filter subjected to a collimated beam with 0° AOI

4.2 Instrument Spectral Response

As shown in the previous sections, the IF's bandpass characteristics is dependent on the AOI of the cone of light. Thus to properly model the bandpass seen by each pixel in the focal plane array (FPA), we need to map the correspondent AOI of the cone of light formed by instantaneous field of view (IFOV). Fig. 4.4 presents a simple pinhole camera model used to define the relative position of the IF plane, tilted around the y-axis by an angle γ.

First, let us consider the center ray of the IFOV cone seen by the pixel located at $(x_i, y_i, 0)$ on the image plane. A unit vector v, defined by the Eq. (4.5), passes over the focal point at $(0, 0, f)$, where f is the sensor effective focal length.

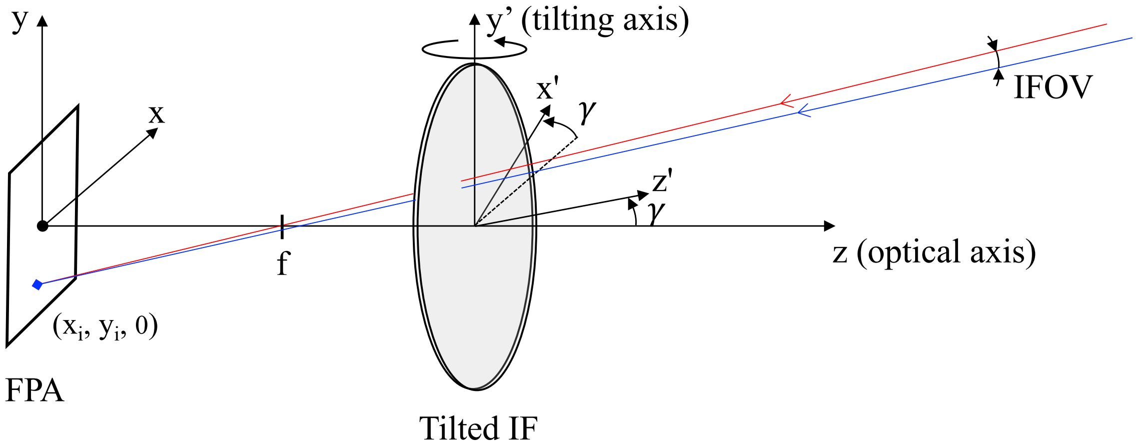

Fig. 4.4: Camera pinhole model showing the tilted interference filter plane relative to the focal plane array. γ is the IF's tilt angle around the y-axis.

$$v = \frac{1}{\sqrt{x_i^2 + y_i^2 + f^2}} \begin{bmatrix} -x_i \\ -y_i \\ f \end{bmatrix} \tag{4.5}$$

To determine the AOI on IF plane, the vector v defined in the focal plane reference frame needs to be written in terms of the IF's body reference frame, which is rotated around the y-axis. Eq. (4.6) describes how the vector v can be rewritten in terms of the IF's reference frame, defined as v'.

$$v' = \begin{bmatrix} \cos\gamma & 0 & \sin\gamma \\ 0 & 1 & 0 \\ -\sin\gamma & 0 & \cos\gamma \end{bmatrix} v = \frac{1}{\sqrt{x_i^2 + y_i^2 + f^2}} \begin{bmatrix} -x_i\cos\gamma + f\sin\gamma \\ -y_i \\ x_i\sin\gamma + f\cos\gamma \end{bmatrix} \tag{4.6}$$

The AOI of the cone of light ray is defined by the angle between the vector v' and the IF's normal vector z', which can be calculated by their dot product, as shown by Eq. (4.7).

$$\cos\theta = v' \cdot z' \implies \theta(x_i, y_i) = \arccos\left(\frac{x_i\sin\gamma + f\cos\gamma}{\sqrt{x_i^2 + y_i^2 + f^2}}\right) \tag{4.7}$$

For the FINIS scenario, the calculation of the AOI for the light cone on each of its two

FPAs can be performed using the formula presented in Eq. (4.7). Tilted angles of ±10° are considered, as depicted in Fig. 4.5. The orientation of both FPAs aligns their longest side (640 pixels) with the y-axis, which corresponds to the tilting axis of the IFs. In this alignment, the center wavelength is spread across the smallest side of the FPA (512px), while the 640px side defines the swath. While this configuration imposes constraints on the achievable range of AOIs and, consequently, the spectrum coverage, it maximizes the sensor's swath.

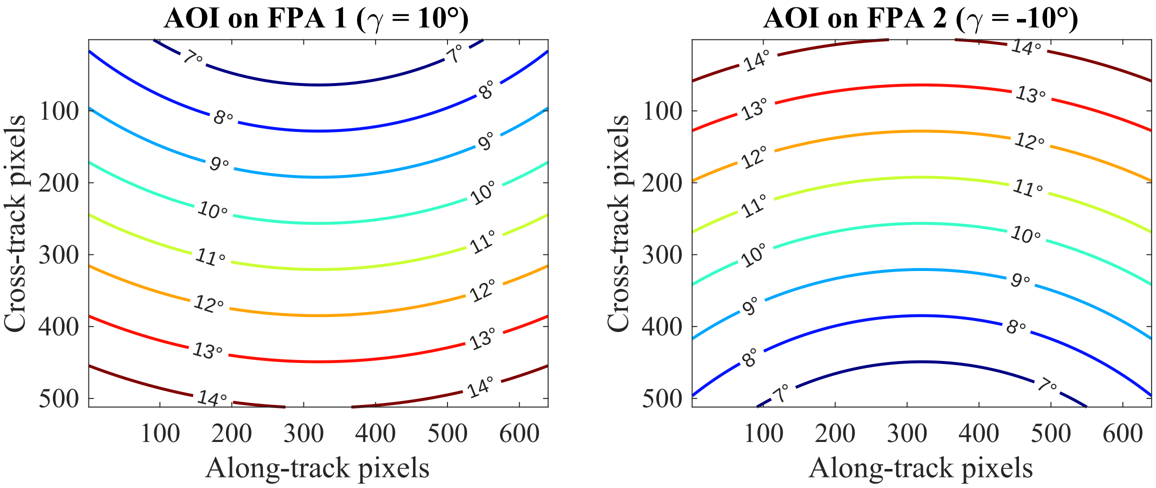

Fig. 4.5: Figure of merit of the angle of incidence (AOI) of the light cone formed by the instantaneous field-of-view across FPA 1 and FPA 2, where the tilted angles in each optical assembly are set to $\gamma = 10°$ and $\gamma = -10°$, respectively.

With the AOI calculated for the image plane, the effective center wavelength (CWL) for each pixel can be computed using Eq. (4.3), which takes into account the convergent light cone semi-angle α defined by half of the IFOV listed on Table 4.1. Since the IFOV is quite narrow, the CWL and bandwidth do not undergo any considerable change, and the problem can be treated as collimated light. For reference, the effects of varying the AOI for uncollimated light conditions are covered in Appendix A.

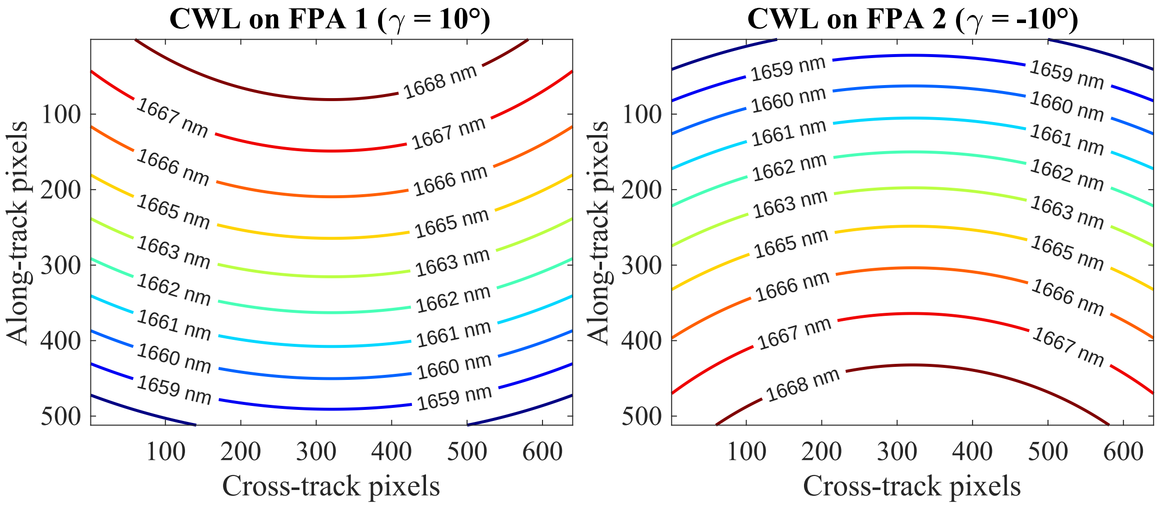

Fig. 4.6: Figure of merit of the peak transmission wavelength, also called center wavelength (CWL), across FPA 1 and FPA 2, where the tilted angles in each optical assembly are set to $\gamma = 10°$ and $\gamma = -10°$, respectively.

4.3 Radiative Transfer Model

A Radiative Transfer Model (RTM) is essential for simulating the interaction of sunlight with Earth's atmosphere and surface. As outlined in the retrieval method description, the RTM serves as the forward model. When the sensor operates from space, pointing nadir, the light it receives undergoes absorption and scattering in the atmosphere, as well as surface reflection. To perform RTM computations, inputs such as atmosphere pressure, temperature, and composition profiles are required. For each air constituent, knowledge of its molecular extinction cross-sections across the desired wavelength range is necessary. These cross-sections determine the amount of light lost in the path due to absorption and scattering, while light intensity may also be influenced by multiple scattering and thermal emissions. Additionally, surface reflection properties must be adequately modeled.

Fortunately, there are several RTMs available to researchers, offering efficient computational models that handle this complexity. One such RTM, SCIATRAN, is freely available and was primarily designed for retrieving atmospheric composition from data of the SCIAMACHY satellite spectrometer [48]. Apart from its lineage in similar trace gas retrieval missions, SCIATRAN was selected because it provides all the simulated data required to estimate FINIS retrieval performance. This encompasses top-of-atmosphere radiance, weighting functions (aka Kernel or Jacobian), air mass factors (AMF), and vertical optical depth. The subsequent subsections elucidate the principal control parameters utilized in all RTM simulations employed in this study.

The version of the SCIATRAN software package utilized in this study is 4.6.7, released in 2023 [49].

4.3.1 Geometry

The atmosphere geometry was modeled as plane-parallel, which means that all radiate transfer calculations were performed neglecting the sphericity of the Earth's atmosphere. This simplification still provides sufficient accuracy considering the nadir viewing geometry and solar zenith angle lower than 60°, assumed for FINIS operation.

The atmospheric altitude grid was specified from 0 to 100km in intervals of 1km. Since the Permian Basin region (baseline scenario) is located in a region with an elevation ranging from approximately 600 to 1200 meters above sea level [50], the Height above sea level parameter in SCIATRAN was set to 1km.

The simulation considered the instrument at the top of atmosphere (TOA), which is set to the maximum level in the altitude grid, 100km. The viewing angle was fixed at the nadir, and the solar zenith angle was specified, ranging from 0°to 60°, at intervals of 10°.

4.3.2 Spectrum range

The spectrum simulated ranges from 1630nm to 1710nm, in intervals of 0.1nm. This range completely covers the instrument's spectral range and allows margin for trade studies. The output spectrum is later convolved with the sensor spectral response function presented in Section 4.2.

4.3.3 Absorbers

SCIATRAN implements an extensive list of atmospheric trace gases: BrO, NO_3, OCLO, O_4, O_3, NO_2, SO_2, ClO, HCHO, O_2, H_2O, CO_2, N_2O, CO, CH_4, NO, NH_3, HNO_3, OH, HF, HCL, HBr, HI.

For the weighting function simulations, only the data for H_2O, CH_4, CO_2, and CO was generated, since the other trace gas does not have significant absorption features in the studied spectrum range.

4.3.4 Trace gases, pressure and temperature profiles

SCIATRAN incorporates a climatological database containing monthly and zonally averaged profiles of atmospheric trace gases. These profiles were derived from a 2D chemical transport model developed by the University of Bremen [51]. Given that the selected baseline region is situated in Texas, USA, which experiences optimal illumination conditions during the northern summer solstice, the atmospheric profile was configured for month 6 (June) and latitude 35°N. Within the software package, the paths to the profile data for both continuous and line absorbers are specified as follows:

Continuous absorbers: `DATA_BASES/PROFILES/B2D/UV-Vis/mon06lat35n.b2d`

Line absorbers: `DATA_BASES/PROFILES/B2D/IR/mon06lat35n.b2d`

Fig. 4.7 presents the temperature and pressure profiles, and Fig. 4.8 shows the main gaseous absorbers concentration profile employed in the reference atmosphere. The vertical column density of methane is 3.17E19 molecules/cm^2, and its total mixing ratio is 1694ppbv.

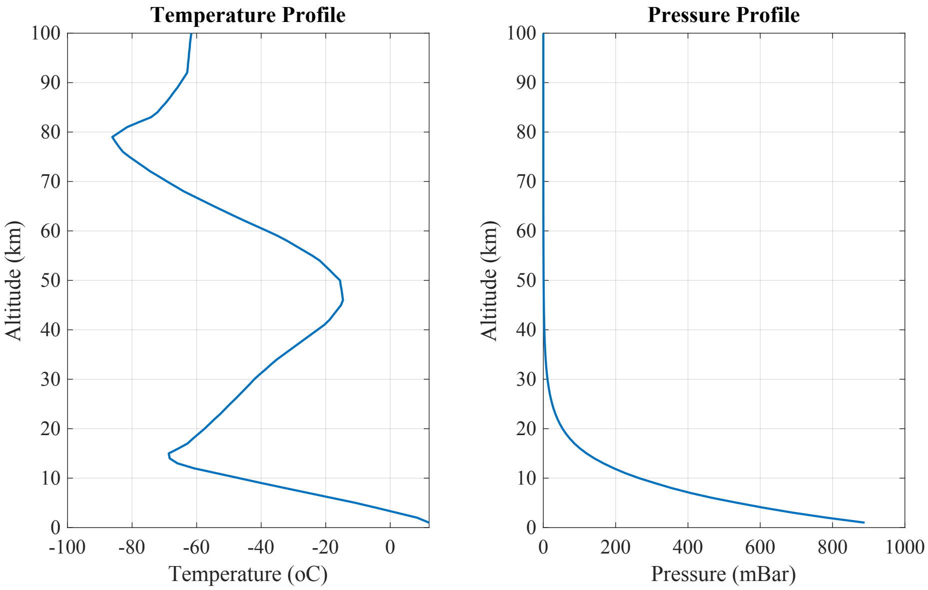

Fig. 4.7: Temperature and pressure profile for the reference atmosphere

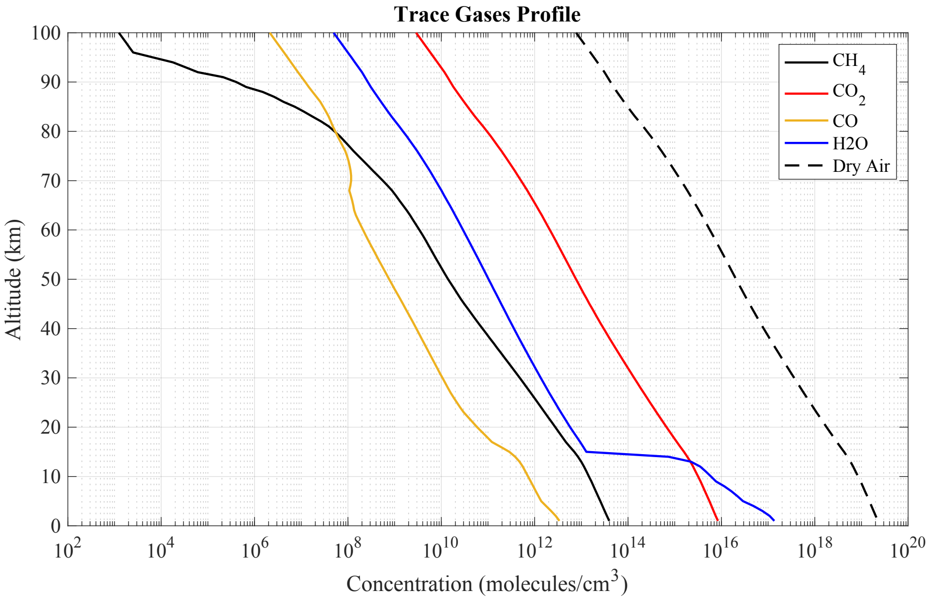

Fig. 4.8: Trace gases concentration profile for the reference atmosphere

4.3.5 Surface reflection

For the general case, the albedo was specified as wavelength-independent Lambertian reflection. The spherical albedo was specified as equal to 0.2, and the albedo weighting function was used to adjust the radiance spectrum for different spherical albedo values.

4.3.6 Rayleigh Scattering

The SCIATRAN default setup for Rayleigh scattering computation is used. In this case, the Rayleigh scattering coefficients and the King factor are computed using the Bates approach [52].

Since the scattered intensity is inversely proportional to the wavelength to the fourth power $I_\lambda \sim 1/\lambda^4$ [53], the Rayleigh scattering effect is expected to be negligible in the spectrum range covered by FINIS.

4.3.7 Aerosol and Clouds

Aerosol and clouds were not considered in the simulation. Future work should address the impact of the different clouds and aerosols on the system performance.

4.4 Plume Model

This section presents the plume model used to simulate methane dispersion in the atmosphere from a point source emission. The model is based on the steady-state The Gaussian plume equation utilized in this study is derived from the Industrial Source Complex (ISC3) Short-Term model [54]. Prior to 2017, the ISC3 model held the status of the preferred air dispersion model by the Environmental Protection Agency (EPA) until it was replaced by the AERMOD model. While the ISC3 model employs a Gaussian treatment in both the horizontal and vertical directions, the AERMOD model adopts a Gaussian treatment in the horizontal and vertical directions only under stable atmospheric conditions. In contrast, for unstable conditions, AERMOD employs a non-Gaussian probability density function in the vertical direction. Since our primary interest lies in estimating the vertical column density enhancement due to the point source, and considering that both models should yield similar

Table 4.6: Wind profile exponent p as a function of stability category and wind speed class

Stability Category	Rural Exponent	Urban Exponent
A	0.07	0.15
B	0.07	0.15
C	0.10	0.20
D	0.15	0.25
E	0.35	0.30
F	0.55	0.30

results based on their common horizontal Gaussian treatment, we have opted for the ISC3 model for its simplicity.

For a steady-state Gaussian plume, the hourly concentration at downwind distance x (meters), crosswind distance y (meters), and vertical distance from stack z (meters) is given by Eq. (4.8).

$$C(x,y,z) = \frac{rQ}{2\pi u_s \sigma_y(x)\sigma_z(x)} exp(-0.5(\frac{y}{\sigma_y(x)})^2 - 0.5(\frac{z-h_s}{\sigma_z(x)})^2) \tag{4.8}$$

where:

Q = pollutant emission rate (g/s)

r = ground reflection factor (2 if assumed ground reflection, otherwise, 1)

σ_y = standard deviation of the lateral concentration distribution (m)

σ_z = standard deviation of the vertical concentration distribution (m)

u_s = mean wind speed (m/s) at release height

The stack height wind speed, u_s, is computed by adjusting the observed wind speed, u_{ref}, from a reference measurement height, z_{ref}, to stack release height, h_s, using the wind power law as shown by Eq. (4.9). The model requires a minimum stack height wind speed, u_s, of at least 1 m/s.

$$u_s = u_{ref}(\frac{h_s}{z_{ref}})^p \tag{4.9}$$

Where p is the wind profile exponent defined as a function of the atmospheric stability category and wind speed class, default values are listed in Table 4.6.

For the rural environment, the values of σ_y and σ_z are computed using the Eq. (4.10), which approximately fit the Pasquill-Gifford curves [55].

$$\begin{aligned} \sigma_y &= 465.11628x\tan(TH) \\ \sigma_z &= ax^b \\ TH &= 0.017453293[c - d\ln(x)] \end{aligned} \tag{4.10}$$

where:

x = downwind distance in kilometers

a, b, c, d = Pasquill-Gifford coefficients dependent on the stability class

As an example of the model application, Fig. 4.9 shows the steady-state Gaussian plume dispersion pattern for a point source with a 1 ton/h leak rate subjected to a wind speed of 5 m/s at 30m altitude for the different Guifford-Pasquill stability classes. The grid size is 150x150 meters, approximately equal to FINIS' GSD. The plume's outermost contour was set to 5% (90 ppb) of the methane background concentration, assumed to be 1800 ppb. Since the methane deposition on the ground is considered insignificant, the reflection factor was set to 2.

Fig. 4.10 shows the vertically integrated plume concentration dispersion for different methane leak rates ranging from 250 kg/h to 2000 kg/h. All plumes were simulated considering stability class B and the same previous wind speed and stack parameters.

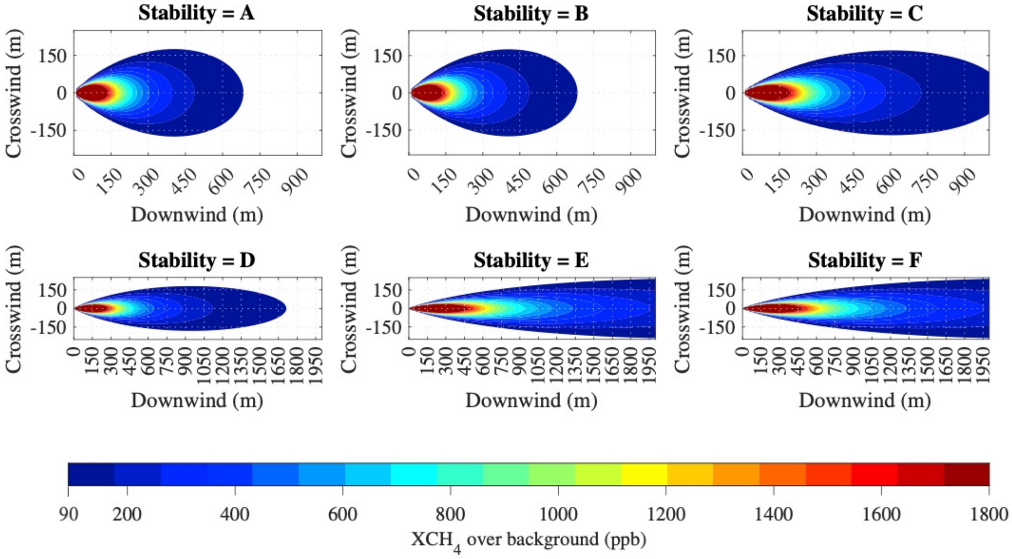

Fig. 4.9: Methane concentration over the background from point source modeled as a Gaussian plume for the different atmospheric stability conditions (A-F). Simulation parameters: leak rate 1 ton/h, reference wind speed u_{ref} = 5 m/s, reference height z_{ref} = 30 m, stack height h_s = 10 m.

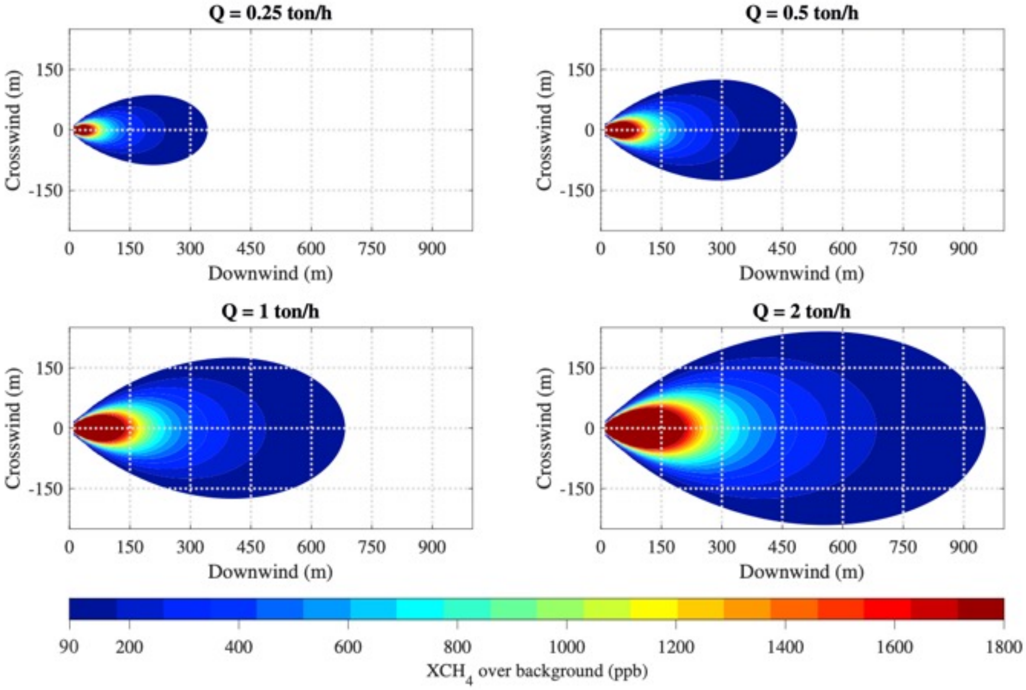

Fig. 4.10: Methane concentration over the background from point source modeled as a Gaussian plume for the different leak rate levels, considering B class stability. Simulation parameters: reference wind speed u_{ref} = 5 m/s, reference height z_{ref} = 30 m, stack height h_s = 10 m.

4.5 Optimal Retrieval Method

Estimating the atmospheric state vector from the measured spectrum radiance data is known as an inversion problem. This problem can be formulated using the Bayesian approach, within which the atmospheric state can be estimated by computing its posterior probability density function (pdf) based on the measured data, a forward model, and a priori information [56]. If the state vector is represented by x, with n elements, and the measurement vector y, with m elements, the posterior pdf of the state vector given the set of measurements is described by Eq. (4.11).

$$P(x|y) = \frac{P(y|x)P(x)}{P(y)} \tag{4.11}$$

Where $P(x|y)$ is the posterior pdf, representing the updated state vector knowledge after measurements were taken. $P(x)$ represents the prior knowledge about the state vector. $P(y|x)$ describes the pdf for the measured radiance y given a state vector x, which can be determined using a forward model and the statistical description of the measurement errors. In the denominator, $P(y)$ is the normalizing factor that can be computed by integrating $P(y|x)P(x)$ over all x.

This approach becomes very practical when a Gaussian distribution is assumed for all random variables, i.e., measurement errors and prior state knowledge, and when the forward model is linear or linearized around a state. Let $F(x)$ be the forward model, which describes the physics of the measurement process and ϵ the measurement error, as shown in Eq. (4.12).

$$y = F(x) + \epsilon \tag{4.12}$$

Considering the first two terms of the Taylor expansion, it is possible to linearize $F(x)$ around a reference state x_0, so Eq. (4.12) can be rewritten as Eq. (4.13).

$$y - F(x_0) = \frac{\delta F(x)}{\delta x}|_{x_0}(x - x_0) + \epsilon = K(x - x_0) + \epsilon \tag{4.13}$$

The matrix of partial derivatives K (mxn) is called the weighting function, the Jacobian, or even the Kernel. Now, if redefining y as the difference between the measurement and the forward model evaluated at the reference state, $F(x_0)$, and the state vector as the deviation from the reference state, x_0, we have Eq. (4.14).

$$y = Kx + \epsilon \tag{4.14}$$

With the Gaussian distribution assumption for the measurement error ϵ, the pdf of $P(y|x)$ can be expressed by Eq. (4.15), where S_ϵ represents the measurement error covariance matrix, and c_1 a constant.

$$-2\ln P(y|x) = -\frac{1}{2}(y - Kx)^T S_\epsilon^{-1}(y - Kx) + c_1 \tag{4.15}$$

Similarly, assuming the prior information also has a Gaussian distribution, $P(x)$ can be written as shown in Eq. (4.16), where x_a and S_a represent the prior state vector and its associated covariance matrix.

$$-2\ln P(x) = -\frac{1}{2}(x - x_a)^T S_a^{-1}(x - x_a) + c_2 \tag{4.16}$$

By taking the natural log on Eq. (4.11), and using Eqs. (4.15) and (4.16), the natural log of the posterior pdf can be written as Eq. (4.17).

$$\begin{aligned} lnP(x|y) &= lnP(y|x) + lnP(x) + c_3 \\ -2\ln P(x|y) &= (y - Kx)^T S_\epsilon^{-1}(y - Kx) + (x - x_a)^T S_a^{-1}(x - x_a) + c_3 \end{aligned} \tag{4.17}$$

Since the posterior pdf is also a Gaussian distribution, Eq. (4.17) can be factored into the form Eq. (4.18).

$$-2\ln P(x|y) = \frac{1}{2}(x - \hat{x})^T \hat{S}^{-1}(x - \hat{x}) + c_4 \tag{4.18}$$

After some algebra, it is possible to show that the estimated state vector $\hat{x}$ is given by Eq. (4.19), and the estimated covariance matrix $\hat{S}$ is given by Eq. (4.20).

$$\hat{x} = x_a + (K^T S_\epsilon K + S_a^{-1})^{-1} K^T S_\epsilon^{-1} (y - K x_a) \tag{4.19}$$

$$\hat{S} = (K^T S_\epsilon K + S_a^{-1})^{-1} \tag{4.20}$$

The estimated state vector $\hat{x}$ given by Eq. (4.19) is known as the *maximum a posterior solution* (MAP), since it maximizes the posterior pdf $P(x|y)$. The covariance matrix $\hat{S}$ describes the uncertainty of the retrieval, in which the retrieval standard deviation is expressed by the square-root of the diagonal elements of $\hat{S}$, as shown by Eq. (4.21).

$$\hat{\sigma}_j = \sqrt{\hat{S}_{jj}} \tag{4.21}$$

The following section describes the application of this method for the specific FINIS case.

4.5.1 FINIS optimum retrieval method

As detailed in FINIS's Concept of Operation (Section 3.2), spectral radiance is acquired by simultaneously capturing pairs of frames with CAM1 and CAM2 while the satellite traverses the target area. Despite sharing the same FOV, each frame captures radiance at different wavelengths due to their distinct spectral responses, as shown in Fig. 4.6. By capturing these pairs of radiance measurements simultaneously, both cameras observe the ground samples under identical illumination and atmospheric scattering conditions. This simultaneous capture ensures that the measurements, computed as the natural log difference between the paired frames, are independent of surface reflectance variations.

To further illustrate this concept, consider the plots in Fig. 4.11. The spectral radiance collected by CAM1 and CAM2 as the sensors pass over the target is depicted, considering three different surface reflectance scenarios: constant albedo (unrealistic), Lambertian (ideal), and a Bidirectional Reflectance Distribution Function (BRDF), which describes surface reflectance as a function of illumination and viewing geometry. The BRDF profile was computed using the empirical model for a Savannah-covered surface presented in [57], with a Solar Zenith Angle (SZA) of 60° and 0° azimuth, and for viewing angles ranging from -5° to 5°, corresponding to FINIS' FOV.

Notice that while the Lambertian albedo yields a similar profile to the constant albedo (with no significant distortion), the spectral radiance of the BRDF decreases notably as the target crosses the FOV. This distortion would typically require modeling and fitting, possibly using a second-order polynomial. However, FINIS circumvents this issue by combining the spectra from CAM1 and CAM2 and computing the natural log difference of both spectra. As a result, the measurement becomes normalized and independent of the surface reflectance function, as shown in Fig. 4.12.

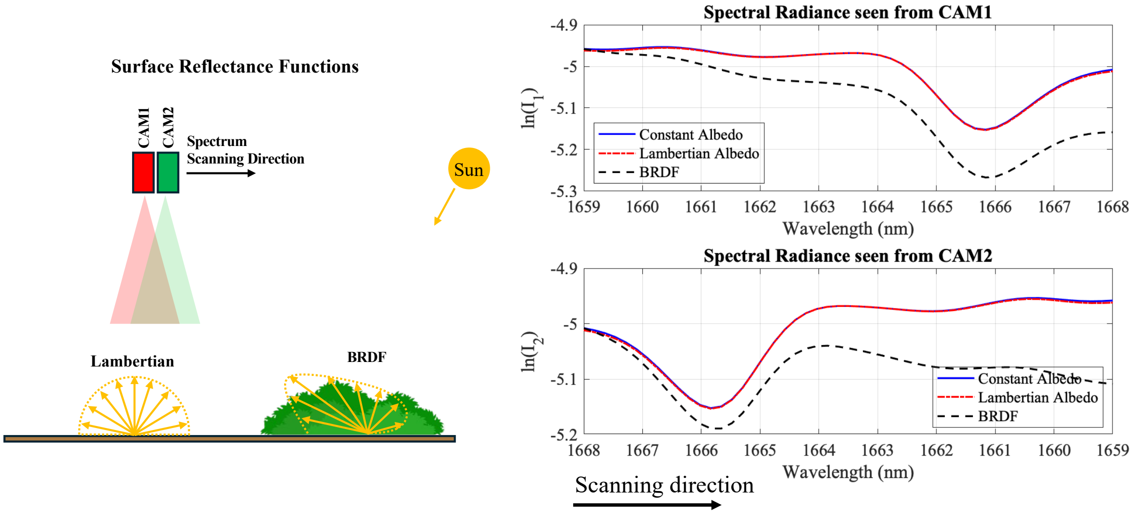

Fig. 4.11: Simulated natural log of the spectral radiance (units: W/m^2/nm/sr) observed for CAM1 and CAM2 as the sensors pass over the target considering three different surface reflectance functions.

The measurement vector y, therefore, can be defined as the natural log difference of CAM1 and CAM2 radiance measurements (L) plus the measurement error ϵ, as shown in Eq. (4.22).

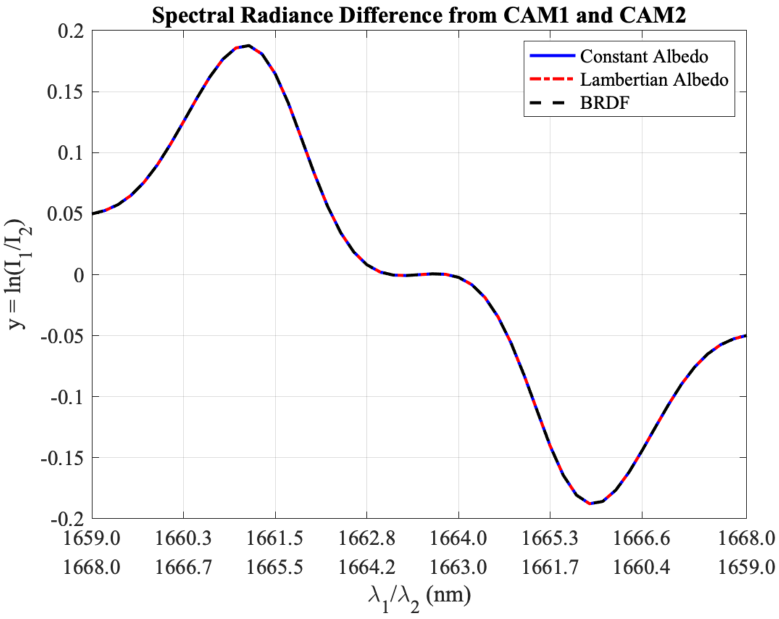

Fig. 4.12: The natural log difference of the radiance simultaneously measured from CAM1 and CAM2 showing independence from surface reflectance functions.

$$y = \ln \frac{L_1}{L_2} + \epsilon \tag{4.22}$$

The partial derivative of y with respect to a state x_i is given by Eq. (4.23).

$$\frac{\delta y}{\delta x_i} = \frac{1}{L_1} \frac{\delta L_1}{\delta x_i} - \frac{1}{L_2} \frac{\delta L_2}{\delta x_i} \tag{4.23}$$

The state vector x incorporates all the atmospheric parameters retrieved in the inversion algorithm. For FINIS retrieval, the state vector is defined with four elements as shown in Eq. (4.24). In terms of atmospheric composition, only the relative H_2O and CH_4 vertical column concentrations are retrieved since no other trace gas presents significant absorption features in the instrument fitting window. The parameters a_1 and a_0 are polynomial coefficients that account for possible linear and offset deviations (albedo), respectively. Higher-order polynomial fitting is not necessary since the measurement is independent of the surface reflectance function.

$$x = \begin{bmatrix} x_{CH4} & x_{H2O} & a_1 & a_0 \end{bmatrix}^T \tag{4.24}$$

The kernel matrix K is assembled as shown by Eq. (4.25), where f_1 is a linear function of the wavelengths measured by CAM1, defined as $f_1(\lambda_1) = \lambda_1/median(\lambda_1) - 1$.

$$K = \begin{bmatrix} | & | & | & \\ \frac{\delta y}{\delta x_{CH4}} & \frac{\delta y}{\delta x_{H2O}} & f_1(\lambda_1) & 1 \\ | & | & | & \end{bmatrix}_{(n,4)} \tag{4.25}$$

K is evaluated at the reference atmosphere state parameters, x_a, i.e., the a priori information. Fig. 4.13 shows the weighting functions output by the Radiative Transfer Model across the measurement vector. The reference atmosphere's methane and water vapor concentration profile is presented in Fig. 4.8.

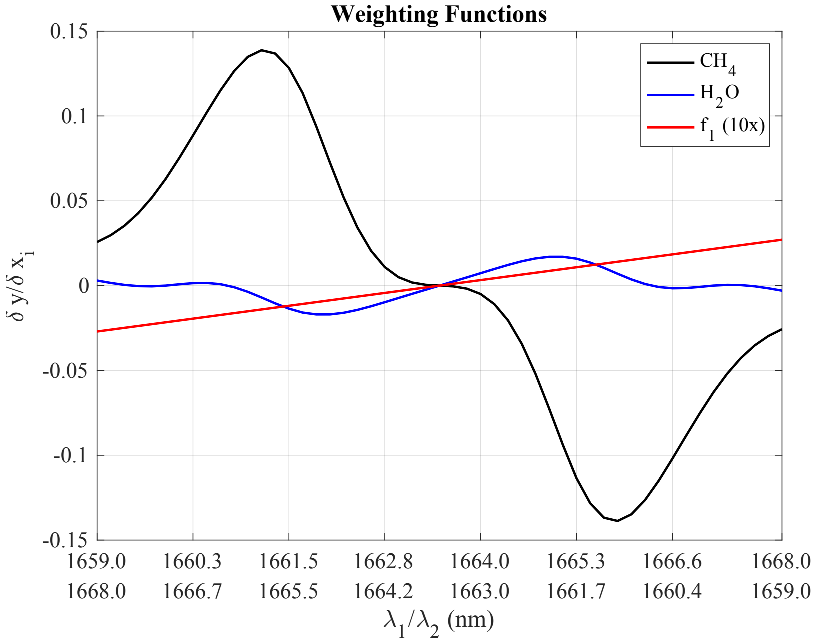

Fig. 4.13: Weighting Functions (K) evaluated using the reference atmosphere state parameters

With the K matrix defined and the measurement noise characterized in terms of its covariance matrix S_ϵ, the retrieval covariance matrix can be computed using Eq. (4.20) by estimating the a priori information uncertainty expressed in the a priori covariance matrix S_a.

4.6 Fast Retrieval Method for Plume Detection

For the most precise methane concentration retrieval from CAM1 and CAM2 data, the optimal inversion method described in Section 4.5 is recommended. That method offers the most accurate estimation of the state vector considering the initial uncertainties and measurement noise. However, it comes with the drawback of demanding significant computational resources to compute the estimated full state vector for all scene pixels using Eq. (4.19). As a faster alternative, a methane-only retrieval can be employed to expedite the processing time. In this section, we delve into this fast retrieval method in detail, particularly focusing on its application for plume detection purposes.

In a simple approximation, with no scattering, the measurement, defined as $y = ln(L_1(\lambda_i)/L_2(\lambda_j))$, can be approximated by the difference between the optical depth (τ^S) of λ_j and λ_i, adjusted for the slant path ("S" superscript).

With no scattering, the radiance measurement by the sensor on top of the atmosphere can be computed from Beer's law equation written in terms of the column-integrated optical depth (also called optical thickness), as shown in Eq. (4.26).

$$ln(\frac{L(\lambda)}{L^0(\lambda)}) = -\tau^S(\lambda) \tag{4.26}$$

where:

$L(\lambda)$ = spectral radiance measured by the sensor
$L^0(\lambda)$ = solar spectrum radiance (before atmosphere)
τ^S = total optical depth for the slant path

Writting Eq. (4.26) for the spectrum radiance measured by CAM1 ($L_1(\lambda_i)$) and by CAM2 ($L_2(\lambda_j)$), we have Eq. (4.27).

$$\begin{aligned} ln(\frac{L_1(\lambda_i)}{L_1^0(\lambda_i)}) &= -\tau^S(\lambda_i) \\ ln(\frac{L_2(\lambda_j)}{L_2^0(\lambda_j)}) &= -\tau^S(\lambda_j) \end{aligned} \tag{4.27}$$

Subtracting the first equations by the second in Eq. (4.27), we can now express the measurement vector y as in Eq. (4.28).

$$y = ln(\frac{L_1(\lambda_i)}{L_2(\lambda_j)}) = \tau^S(\lambda_j) - \tau^S(\lambda_i) + ln(\frac{L_1^0(\lambda_i)}{L_2^0(\lambda_j)}) \tag{4.28}$$

Considering that FINIS operates in a narrow wavelength window (<10nm), the natural log difference of the solar radiance at λ_i and λ_j can be approximated to zero, so the measurement y can be written as a function of the optical depth difference plus some random noise ϵ.

$$y = \tau^S(\lambda_j) - \tau^S(\lambda_i) + \epsilon \tag{4.29}$$

Now if consider that only the methane absorption affects the optical depth difference, we can rewrite Eq. (4.29) as Eq. (4.30), where $X_{ji} = \tau_j^S - \tau_i^S$ is the slant optical depth difference of wavelength λ_j and λ_i, computed for a reference atmosphere (first guess state). Assuming linearity for small deviations from the reference state, the relative methane concentration α_{CH_4} can be computed by a linear least square fit of equation Eq. (4.31), where α_{CH4} is the slope of the curve formed by the measurements and the reference optical depth difference.

$$y = \alpha_{CH_4} X_{ji} + \epsilon \tag{4.30}$$

$$\hat{\alpha}_{CH_4} = (X^T X)^{-1} X^T Y \tag{4.31}$$

Although less accurate than the optimum retrieval, this simplified retrieval method can be performed with much less computational power. Moreover, assuming an approximated uniform distribution of the water vapor in the background, the error caused by not retrieving water will also be uniformly distributed across the samples. Thus, the method can be seen as a Level-1 retrieval product, whereas a Level-2 would be after a full state vector retrieval using the optimum method.

CHAPTER 5

ANALYSIS AND SIMULATION

This chapter explores a comprehensive analysis and simulation of FINIS' capabilities in detecting methane plumes based on relative spectral radiance measurements. It commences with a radiometric performance analysis, estimating the SNR considering various camera gain modes and integration times. Following this, the retrieval noise analysis incorporates the computed SNR into the optimal retrieval algorithm to evaluate the retrieval noise, crucial for assessing instrument precision in measuring methane vertical column density. Subsequently, a plume detection simulation is presented using simulated images from both of FINIS' imagers, outlining the image processing steps akin to those with real data. Lastly, the chapter details the ray tracing simulation results of the onboard calibration unit, employing an embedded LED ring to illuminate the shutter. This feature is crucial for the flat-fielding process, ensuring uniform measurement gains across the FPA.

5.1 Radiometric Performance Analysis

The radiometric performance analysis provides the estimated SNR of the FINIS spectrum radiance measurements in different illumination conditions and camera settings. Since the measurement noise is propagated to the retrieval, this analysis's output is an input of the retrieval noise analysis.

First, the spectral radiance incident on the sensor, assuming nadir-pointing, was simulated using the RTM for different illumination conditions and surface reflectance. The simulated results are summarized in Section 5.1.1.

Second, using the camera's performance parameters provided in Section 4.1.1, the spectrum SNR is estimated using two different approaches. In the first approach, presented in Section 5.1.2, the SNR is estimated using the ratio of the effective radiant flux at the FPA by the NEP, which is described in terms of the normalized detectivity D^*. This first approach simplifies the analysis; however, its results should be seen only as a first approximation since the D* method is only appropriate for detectors that operate in background-limited conditions (BLIP) [58]. As will be seen, this condition is not entirely valid for FINIS, since the intrinsic camera noise has a significant contribution to total noise.

The second approach, presented in Section 5.1.3, computes the SNR by estimating the noise components: shot noise, dark noise, read noise, and quantization noise. Compared to the D* method, this approach provides a more realistic estimate of the SNR, as it takes into account the intrinsic noise components of the camera.

In both SNR estimation approaches, the optimum integration time is defined using the following criteria:

$$t_d = \min\left[t_{80\%saturation}, t_{1GSDsmear}\right] \tag{5.1}$$

Where $t_{80\%saturation}$ is defined as the integration time that results on 80% well size filled, assuming the maximum electron flux expected in the operational radiance range and the dark current. The remaining 20% of the well is reserved as a margin for the detector bias and other fluctuations to avoid saturation. The $t_{1GSDsmear}$ corresponds to the integration that limits an in-track smear of one GSD. Considering the projected ground scanning velocity for an orbital altitude of 550km at 98° inclination, $t_{1GSDsmear}$ was estimated to be 21.2 ms.

5.1.1 Spectral Radiance Range

The TOA spectral radiance $L^{TOA}(\lambda)$ for the lowest and highest light conditions in the operational range is presented in Fig. 5.1. The atmospheric parameters considered in the radiative transfer simulation are presented in Section 4.3.

The effective flux Φ_{eff} is defined as the magnitude of incident flux upon the detector that is effectively converted into electrons. From the spectrum radiance results, the Φ_{eff} can be computed using Eq. (5.4) and the electron flux is defined as shown in Eq. (5.2), where E_λ is 1666nm photon energy, equal to 1.19E19J. Fig. 5.2 presents both flux measurements across the instrument spectrum range for the different illumination conditions.

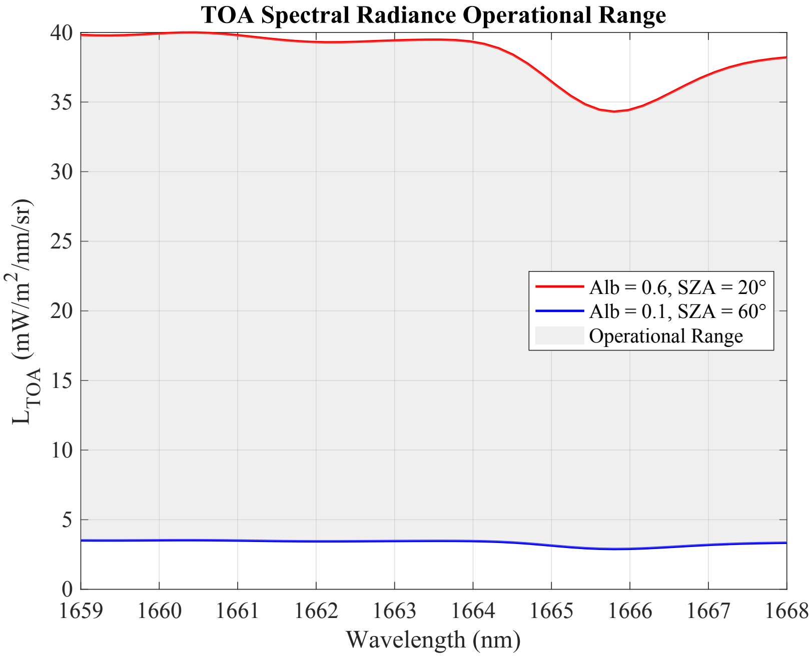

Fig. 5.1: Simulated TOA spectral radiance range considered in the radiometric analysis

$$\Phi_{e-} = \frac{\Phi_{eff}}{E_\lambda} \tag{5.2}$$

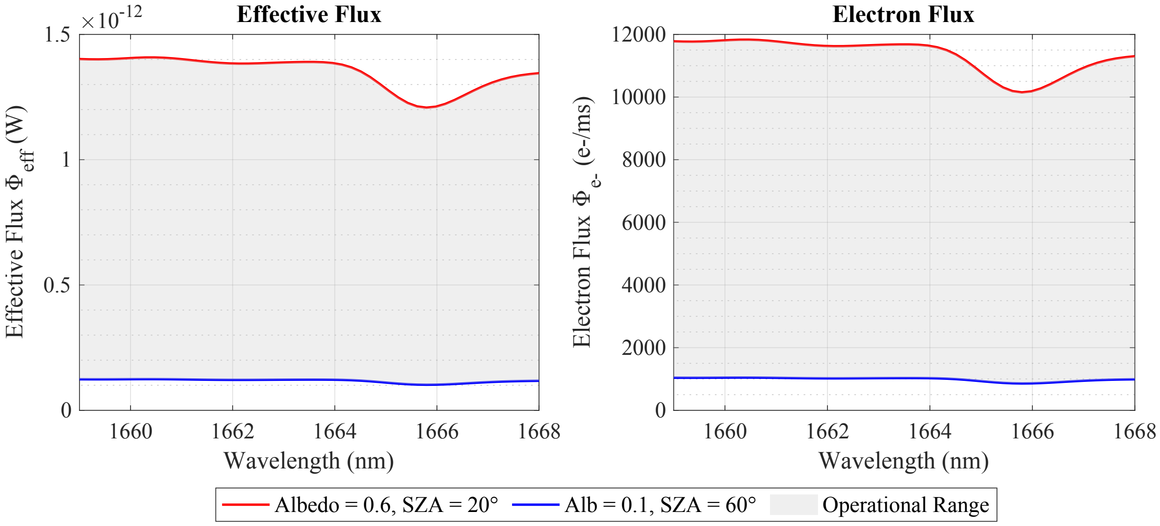

Fig. 5.2: Effective radiant and electron flux for the operational range

5.1.2 SNR estimated from D*

A general form of the radiometric performance equation is given by the ratio of the effective flux Φ_{eff} to the noise equivalent power (NEP), as given by Eq. (5.3). [58]

$$SNR = \frac{\Phi_{eff}}{NEP} \tag{5.3}$$

The effective flux incident to the detector from an extended area is a function of the radiance on top of the atmosphere (TOA) $L^{TOA}(\lambda)$, the effective bandwidth $\Delta\lambda$, the optical efficiency η_o, the quantum efficiency η_Q, the clear aperture area A_c, and the solid angle of the projected IFOV Ω_c, as given by Eq. (5.4).

$$\Phi_{eff} = L^{TOA}(\lambda)\eta_o A_c \Omega_c \Delta\lambda \eta_Q \tag{5.4}$$

Given the f-number, defined as $F = f/D$, where f and D are the effective focal length and the clear aperture diameter, respectively, Eq. (5.4) can also be written in terms of the instrument's f-number F and the detector area A_d as shown in Eq. (5.5).

$$\Omega_c = \frac{A_d}{f^2} \text{ and } A_c = \frac{\pi D^2}{4} \implies \Phi_{eff} = \frac{L^{TOA}(\lambda)\eta_o A_d \pi \Delta\lambda \eta_Q}{4F^2} \tag{5.5}$$

FINIS's parameters required to compute the effective radiant flux incident to the detector are listed in Table 4.1, in the sensor model section.

The NEP can be derived from the D* figure merit, as shown by Eq. (5.6). The $\sqrt{2}$ factor is added to the equation to account for the noise effects associated with DC rectification in the detector, as described in [58]. The D* values for each camera gain mode are listed in Table 4.4.

$$NEP = \frac{\sqrt{A_d \Delta f}}{D^*(\lambda)}\sqrt{2} \tag{5.6}$$

The noise bandwidth can be approximated as $\Delta F \approx 1/(2t)$ [59]. From Eq. (5.4) and Eq. (5.6), the SNR* (estimated from D*) can be computed by Eq. (5.7).

$$SNR^* = \frac{L^{TOA}(\lambda)\eta_o \pi D^*(\lambda)\Delta\lambda\eta_Q\sqrt{A_d t}}{4F^2} \tag{5.7}$$

Results:

Fig. 5.3 presents the spectrum SNR* estimated for the three gain modes, assuming a constant D* across the spectrum window. The low gain mode offers the lowest performance in terms of SNR range and integration time, which degrades the instrument's spatial resolution. The medium and high gain offer a similar range of SNR, with the minimum SNR being around 50 for the low-light condition (Albedo=0.1, SZA=60°). The high gain, however, can achieve that range with one-third of the integration time required in the medium gain.

It is important to note that before making any conclusions, the SNR that is obtained from the D* parameters should only be used for BLIP detectors, as pointed out in [58]. The next subsection aims to verify if this assumption is also applicable to FINIS. This will be done by estimating the contribution of the camera's inherent noise compared to the photon noise.

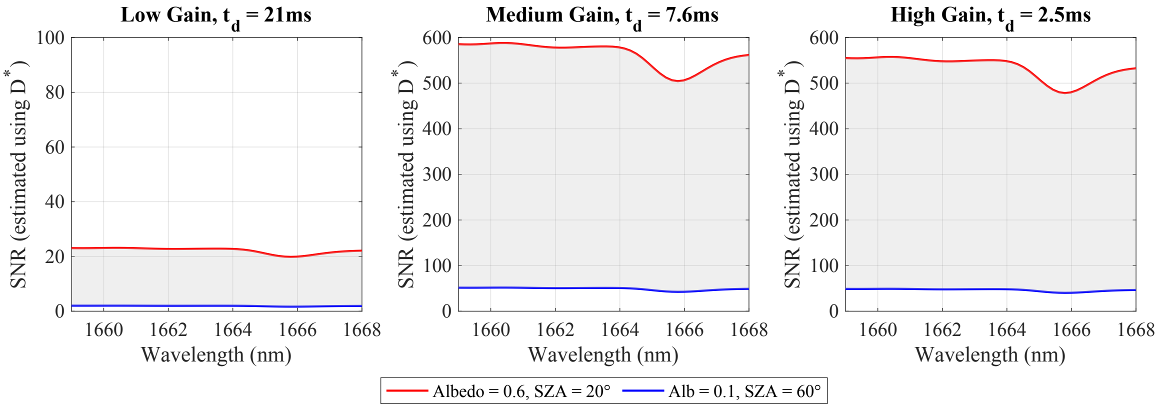

Fig. 5.3: SNR estimated from D*

5.1.3 SNR estimated from noise components

An alternative method for estimating the SNR (Signal-to-Noise Ratio) is by calculating the ratio of the signal shot (i_s) by the total noise (RMS) (σ_n). The total noise RMS can be computed from the square root of the sum of the variances of the independent noise sources, as shown in Eq. (5.8). [59]

$$SNR = \frac{i_s}{\sigma_n} = \frac{i_s}{\sqrt{\sigma_s^2 + \sigma_{dc}^2 + \sigma_r^2 + \sigma_q^2}} \tag{5.8}$$

where the noise major components are:

σ_s = shot noise

σ_{dc} = dark current noise

σ_r = read noise

σ_q = quantization error

The shot signal i_s, measured in electron (e-), is the result of the electron flux, shown in Fig. 5.2, integrated during the integration time t_d. Assuming the electron flux is constant during the integration time, the shot signal is computed using Eq. (5.9)

$$i_s = \Phi_{e-} t_d \tag{5.9}$$

Both shot and dark noise are assumed to have a Poisson distribution that can be approximated to a Gaussian when there is sufficient emission. Based on that assumption, the standard deviations can computed as the square root of their respective mean signal count as shown in Eq. (5.10), where Φ_{dc} is the dark electron flux.

$$\begin{aligned} \sigma_s(t_d) &= \sqrt{i_s} = \sqrt{\Phi_{e-} t_d} \\ \sigma_{dc}(t_d) &= \sqrt{i_{dc}} = \sqrt{\Phi_{dc} t_d} \end{aligned} \tag{5.10}$$

Since the read and quantization noise are assumed to be time-invariant, the Eq. (5.8) can be rewritten in terms of the shot and dark electron fluxes, shown in Eq. (5.11).

$$SNR = \frac{\Phi_{e-} t_d}{\sqrt{(\Phi_{e-} + \Phi_{dc}) t_d + \sigma_r^2 + \sigma_q^2}} \tag{5.11}$$

The dark electron flux is computed from the dark current density ρ_{dc} using Eq. (5.12), where C is one Coloumb equal to 6.24E18e-. Using the dark current density listed in Table 4.4, we find that the Φ_{dc} is equal to 140e-/ms for all three gain modes.

$$\Phi_{dc} = \rho_{dc} A_d C \tag{5.12}$$

In addition to the dark noise, the read noise and quantization noise are listed in Table 4.4.

Results:

The Fig. 5.4 shows the estimated SNR range obtained from the analysis of the noise components, based on the camera's specifications provided by the manufacturer. It is noteworthy that the low gain setting provides the highest performance for the high-light condition, offering the maximum SNR value (~ 340) followed by 285 and 165 for the medium and high gain, respectively. However, the low gain requires the longest integration time, which is limited by the smear threshold of 1GSD, rather than saturation, as in the case of the medium and high gain settings. In terms of minimum SNR, both low gain and high presents a lower performance in low-light conditions when compared to the medium gain. The spectrum average SNR in low light conditions is 68 for the medium gain and approximately 40 for both low and high gains.

When Fig. 5.4 is compared to Fig. 5.3, which shows the SNR range estimated using the D* method. There is a noticeable difference in the predicted performance for the low gain modes. While the D* method predicts poor performance with low gain, the SNR estimated from the noise components has a reasonable range of performance if the assuming 1GSD smear trade-off due to the long integration time. Second, the D* method predicts a much higher SNR performance for the high-light conditions in medium and high gains but suggests similar SNR levels for the low-light condition.

Fig. 5.5 displays the relative contribution in the total noise of the different independent noise sources considered in the analysis. Note that the pie plots present the standard

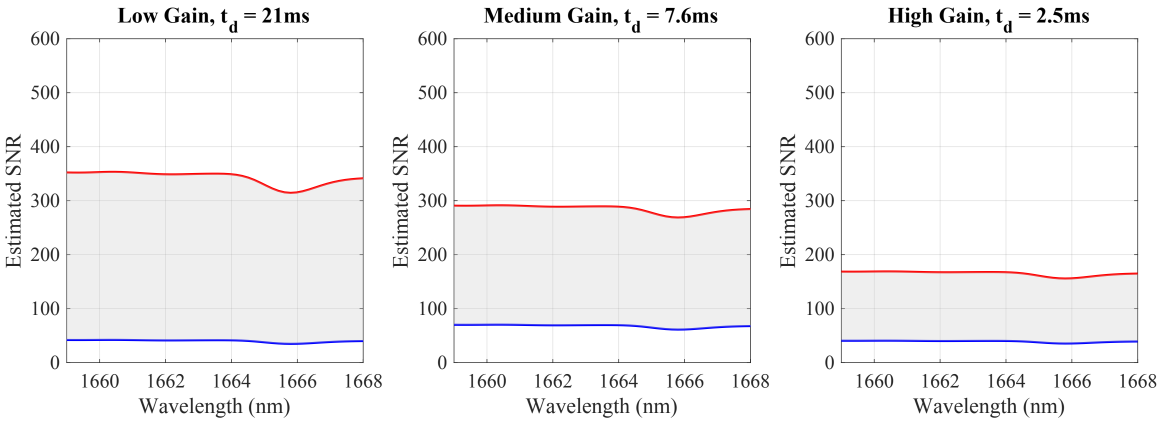

Fig. 5.4: SNR range estimated from noise components. The lower bound (blue line) corresponds to the low-light condition, and the upper bound (red line) corresponds to the high-light condition.

deviation (σ) of each noise source, but the contribution for the total noise must take into account the relative noise variance (σ^2). The BLIP hypothesis assumes that the shot noise is significantly larger than the camera-related noise, which includes the dark, the read, and the quantization noise. For the low gain case, the shot noise is significantly lower than the camera noise. The medium and high gain modes, even in high light conditions, also do not present high enough shot noise relative to camera noise to be considered as BLIP.

In summary, this analysis indicates that FINIS is limited by the camera noise. In addition, the medium gain is expected to provide the most balanced performance in terms of SNR when operating with an integration time of around 8 ms. Fig. 5.6 presents the spectrum average SNR computed for the different SZA and albedo, considered in the operational range.

It is important to note these results indicate the measurement noise performance of a single camera. FINIS, however, will provide the methane retrieval using data from both cameras, combined as described in Section 4.5, thus a proper error propagation must be carried out to derive the methane retrieval noise. This is done in the next section.

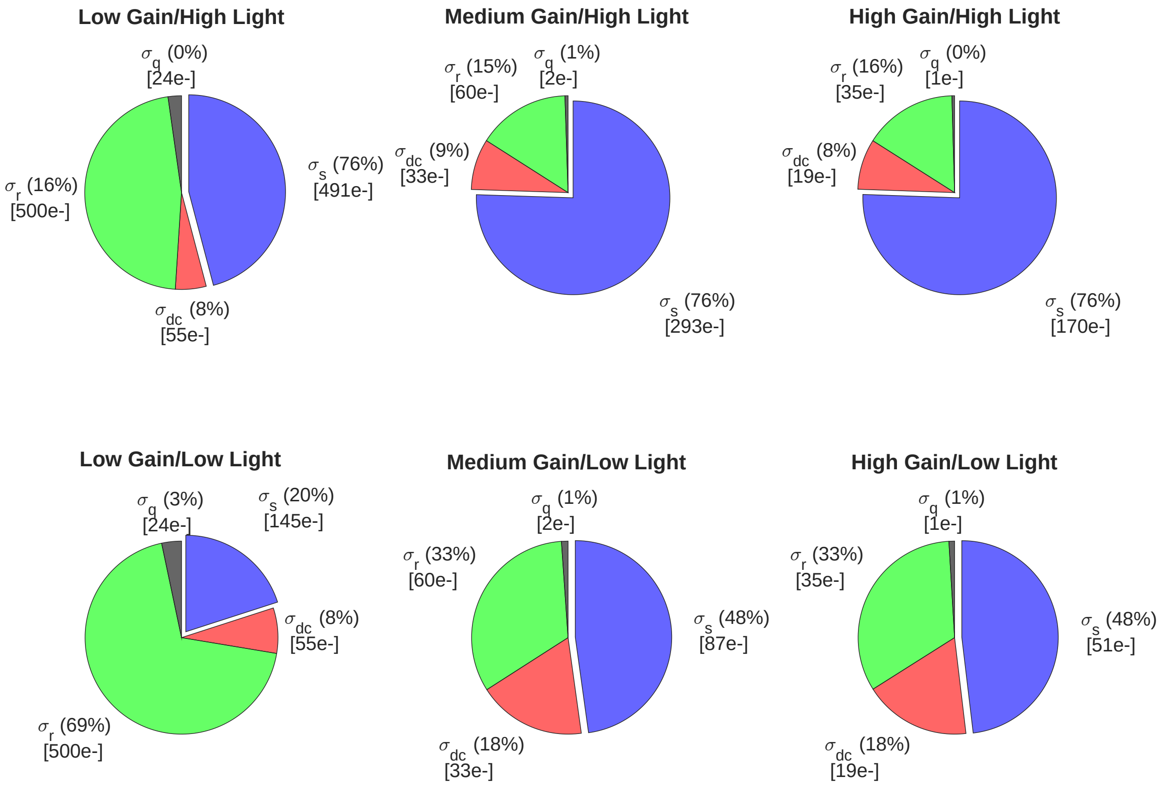

Fig. 5.5: Spectrum averaged noise composition for the three gain modes in low-light (Alb=0.1, SZA=60°) and high-light (Alb=0.6, SZA=20°) conditions. Integration times: low gain (21ms), medium gain (7.6ms), and high gain (2.5ms).

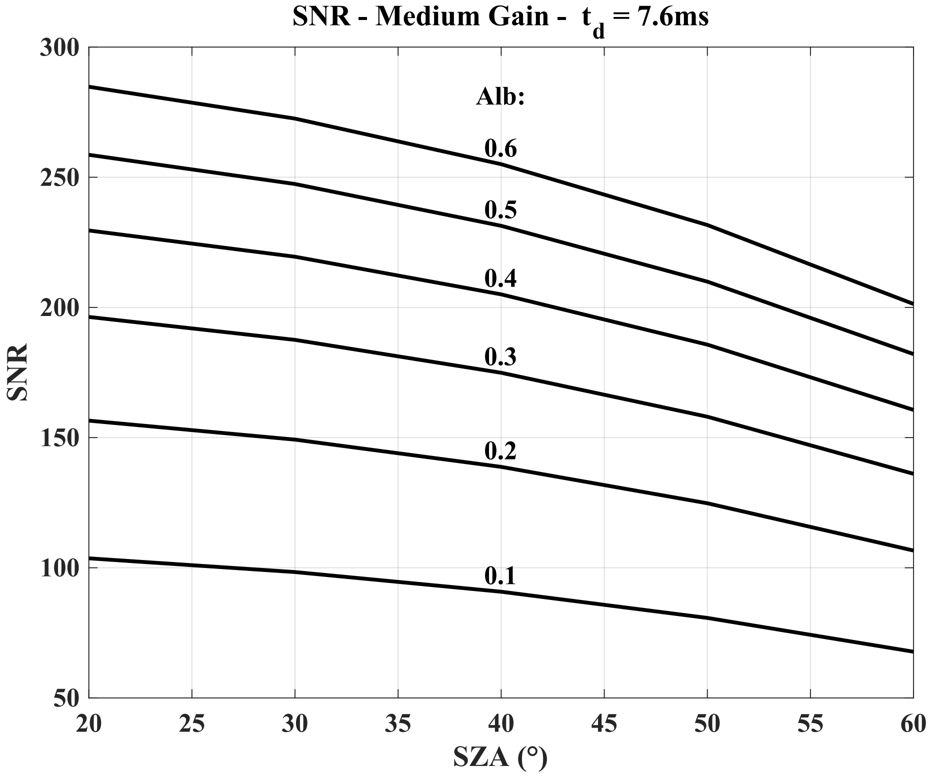

Fig. 5.6: Estimated SNR of a single camera measurement in medium gain mode at different illumination conditions

5.2 Retrieval Noise Analysis

The retrieval noise is estimated by computing the retrieval covariance expressed in Eq. (4.20). Since the measurement vector y is defined as the natural log difference of the measurements from CAM1 and CAM2, as shown in Eq. (4.22), the measurement noise can be computed using Eq. (5.13), where λ_1 and λ_2 represent the center wavelength of the CAM1 and CAM2 samples, respectively. The spectrum SNR functions of CAM1 and CAM2 are considered to be equal, $SNR_1(\lambda) = SNR_2(\lambda)$, since the cameras are assumed to have identical noise characteristics.

$$\sigma_y(\lambda_1, \lambda_2) = \sqrt{(\frac{1}{SNR_1(\lambda_1)})^2 + (\frac{1}{SNR_2(\lambda_2)})^2} \tag{5.13}$$

Considering that the spectrum response of CAM1 is rotated 180° with respect to the CAM2, see Fig. 4.6, the SNR of CAM1 data array also becomes a rotated version of CAM2. Fig. 5.7 presents the SNR values estimated for the low illumination condition (minimum radiance). The blue arcs (lower SNR region) indicate where each sensor is most sensitive to methane absorption.

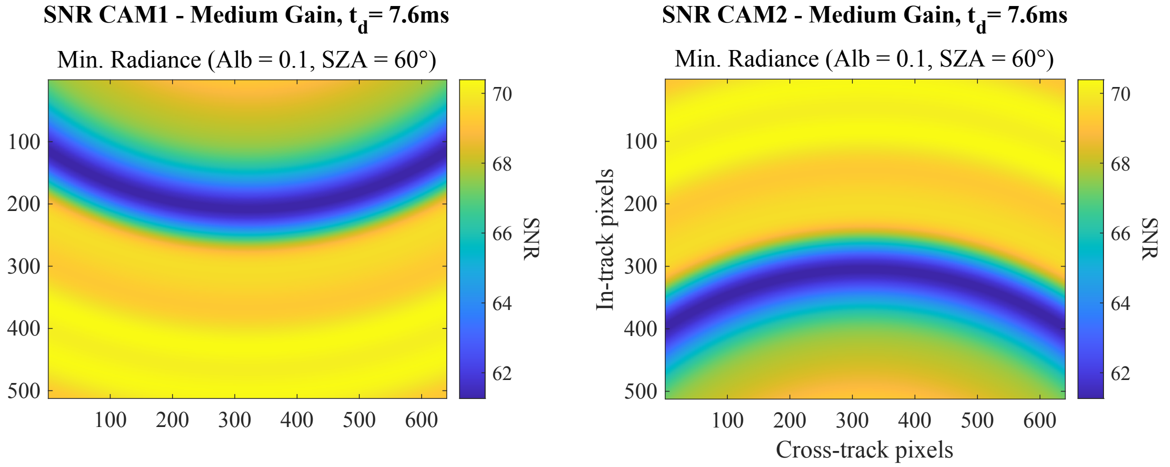

Fig. 5.7: SNR of CAM1 and CAM2 data array measurements, considering the low light condition and medium gain settings. The 180° rotation is caused by the tilted narrowband interference filter configuration

Since both cameras share the same FOV, a ground cell will be measured at different positions across both FPAs during the satellite pass. Assuming nadir-pointing, the ground scanning pattern can be simulated considering the relative Earth-satellite velocity, which depends on the target latitude and orbital parameters. Fig. 5.8 illustrates this data sampling concept with a 5 fps acquisition rate for two targets that cross the field in different positions. Target 1 crosses near the center of the FOV, and Target 2 crosses closer to the edge. The following derivations examine the difference in retrieval noise performance for each target.

The targets are assumed to be located at the equator (0° latitude), and the satellite in a 550 km SSO orbit. The data acquisition is considered during the orbital descent. The lateral motion is the result of the orbital velocity component, considering the 98° inclination (retrograde orbit), coupled with the Earth's rotation velocity, which is maximum at equator. Targets located at higher latitudes will experience less lateral motion across the frames, and the track will appear more vertical.

Fig. 5.9 presents the simulated measurements for Target 1 and Target 2 collected through the sequence of overlapping frames. The time to cross the FOV is approximately 11 ms. While the GSD is 149.6 m at the nominal orbital altitude, the pixel size projected on the ground during the 7.55 ms integration is 202.8 m and 153.0 m in the in-track and cross-track directions, respectively.

Fig. 5.10 displays the center wavelengths recorded by CAM (λ_1) and CAM2 (λ_2) during the data acquisition of Targets 1 and 2. The graph indicates that the spectrum range near the edge of the field of view varies from that near the center by around 1 nm. Nevertheless, in both cases, the captured spectrum window includes the primary methane absorption range between 1664 nm and 1668 nm.

The retrieval noise is estimated from the posterior covariance matrix given by Eq. (4.20). The retrieval noise depends on how uncorrelated the weighting function of each state vector element is. The computed weighting functions, using Eq. (4.23), for Target 1 and 2 data are plotted in Fig. 5.11 for comparison. The weighting functions of the linear and offset states are not shown.

The difference in the weighting function values for a given λ_1 is explained by observing

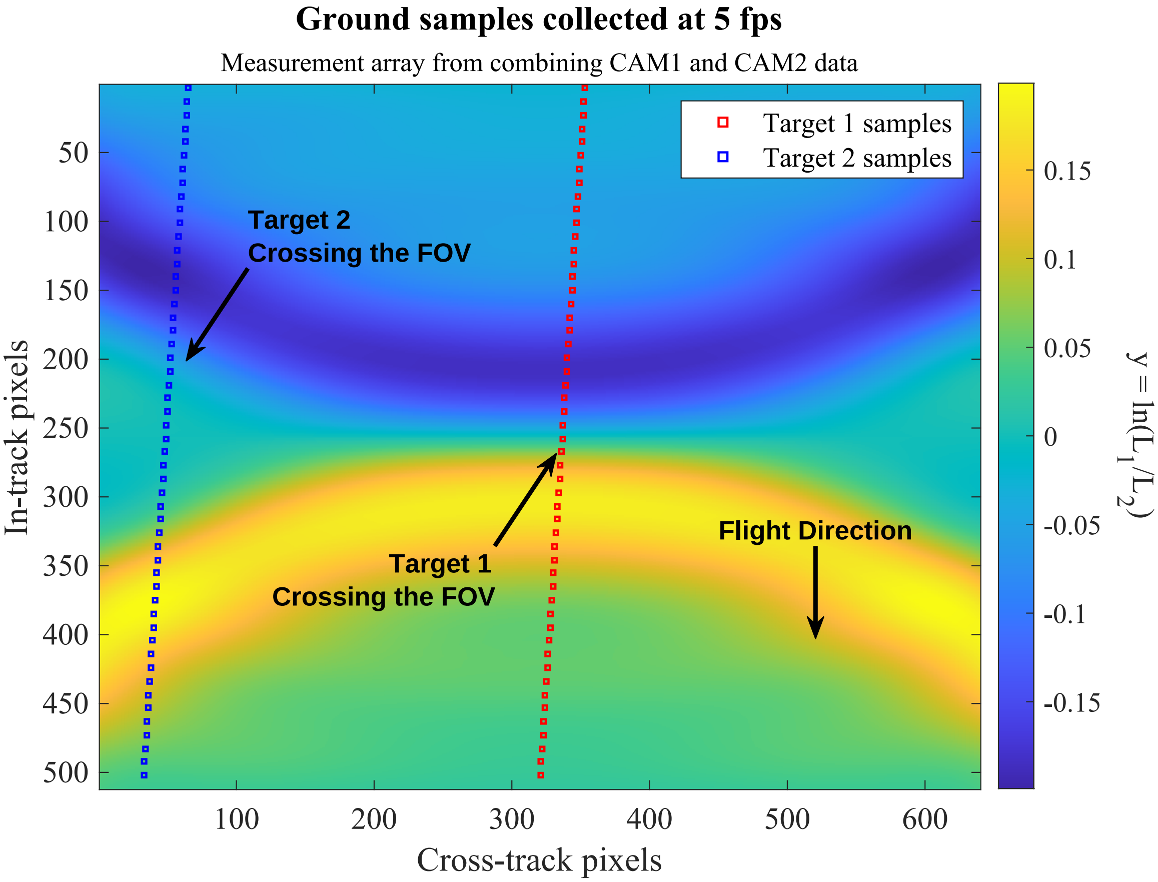

Fig. 5.8: Measurement array formed by the natural log difference of CAM1 and CAM2 simulated data for the low light condition. The overlay shows the track of samples for Target 1 (at center) and Target 2 (at edge) collected during the satellite pass at 5fps.

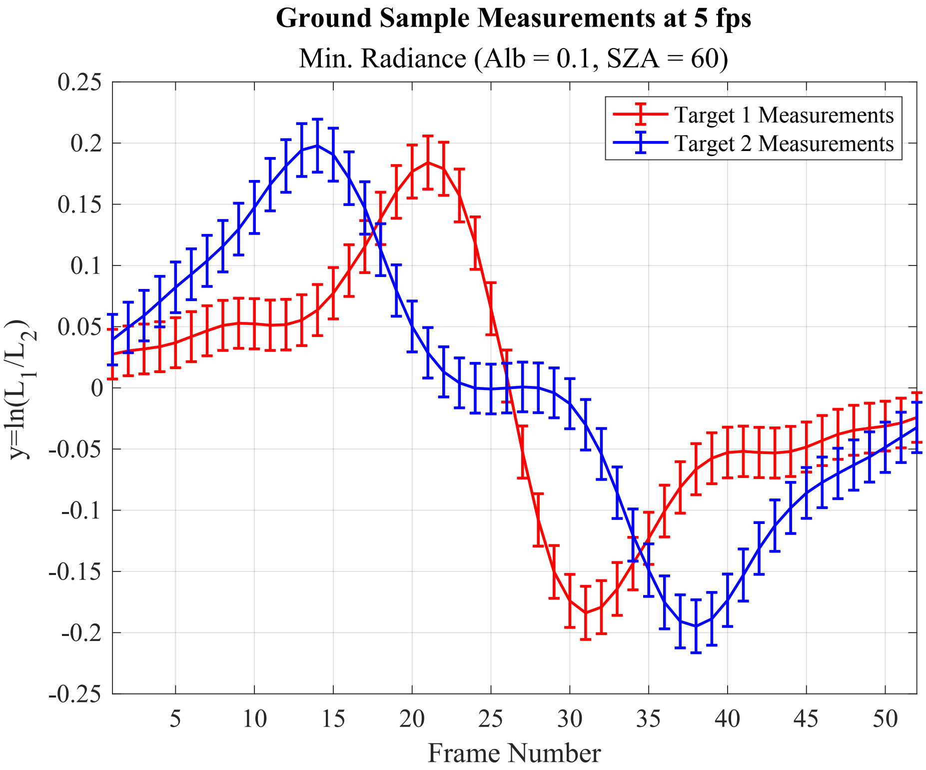

Fig. 5.9: Simulated measurements and uncertainty (2σ error bar) for Target 1 (FOV center) and Target 2 (FOV edge) collected during the satellite pass at 5fps.

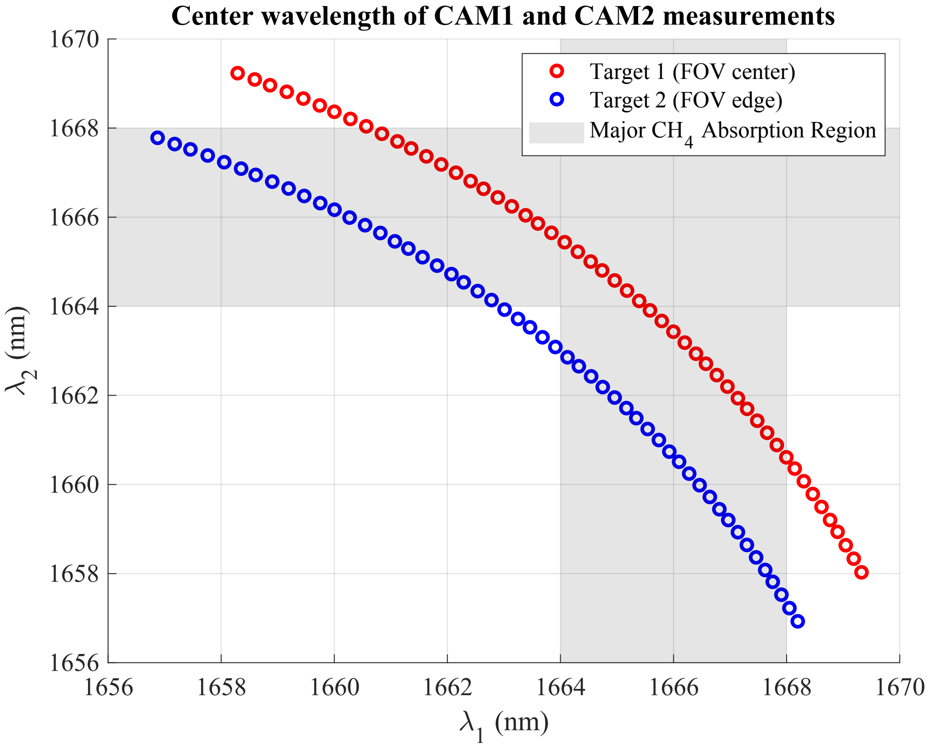

Fig. 5.10: Center wavelength of CAM1 and CAM2 measurements of Target 1 and Target 2 during simulated pass. The gray area indicates the main methane absorption region of the fitting window.

the correspondent λ_2 used in the measurement assembly, see Fig. 5.10. For λ_1 =1666nm in Target 1 data, for example, λ_2 is measured around 1664nm, whereas in Target 2, λ_2 is measured around 1661nm. This difference results in a more uncorrelated albedo function with the methane function in the case of Target 2 when compared to Target 1. The difference on the retrieval performance between the two cases are examined in the following subsections.

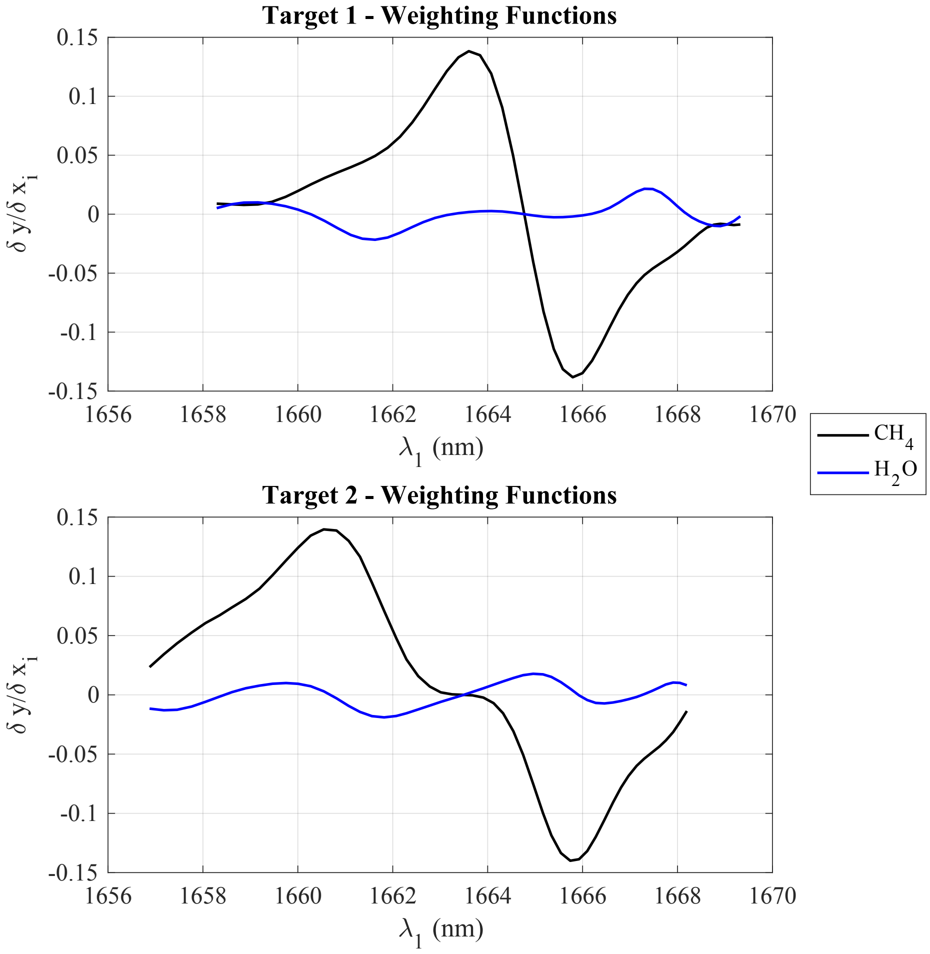

Fig. 5.11: Methane and water vapor weighting functions computed for the differential measurements from CAM1 and CAM2 of the Target 1 (crossing FOV center) and Target 2 (crossing FOV edge).

5.2.1 Retrieval performance with only methane concentration uncertainty

This analysis assumes only the methane concentration in the state vector with no prior information. In such a case, the prior covariance matrix (S_a) has all values set to zero except for the methane, which is set to infinity. This metric indicates the retrieval noise performance when only the methane concentration is estimated using the noisy measurements. The retrieval covariance is computed using Eq. (5.14).

$$\sigma^2_{CH_4} = (k^T_{CH4} S_\epsilon k_{CH4})^{-1} \tag{5.14}$$

where:

σ_{CH_4} = methane retrieval noise (std. deviation) relative to background

k_{CH4} = methane weighting function (first column of Eq. (4.25))

S_ϵ = measurement noise covariance matrix (diagonal matrix)

The retrieval noise for Target 1 and 2 data was computed considering a low acquisition rate of 5 fps and the maximum achievable acquisition rate of 60 fps per camera. Fig. 5.12 presents the results. The maximum and minimum radiance conditions are covered when the SZA is equal to 20° and 60°, respectively.

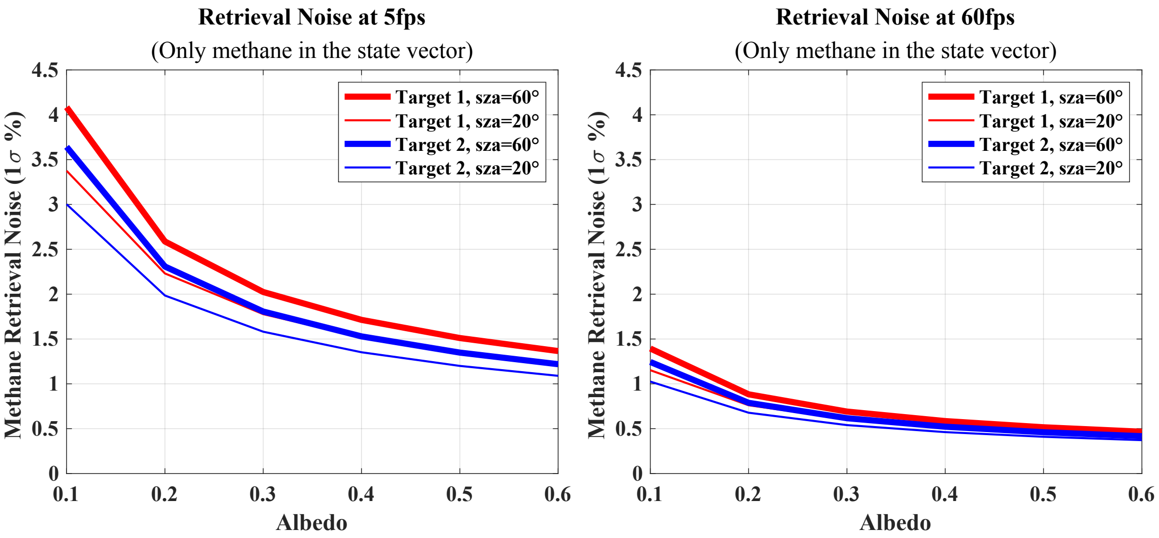

Fig. 5.12: Estimated retrieval noise limited only by camera noise computed for Target 1 (FOV center) and Target 2 (FOV edge) considering 5fps (left plot) and 60fps (right plot) acquisition rate.

5.2.2 Retrieval performance without *a priori* knowledge

In contrast to the previously presented ideal case, the worst case of the retrieval noise can be estimated considering the retrieval of the full state vector, but with no a priori information. In such case, all atmospheric states are considered completely uncertain, so the inverse of the a priori covariance matrix becomes zero ($S_a^{-1} = 0$), and the posterior covariance matrix can be computed using Eq. (5.15).

$$\hat{S} = (K^T S_\epsilon K)^{-1} \tag{5.15}$$

Fig. 5.13 presents the methane retrieval standard deviation for the case where no prior knowledge about the state vector is provided. Again, we note a difference in performance between the two targets. But in this case, the measurements collected closer to the edge (Target 2) provide a slightly worse retrieval precision in comparison to the data collected in the center of FOV (Target 1). This difference becomes less evident as the sensor acquires more samples, as show in the 60 fps plot.

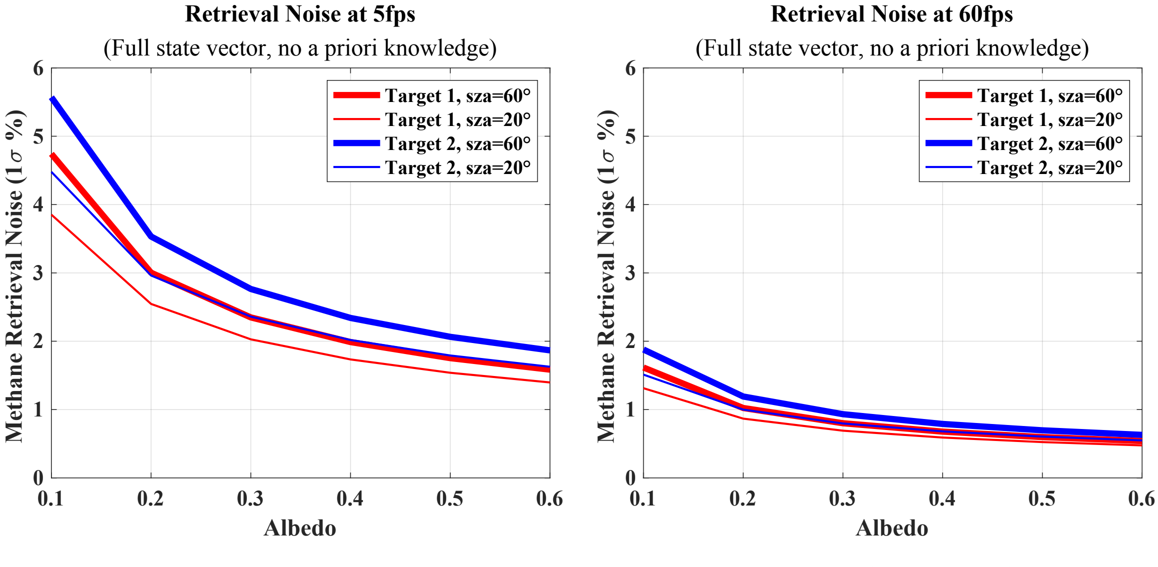

Fig. 5.13: Estimated retrieval noise with no a priori information (worst case) computed for Target 1 (FOV center) and Target 2 (FOV edge) considering 5fps (left plot) and 60fps (right plot) acquisition rate.

5.2.3 Retrieval performance with *a priori* knowledge

The operational retrieval strategy is to consider a priori information about the atmospheric state elements (CH_4 and H_2O). For this analysis, the prior standard deviations are listed in Table 5.1. The magnitude of the prior standard deviations is aligned with values reported by other methane retrieval missions, [22]. The methane retrieval noise is computed using the standard posterior covariance matrix equation, shown by Eq. (5.16).

Table 5.1: Prior knowledge about the state vector elements

Parameter	Prior Mean	Prior std deviation
Methane vertical column density, x_{CH4}	3.176E19 mol/cm^2	5%
Water vapor vertical column density, x_{H2O}	4.049E22 mol/cm^2	30%
Linear term, a_1	0	10%
Albedo offset, a_0	0.2*	50%

* Representative value

$$\hat{S} = (K^T S_\epsilon K + S_a^{-1})^{-1} \tag{5.16}$$

Fig. 5.14 presents the retrieval noise estimated using the optimal method, taking into account a priori information. Although there is still a slight difference in performance from the edge to the center of the field, both cases show a methane retrieval noise lower than 2.5% for an albedo of 0.2 and a SZA of 60 degrees when operating at 5 fps. At the maximum acquisition rate of 60 fps, the retrieval noise is under 1% for the same illumination conditions. These results indicate that FINIS can successfully fulfill its retrieval precision requirements as presented in Section 3.1.

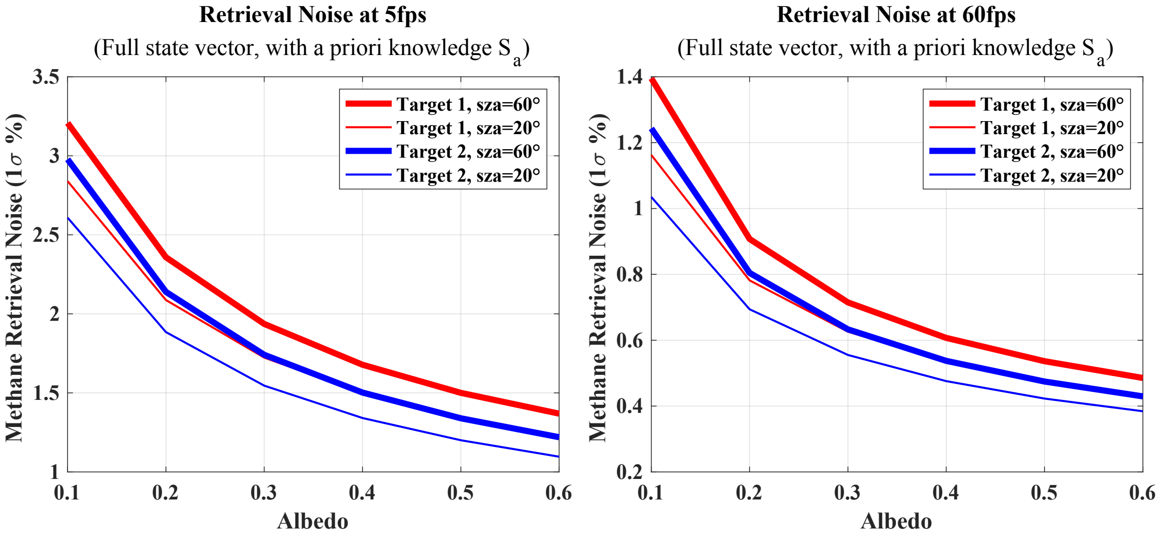

Fig. 5.14: Estimated retrieval noise, computed with the a priori information. The plot shows the retrieval noise for Target 1 (FOV center) and Target 2 (FOV edge) considering 5 fps (left plot) and 60 fps (right plot) of acquisition rate.

5.3 Filter Parameters Optimization

The fitting window optimization, detailed in Section 3.3, proposed a method to define the optimal spectral coverage that generates the most accurate methane retrieval. In that analysis, we simplified how the center wavelengths (CWL) of the CAM1 and CAM2 measurements are combined to form the relative measurement, assuming that CAM2 wavelengths are the same as CAM1 but in reverse order. However, using the tilt interference filter (IF) technique, the CWL distribution across the focal plane array (FPA) is not linear; instead, CWL is distributed in the form of concentric arcs, as shown in Fig. 4.6. Due to this effect, the center wavelengths of CAM1 and CAM2 measurements are combined in different ways depending on the location of the target crossing the FOV (see Fig. 5.10). In this analysis, we assess how different IF's CWL at normal incidence (λ_0) and tilt angle (γ) affect the retrieval precision for targets crossing near the center and edge of the FOV.

In this analysis, all optical parameters of FINIS imagers are fixed, including the IF's effective refractive index and bandwidth, focal length, and detector size. The only two optimization variables are the IF's tilt angle and the IF's center wavelength at normal incidence. The methane retrieval noise computation is performed using Eq. (5.15), where no prior information about the methane and water vapor concentration is considered. Moreover, all measurements are assumed to have the same SNR of 100. The data acquisition rate is assumed to be 5 fps, which generates approximately 50 relative radiance measurements for each target.

The search space covers tilt angles ranging from 6 to 15 degrees in intervals of 0.1 degrees and CWL at normal incidence ranging from 1668 nm to 1678 nm in intervals of 0.1 nm. Fig. 5.15 presents the optimization figure of merit for the case of Target 1 (crossing the center of the FOV). Note that FINIS's current IF parameters are indicated on the plot by the red cross. The darkest blue region represents the optimal area, where the retrieval noise is estimated to be between 2% and 3%.

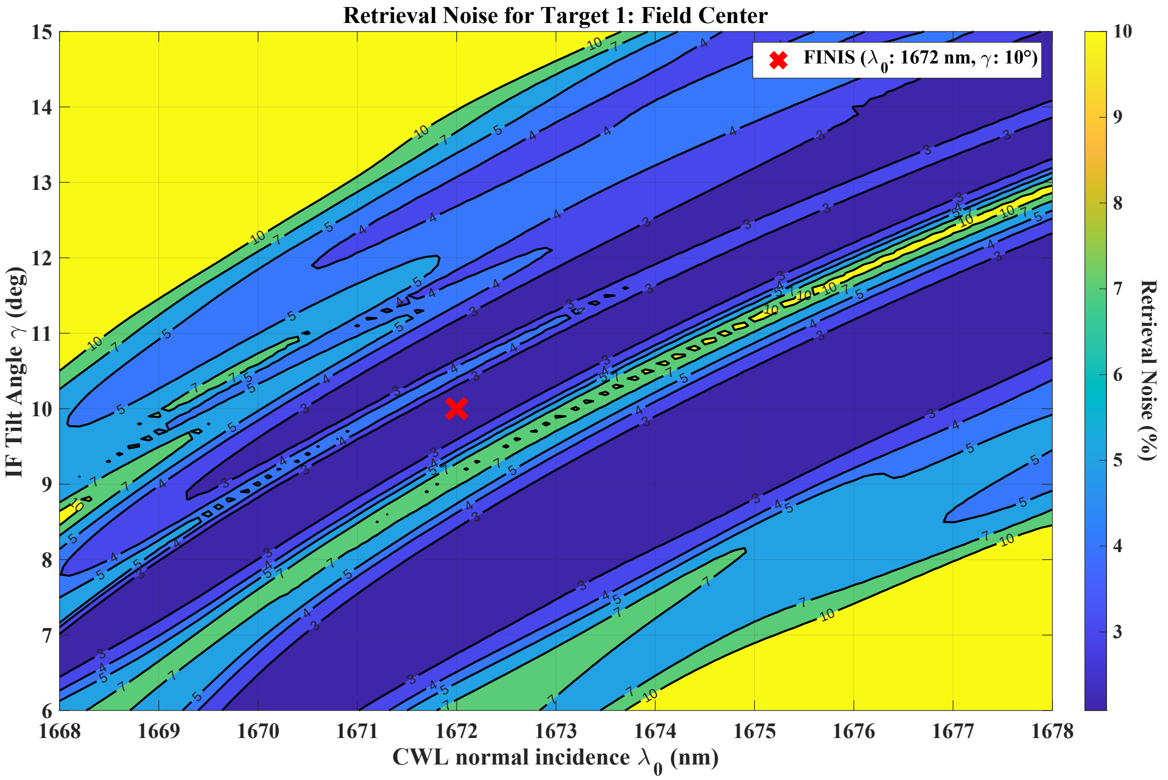

Fig. 5.15: Retrieval Noise computed for Target 1 (FOV center) for different filter normal incidence CWL and tilt angle.

Fig. 5.15 presents the optimization figure of merit result for the case of Target 2 (crossing near FOV's edge). The current FINIS' IF parameters is also indicated in most optimal region, with noise between 2–3%.

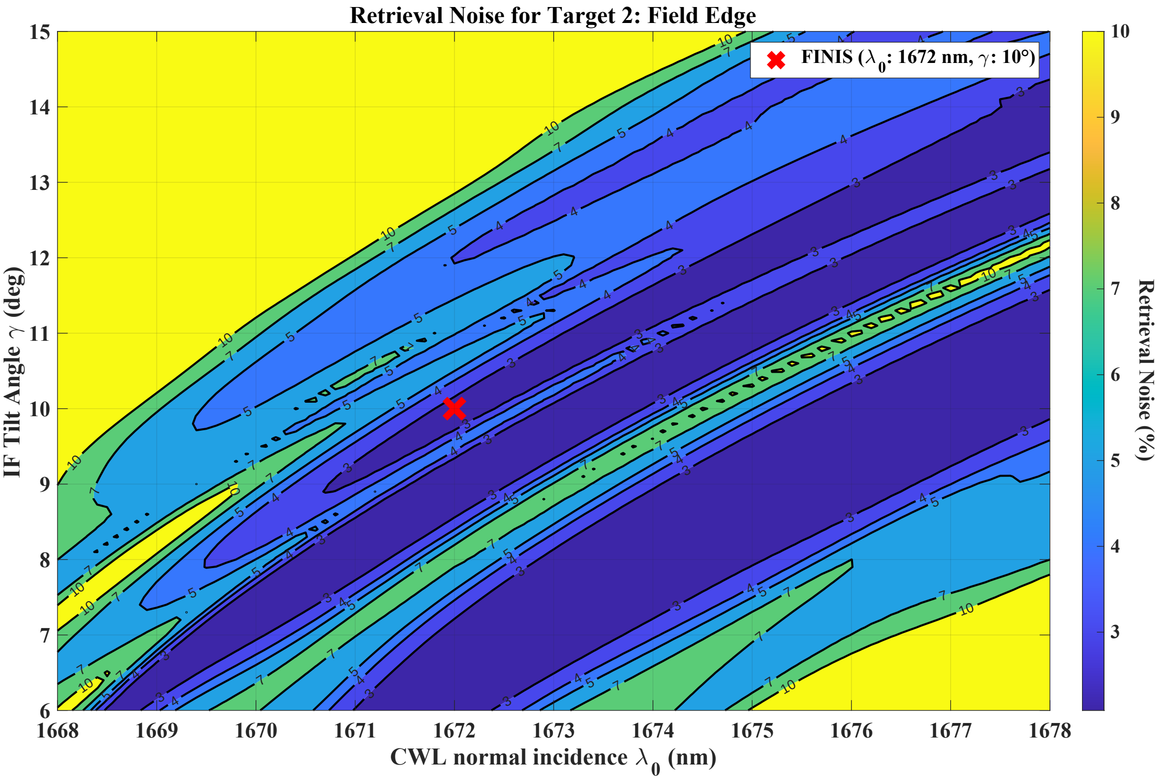

Fig. 5.16: Retrieval Noise computed for Target 2 (FOV edge) for different filter normal incidence CWL and tilt angle.

To better assess the filter parameters that provide the best overall performance across the FOV, the retrieval noise values previously computed for Target 1 and Target 2 are combined using the root sum square method. The results are presented in Fig. 5.17. We can see that FINIS's current IF parameters fall within the optimal region. Additionally, similar retrieval performance could be achieved using a tilt angle of 7 degrees with the same IF. Conversely, the instrument's performance is considerably degraded if the angle is around 8 or 9 degrees. For future iterations, if the instrument's F-number remains the same, we suggest using an IF with a higher CWL at normal incidence, such as 1676 nm, as it provides a broader range of optimal tilt angles around 10 degrees.

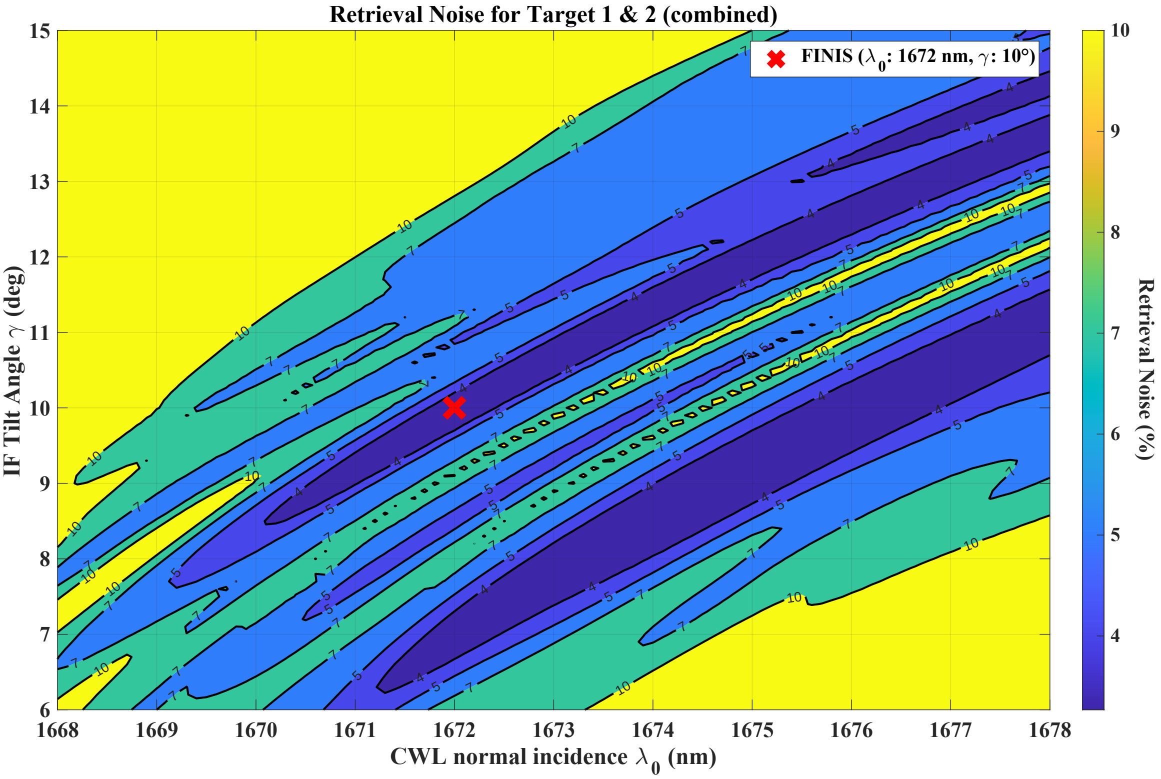

Fig. 5.17: Retrieval Noise computed for Target 1 and Target 2 (combined) for different filter normal incidence CWL and tilt angle.

5.4 Plume Detection Simulation

The main goal of the plume detection simulation is to evaluate the ability to detect methane point sources (methane plumes) using simulated images from CAM1 and CAM2. In this simulation, we examine the generated methane concentration maps to identify the point sources by detecting the contrast between the plume tail and the cluttered background.

The next subsection explains how the simulated images from CAM1 and CAM2 were generated from Landsat-9 imagery.

5.4.1 Simulated Images

The process of simulating the stack of images captured by CAM1 and CAM2 is summarized in the diagram shown in Fig. 5.18. The white boxes with bold font indicate the user inputs, the white boxes with regular font are intermediate results, and the blue boxes are procedures.

The data acquisition rate was set to 5fps, and both cameras were considered perfectly synchronized. The integration time was set to 8ms, with both cameras operating with medium gain settings.

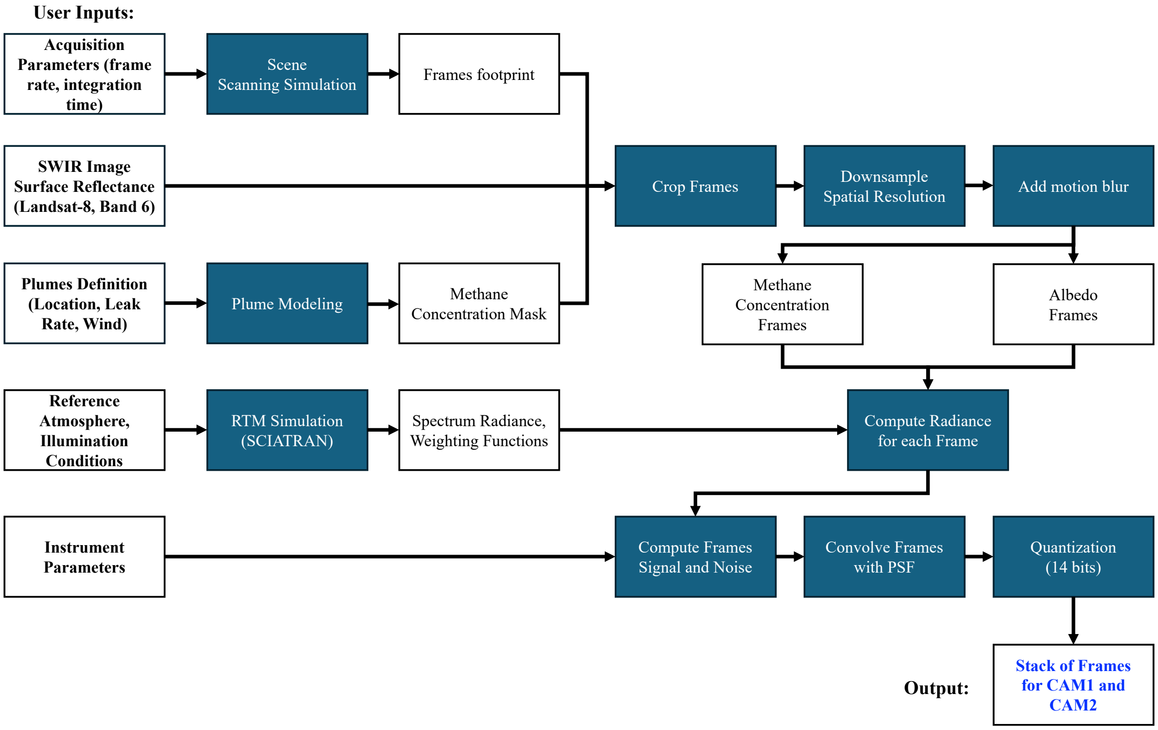

Fig. 5.18: Imagery synthesis process diagram

The baseline image of the scenario was formed by combining two Landsat-9 Collection 2 Level 2 images, which encode the surface reflectance (albedo) for each spectral band. Fig. 5.19 shows an RGB composite using Bands 2,3 and 4. While the RGB composite was only used for display purposes, the surface reflectance information was extracted from Band 6 (SWIR 1: 1.57-1.65μm).

The methane concentration mask was created with the addition of 25 point sources arranged in a uniform grid of 5 rows by 5 columns, as shown in Fig. 5.20. The leak rates of these sources vary for each row, with the top row having the highest leak rate of 5 metric tons per hour, followed by 3, 2, 1, and 0.5 th^{-1} for the subsequent rows. These leaks are considered medium and small-size leaks in the context of space-based measurements. A

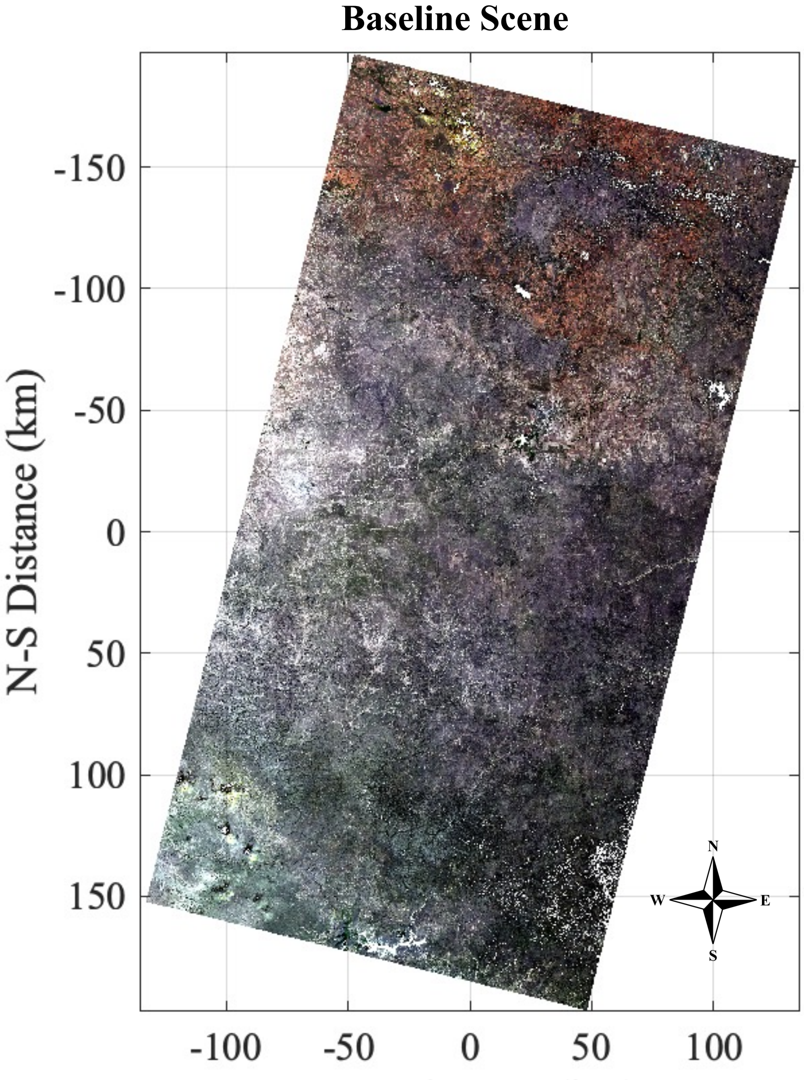

Fig. 5.19: Baseline scene formed by combining two Landsat-9 frames (courtesy of the U.S. Geological Survey). Central coordinates: (31.0124°, -100.9619°)

plume model, discussed in Section 4.4, was used to simulate the plume methane distribution, with all plumes considered to have stability class B and with a 5km/h wind coming from the northeast. The vertical column concentration from the plumes was added to a uniform 1800ppb methane background.

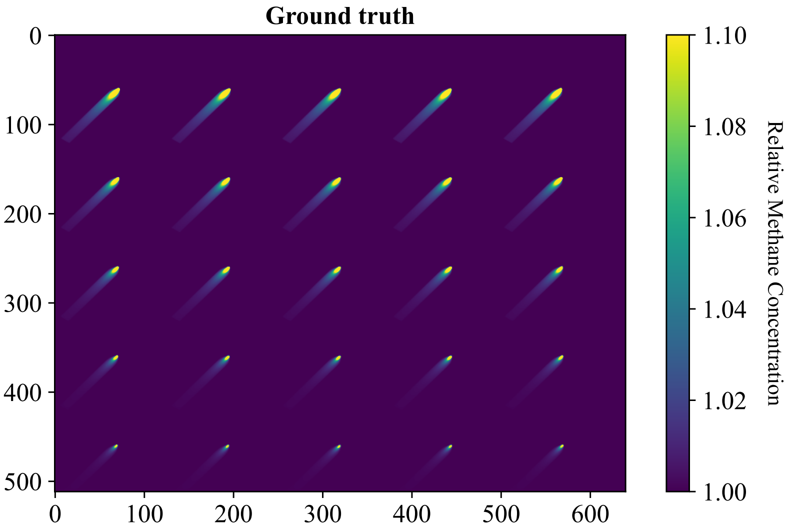

Fig. 5.20: Relative methane concentration in simulated methane plumes scenario. Leak rates are defined in descending magnitude per row: 5, 3, 2, 1, 0.5 tons/h. Wind speed: 5km/h. Wind direction: 45° azimuth. Plume model: Gaussian, stability B.

Fig. 5.21 presents the 5fps ground scanning pattern, considering the relative motion between the satellite and ground. The satellite was considered at 550km altitude, 98° inclination circular orbit. The total acquisition duration was around 30s, where 151 frames were collected from each camera. The highlighted frame 75 indicates the central frame containing the entire plume grid.

In the baseline scenario, the scanning pattern determined the area covered by each acquired frame. These footprints were then used to crop the Landsat-8 (Band 6) image and the methane concentration mask. The resulting frames were downsampled, and integration blur was added to create the albedo and methane concentration frames. Combining this information with each camera's spectrum response, it is possible to compute the spectrum-dependent radiant fluxes incident on each detector.

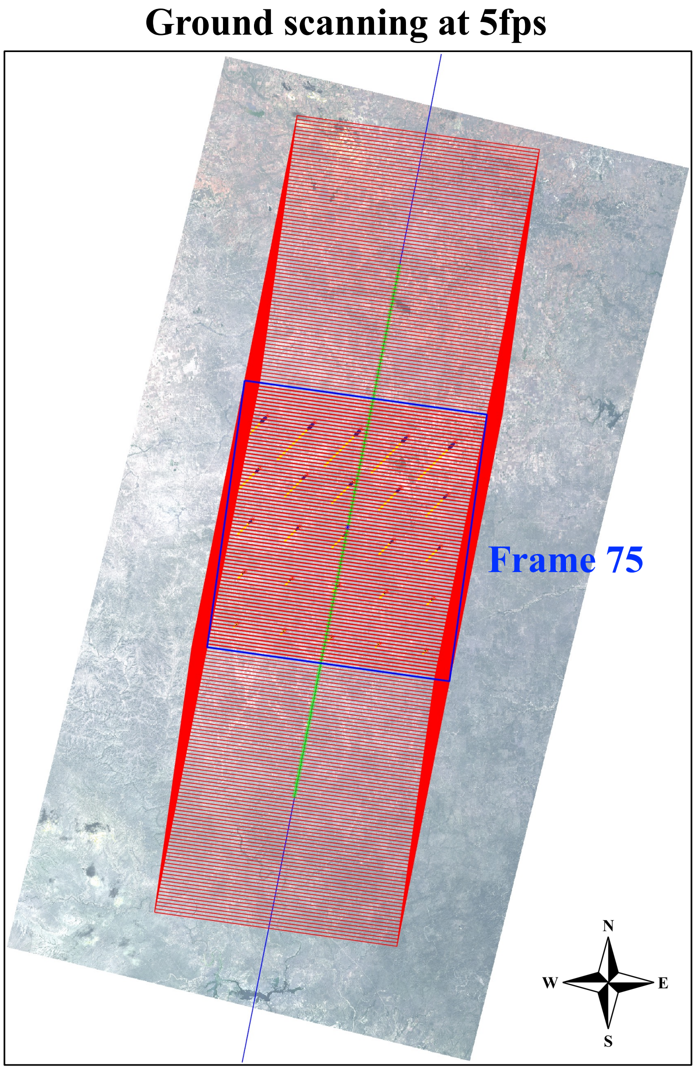

Fig. 5.21: Simulated ground scanning at 5fps, with 8ms integration time. Target central coordinates: (31.0124°, -100.9619°). Orbital altitude: 550km, inclination: 98°. Frame 75 is the central frame that covers all simulated plumes.

After determining the radiant flux, the signal was calculated using the equation Eq. (5.9), taking into account the 8ms integration time. The dark current electrons were then added to the signal average. To compute the total noise standard deviation, the various noise components were estimated - shot noise, dark current noise, and read noise. The total noise was added to the signal, considering a Gaussian distribution. To account for the optical performance, each frame was convolved with the instrument's estimated PSF. Finally, during the conversion from electrons to digital numbers (14-bit quantization), the quantization noise was automatically added to the data.

Fig. 5.22 presents the simulated pair of images at frame numbers 25, 50, and 75 (central frame). With a closer look, it is possible to notice the dark arc regions in the top half of the CAM1 images and in the bottom half of the CAM2 images. That corresponds to the 1664-1668nm wavelength window, which is more sensitive to the background methane absorption.

CAM1 **CAM2**

Frame 25 Frame 25

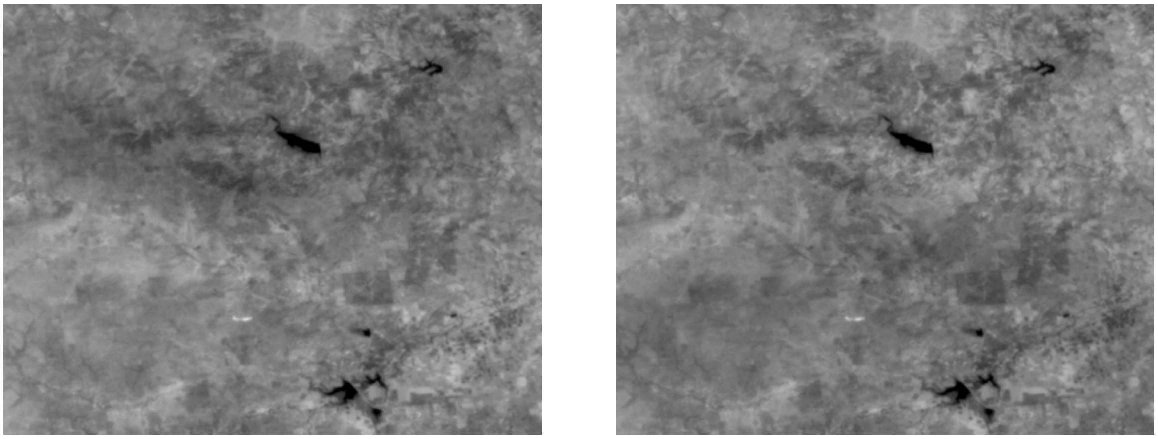

Frame 50 Frame 50

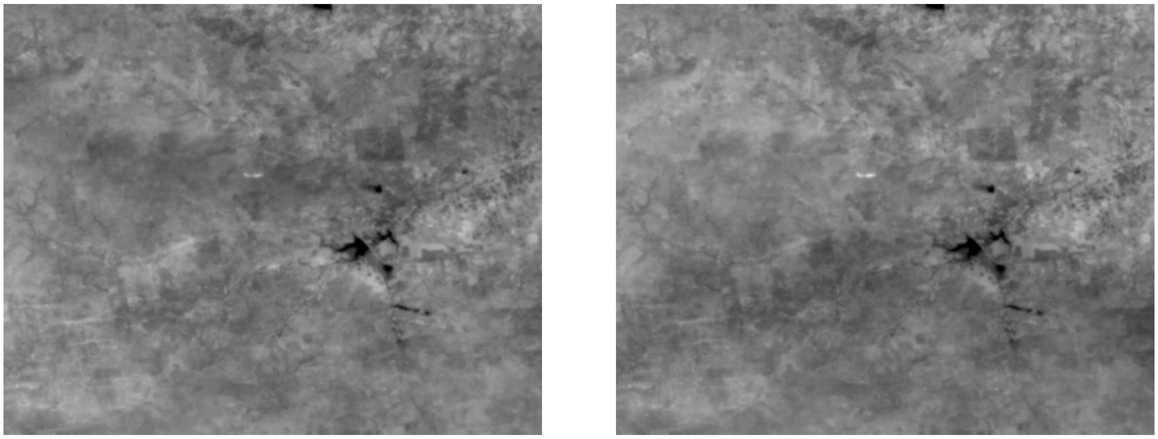

Frame 75 Frame 75

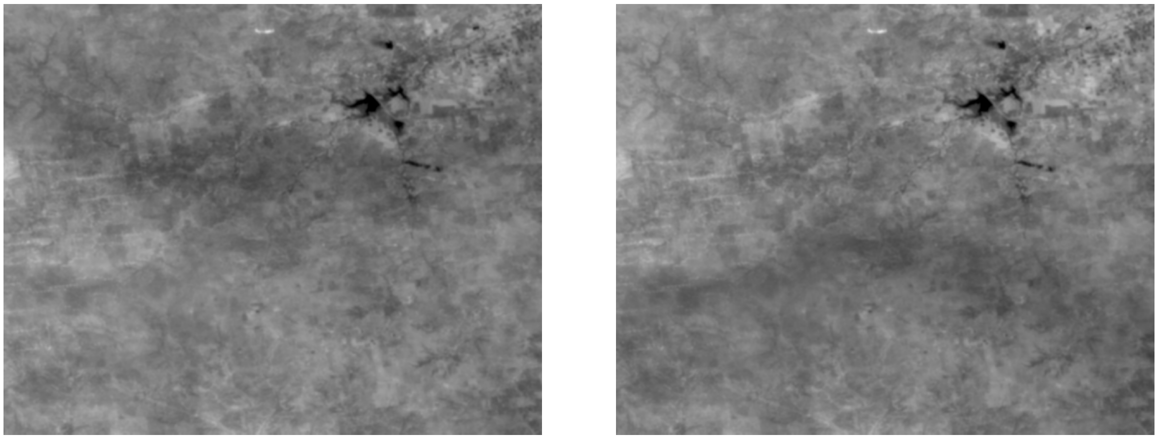

Fig. 5.22: Example of synthesized frames from CAM1 and CAM2

5.4.2 Retrieval Processing

The process diagram shown in Figure 5.23 illustrates the series of image processing steps required to retrieve methane data from CAM1 and CAM2 stacks of raw images using the fast retrieval method. The first step involves applying corrections to the raw image stacks, including dark current, offset, detector gain, geometry, and bad pixel removal. This process utilizes information obtained from both the ground calibration and the onboard calibration unit.

Second, the corrected stacks of frames go to the Image Registration phase. CAM1 images are registered assuming only translation and rotation between frames (rigid body transformation). The transformation matrix resulting from CAM1 registration is used to register the CAM2 stack of frames since the difference between CAM1 and CAM2 is assumed to be known from ground calibration. The optical depth table of CAM1 and CAM2 are also registered using the computed transformation matrices. Those tables are loaded using a lookup table of Slant Optical Depth values, pre-computed with the reference atmosphere at different Solar Zenith Angles.

Third, the registered stacks of CAM1 and CAM2 frames, along with their corresponding registered stack of slant optical depth, are fed into the fast methane retrieval process. Where the natural log difference of CAM1 and CAM2 values are linearly fit with the optical depth difference, using Eq. (4.31).

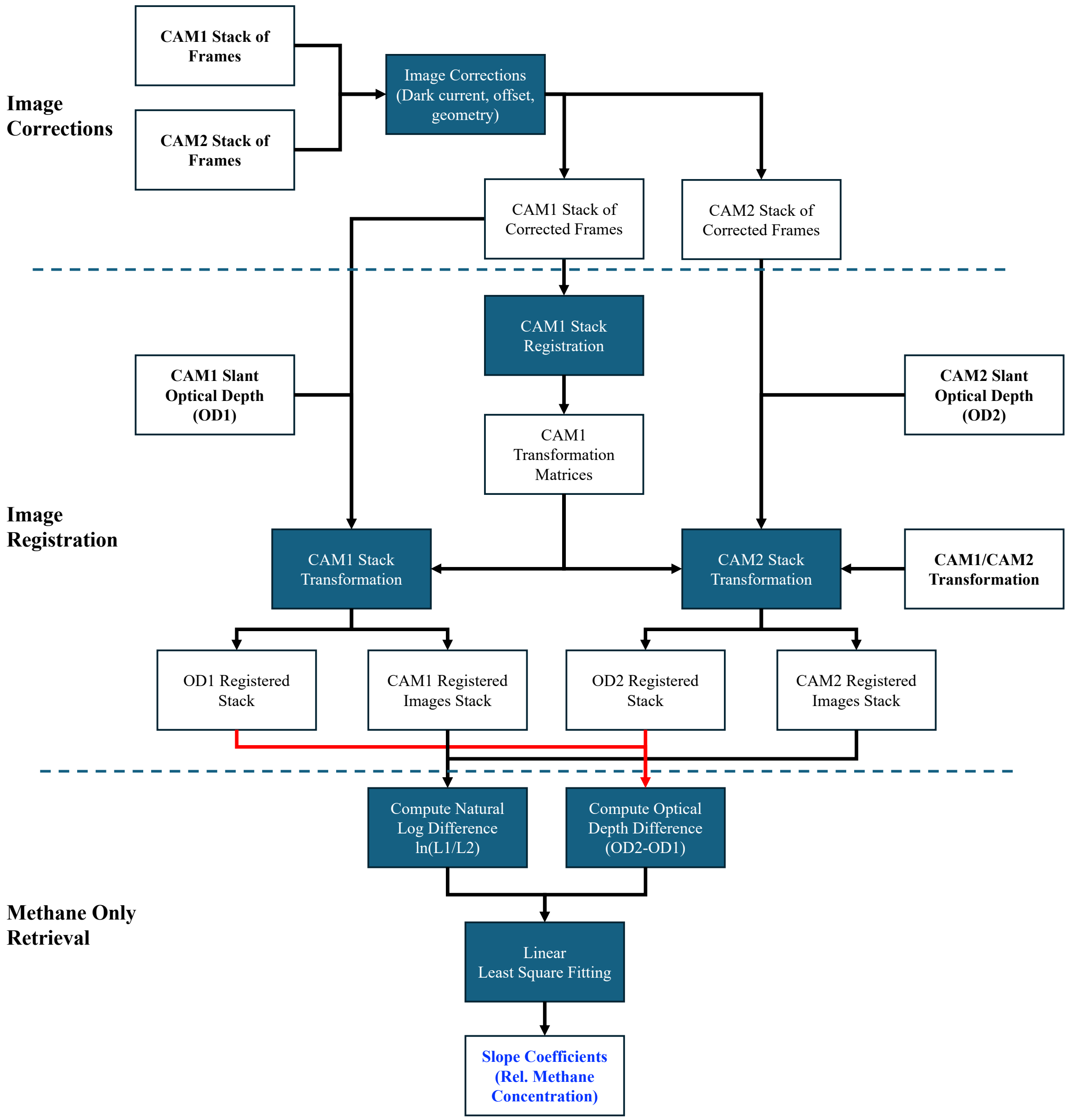

Fig. 5.23: Methane only retrieval process diagram

5.4.3 Simulated Retrieval Results

This subsection presents the simulated fast retrieval results of the synthesized data collected from both CAM1 and CAM2 for the scenario described in Section 5.4.1. Fig. 5.24 presents a side-by-side comparison between the retrieval map computed from noiseless and unblurred frames (left) and from the synthesized raw images (right) containing the estimated measurement noise and convolved with the instrument modeled PSF, which reduces the effective spatial resolution. Note that the relative methane concentration range was limited to 1.10 to increase the contrast of the plume core against the clutter background.

Besides the noticeable plume tails in both maps, we can observe that the lakes presented in the northeast part of the scene presented erroneous elevated methane measurements. That is caused when the signals from both CAM1 and CAM2 are very low due to the low water surface reflectance in the SWIR. In this situation, the natural log difference of CAM1 and CAM2 data becomes amplified even when there is a small difference in both signals. Luckily, this can be easily overcome by setting a minimum signal threshold for CAM1 and CAM2 to compute the log difference measurement, which will effectively exclude the low albedo pixels from the retrieval map. An example of this is shown Fig. 5.27.

It is important to note that apparent noise in the methane concentration map from the noiseless frames is a result of errors caused by the difference between the albedo of the ground samples and the reference albedo ($Alb_{ref} = 0.2$) that was used to calculate the difference in optical depth.

The average signal-to-noise ratio (SNR) of data obtained from CAM1 and CAM2, considering the nominal noise performance, was calculated as 145. This corresponds to an average albedo of 0.3, given the solar zenith angle (SZA) at 60 degrees. From the results presented in Figure 5.24, it can be observed that the core signal of the plume from 1.0mt/h and 0.5mt/h leaks (4th and 5th rows in the plume grid) became less visible in comparison to the background in the noisy frame retrieval, as opposed to the retrieval of noiseless frames. However, all plumes can still be considered detectable depending on the detection threshold.

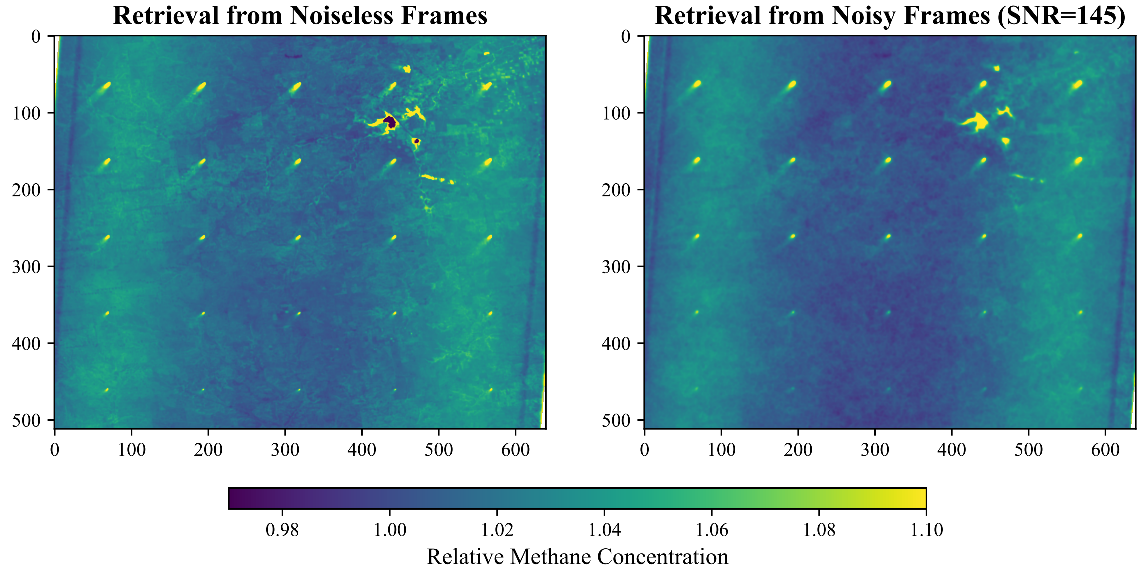

Fig. 5.24: Simulated relative methane concentration retrieval from noiseless frames (left) and frames with the predicted noise level (right)

The impact of much noisier measurements on the plume detection capability was evaluated. To achieve this, the noise floor in the simulated frames was tripled, which reduced the data's average signal-to-noise ratio (SNR) from 145 to 48. In Fig. 5.25, a side-by-side comparison of both retrieval results is presented. The results indicate that while the larger plumes (5, 3, 2 t/h leak rate) signals are still visible in the noisier retrieval, the smaller plumes signals (1 and 0.5 t/h leak rate) became increasingly challenging to distinguish from the cluttered background.

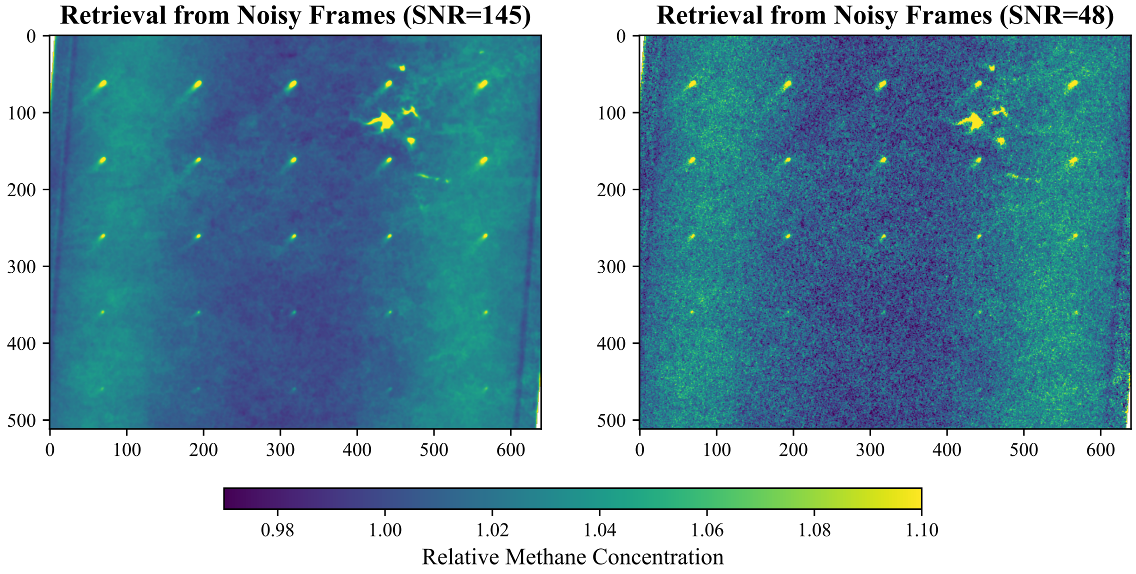

Fig. 5.25: Retrieval comparison with degraded camera noise performance

5.4.4 Flat Background Correction

Along the FOV cross-track direction, the spectrum data collected is slightly different, as previously discussed in Section 5.2. This difference causes the sensor to exhibit a different retrieval bias in the cross-track direction, resulting in two brighter strips along the edges of the methane map.

To reduce this distortion, we can calculate the cross-track bias by using the row average values and then subtracting it from the data. In our simulation, we have five plumes that are vertically aligned, which causes the average row values to spike at the plume locations, as shown in Fig. 5.26. To avoid removing the plume signals, we compute the bias by applying low pass filtering on the row average values. The corrected map shows a flatter background level profile, as depicted in Fig. 5.27.

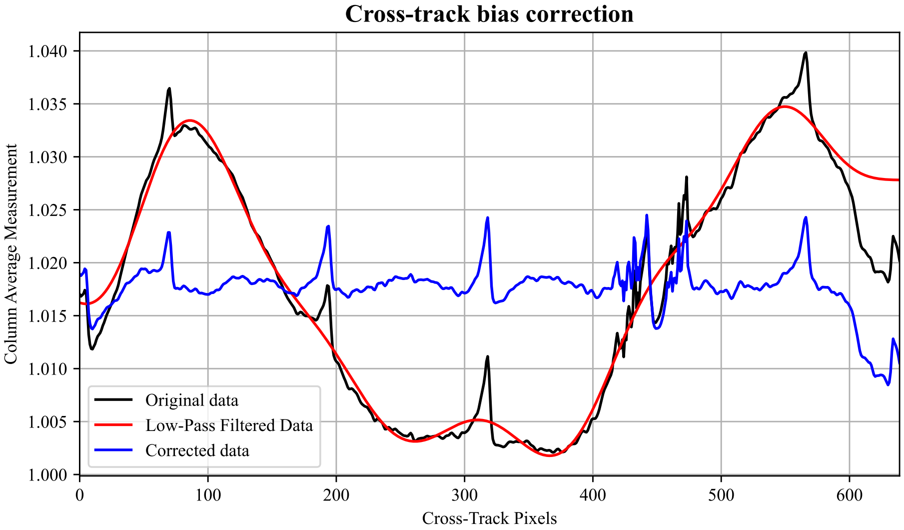

Fig. 5.26: Background cross-track bias correction

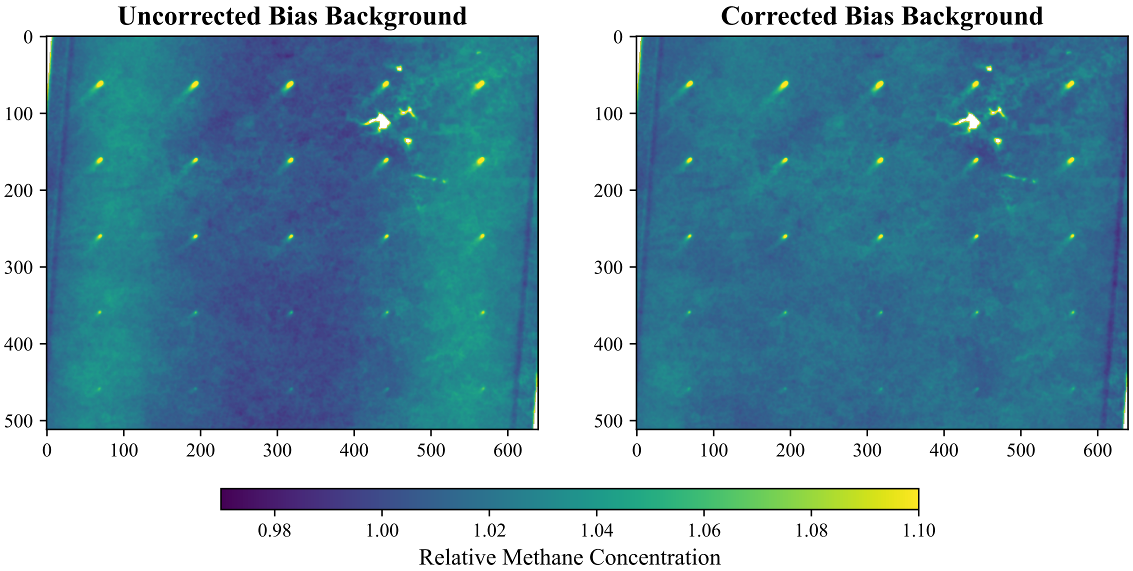

Fig. 5.27: Comparison between the retrieval scene before (left) and after (right) background cross-track bias correction

5.4.5 Non-Uniform Gain Effect

The previously presented retrieval maps were calculated under the assumption of a perfect flat-fielding calibration. However, in reality, there is always a discrepancy in the gain of the detectors in the FPA. To evaluate the impact of this discrepancy, we introduced a different gain mismatch across the FPA of CAM1 and CAM2. Two simulations were conducted, one with a 2% gain standard deviation in both cameras, and another with a 5% gain standard deviation in both cameras. The results of this simulation are presented in Fig. 5.28.

In both cases, we observe the effect of straight lines appearing along the acquisition direction, which degrades our ability to distinguish the plumes from the cluttered background. Moreover, the water removal approach, which is based on the minimum signal threshold, is ineffective in removing the small lakes that are present in both scenes. This could potentially lead to false plume detection.

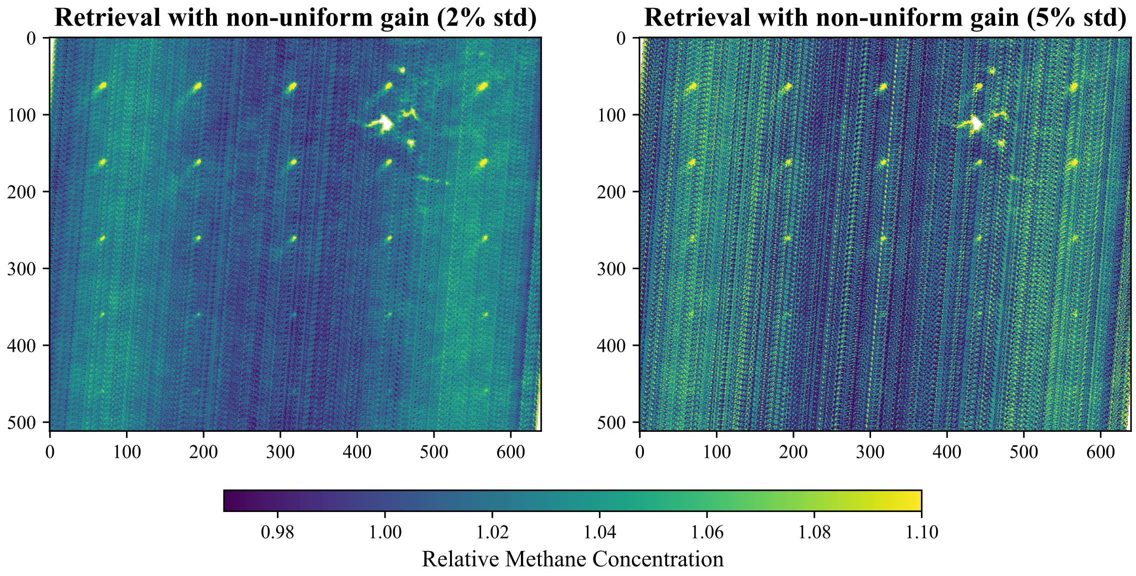

Fig. 5.28: Effect of pixel gain non-uniformity in the retrieval map, caused by poor flat fielding calibration, for example. On the left plot, the pixel gains follow a Gaussian distribution with mean 1 and 2% standard deviation across the FPA, while on the right plot, the distribution has a 5% standard deviation

Since this effect of the non-uniform gain distribution presents as a high-frequency pattern along the cross-track direction, a low pass filtering can help mitigate it. The challenge becomes finding the right filter parameter to properly smooth the straight line aberration without completely erasing the plume signals. Fig. 5.29 shows an example of the application of Gaussian kernel filter over the retrieval map for the 2% non-uniform gain case.

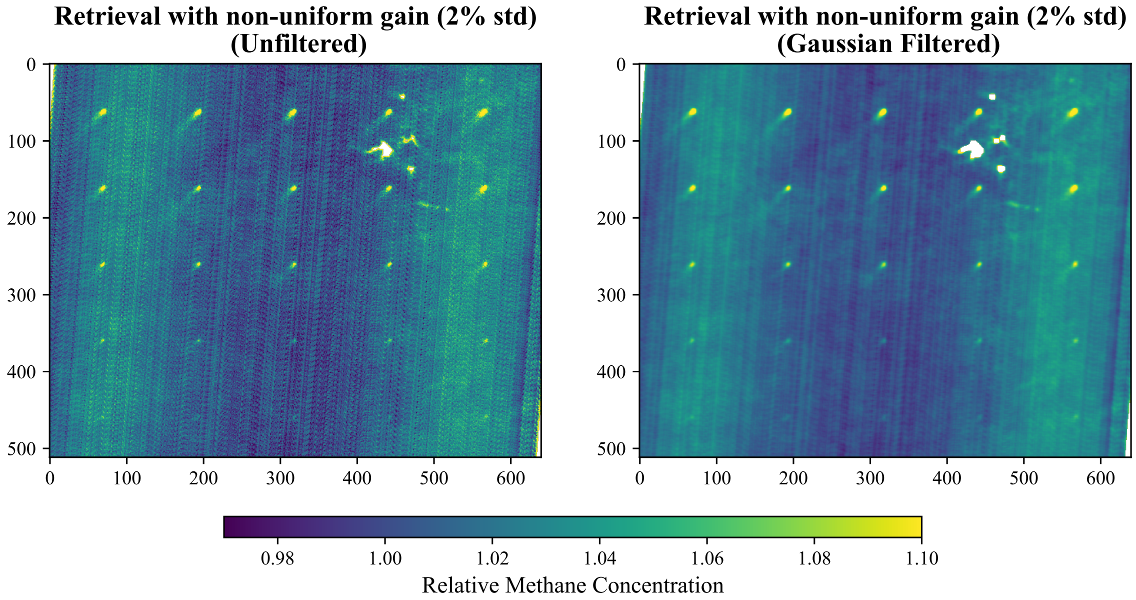

Fig. 5.29: Comparison between the unfiltered retrieval with 2% non-uniform gain across the FPA and its filtered version using a Gaussian kernel of size 5, and sigma 5.

5.4.6 Detection results

The simulated retrieval results are quite promising, especially considering that the scene's radiance level was computed for a solar zenith angle (SZA) of 60 degrees, which represents the maximum SZA for FINIS operation. By closely examining Fig. 5.30, which provides a detailed view of the retrieval along the middle column of plumes, we can compare the peak plume signals relative to the local background level.

In the nominal retrieval scenario, where the scene average SNR was computed to be 145, the plume signals from all tested leak rates exhibited peak levels exceeding three standard deviations (3σ) above the background average level. Conversely, in the retrieval from frames with 2% pixel gain nonuniformities, only the plumes associated with leak rates higher than 2 t/h could be unambiguously detected using the 3σ criterion. This result highlights the critical importance of the flat field calibration procedure.

Moreover, while the retrieval did demonstrate a measurement bias that varied along the cross-track direction, as evidenced by the presence of two vertical wide stripes in the methane concentration map, all plumes across the same rows displayed similar signals relative to the local background.

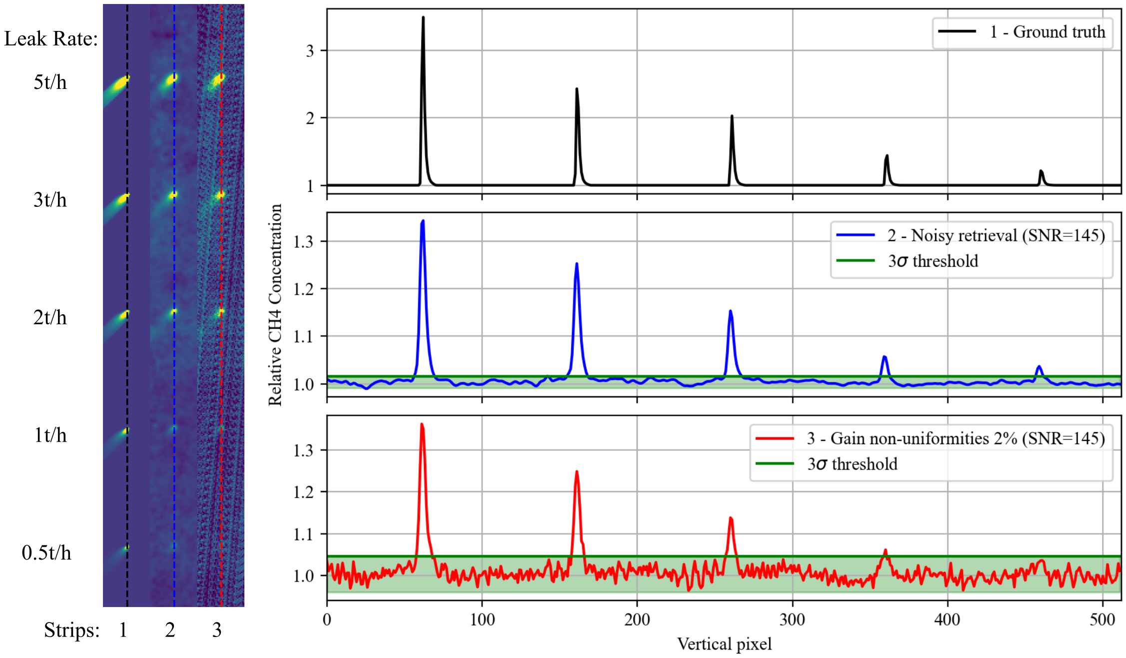

Fig. 5.30: Comparison of plume signals between ground truth, retrieval from frames with nominal noise performance (SNR=145), and retrieval from frames with 2% gain noise. The strips depicted in the left plot represent the middle column of the plume grid. Green areas indicate the 3σ interval from the calculated background mean.

5.5 Ray tracing of the Onboard Calibration Unit

For flat-fielding calibration, ensuring a flux over the FPA that is as uniform as possible is crucial. If the field is not sufficiently uniform, then the illumination pattern characterization becomes necessary to correct the field during calibration. A ray-tracing software was used to simulate the energy flux and the illumination pattern over FPA for different numbers of active LEDs in the ring.

The LED ring, made of a flexible PCB, supports up to eight LEDs connected in parallel and uniformly spaced. The selected LED is the SMT1650S, which the spectral emission and radiation pattern, presented in Fig. 5.31, was incorporated into the ray-tracing simulation as point sources.

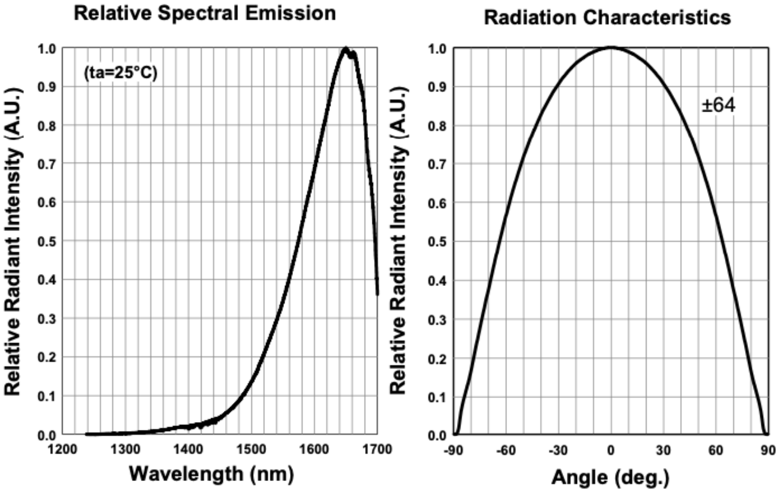

Fig. 5.31: Marubeni SMT1650 LEDs . Source: Datasheet

The detailed onboard calibration unit CAD model was used as the geometry in the ray-tracing simulation as shown in Fig. 5.32. The transparent elements (lenses and camera window) were modeled with N-BK7 glass material. The retaining rings, the lens tube, and the camera frame had their surface properties modeled as black paint. The FPA was modeled as a perfect absorber, and the shutter paddle surface was modeled as a white Lambertian diffuser with 100% reflectivity.

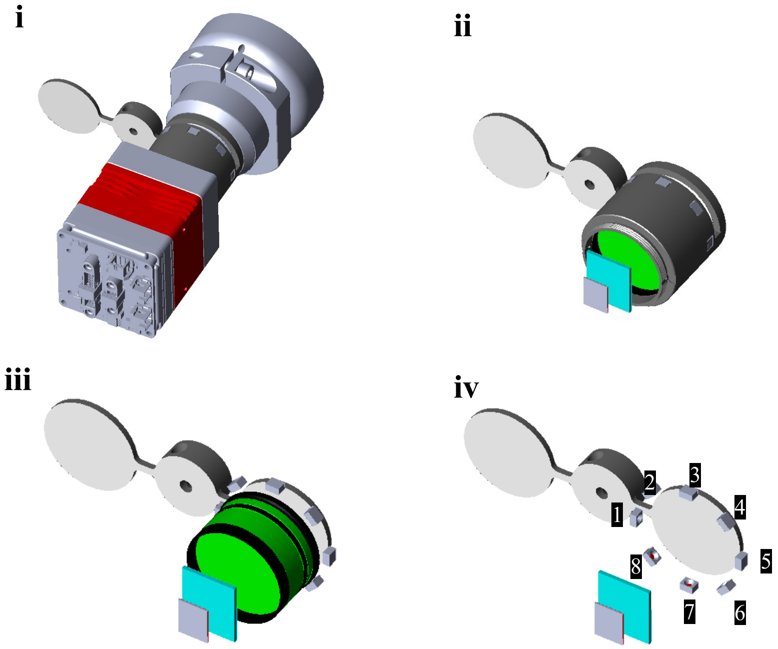

Fig. 5.32: Onboard calibration unit model used in the ray-tracing simulation. (i) Right imager completely assembled showing the shutter paddle in the closed position. (ii) Open camera view showing the FPA (gray) and camera window (light blue). (iii) Complete open view showing lenses L1 and L2 (green) and retaining rings (black). (iv) Shutter paddle with illumination ring composed of eight STM1650 LEDs enumerated from 1 to 8.

5.5.1 Radiant flux transmission

To assess the effective radiant flux on the FPA and understand how the launched rays are being affected by the shutter diffuser and the intermediate components, the TracePro software, [60], was used in the analysis mode. In this mode, it is possible to visualize all rays and track the radiant flux from the LED source passing through all surfaces before reaching the FPA. A limitation of this mode is the large amount of computer RAM that it requires if too many rays are launched. After a couple of test trials, it was observed that 500,000 rays were sufficient to provide a stable radiant flux estimation for different random seeds.

Table 5.2 presents the radiant flux values transmitted from LED 1 to the FPA passing through the intermediate surfaces. Less than 1% of the total flux transmitted by the LED reaches the FPA, while most of the energy is scattered and absorbed by the black-painted

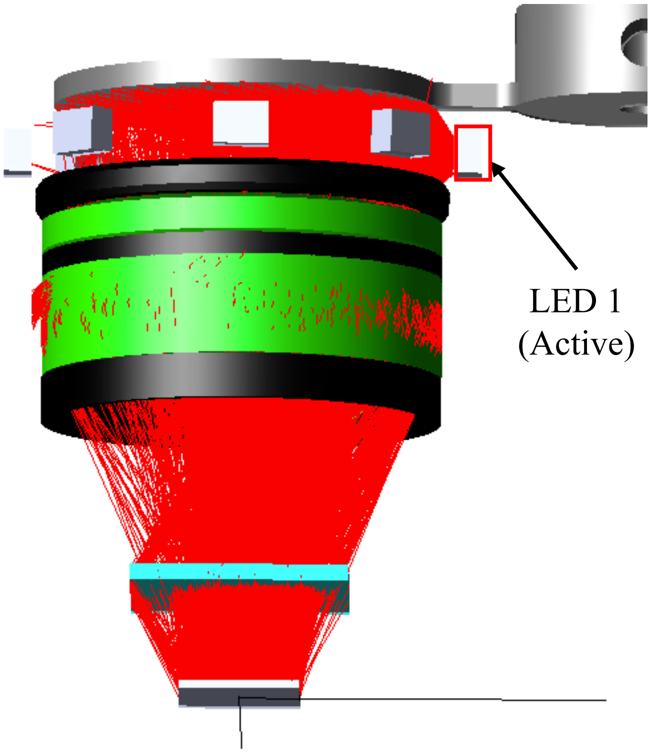

Fig. 5.33: Rays from LED1 that reached the FPA with radiant flux higher than 66% of the initial value. All other LEDs were inactive. From the 500k rays launched, only 4235 rays reached the FPA.

surfaces of the lens tube.

We can also observe that only about 44% of the LED light reaches the diffusive surface, while 81% of the source flux reaches the L2 lens entrance surface, indicating that a significant portion of the light entering L2 came from directed LED illumination. In fact, about 51% of the L2 incident rays were specular rays coming directly from the LED, 31% were single surface scatter rays, and 18% were rays arriving from multiple surface scatter. This is an expected result since the LEDs are pointed toward the center of the lens tube and not toward the shutter.

This analysis modeled the diffusive surface as a perfect Lambertian surface with 100% reflectance. In reality, FINIS' shutter is covered with 0.5mm thick diffusive Optopolymer film with a reflectance of around 80% in the LED's spectrum range, as reported by the manufacturer. On the other hand, the analysis did not consider AR coating over the lenses

Table 5.2: Total flux transmitted from LED 1 to FPA

Element	Total flux (mW)	Rel. flux
LED 1	1.7000	100%
Shutter diffusive surface	0.7534	44.32%
L2 (entrance surface)	1.3807	81.22%
L2 (exit surface)	1.1453	67.37%
L1 (entrance surface)	0.8018	47.17%
L1 (exit surface)	0.5309	31.23%
Camera Window (entrance surface)	0.0491	2.89%
Camera Window (exit surface)	0.0463	2.72%
FPA	0.0103	0.61%

and camera windows, which underestimates the actual optical transmission of the system. Considering that the AR coating applied over L2, L1, and the camera window increases the transmission of each element from about 92% to 98% at 1666μm, the actual total transmission of the three elements is about 94% rather than the 78% from simulated uncoated lenses. Overall, it is safe to assume that the lower optical transmission compensates for the higher diffusive reflectance assumed in the model.

In summary, considering the overall modeling imperfection due to the uncertainties about the surface properties, this analysis shows that the relative total flux reaching the FPA can be expected to be between 0.5% to 1.5% of the light source. A higher value of this would be only anticipated if the actual lens tube coating absorbs less radiation than the considered black paint.

Although the radiant flux transmission from the LEDs to the FPA is significantly low, achieving the flux needed for the flat-fielding calibration should not be an issue. During operation, the highest radiant flux over the FPA is estimated to be around 0.0008mW, when imaging a target at low SZA (20°) and with 0.6 albedo. This is, in fact, about 13 times less than the simulated total flux reaching the FPA when only one LED is active, see Table 5.2.

During the bright frames acquisition (shutter closed and LEDs on), it is crucial to use the same camera gain and exposure time used during the target imagery acquisition. This ensures the calibration data is valid to correct the raw images with the detectors' sensitivities, which might depend on the flux and exposure time. Considering the use of the

Table 5.3: PWM duty cycle estimation for the eight active LEDs

Individual LED radiant flux (mW)	0.68
Number of active LEDs	8
Total radiant flux from all LEDs	5.44
Flux transmission from LED rings to FPA	0.61%
Flux at FPA in continuous mode (mW)	0.3305
Desired flux at FPA (mW)	0.0008
PWM required duty cycle	2.42%

eight LEDs operating with a radiant flux of 0.68mW per LED, a pulse width modulation (PWM) operation becomes required to lower the total flux reaching the FPA during the bright frames acquisition. Table 5.3 presents an estimation of the required LED's PWM duty cycle to achieve the same radiant flux expected from operation, which drives the operational exposure time. This value will be confirmed during the lab tests.

5.5.2 Illumination pattern

To assess the illumination uniformity of FPA, the TracePro software were used in the Simulation mode, which allows a significantly high number of rays to be traced without overloading the computer RAM. In this mode, the FPA and the shutter surface were selected as the exit surfaces, which means that the simulation is limited to providing irradiance maps to only those surfaces. For each LED ring configuration simulation, a total number of 24 million rays were traced, where roughly 400k reached the FPA. Since the FPA has a total of 327,680 detectors, the simulations provide an average of 1.2 incident rays per detector.

A total of four LED configurations were studied in the ray-tracing simulation. The list of active LEDs for each configuration, as well as the number of rays that reached the shutter surface and the FPA are presented in Table 5.4. In each run, the total sum of 24E6 rays were launched from all active LEDS, with each LED launching the same number of rays. Around 1.6% of the total launched rays reached the FPA.

TracePro simulations output the irradiance distribution over both the shutter surface and the FPA. The irradiance distribution output was smoothed using a Gaussian kernel to deal with the limited number of rays reaching the surfaces; otherwise, the irradiance plots

Table 5.4: LED configurations tested in the ray-tracing simulation

Conf.	Active LEDs	Num. shutter incident rays	Num. FPA incident rays
1	1	20,469,243	474,081
2	1,5	20,432,226	409,345
4	1,3,5,7	19,945,665	401,026
5	1-8 (All)	19,781,784	397,432

would appear noisy due to aliasing. TracePro provides this smoothing feature by default. The waist radius of the Gaussian is determined by the Map Count parameter. For example, in the FPA irradiance map generation case, the Map Count parameter was set to 15, which means that the waist radius of the smoothing kernel was set as 1/15 of the width of the irradiance map. [60]

For the FPA map, which is 640 pixels wide, a Map Count of 15 with smoothing indicates that the irradiance map has approximately 86 pixels of spatial resolution, which is sufficient to detect significant illumination non-uniformities across the FPA. Besides that, the irradiance values become more statistically significant by aggregating neighbor rays. Considering the average of 1.2 rays per pixel, a circle area of 83 pixels diameter aggregates more than 6 thousand rays into the mean irradiance calculation.

Fig. 5.34 presents the irradiance maps of the shutter surface and FPA for each LED configuration case. The FPA irradiance maps show a slight uniformity improvement when more active LEDs are considered. This improvement can be better understood by analyzing the FPA normalized irradiance histograms shown in Fig. 5.35. Although all distributions have a similar Gaussian shape, the 8-LED configuration presented the lowest standard deviation of all tested configurations: 6.2%, against 6.8%, 6.5%, and 6.7% for the 1-LED, 2-LED, and 4-LED configurations, respectively. Additionally, about 70% of the FPA area is illuminated with irradiance levels falling within one standard deviation (1-σ) from the mean irradiance.

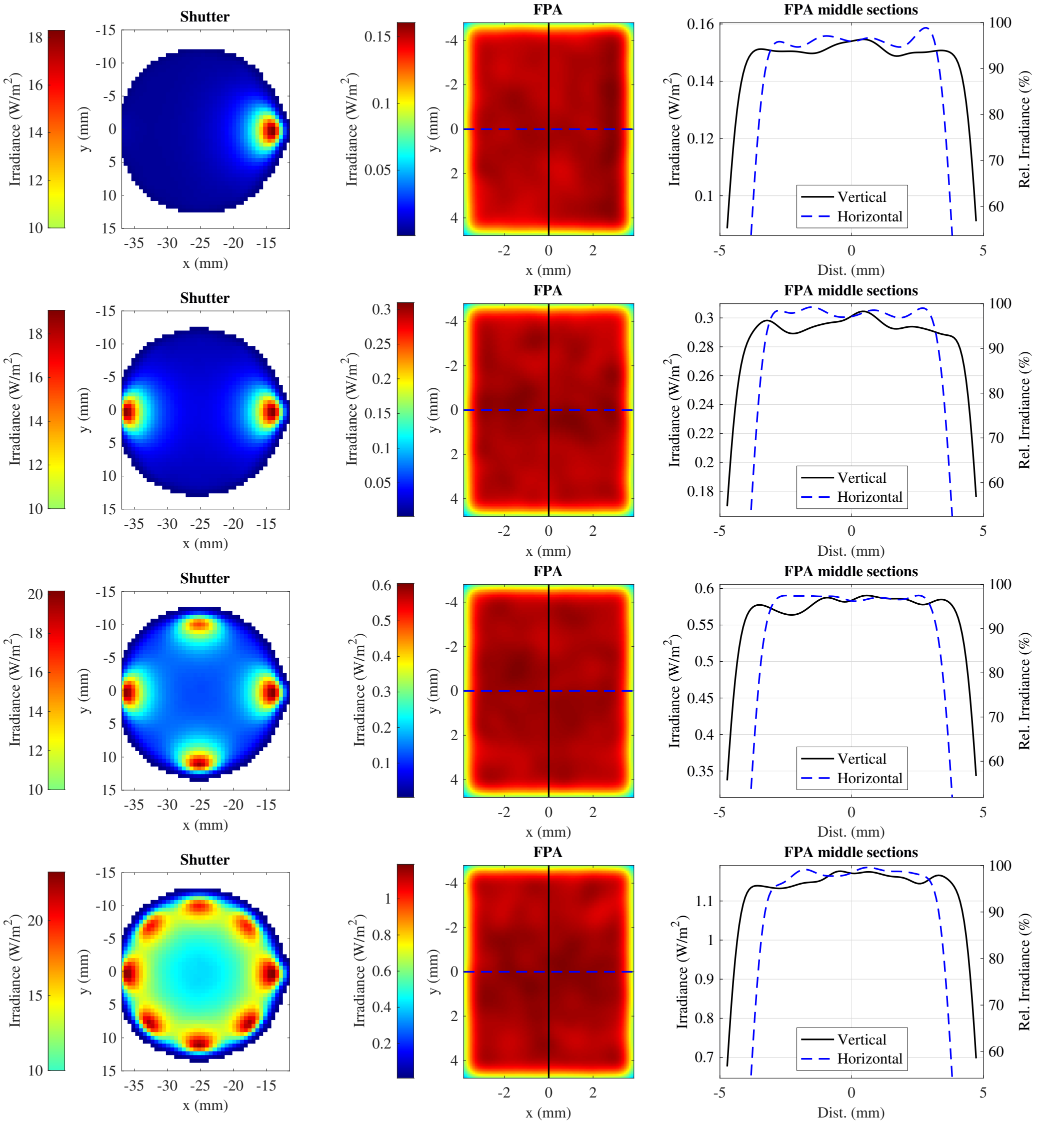

Fig. 5.34: Ray-tracing simulation results. (left) Shutter incident irradiance. (middle) FPA incident irradiance. (right) Irradiance along the FPA's vertical and horizontal middle sections.

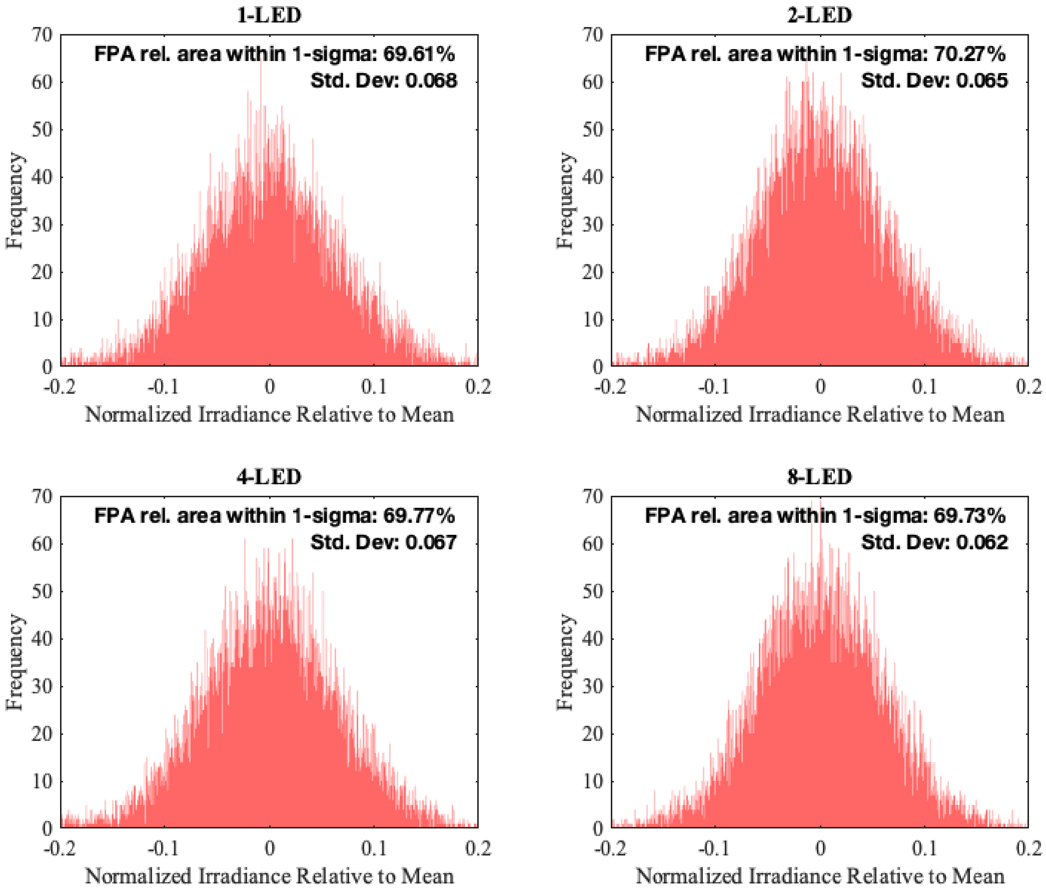

Fig. 5.35: Illumination histogram for the different LED configurations

CHAPTER 6

TESTING AND CALIBRATION

FINIS had to undergo a series of calibration procedures to ensure its functionality and characterize its performance. The list of calibration procedures, along with their brief descriptions and main outputs, is provided in Table 6.1. All calibration and tests discussed in this chapter were performed in a clean room (class 1000) in the USU Engineering Lab facilities.

Table 6.1: Summarized calibration description and main outputs

Type	**Brief description**	**Main outputs**
Focus calibration	The instrument focus is adjusted using images of a 1951 USAF resolution target.	Fine lenses spacing adjustment. Comparison between both cameras optical performance.
Stereo calibration	Multiple pair of images of an asymmetric calibration pattern are captured. The images are processed using MATLAB's Stereo Camera Calibrator App, assuming a pinhole camera model.	Intrinsic parameters, radial distortion, and tangential distortion coefficients. Translation and rotation between the two cameras.
Dark frame calibration	Several images are taken with no light source using various exposure times. The test is performed for the three camera gains and different FPA set point temperatures.	Pixel noise as a function of exposure time, camera gain, and FPA set point temperature.
Flat Field calibration	Several images of a uniformly illuminated target is acquired.	Flat field correction. Bad pixel mapping.
Onboard Flat Field	The onboard shutter is illuminated using the LED ring. Several images are taken using the camera operational settings.	Shutter illumination pattern.
Methane cell calibration	Multiple images of a uniformly lit surface are captured through a 10 cm gas cell containing various concentrations of pure methane gas at room temperature.	Methane absorption spectral response.

The following sections present a more detailed description of the setup and procedures involved in each calibration, besides the preliminary results.

6.1 Focus Calibration

After the instrument assembly, the focus of both cameras was fine-tuned by changing the spacing between the lens L1 and the blocking filter inside the 30 mm diameter tube, see Fig. 3.10. Once the best focus was found, L1 was secured using retaining rings. A 1951 USAF resolution bar target was used to assess the quality of the focus during the fine-tuning of the L1 spacing.

Fig. 6.1 shows images of the same target taken by CAM1 and CAM2, demonstrating the best achieved focus for both cameras. The relative motion between CAM1 and CAM2 is due to the parallax, caused by the proximity of the target to the pair of cameras. Note that both cameras are tilted 90 degrees counterclockwise, so the 640 pixel side is along the vertical direction.

Fig. 6.2 and Fig. 6.3 offer a comparative evaluation of focus quality achieved by CAM1 and CAM2, employing a 1951 USAF resolution bar target. In the top images, CAM1 (left) and CAM2 (right) depict the target at their respective best achieved focus. The blue and red vertical lines in CAM1 and CAM2 images, respectively, denote the pixel lines utilized for intensity profile analysis. The subsequent bottom plot displays pixel values along these lines, elucidating focus performance discrepancies between the two cameras.

Evidently, CAM2 exhibits superior overall performance in terms of MTF compared to CAM1 across various analyzed spatial frequencies. This difference in image quality may stem from disparities in the optical performance of lenses utilized in each camera system.

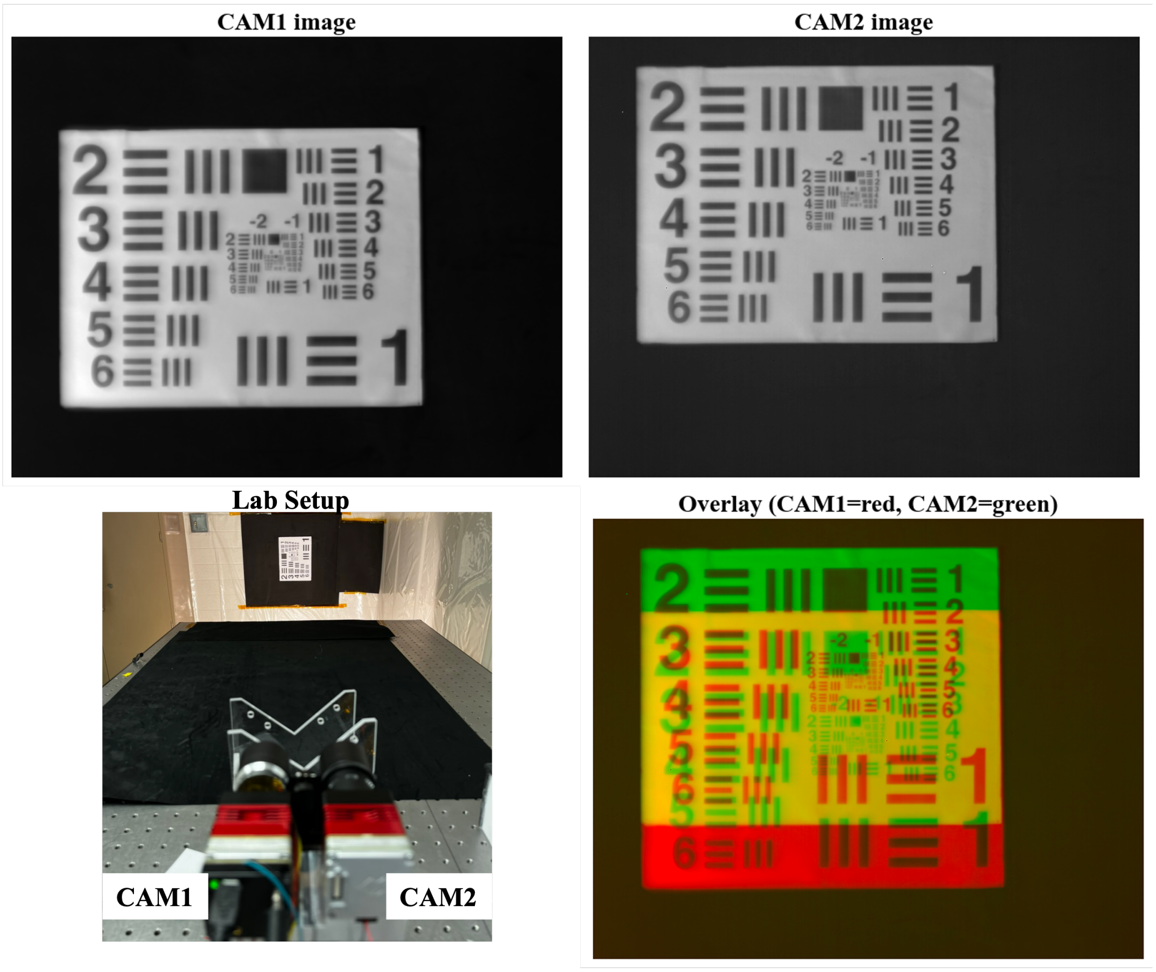

Fig. 6.1: Resolution bar target images from CAM1 and CAM2 with their achieved best focus. Overlay of images shows the parallax due to target proximity.

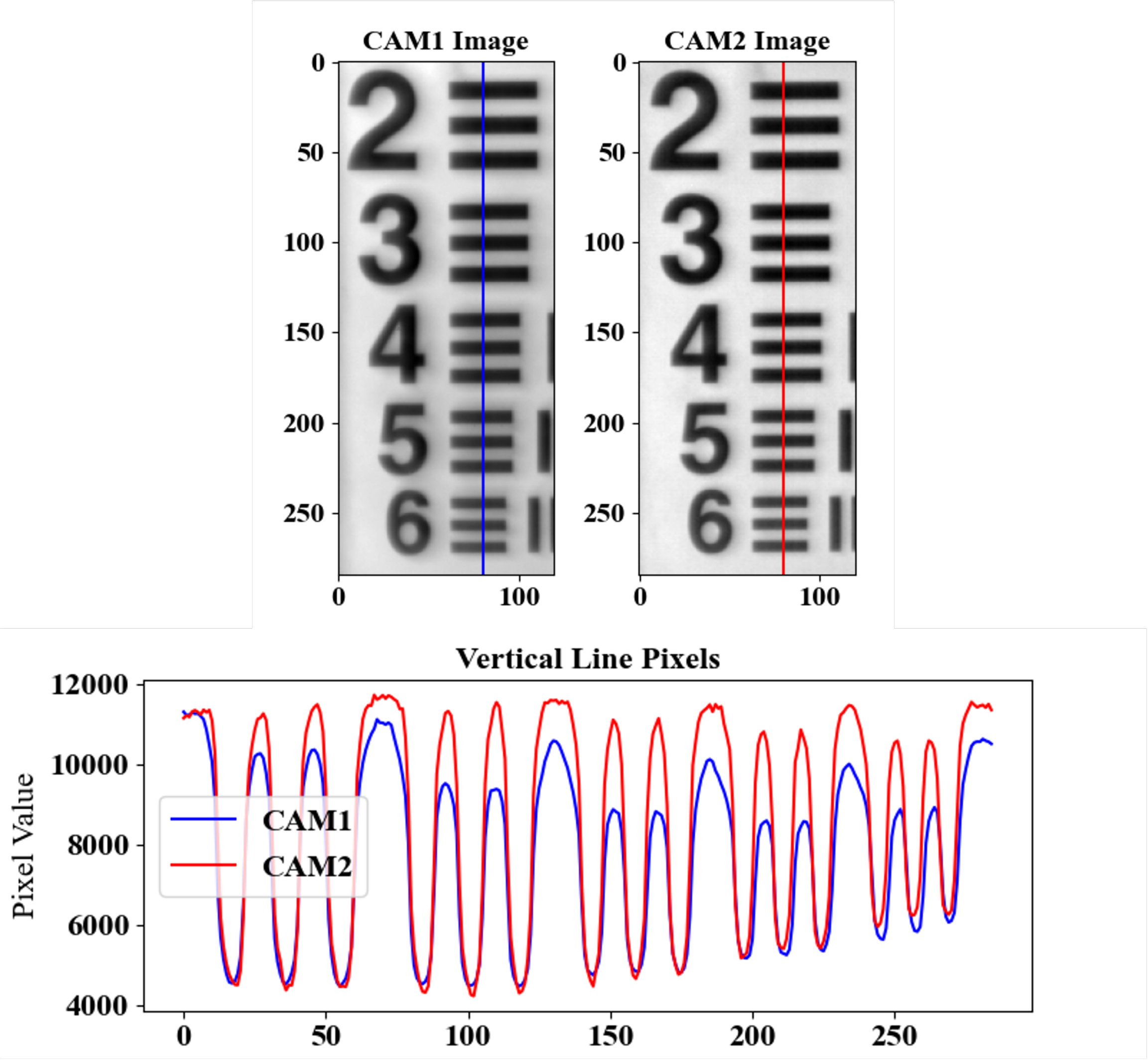

Fig. 6.2: Comparison of the focus quality between CAM1 and CAM2 using a 1951 USAF resolution bar target. Close up on the left column of number and horizontal bars.

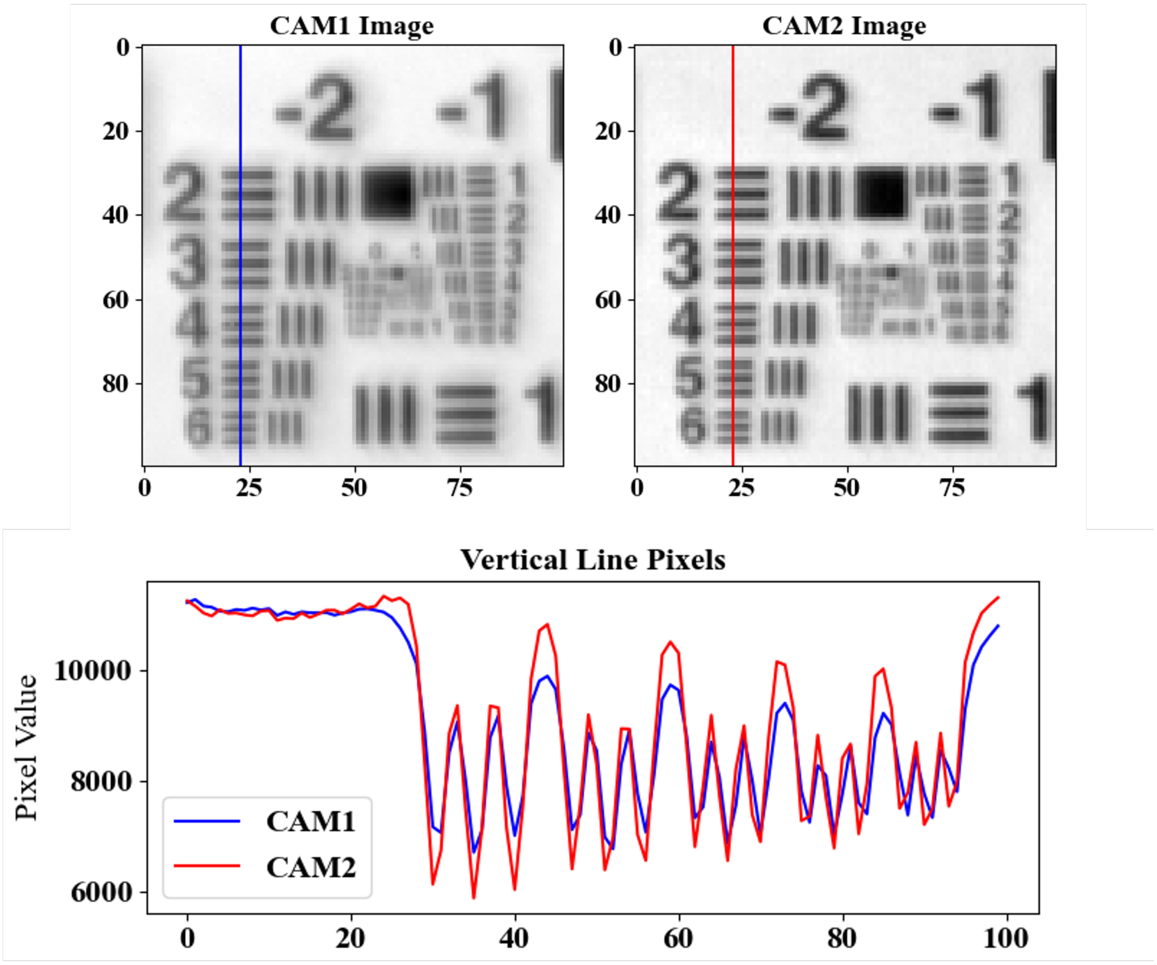

Fig. 6.3: Comparison of the focus quality between CAM1 and CAM2 using a 1951 USAF resolution bar target. Close up at the center of the target.

6.2 Stereo Calibration

The stereo calibration was conducted to verify the alignment of both cameras and the projected FOV. This calibration was conducted using MATLAB Stereo Camera Calibration tool [61]. A total of seven pairs of images were captured with the target at different positions and orientations, and inside both cameras' FOV. Fig. 6.4 shows the results of the calibration. The mean reprojection error per image was computed to be under 0.3 pixels, indicating an accurate calibration.

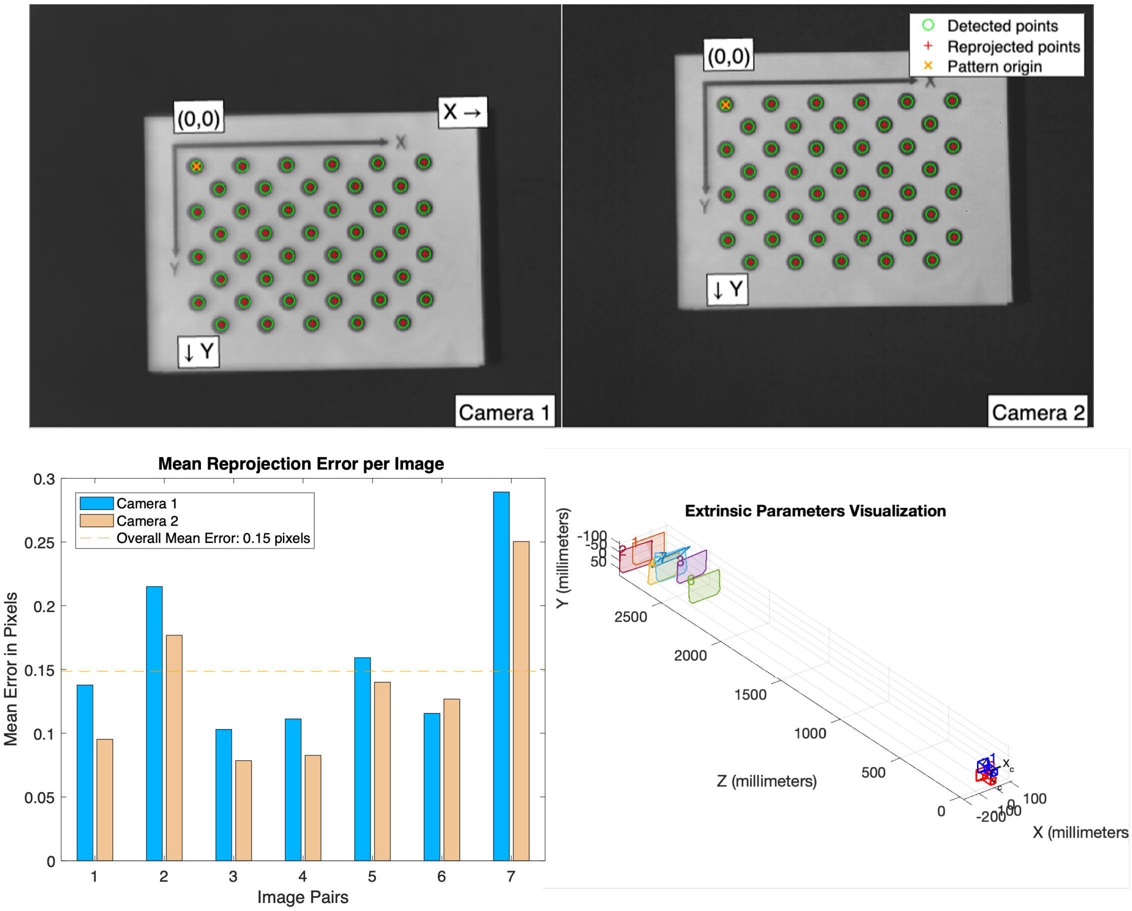

Fig. 6.4: Stereo Camera Calibration. (Top) First pair of target images showing detected and reprojected points. (Bottom Left) Mean Reprojection Error. (Bottom right) Extrinsic parameters visualization.

The intrinsic parameters obtained for CAM1 and CAM2 during stereo calibration are detailed in Table 6.2. Based on the estimated focal lengths, both cameras exhibit a field

Table 6.2: Cameras intrinsic parameters

CAM1 Intrinsics		
Focal Length f_x, f_y (pixel)	3986.9728 ± 44.4365	3985.2386 ± 44.7557
Focal Length f_x, f_y (mm)	59.80 ± 0.66	59.77 ± 0.67
Principal point c_x, c_y (pixels)	374.7660 ± 23.8480	309.3435 ± 27.1945
Radial distortion k_1, k_2	0.4310 ± 0.1766	17.6957 ± 26.5709
Tangential distortion p_1, p_2	0.0143 ± 0.0062	0.0093 ± 0.0051
CAM2 Intrinsics		
Focal Length f_x, f_y (pixel)	3963.0962 ± 44.3498	3965.0410 ± 44.6376
Focal Length f_x, f_y (mm)	59.45 ± 0.66	59.47 ± 0.67
Principal point c_x, c_y (pixels)	369.8933 ± 22.5509	275.9590 ± 20.3294
Radial distortion k_1, k_2	0.1928 ± 0.1453	35.7231 ± 18.8873
Tangential distortion p_1, p_2	0.0118 ± 0.0042	0.0140 ± 0.0043

of view (FOV) of approximately 9.2 degrees across-track and 7.3 degrees in-track. Consequently, the calibration results suggest an instantaneous field of view (IFOV) of roughly 0.25 milliradians. This IFOV corresponds to a GSD of approximately 137 meters at an orbital altitude of 550 kilometers, a reduction from the predicted GSD of 150 m.

Table 6.2 also lists the computed radial and tangential distortion coefficients. The radial distortion occurs when light rays bend more near the edges of the lens than at its optical center. The parameters k1 and k2 quantify the magnitude of this distortion. Positive values indicate barrel distortion, where straight lines appear to curve outward, while negative values signify pincushion distortion, causing straight lines to curve inward. Tangential distortion occurs when the lens and the image plane are not perfectly parallel. The parameters p1 and p2 quantify the tangential distortion by correcting for the displacement of the lens relative to the image plane. They account for minor misalignments between the lens and the image sensor, ensuring more accurate geometric representation of objects in the image.

Fig. 6.5 illustrates the field distortions of both cameras, simulated using their calibrated radial and tangential coefficients. These distortions are primarily observable near the edge of the field and are not expected to significantly impact the instrument performance.

Table 6.3 presents the relative position and orientation of CAM2 relative to CAM1 estiamted in the stereo calibration process. The results indicate the both cameras are

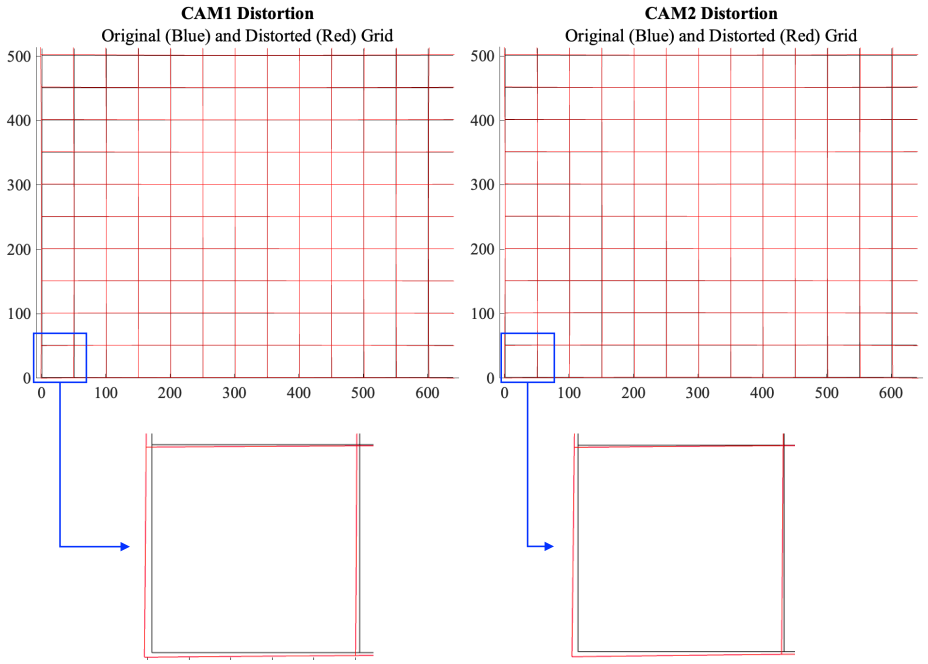

Fig. 6.5: Cameras radial and tangential distortion applied to a grid

Table 6.3: CAM2 position and orientation relative to CAM1

Rotation of CAM2 (rad)	-0.0088 ± 0.0077	-0.0003 ± 0.0071	0.0028 ± 0.0002
Rotation of CAM2 (deg)	-0.5042 ± 0.4412	-0.0172 ± 0.4068	0.1604 ± 0.0115
Translation of CAM2 (mm)	0.8554 ± 0.1529	-54.5039 ± 0.1522	-11.4973 ± 3.7802

aligned with less than 1 degree of pointing difference.

Using the estimated intrinsic and extrinsic parameters, we can also analyze the FOV projection of CAM2 relative to CAM1. Fig. 6.6 shows the both cameras'FOV projection for a target at 2.8m. The presented result matched the overlap of the target images seen in Fig. 6.1.

In Fig. 6.7, the overlap of both cameras' fields of view (FOV) is depicted in consideration of the orbital altitude. Although the overlap is nearly complete, a slight variance is evident in one corner, as highlighted. This non-overlapping region corresponds to less than one pixel in both cross-track and along-track directions

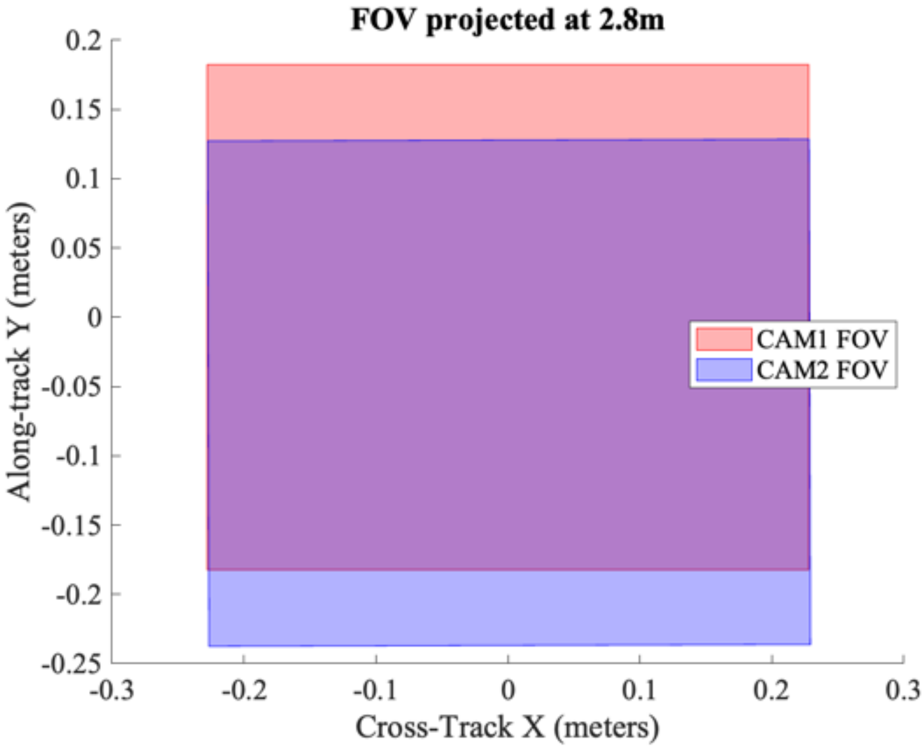

Fig. 6.6: FOV of CAM1 and CAM2 projected at 2.8 m distance

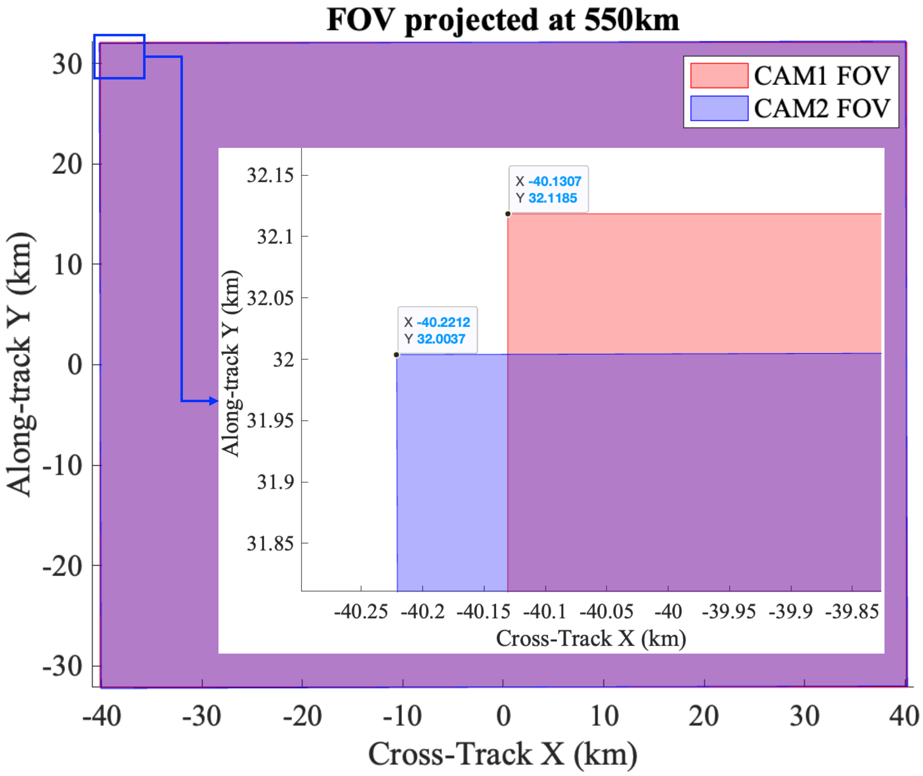

Fig. 6.7: FOV of CAM1 and CAM2 projected at 550 km distance (orbital altitude), with a close view of the corner points.

6.3 Dark Frame Calibration

Setup: To perform the dark frame calibration, it is necessary to completely block the light from reaching the FPA. This was performed by covering the camera's entrance with an opaque cap, see Fig. 6.8.

The calibration was performed for two FPA set point temperatures: 20°C and 40°C. When attempting to set the FPA set point temperature to 0°C, the TEC was unable to sufficiently cool the FPA. The room temperature was at 23°C during the test. When this occurs, the set temperature is automatically reset to the next higher set point, in this case, 20°C.

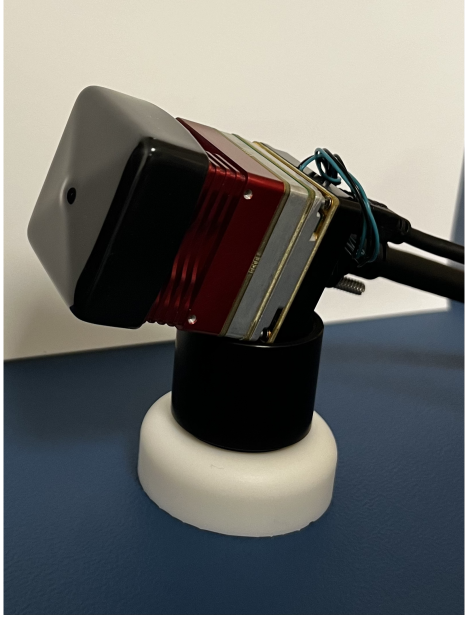

Fig. 6.8: Tau SWIR camera setup with FPA covered for dark frames acquisition

For each integration time tested, 100 dark frames were collected. After collecting the frames for the minimum integration time (0.011ms), the integration time was set from 1 ms to 30 ms in intervals of 1 ms. During acquisition, the FPA temperature was monitored to ensure a maximum difference of 1.0°C between the set point and the actual FPA temperature. The following subsection provides a summary of the results for the CAM1 running 10fps.

Results for CAM1 at 10fps

The mean dark counts as a function of the integration time and gain mode are presented in Fig. 6.9. The samples were collected using CAM1 at 10 fps, with the FPA temperature set to 20°C (left plot) and 40°C (right plot). The error bars represent the mean temporal variation of all pixels in the FPA, measured by the standard deviation of the pixel values across the 100 samples. By comparing the two plots, it is evident that the 20°C increase in FPA temperature significantly raises the dark count rate (dark current), especially for the low and medium gain settings.

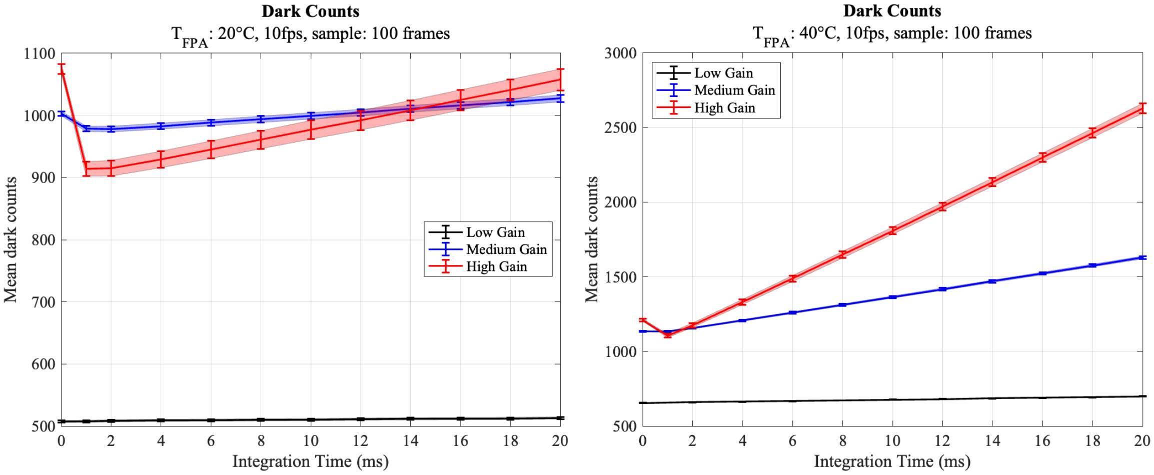

Fig. 6.9: Mean dark counts in DN measured at different integration times for CAM1 at 10fps, with FPA temperature at 20°C (left), and 40°C (right). The error bar represents the average pixel temporal variation (2σ) measured over 100 samples.

Table 6.4 lists the linear fit results for the curves presented in Fig. 6.9. In this table, the slope represents the dark current measured in terms of Digital Number (DN) per 1 ms of integration time, and the offset is given by the y-axis intercept.

According to the camera's manufacturer, the expected median dark current density should be less than 10 nA/cm^2 for the industrial camera version at 20°C [1]. Considering the well depth for low, medium, and high gain settings listed in Table 4.4, and a pixel depth of 14 bits, the expected dark count rates (in DN) for low, medium, and high gain should be less than 1.7, 20.36, and 60.55 DN/ms, respectively, at 20°C.

Table 6.4: Linear Fit Results for FPA averaged dark counts in CAM1 running at 10fps

	FPA Temp: 20°C		**FPA Temp: 40°C**	
	Slope (DN/ms)	Offset (DN)	Slope (DN/ms)	Offset (DN)
Low Gain	0.26	508	2.17	655
Medium Gain	2.67	973	26.17	1103
High Gain	7.77	900	80.42	1011

Therefore, based on our measurements, we confirm that CAM1 complies with its specification at 20°C in terms of dark current.

The pixel noise (RMS) is computed from the 100 samples of dark frames taken for each integration time point. The mean RMS of all pixels as a function of the integration time is presented in Fig. 6.10.

In the left plot, we observe that the measured pixel noise is below the predicted values for all gain modes and integration times. The right plot shows the ratio between measured and predicted noise values. For the medium gain, the measured noise is about half of the modeled noise. This indicates that the SNR performance will likely exceed the predicted values presented in the radiometric analysis in Section 5.1.

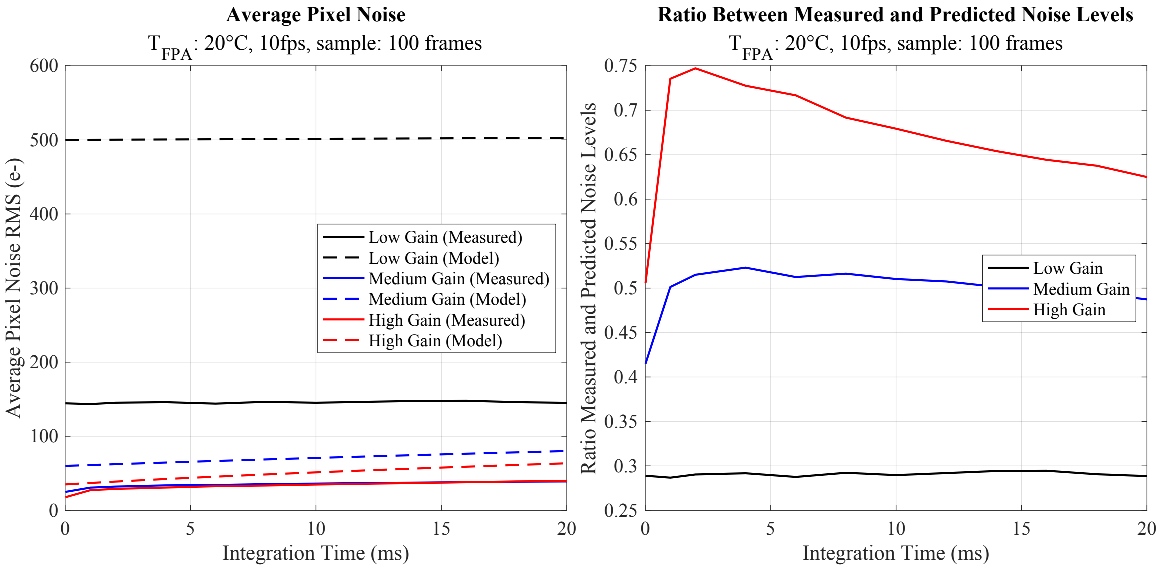

Fig. 6.10: Measured noise from 100 dark frames with CAM1 running at 10fps and FPA temperature at 20°C.

Table 6.5: Comparison between predicted and measured readout noise (RMS)

	Predicted (e^-)	Measured (e^-)
Low Gain	500	145
Medium Gain	60	31
High Gain	35	18

By assuming the time-invariance of readout noise, the measured readout noise is the noise at the shortest integration time, after which time-dependent noise, such as dark noise, starts to accumulate. The measured readout noise (RMS), represented in terms of electrons, is presented in Table 6.5. The values for the high and medium gain were taken at 1 ms since the 0.011 ms presented a discontinuity. The cause of the spike in noise at the shortest exposure time is unclear.

The time-dependent component of the measured noise is presented in Fig. 6.11. This component was computed by subtracting the measured readout noise from the total noise curve. For low gain, the measured time-dependent noise closely follows the modeled curve across the entire range of integration times. However, for medium and high gain, the measured values exceed the dark current model for integration times up to 11 ms.

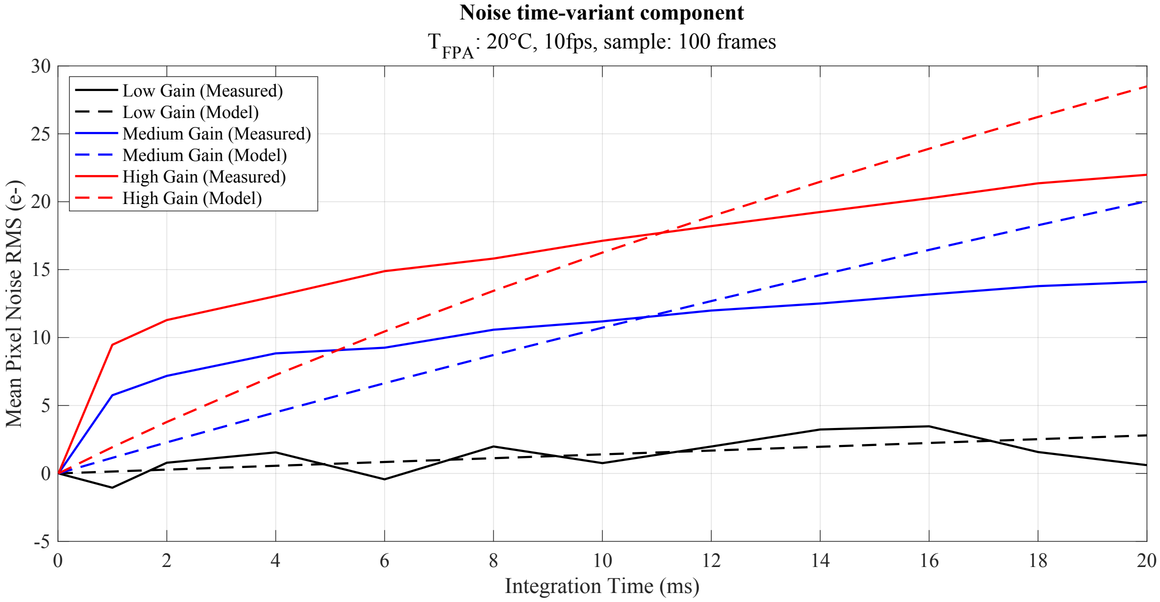

Fig. 6.11: Time-variant component of the measured noise in comparison to values predicted using the camera noise specification parameters

Fig. 6.12 presents the mean dark count distribution and the camera noise for an integration time of 8 ms, with the FPA at 20°C. The histograms in the left column show a single-mode distribution for all gain settings. The histograms in the right column depict the pixel noise (RMS) distribution in terms of DN, with the vertical black line indicating the predicted noise level.

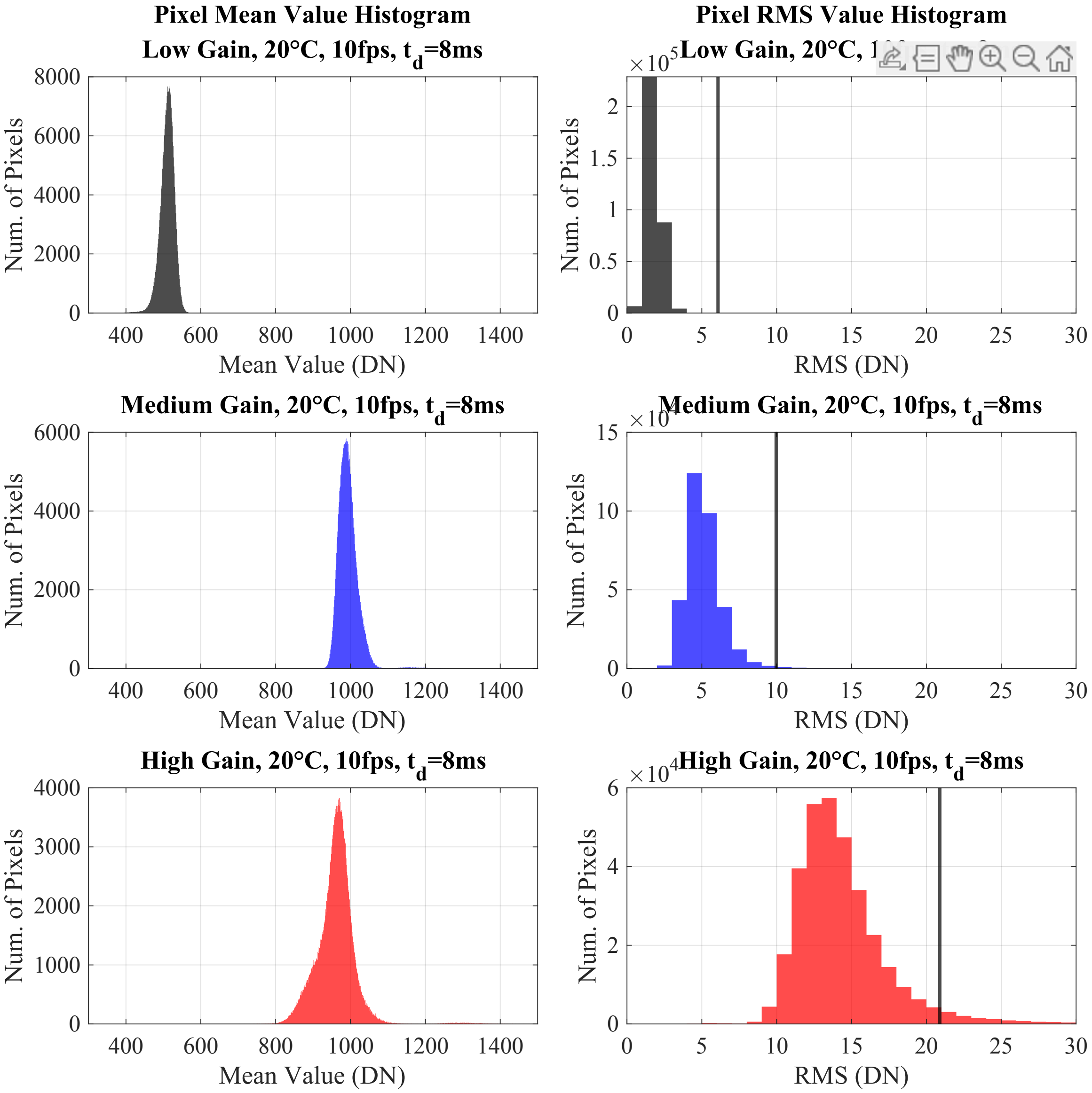

Fig. 6.12: Dark frame histograms of the mean dark counts (left) and the pixel noise for the different gain modes for CAM1 running 10fps, with FPA at 20°C, and integration time of 8ms. The vertical lines in the left histogram indicate the predicted pixel noise RMS in terms of counts.

Fig. 6.13 presents a deeper view in dark frame data for the CAM1 operating in the medium gain mode at 8 ms. Besides the histogram on the left, the plot also presents the mean dark counts distribution across the FPA.

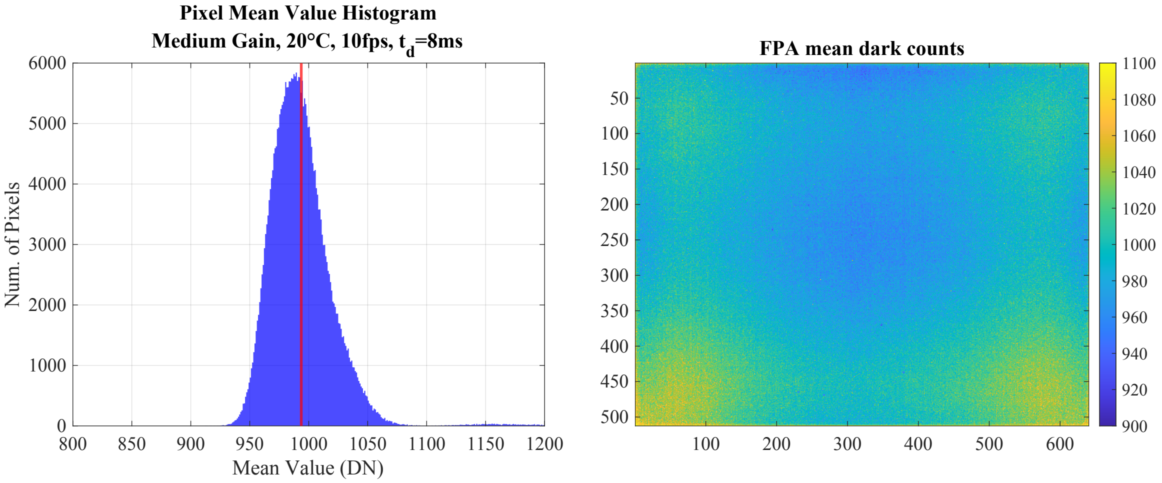

Fig. 6.13: (left) Distribution of CAM1 dark counts for medium gain mode at 8ms, and FPA at $20^{\circ}C$. (right) Mean dark frame

6.4 Flat Field Calibration

Setup: Flat frame calibration, also called bright frame calibration, requires the setup of a uniform diffusive light source with a compatible emission spectrum. The use of an integrating sphere is preferable to achieve the highest calibration fidelity. However, for a first flat-fielding approximation, we conducted the flat-field calibration within our lab using the setup depicted in Fig. 6.14.

The sensor FOV was pointed towards the center of the target made of a diffuse reflecting Film (20x30cm, Optopolymer), which is the same material selected to cover the shutter paddles in the calibration unit. The reflection from this material can be considered Lambertian. The camera aperture was also covered with a broadband diffusive glass to further increase the diffusivity of the incoming light.

The light source was a 12V (11W) incandescent lamp powered by a DC voltage source. It was positioned behind the camera and aligned with the target to ensure symmetrical

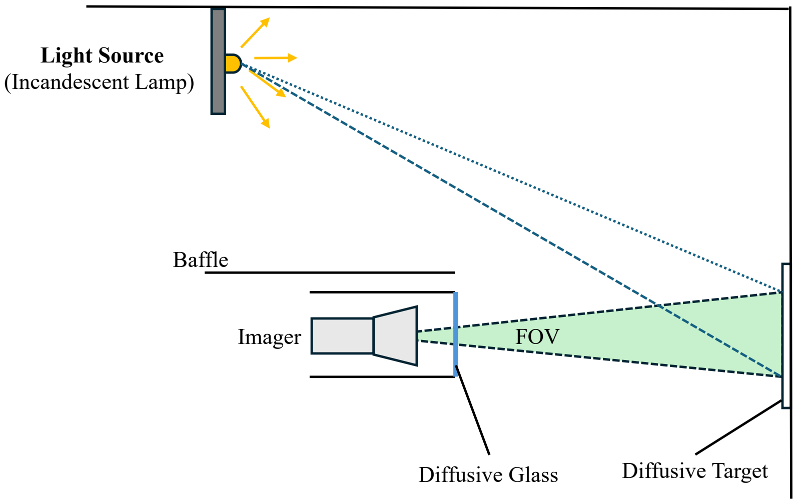

Fig. 6.14: Flat field calibration setup

horizontal illumination. It was placed at a high enough elevation to reduce shadows casting over the target. No other light source was turned on during the flat frame acquisition.

Based on the measured geometry of the setup and assuming no reflections, it was possible to model the illumination pattern over the target. This can be simply done by computing the cosine of the local zenith angle of the light source for every positioned inside the FOV. Fig. 6.15 presents the result.

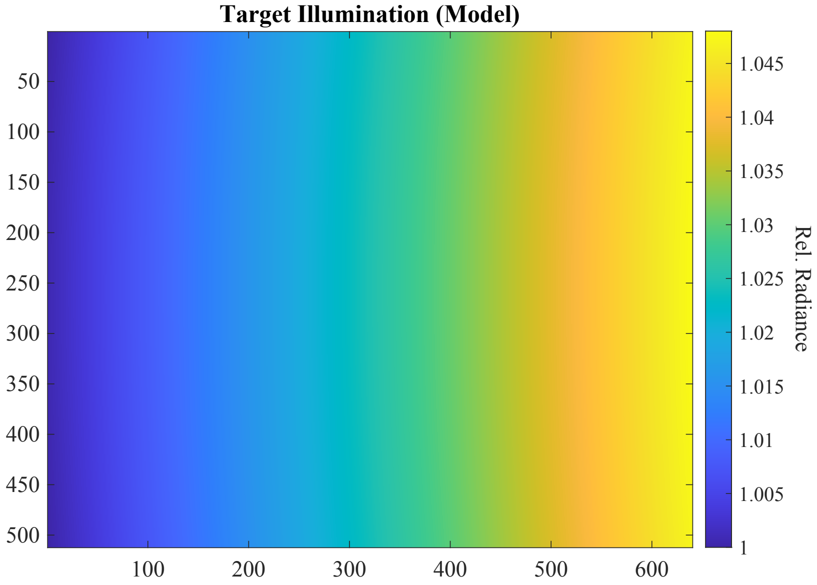

Fig. 6.15: Target Illumination Model

Results

The camera was set to high gain, with an integration time of 20 ms, an FPA temperature of 20°C, and a frame rate of 10 fps. A total of 100 flat frames were acquired, and the following results are based on the average of those frames. Only the analysis of the results for CAM1 with the optics are described here, although the same approach was conducted for CAM2.

The pixel values of the flat frame were corrected using the dark frame acquired at the same frame rate, gain, and integration time. Fig. 6.16 shows the flat frame image with enhanced contrast for better visualization. Additionally, the plot shows the vertical and horizontal cross-sections of the field, both before and after applying the target illumination correction.

As an alternative to the modeled correction using the scene geometry, we also tested a linear fit of the vertical illumination decay from the data to create a linear illumination correction, as shown in Fig. 6.16-(d). Similar results were obtained from both methods, indicating that the modeled illumination pattern is sufficiently accurate to compensate for the light decay along the target.

Fig. 6.17 presents the flat field gain correction for both CAM1 and CAM2. The results indicate that CAM2's gain is more uneven compared to CAM1's gain.

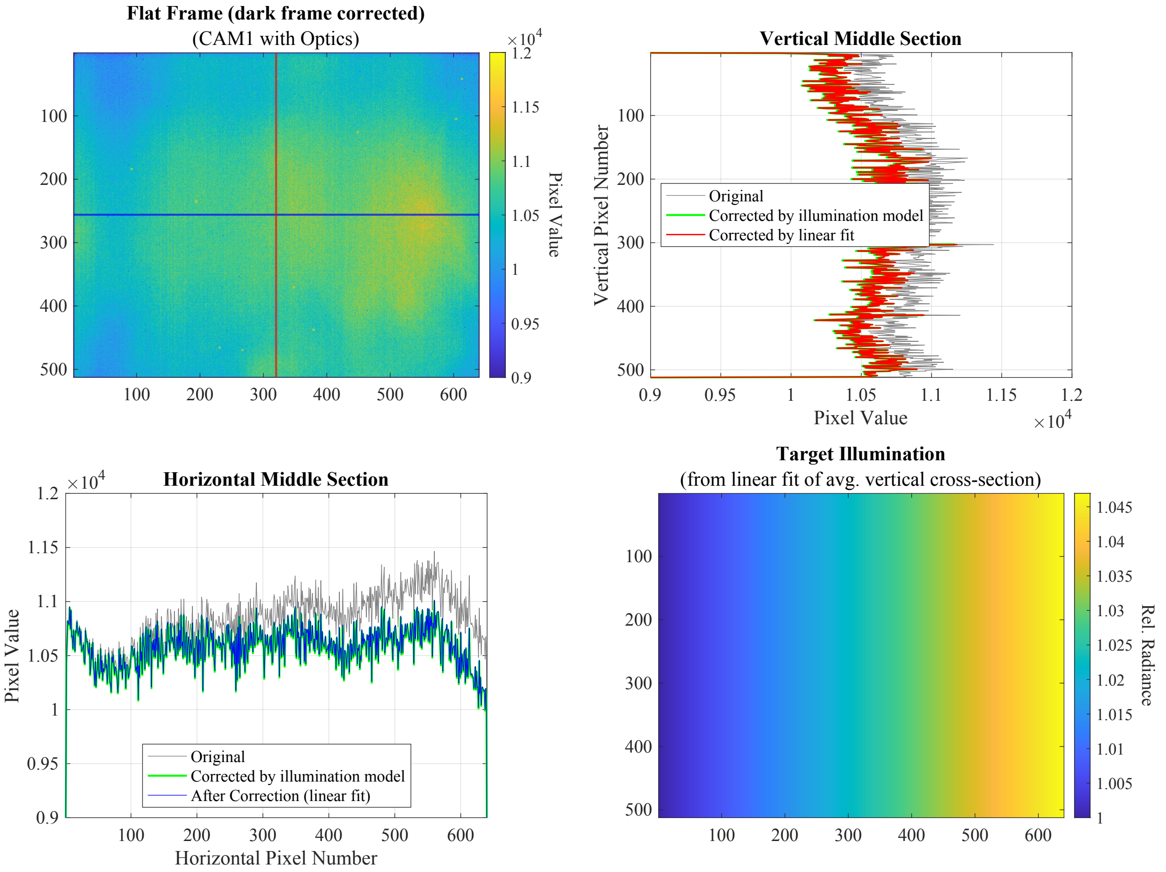

Fig. 6.16: (a) is field image with enhanced contrast, (b) and (c) are the horizontal and vertical field cross-section, respectively, with the before and after correction comparison, and (d) shows the target illumination derived from the linear fit

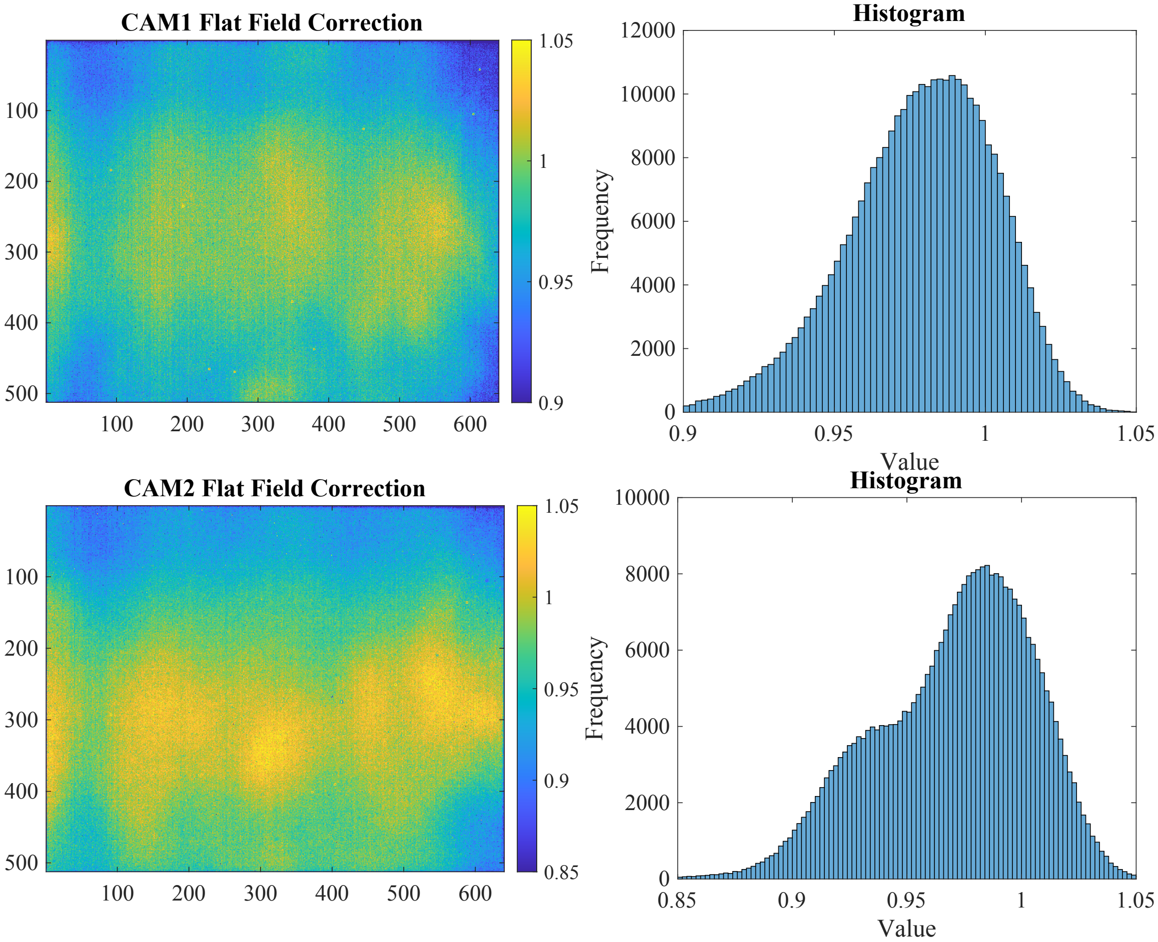

Fig. 6.17: Flat field gain corrections measured for CAM1 (top) and CAM2 (bottom) with their respective histograms

6.5 Onboard Flat Field

As described in Section 3.6, FINIS onboard calibration unit features an illumination ring containing 8 SWIR LEDs enumerated as shown in Fig. 6.18.

To assess the field created by the LED ring, CAM1 was configured with medium gain and an integration time of 8 ms. With the shutter closed, the LED ring was powered by a PWM signal at 1 kHz and a duty cycle of 0.3%. A total of 100 frames were acquired. The average frame was corrected by removing the dark offset and applying flat-field correction using the results presented in Fig. 6.17. The result was then normalized by the mean pixel value. Fig. 6.18 shows the field created by the 8 LEDs. The center of the frame receives approximately 5% higher counts than the average, while the edges receive about 10% less than the average.

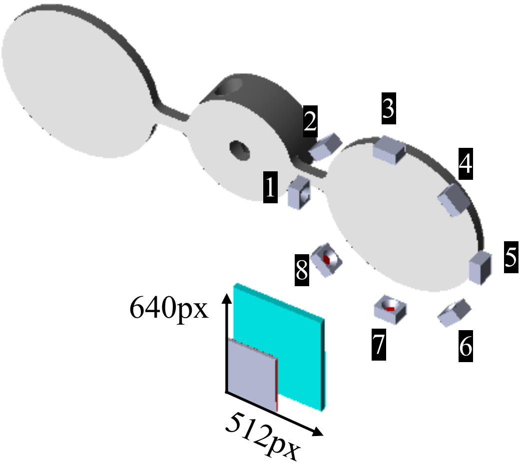

Fig. 6.18: LED ring and FPA orientation

Fig. 6.19 presents the normalized bright frame on the left. Given that the shutter illumination is expected to have a smooth pattern, the field correction can be extracted by filtering out the high frequencies from the normalized bright frame. The result of this smoothing, using a Gaussian filter, is shown in the right plot.

The illumination pattern can then be used to correct the uncorrected bright frames,

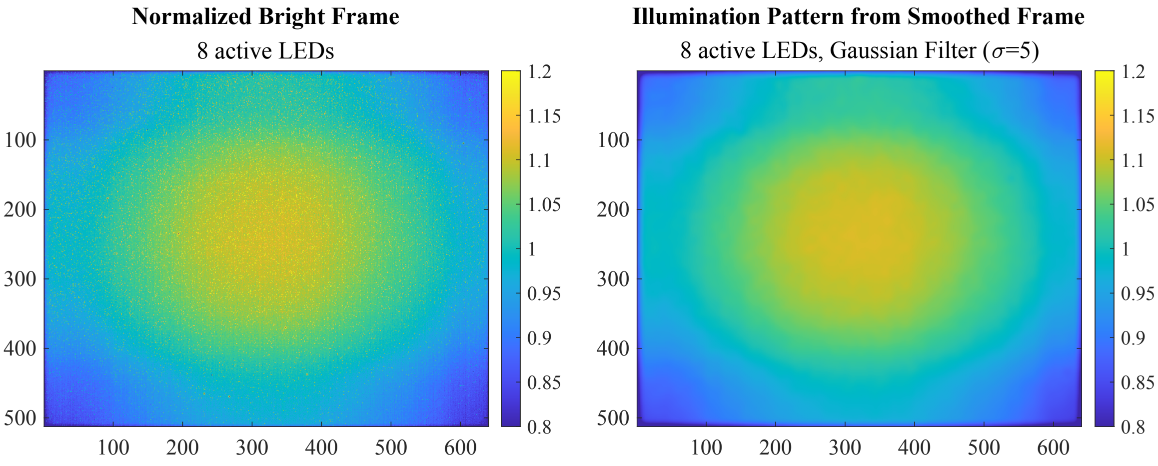

Fig. 6.19: (right) Normalized mean bright frame taken with all LEDs active. (left) Illumination pattern extracted by smooth the normalized bright frame using a Gaussian filter.

effectively extracting the flat field. Fig. 6.20 presents the flat field correction after applying the illumination pattern. The histogram indicates that the gain nonconformities across the FPA follow an approximate Gaussian distribution with a standard deviation of about 1%.

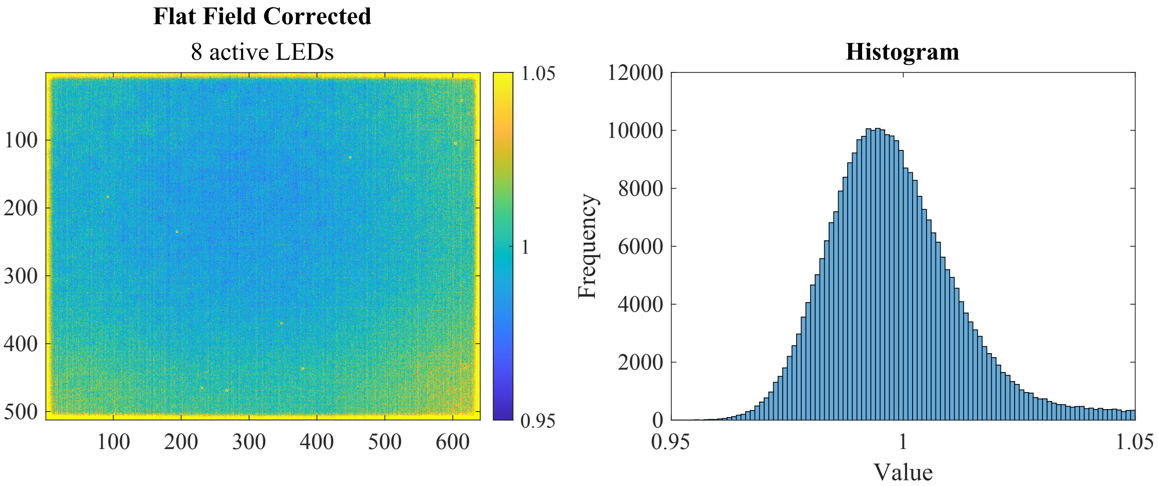

Fig. 6.20: Flat field corrected using the illumination pattern derived from the smoothing the bright frame data

To assess the sensitivity of the illumination pattern to the brightness of a single LED, we performed the same shutter illumination test after blocking the light output of LED 7 of the ring (see Fig. 6.18). Fig. 6.21 presents the relative change in the illumination pattern from the 7-LED to the full LED ring, highlighting the decrease in light intensity along the longest side of the FPA. Despite the significant change from eight to seven active LEDs, the histogram indicates that the relative difference in the illumination pattern was less than 1% for most of the FPA. This result suggests that the illumination pattern will remain relatively stable, as the expected brightness fluctuations and variations among the LEDs in the ring are less drastic than having one LED completely off.

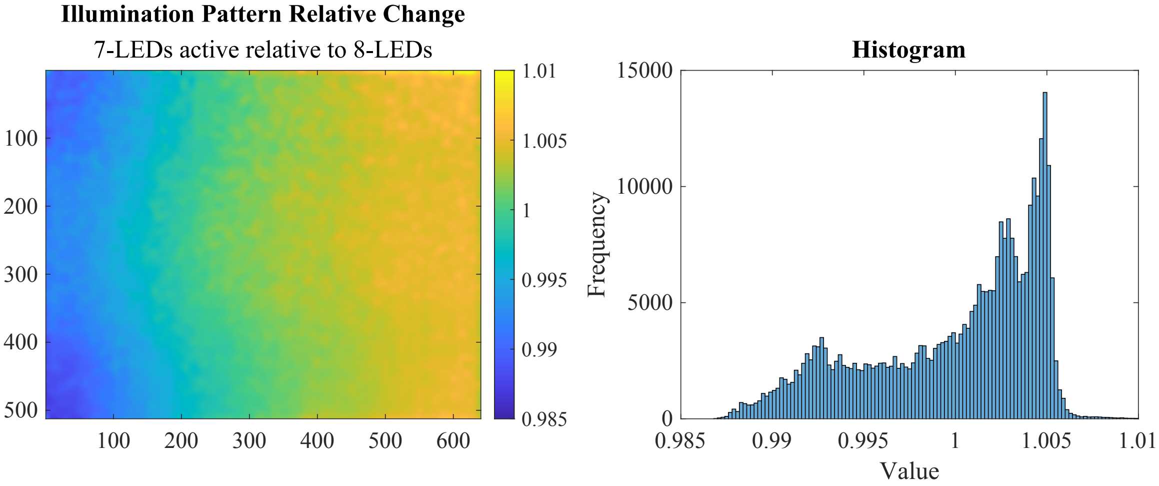

Fig. 6.21: Flat Field pattern change after deactivating one (LED 7) of the eight LEDs in the ring.

6.6 Methane Cell Calibration

Setup: The methane cell calibration checks the instrument's spectrum response to the methane absorption lines. This test allows us to verify the instrument spectrum resolution (filter bandwidth) and to map CWL across the FPA. In this test, a gas cell is filled with a known methane concentration and placed between the sensor and the light source. The lab setup used to test the CAM1 is shown in Fig. 6.22. During the frame acquisition, additional baffles were added, covering both the methane cell and the instrument. The light source was a halogen lamp powered by AC voltage, and placed underneath the table pointing to the target center.

The 10 cm methane cell was mounted with a small tilt ($\approx 10^\circ$) to reduce the reflection

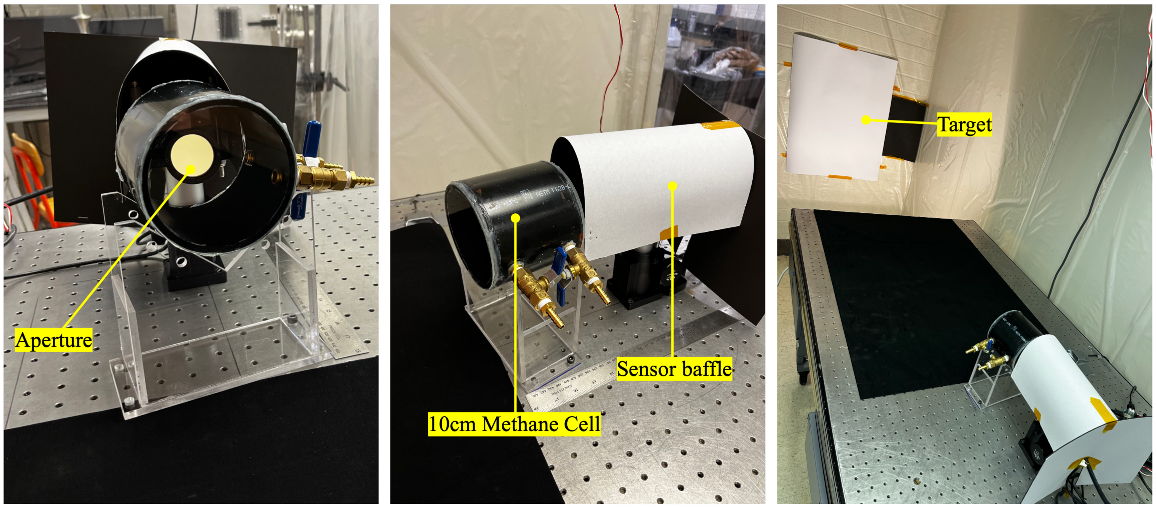

Fig. 6.22: Methane cell calibration lab setup

(glare) from the cell's windows. This tilt reduced the optical path of the cell to approximately 9.85cm.

The CAM1 was adjusted to high gain mode, 15ms of exposure time, and 10fps. These settings provided frames with pixel values ranging from 6000 to 11000, which corresponded to 36% and 67% of the well size, respectively.

Five methane cell pressures were tested: 1.5, 3, 5, 7.5, and 10 psi. For each test, 100 frames were taken and averaged to form the test frame. All frames were corrected by the mean dark frame measured with the same integration time. The control frame was taken with the cell filled with air at ambient pressure. Considering the atmospheric scale height of 8.0km for representative air temperature at 273K, the methane background concentration of 1800pbbv (mixing ratio) converts to a vertical column concentration of 3.79E19 molecules/cm^2. The vertical column concentration of each cell can be obtained by the ratio of the molecular density of methane (molecules/cm^3), computed from the pressure using the ideal gas equation, by the light path length (cm). Fig. 6.23 presents the calculated relationship between the tested cell pressures and the equivalent methane concentration relative to the atmospheric background concentration.

Fig. 6.24 presents the predicted methane image and the transmission across the middle section for a 10cm methane cell at the test point pressures, assuming the IF's tilt angle of

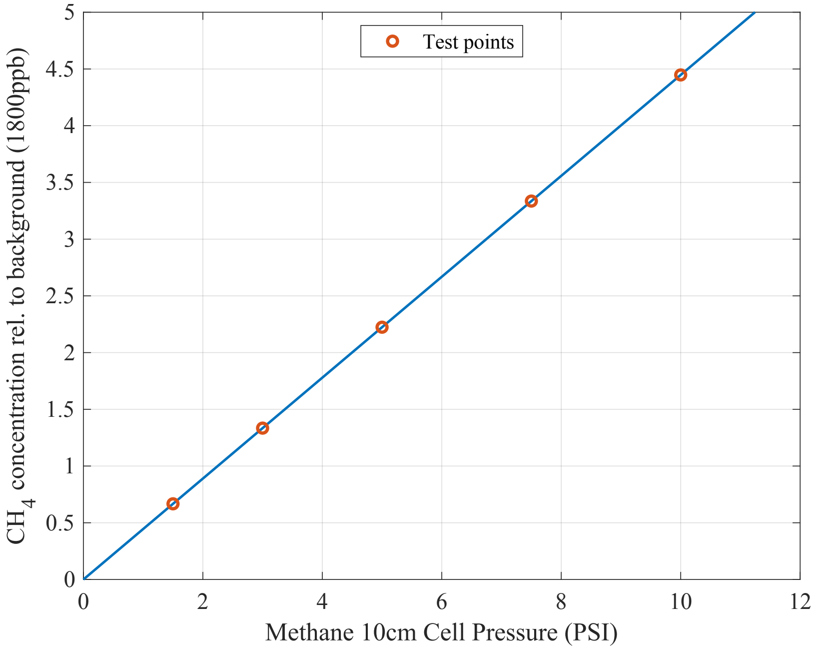

Fig. 6.23: Equivalence between methane 10cm cell pressure and the methane concentration relative to atmospheric background (1800ppb).

10°.

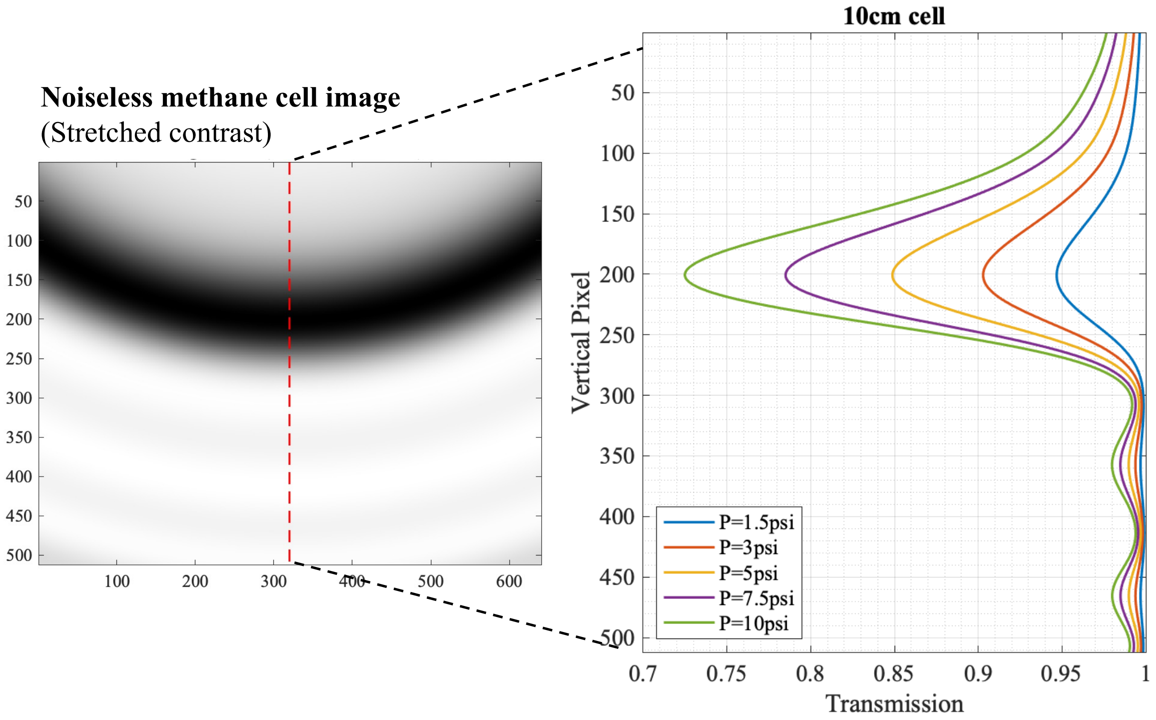

Fig. 6.24: (left) Noiseless methane cell image (gray scale) with stretched contrast to highlight the methane absorption band. (right) Transmission over FPA middle section for 10cm cell at different pressures. Considered temperature: 296K.

Results

Fig. 6.25 shows the control frame taken with the cell filled with air at ambient pressure. The nonuniform illumination of the target caused the bottom pixels to have almost double the signal of the top pixels. The 10psi frame shows the noticeable methane absorption arc on the top part of the image.

The measured transmission is computed by taking the ratio of the test frame with the control frame. Fig. 6.26 presents the measured transmission of the methane cell at 10psi compared with the predicted value. The similarity between the two plots shows that the axis of rotation of the IF is properly aligned with the image's x-axis. Moreover, the position and width of the absorption band indicate that the actual IF's tilt angle matches the designed 10° within a 0.2° margin. In the measured transmission frame, there is a presence of a wave-like fluctuation with concentric arcs that appear to expand from the bottom of the frame. Those effects are due to the aliasing caused by the light source being powered by a

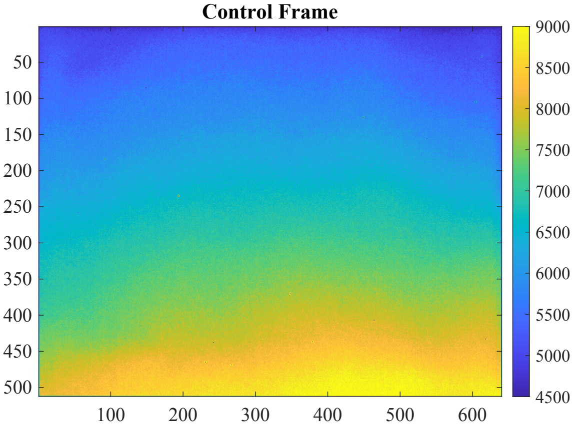
Control Frame
10psi Frame

Fig. 6.25: Control frame taken with cell filled with air (left), and the frame with the cell at 10psi of methane pressured (right).

60Hz AC power supply and the camera operating at a 10Hz frame rate.

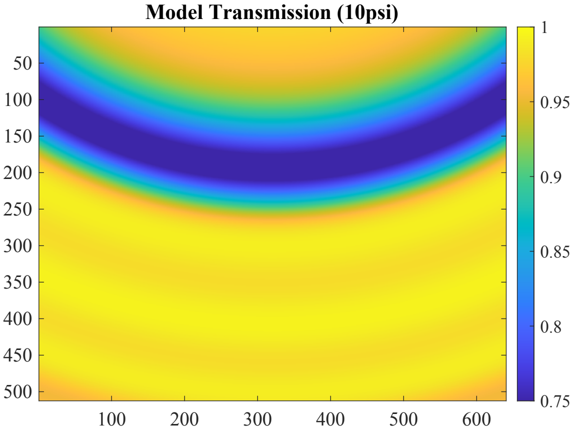
Model Transmission (10psi)
Measured Transmission (10psi)

Fig. 6.26: Predicted transmission (left) compared to measured transmission (right) for the 10cm methane cell at 10psi.

The transmission results measured at different pressure levels can be better understood through a plot of the vertical middle cross-section of the measured transmission along with the predicted transmission, which is displayed in Fig. 6.27. In this plot, the measured data is presented after removing the mean error, which is defined by the difference between the measured and predicted transmission values. The calculated measurement bias has been documented in Table 6.6. The main contributing factors to this measurement bias are likely fluctuations in the light source due to the AC power supply, stray light due to changes on the baffle configuration between tests, and inaccurate measurement of the methane pressure during the cell filling.

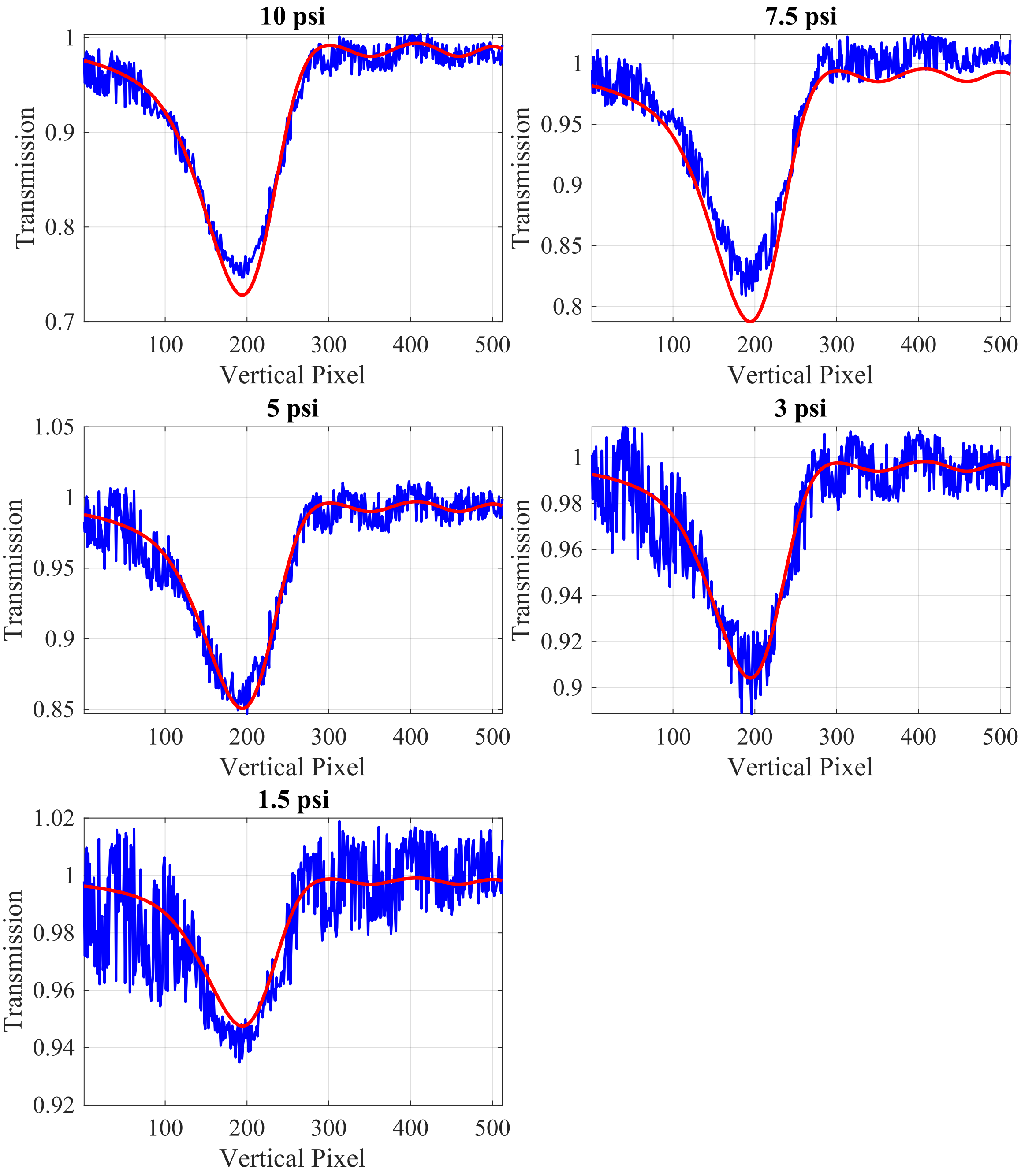

Fig. 6.27: Middle section measured transmission compared to predicted. The measurements are presented unfiltered and unbiased.

Table 6.6: Transmission measurement bias

	10 cm Cell Pressure (psi)				
	1.5	**3**	**5**	**7.5**	**10**
Mean Error (bias)	3.14%	1.62%	1.37%	4.62%	1.05%

The concentration of methane in the cell can be determined by fitting the natural logarithm of the transmission measurement against the absorption cross-section, taking into account the CWL distribution across the FPA model. In Fig. 6.28, the linear least square fit of the measured data for the 1.5, 5, and 10 psi tests is shown. The slope of the curve represents the estimated vertical column concentration of methane for each case. The values deviated from the expected concentration by 11.4%, 8.3%, and 7.4% at 1.5, 5, and 10 psi, respectively. Apart from the noise in the data, fluctuations in the light source, and stray light, the deviation could be due to imprecision in measuring the methane pressure during filling.

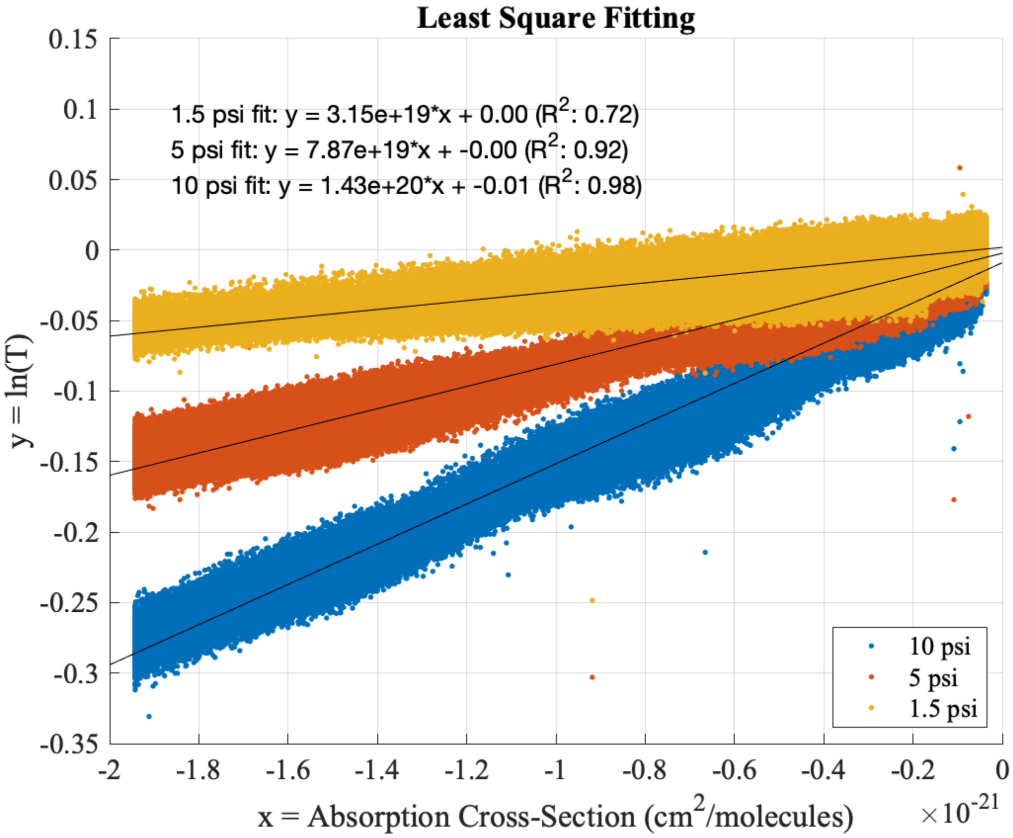

Fig. 6.28: Linear least square fit of the natural log of the measured transmission as a function of the estimated absorption cross-section.

CHAPTER 7

MISSION INTEGRATION

FINIS will soon be integrated into the ACMES bus and launched into space to begin its operation. This chapter covers the key information required for its successful integration and operation within the mission.

In the Interface section, we present both the mechanical and electrical interfaces. Next, in the Instrument Operation Plan section, we discuss the regions of the globe that provide sufficient illumination as a function of the seasons, the nominal camera settings, the on-board calibration and data acquisition procedures, and the primary targets required for measurement validation. Finally, in the Data section, we define the data product levels and the expected format for the raw data catalog.

7.1 Interface

This section describes FINIS' mechanical and electrical interfaces.

7.1.1 Mechanical Interface

The mechanical drawings with relevant dimensions for the spacecraft assembly are presented in Fig. 7.1 (front-view) and Fig. 7.2 (bottom-view).

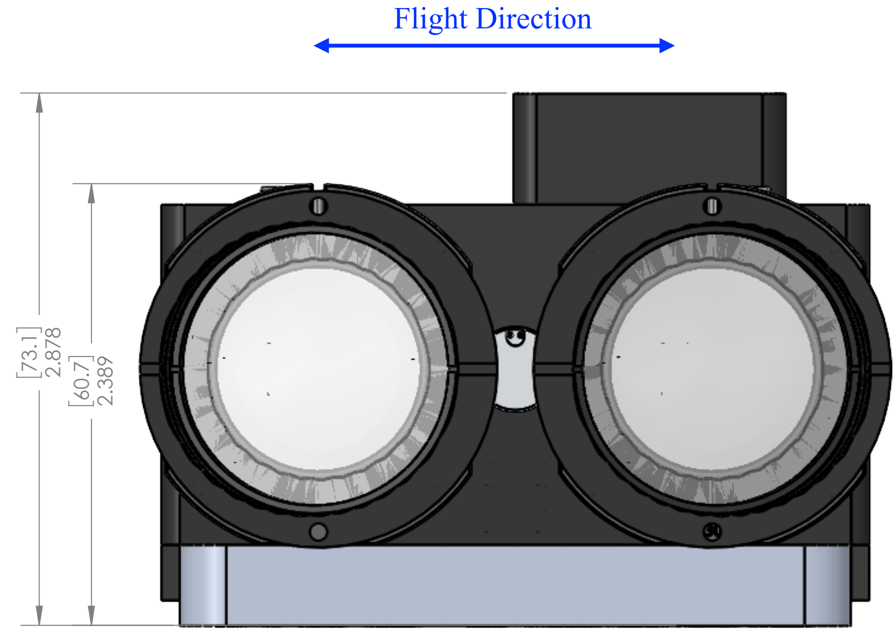

Fig. 7.1: FINIS mechanical interface - front view. Units: Numbers in brackets are millimeters; otherwise, in inches. Credits: Michael Kirk.

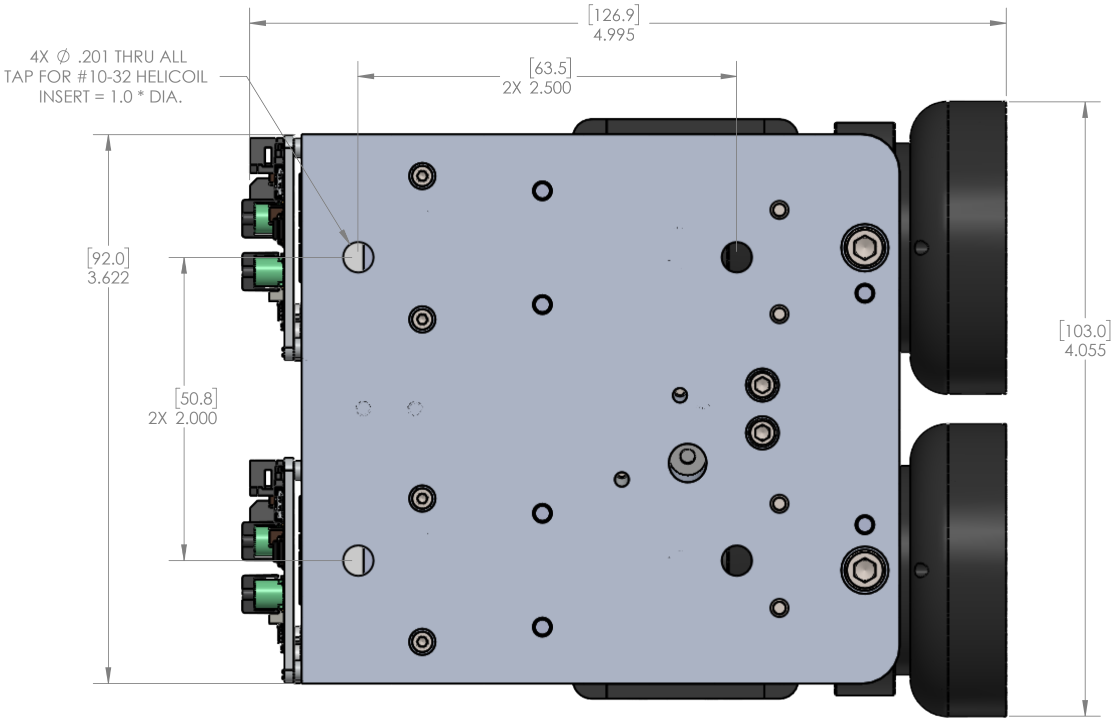

Fig. 7.2: FINIS mechanical interface - bottom view. Units: Numbers in brackets are millimeters; otherwise, in inches. Credits: Michael Kirk.

7.1.2 Electrical Interface

Fig. 7.3 shows the electrical interface for all electrical components inside the instrument assembly. The FINIS payload board, which receives all these connections, is not shown here since its design and fabrication were the responsibility of the spacecraft bus manufacturer, Orion Space Solution. In addition to the thermocouples (TC) incorporated into the LED ring flex PCB, the FINIS payload board can support up to four additional TCs, which can be installed on the optical table and over the IF holder ring to monitor temperature across the instrument and study the effects of temperature variation on the spectrum response.

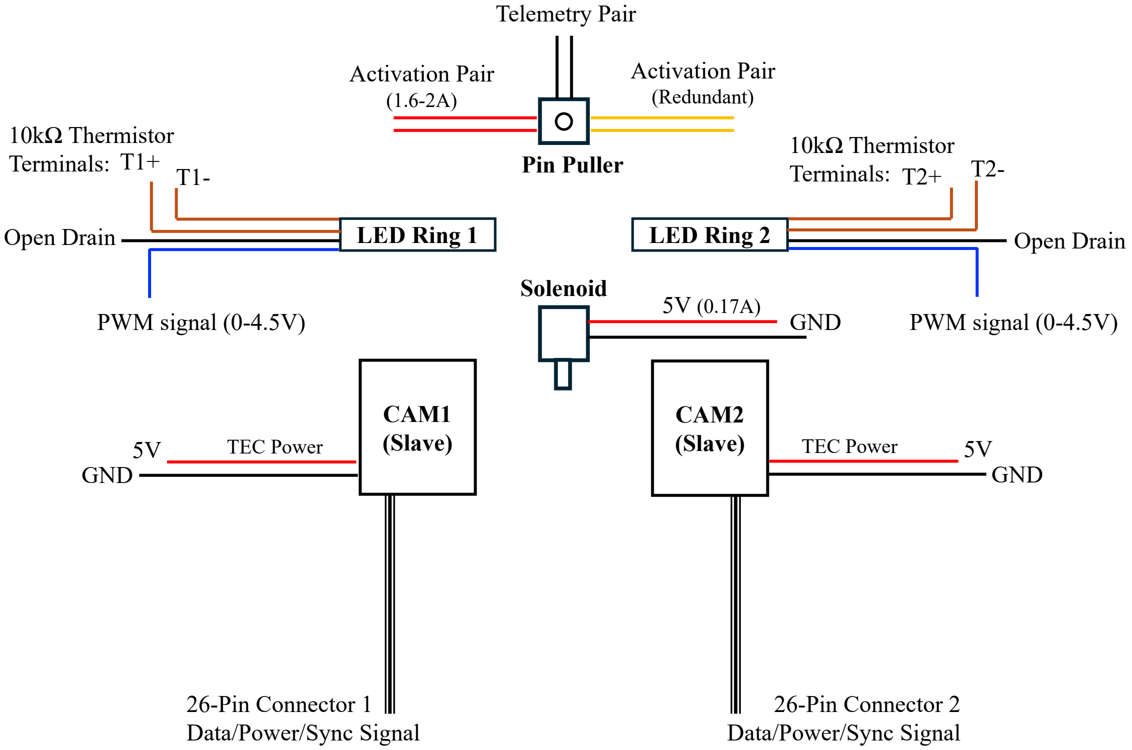

Fig. 7.3: FINIS electrical interface. Unit in brackets in millimeters.

The following subsections describe in more detail each component's electrical interface and power requirements.

Pin Puller

The Pin Puller used is the Nano Pin Puller (nD3PP), provided by DCUBED. A current between 1.6A and 2A must be applied across one of its actuation lines to trigger the pin puller (retract the pin). There are two actuation lines: the red pair and the yellow pair of wires, as shown in Fig. 7.3. The resistance across the actuation line was measured at 0.82Ω, for both red and yellow lines. This resistance measurement was taken with each wire measuring 33cm in length. The voltage supplied must be adjusted accordingly to compensate for additional resistance added to the line.

With a current between 1.6 and 2A, the pin puller retracts the pin in less than 2s. During lab tests, when a current of 1.13A was supplied, the pin puller triggered after 12s. A lower current than that might not trigger the pin puller.

The Telemetry Pair (black wires) indicates whether the pin is extended (open position - open circuit) or retracted (closed position - closed circuit). This telemetry shall be used to indicate when to turn the current supply off.

Solenoid

The solenoid model is the A1489 from Brandstrom Instruments. The solenoid is activated to close the shutter when 5V is supplied to its terminals. During lab tests, the solenoid drew 0.175A when supplied with 5VDC. Thus, approximately 0.9W of power is required to keep the solenoid activated during the onboard calibration procedures. When power is off, the solenoid restores itself to the open shutter position.

LED Ring 1 and 2

The LED rings must be constantly supplied with 5VDC. In continuous operation (100% PWM duty cycle), each LED ring draws around 120mA. The brightness control is performed by the PWM signal with parameters listed in Table 7.1. The same PWM signal shall feed both LED rings.

The LED ring PWM pulses need to be synchronized with the external sync pulses to ensure the same light exposure in all frames. Fig. 7.4 presents the timing requirement for

Table 7.1: LED Rings PWM signal

PWM Frequency	1kHz
Duty Cycle	0.1%-5%
Voltage range	0-4.5V
PWM current	< 1mA

the pulses.

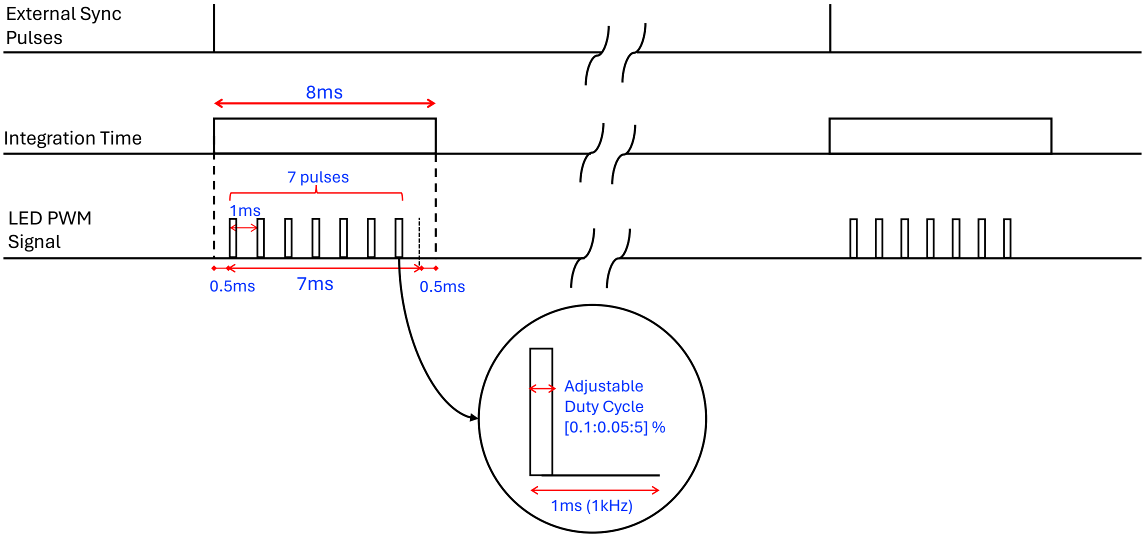

Fig. 7.4: LED PWM pulses timing requirement

CAM1 and CAM2

The Tau SWIR camera's TEC requires 4.9V-5.5V input. The TEC's peak power is 2.5W, but its average power can be much lower depending on the heat dissipation condition. The camera datasheet reports that the TEC power is about 0.3W at room ambient temperature with the camera mounted on a tripod. [1]

The external sync signal generated in CAM1 (Master) shall be supplied to CAM2 (Slave) to ensure the frame acquisition synchronization. This can be performed by interconnecting the PIN 21 (External Sync) between the two cameras' 50-pin connectors (for pinout information, refer to Table 3-1 in [1]). Both cameras shall share the same GND.

Both cameras require 4.9V-5.5V input. According to [1], the peak power of each camera core is 3W.

The total peak power, considering both CAM1 and CAM2, with both TECs operating at maximum capacity, is 11W.

7.2 Instrument Operation Plan

Fig. 7.5 presents a summary of the main space and ground operational phases, from onboard calibration and imagery acquisition to the methane concentration maps production. FINIS is scheduled to be deployed in space onboard the ACMES mission, a 16U CubeSat that will also carry other payloads, including a hyperspectral thermal imager (HyTi). The launch of ACMES is scheduled for 2025, after which it will be placed in a sun-synchronous orbit (SSO) at an altitude of 550km. During its approximately four-year lifetime, the orbital local time of the ascending node (LTAN) will be between 10 am and 12 pm. This configuration will ensure that FINIS acquires imagery while pointing towards the nadir, with a low solar zenith angle (SZA$\leq$60°) suitable for a wide range of latitudes as shown by Fig. 7.6.

The onboard calibration unit will perform the dark frame and flat-fielding calibration once per orbit before initiating the data acquisition. During the calibration phases, multiple dark frames and bright frames will be taken using the same exposure time and camera settings scheduled for the next acquisition sequence. Since the camera's settings or exposure times might change depending on the target's latitude, albedo, or solar zenith angles, a more frequent calibration frame acquisition might be needed.

During the first year of operation, the imagery acquisition will focus mainly on planned targets where high levels of methane emissions are anticipated, such as the Permian Basin, which is the largest oil-producing basin in the United States and is located in Texas. These areas will serve as a benchmark for FINIS's ability to identify and measure point source emissions. Once the instrument sensitivity is characterized, other areas will be mapped to detect new emitters worldwide.

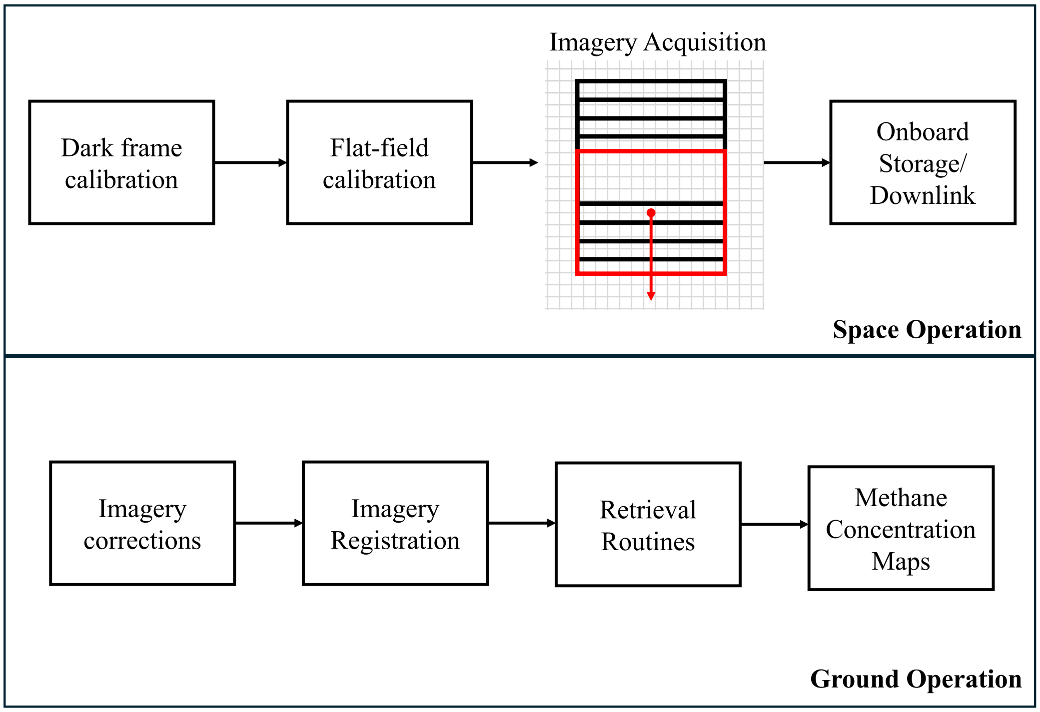

Fig. 7.5: Major space and ground operation modes

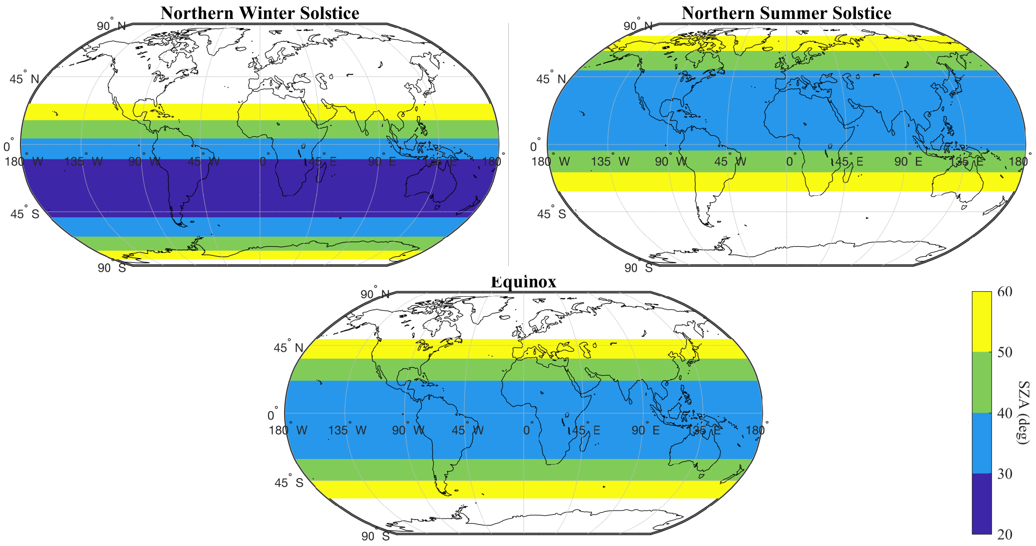

Fig. 7.6: Solar zenith angle ($\leq 60°$) over the world map considering SSO orbit at 550km altitude 10 am LTAN

7.2.1 Nominal Camera Settings

Table 7.2 presents the default operational setting for both FINIS cameras. The setting commands must be sent in the exact order listed in Table 7.2. This is important since some commands affect other settings undesirably. The frame rate command, for example, shifts the sensor gain back to "low", therefore, the set sensor gain command shall always be transmitted after setting the frame rate. Another example is the set integration time command, which shifts the priority back to readout. To ensure the correct sync between the two cameras, the payload board shall provide the external sync pulses for both cameras that will be operating in SLAVE mode. Priority setting shall be set to Integration to enable the start of integration time right after the sync pulse. The camera gain and exposure might be adjusted during the commissioning phase to ensure optimum performance.

Table 7.2: Nominal Camera Settings

Setting	CAM1	CAM2
External Sync Mode	SLAVE	SLAVE
Analog mode	DISABLED	DISABLED
Automatic Gain Control (AGC)	MANUAL	MANUAL
Auto-Exposure	DISABLED	DISABLED
CMOS bit depth	14-bits	14-bits
Camera Link bit depth	14-bits	14-bits
Integration mode	UNRESTRICTED	UNRESTRICTED
FPA Set Point Temperature	20°C	20°C
Frame Rate (FPS)	10	10
Sensor Gain	MEDIUM	MEDIUM
Integration Time (ms)	8	8
Priority	INTEGRATION	INTEGRATION

7.2.2 Onboard Calibration Procedure

At the beginning of every orbit cycle, a stack of 100 dark frames and 100 flat frames must be acquired from each camera using the onboard calibration unit following the steps below.

Step 1: Command shutter to close.

Step 2: Collect 100 dark frames from each camera using the nominal camera settings.

Step 3: Activate both LED rings by supplying the PWM signal required to achieve satisfactory SNR with nominal camera settings.

Step 4: Collect 100 flat frames from each camera using the nominal camera.

7.2.3 Scene Acquisition Procedure

To achieve sufficient frame overlap, the acquisition must start right before the target region appears at the front edge of the FOV and end only after the target region has completely crossed the FOV. For the nominal orbital altitude (550 km), the satellite will take approximately 11 s to cover the distance of the projected in-track FOV on the ground (≈77 km). Therefore, the minimum acquisition period to generate a base frame (77×96 km^2) is 22 s (twice the time to cover the in-track FOV).

The required acquisition time (t_{Aq}), defined as the time at which the camera is collecting and storing the stack of frames, can be computed as $t_{Aq} = (N_f + 1) \times 11$s, where N_f is the number of base frames in the strip. Considering the nominal 10 fps data rate, Table 7.3 lists the approximated strip spatial and data sizes for acquisition times ranging from 22 s to 55 s. The strip containing four base frames is defined as the base scene size. In this case, the total data size of the uncompressed stacks is under 700 MB, which means each individual stack is about 350 MB. This data size can be easily handled during the storage and processing phases.

Table 7.3: Data generated by different acquisition times (CAM at 10 fps)

Num. of Base Frames in strip	Strip Dimensions (km×km)[a]	Acquisition Time (s)	Num. of Frames (both CAMs)	Data size (MB) (16-bit word)
1	96 × 77	22	440	275
2	96 × 154	33	660	413
3	96 × 231	44	880	550
4*	**96 × 308**	**55**	**1100**	**687**

[a] Strip width (swath) by the length along the flight path

* Defined as Base Scene Size

The following subsection covers the primary target regions for the instrument validation phase.

7.2.4 Primary Targets

During the first two years of the ACMES mission, the FINIS data acquisition plan will prioritize the regions where other GHG satellites have recently detected the presence of methane emitters and the regions near the TCCON (Total Carbon Column Observing Network) stations. The data from the emitter regions will serve to test FINIS's performance in detecting the plumes of the known emitters and compare the results with those of other missions. The data collected near the TCCON stations will be used to calibrate the retrieval algorithm and validate the methane background concentration measurements. The selected primary target regions for the FINIS data acquisition plan are presented in Fig. 7.7.

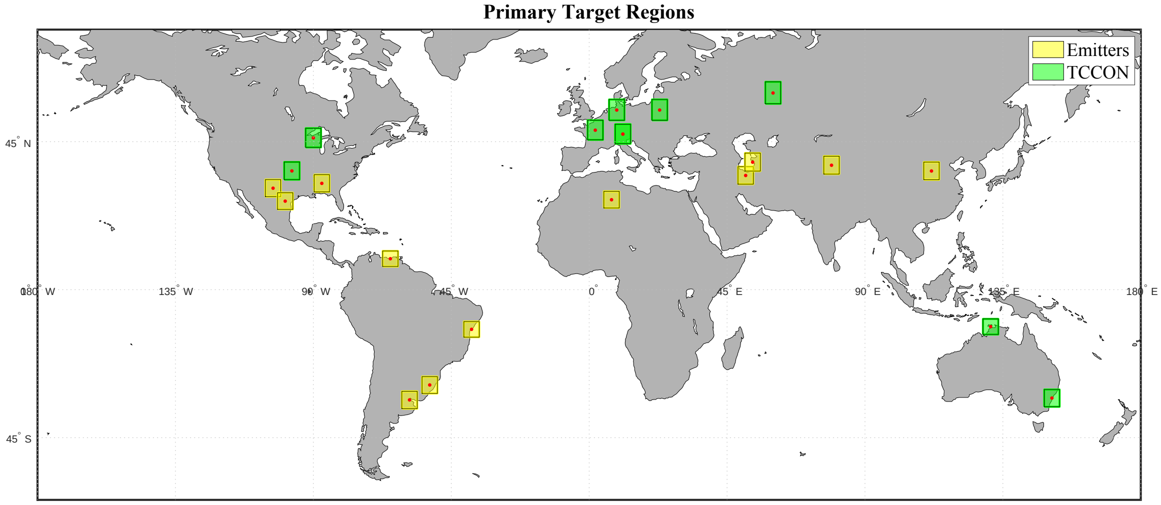

Fig. 7.7: Primary target regions for the instrument validation. Each region polygon spans 5° in latitude and 5° in longitude.

Fig. 7.8 presents four examples of recently detected point-source emissions by the Earth's surface Mineral dust source InvesTigation (EMIT), which is a remote visible to shortwave infrared (VSWIR) imaging spectrometer that operates from the International Space Station (ISS) since July 2022. The complete list of the emitter regions' center coordinates is presented in Table 7.4.

The TCCON (Total Carbon Column Observing Network) is the current most recognized validation system for space-based GHG total column measurements. It consists of

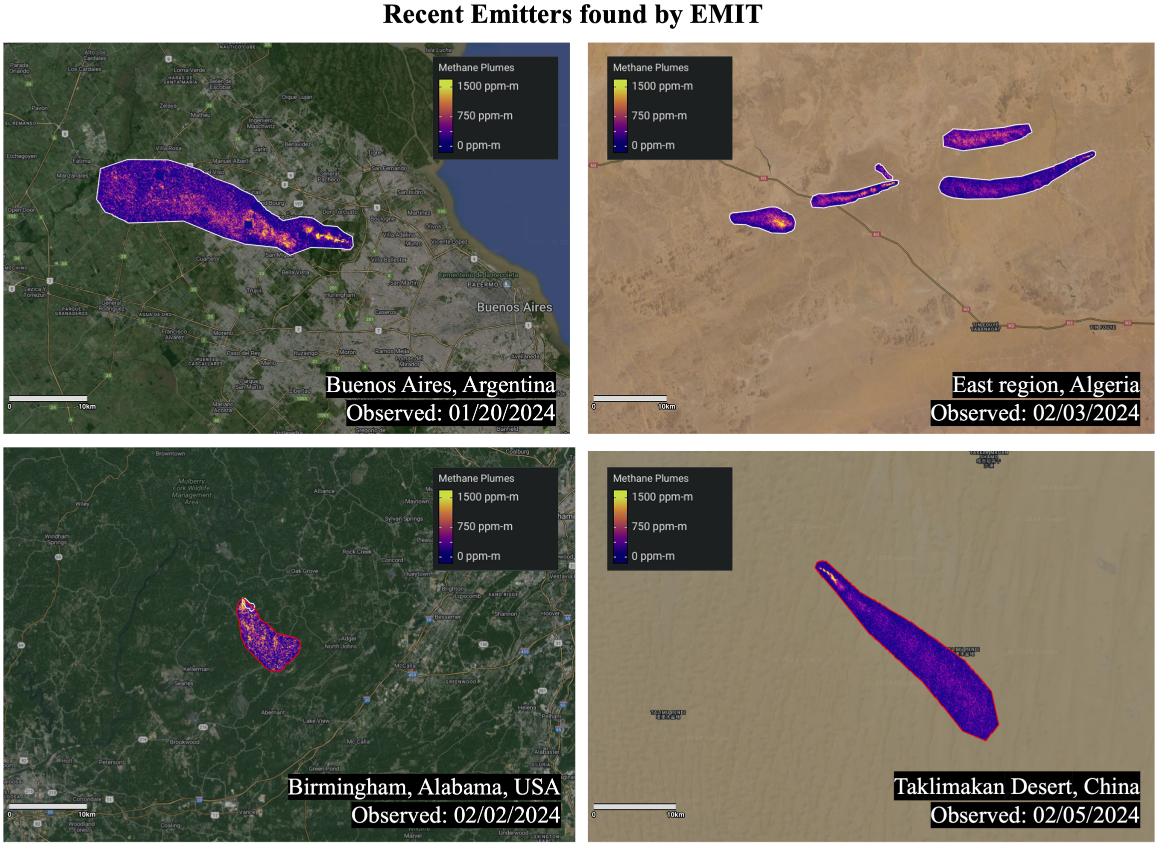

Recent Emitters found by EMIT

Buenos Aires, Argentina
Observed: 01/20/2024

East region, Algeria
Observed: 02/03/2024

Birmingham, Alabama, USA
Observed: 02/02/2024

Taklimakan Desert, China
Observed: 02/05/2024

Fig. 7.8: Example of Emitters Recently found by EMIT (onboard ISS). Credits: NASA/JPL-Caltech. Source: EMIT Open Data Portal.

Table 7.4: Target emitter regions

Emitter #	Lat	Lon	Country	Source	Target ID	Polygon Dimension
1	32.003	-103.14	USA	Oil & Gas	E1	5° × 5°
2	28.15	-99.181	USA	Oil & Gas	E2	5° × 5°
3	33.42	-87.238	USA	Oil & Gas	E3	5° × 5°
4	10.078	-64.875	Venezuela	Oil & Gas	E4	5° × 5°
5	-34.534	-58.616	Argentina	Landfill	E5	5° × 5°
6	-30.149	-52.023	Brazil	Landfill	E6	5° × 5°
7	-12.857	-38.371	Brazil	Landfill	E7	5° × 5°
8	28.572	7.3031	Algeria	Oil & Gas	E8	5° × 5°
9	35.696	51.065	Iran	Landfill	E9	5° × 5°
10	39.458	53.342	Turkmenistan	Oil & Gas	E10	5° × 5°
11	38.603	79.083	China	Oil & Gas	E11	5° × 5°
12	36.98	111.7	China	Oil & Gas	E12	5° × 5°

a global network of ground-based Fourier Transform Spectrometers (FTS). These stations specifically target carbon dioxide (CO_2) and methane (CH_4), though some sites also measure other gases such as carbon monoxide (CO) and nitrous oxide (N_2O) [62]. The current TCCON CH_4 mixing ratio measurements have current systematic errors below 0.5% for SZA below 85°.

The publicly available data will be used for FINIS measurement validation, following the examples of OCO-2 [63], GOSAT [64], SCIAMACHY [65], and S5P [66]. Table 7.5 presents the location of the TCCON stations selected for the FINIS validation plan. The TCCON stations located on islands were not considered appropriate.

Table 7.5: Target TCCON stations regions

Station	Lat	Lon	Altitude (km)	Target ID	Polygon Dimension
Lamont, OK (USA)	37	-97	0.32	TC1	$5° \times 5°$
Park Falls, WI (USA)	46	-90	0.44	TC2	$5° \times 5°$
Orleans, France	48	2	0.13	TC3	$5° \times 5°$
Bremen, Germany	53	9	0.04	TC4	$5° \times 5°$
Garmisch, Germany	47	11	0.74	TC5	$5° \times 5°$
Zugspitze, Germany	47	11	2.96	TC6	$5° \times 5°$
Bialystok, Poland	53	23	0.15	TC7	$5° \times 5°$
Yekaterinburg, Russia	57	60	0.3	TC8	$5° \times 5°$
Darwin, Australia	-12	131	0.03	TC9	$5° \times 5°$
Wollongong, Australia	-34	151	0	TC10	$5° \times 5°$

Fig. 7.9 presents the FINIS base scene footprint (96km×308km) overlaid at the center of target region E2 (defined in Table 7.4). The GHGsat base scene footprint (12km×12km, [22]) is also displayed at the center (blue line) for comparison purposes.

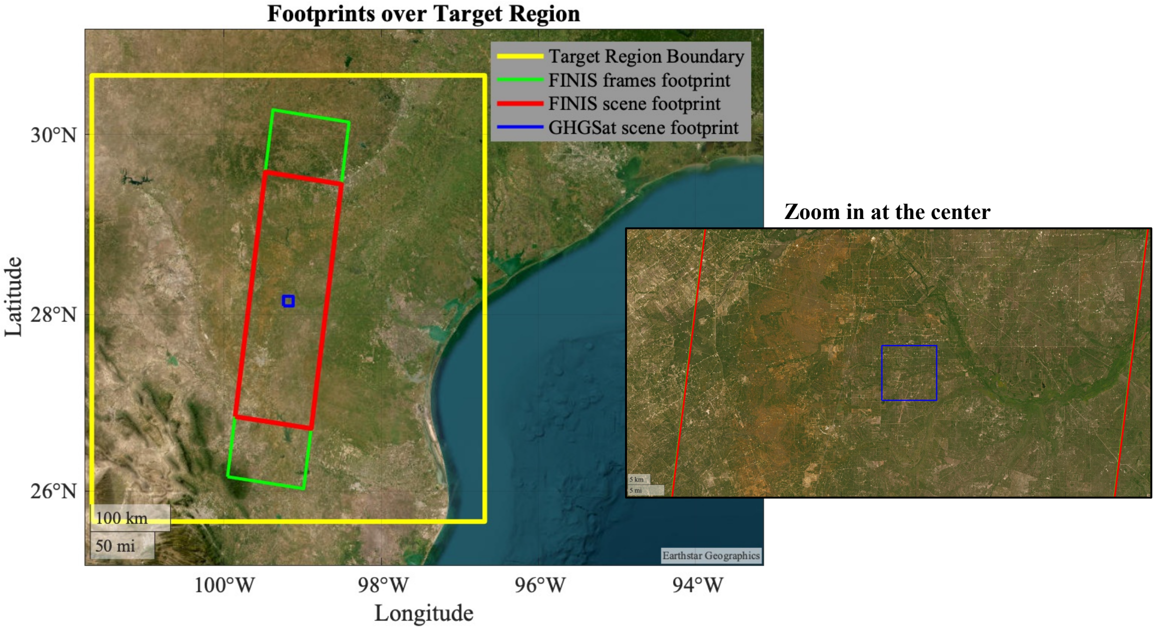

Fig. 7.9: Base scene footprints of FINIS and GHGsat (12km×12km) over the target region E2 (Texas, USA). The green boundary shows FINIS frames' footprint.

7.3 Data Format

Table 7.6 lists the data summarized description for different processing levels, from raw satellite data (Level 0) to methane concentration products (Level 2).

Table 7.6: FINIS data product hierarchy

Data Product	Description
Level 0	Raw collected frames from satellite downlink
Level 1A	Reconstructed, depacketized, uncompressed data, time referenced, annotated with ancillary information, and reassembled into stacks of frames
Level 1B	Corrected and registered images
Level 2A	Fast retrieval relative to background methane concentration maps
Level 2B	Full retrieval methane vertical column concentration maps

The satellite operator will be responsible for processing the acquired data from Level 0 to Level 1A. The data formats expected for Level 1A are described in Fig. 7.10.

The calibration data, which included the Dark Frame (DF) and Flat Frame (FF) stacks for CAM1 and CAM2 are expected for every orbit cycle. This data will be used to generate the dark frame and flat-field corrections required in the Level 1B processing. The calibration ancillary file must contain the calibration parameters, such as integration time, frame rate, sensor gain, LED PWM frequency and duty cycle, and temperature measurements.

The calibration data stack filename must have the following format:

```
FINIS_<CAM_NUM>_<YYMMDDHHMM>_<ORB_NUM>_<CAL_NAME>_<NUM_FRAMES>.tif
```

- `<CAM_ID>`: Identifier for the camera that captured the image (options: CAM1 or CAM2).
- `<YYMMDDHHMM>`: Date and time of image acquisition in the format (YY-year, MM-month, DD-day, HH-hour, MM-minute), in Coordinated Universal Time (UTC).
- `<ORB_NUM>`: Number indicating the orbit in which the satellite was located when the image was captured.
- `<CAL_NAME>`: Identifier of the calibration type (options: DF or FF).
- `<NUM_FRAMES>`: Number of frames in the stack file.

For every target, the data package must contain the stacks from CAM1 and CAM2 assembled as two ".tif" files, a quick-look image generated from the middle frame of the CAM1 stack in ".png" format, and an ancillary ".json" file containing the acquisition parameters (integration time, gain, data rate, FPA temperature, etc) and the satellite attitude and orbital information, including the SZA during the acquisition.

The target data stack filename must have the following format:

```
FINIS_<CAM_NUM>_<YYMMDDHHMM>_<ORB_NUM>_<TARGET_ID>_<NUM_FRAMES>_L1A.tif
```

- `<CAM_ID>`: Identifier for the camera that captured the image (options: CAM1 or CAM2).
- `<YYMMDDHHMM>`: Date and time of image acquisition in the format (YY-year, MM-month, DD-day, HH-hour, MM-minute), in Coordinated Universal Time (UTC).

- `<ORB_NUM>`: Number indicating the orbit in which the satellite was located when the image was captured.
- `<TARGET_ID>`: Identifier for the specific target or area imaged.
- `<NUM_FRAMES>`: Number of frames in the stack file.
- `L1A`: This indicates the level of processing applied to the image, in this case, Level-1A processing.

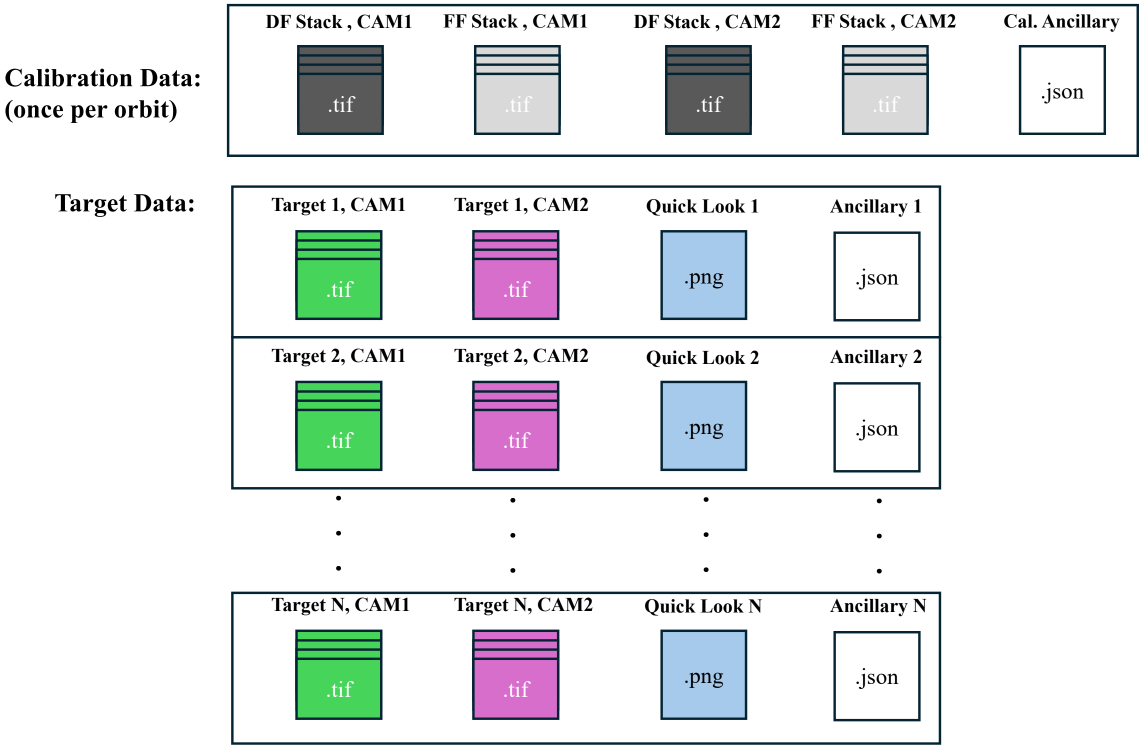

Fig. 7.10: Level 1 data composition and file formats

CHAPTER 8

SUMMARY AND FUTURE WORK

This work provided a comprehensive overview of the development of FINIS, a compact methane sensor designed to facilitate methane monitoring using cost-effective nanosatellite platforms. By introducing an innovative spectrum acquisition technique involving the use of tilted narrowband interference filters in a binocular optical system, this study demonstrates that FINIS can achieve methane detection performance comparable to conventional dispersive imaging spectrometers, commonly found in other greenhouse gas monitoring satellites. Notably, FINIS distinguishes itself by being the lightest space-based methane sensor, weighing under 1 kg, while still capable of detecting small and medium-sized methane leaks when operating in low Earth orbit. Furthermore, FINIS offers wide coverage, essential for mapping emissions on a regional scale, as highlighted in Table 8.1.

Table 8.1: Instrument benchmarking

Instrument	Mass (kg)	Pixel Size (m×m)	Swath (km)	Precision (%)	Detection threshold (t h^{-1})	Ref.
TROPOMI	230	5500×7000	2600	0.8	10	[67] [68]
MethaneSAT	183	100×400	200	0.1 – 0.2	0.5	[69] [19]
GHGSat	6	25×25	12	1.5	0.2	[22] [70]
PRISMA	80	30×30	30	3 – 9	0.5 – 2.0	[71] [72]
FINIS	**0.9**	**150×205**	**96**	**0.4 – 3.2**[a]	**0.5 – 1.0**	Section 5.2.3

[a] Estimated retrieval precision varies with frame rate, SZA, and albedo (see Fig. 5.14).

In Chapter 3, we detailed the substantial enhancements made to FINIS's optical and mechanical design, transitioning from its initial iteration featuring a single folded telescope to its space-optimized version incorporating a binocular optical system equipped with an onboard calibration unit. Leveraged from lessons learned in previous developments of FINIS's operational concept through lab and airborne flight tests, the change to a binocular setup enables relative radiance measurements that are independent of surface reflectance functions, solving the parallax problem found in its original design. Additionally, by optimally tuning the IF's parameters, such as the center wavelength and the tilt angle, it was demonstrated that the differential measurements taken from both imagers significantly reduce the correlation between the methane and water vapor weighting functions, thereby enhancing the retrieval precision. Furthermore, this chapter unveiled the design of the onboard calibration unit, which comprises a rotating double shutter that blocks the light ingress during both dark frame calibration and flat fielding calibration procedures utilizing the SWIR LED ring as the light source.

In Chapter 4, we delved into how FINIS was modeled as an imaging system capable of capturing the scene's spectrum information across its two cameras' FPA. The spectrum response model elucidates how the narrowband interference filter, mounted with a tilt angle at the instrument's aperture, distributes the spectrum center wavelength across each FPA based on the target's location in the field of view. Moreover, we discussed the inputs and assumptions utilized in the Radiative Transfer Model software, used to compute the spectrum radiance reaching the sensor in orbit, along with the weighting functions necessary for the retrieval noise analysis. Additionally, we briefly outlined the modeling of methane plumes using the Gaussian distribution approach later used in the plume detection simulation. Finally, we introduced the optimum retrieval method applied for FINIS's relative radiance measurements and proposed a fast retrieval method to detect methane plumes with reduced computational power.

In Chapter 5, the focus shifted to evaluating FINIS's methane detection and measurement capabilities across varying lighting conditions. The radiometric analysis revealed that under low light conditions, defined by a surface albedo of 0.1 and an SZA of 60 degrees, FINIS is expected to achieve a single measurement SNR surpassing 70 for each camera. Conversely, in high light conditions, characterized by a surface albedo of 0.6 and an SZA of 20 degrees, the anticipated SNR can peak at 280. These performance levels are attainable with both cameras operating at the medium gain and with an integration time of approximately 8 ms, translating to a pixel size of approximately 150 m cross-track by 200 m intrack at ACMES' 550 km orbital altitude and considering the instrument's IFOV.

Subsequently, in the retrieval noise analysis, the radiometric performance outcomes were utilized to compute the relative measurement noise. This analysis was conducted for targets traversing both the center and the edges of the field of view. It was observed that slight variations in performance occurred across the track, with better performance noted at the edges compared to the center, owing to differences in how the pair of wavelengths are combined in these two regions. Given a priori knowledge about the state vector and assuming an albedo of 0.2, along with a data acquisition rate of 5 frames per second, the methane retrieval noise is anticipated to be less than 2.5% for a solar zenith angle (SZA) of 60 degrees and under 2% for a SZA of 30 degrees. Given the mission objectives delineated in Section 3.1, this level of precision is demonstrated to be adequate for detecting plumes stemming from leak rates exceeding 1 ton per hour at a SZA of 60 degrees and 500 kilograms per hour at an SZA of 30 degrees. This performance can be further enhanced by oversampling the scene with a frame acquisition rate of up to 60 frames per second (fps) for each camera.

Next, the plume detection simulation was presented to demonstrate FINIS data acquisition and data processing methods that generate the final methane map products. The simulation involved generating images by simulating the ground scanning, accounting for factors such as field of view (FOV), orbital altitude, inclination, and integration time. By processing the stack of simulated images using the fast retrieval method, the methane map was generated and shown to allow the detection of all simulated plumes with varying leak rates. The results of this simulation, therefore, confirmed that the simulated detection performance meets the requirements, even when employing the fast retrieval method. Addionally, the simulation shows how the retrieval is affected by uncorrected non-uniform detector gains, which results on the appearance of lines in the map aligned with the relative target motion. This undesirable effect introduces additional noise to the retrieval process, which diminishes the plume detection capability and underscores the critical importance of the onboard calibration unit for accurate flat fielding.

In Chapter 6, the preliminary calibration results were outlined. The focus calibration showed that both camera assemblies achieved sufficiently similar focus, with CAM2 exhibiting slightly higher optical performance than CAM1. The stereo camera calibration confirmed that the alignment of both cameras' fields of view (FOV) provided sufficient overlap for the image pairs.

During the dark frame calibration, where the cameras were tested without any light source, an initial analysis revealed higher-than-expected noise levels in the data. Further investigation traced this issue to corruption in the 8th bit of the 14-bit pixel data streamed by the camera and received by the developer FPGA board used in the lab. Fortunately, this issue was resolved by replacing the FPGA board with a frame grabber to collect the frames. After this modification, we verified that CAM1's noise performance was better than the values used in the radiometric analysis, suggesting that the measurements' signal-to-noise ratio (SNR) is likely to exceed the predicted values.

The flat field calibration could not be accurately performed due to limitations in the lab setup and equipment; further work is required to improve the quality of the results. However, for the flat field using the onboard calibration unit, we verified that the illumination pattern created by the LED ring over the shutter could be estimated by filtering the bright frame to remove high-frequency components. Additionally, we confirmed that the illumination pattern remains fairly stable even after the deactivation of one of the eight LEDs. Using the estimated illumination pattern, we corrected the bright frame to extract pixel gain corrections for performing flat fielding.

Lastly, the Methane Cell Calibration was conducted to verify the distribution of the center wavelength across the sensor induced by the tilted interference filter. The results indicated that the measured transmission profile closely matched the modeled spectral response, confirming the accuracy of the filter's performance. However, the data presented for this test exhibited the previously mentioned 8th-bit corruption in the pixel data. While this does not invalidate the results, the noise levels presented are much higher than in reality. Future works include repeating the methane cell calibration using the flight FINIS payload board to register each camera's spectrum response accurately.

Finally, in Chapter 7, the electrical and mechanical interfaces for FINIS were presented, detailing their integration into the ACMES bus. The instrument operation plan covered the main aspects of operation in orbit, including camera settings, data acquisition procedures, primary targets for validating FINIS methane measurement performance using TCCON stations, and plume detection targets to validate FINIS's capability in detecting point sources. Additionally, the required data format for cataloging and processing was presented.

8.1 Future Work

In the upcoming months, prior to its integration into the ACMES bus, the flight payload board will be used for a new set of calibrations and tests. A special effort will be directed toward better characterizing the system-wide flat field and comparing it to the flat field obtained using the onboard calibration unit. Additional tests are also required to ensure the payload board's functionalities in configuring the cameras, providing the external sync signal to run both cameras in slave mode, retrieving the frames, and operating the onboard calibration unit, including powering the LED ring with the PWM signal. Additionally, a new shutter and a new solenoid will be installed in the flight unit. The new shutter's paddles have a slightly larger diameter to reduce the light leak observed during tests, and it is also thinner, which helps mitigate the risk of it getting stuck in the slot during operation. The new self-restoring solenoid will ensure that the shutter remains in its open position when not energized, addressing an issue with the original solenoid, which functioned in reverse due to modifications in the solenoid's assembly orientation. After the integration of FINIS into the ACMES bus, final functionality tests must be conducted to ensure nominal operation before launch.

In terms of additional analysis, we recommend conducting a thermal analysis of the instrument, considering its integration into the ACMES bus. FINIS' cameras are mounted with only one face in contact with the base plate, which serves as the main heat sink. Depending on the base plate temperature, this contact interface might not provide sufficient heat dissipation to maintain both cameras' FPA temperatures at 20°C. If this condition is not met, the cameras may operate at 40°C, increasing thermal noise and reducing the performance of methane measurements.

Once in orbit, FINIS will acquire data following its operation plan. Extensive work will be required to process this data. The algorithms developed in this work will need to be adapted for cloud computing. Additionally, new processing routines may need to be implemented to address unforeseen issues in the data. During operation, vicarious calibration might be necessary to address the limitations of the onboard calibration unit in performing flat-fielding. If the light leak continues with the new shutter, the dark frame calibration will need to be conducted only during the night portion of the orbit.

With FINIS' upcoming first space operation, there will undoubtedly be a series of lessons learned. These must be properly documented to be incorporated into future designs. This documentation will be crucial for improving the system's performance, reliability, and efficiency in subsequent iterations. Capturing and analyzing these lessons will help refine calibration procedures, data processing algorithms, and overall system integration, ensuring that future missions benefit from the insights gained during this space flight demonstration.

Bibliography

[1] FLIR, *Tau SWIR Product Specification, Revision 105, 102-2009-40*, Oct. 2018.

[2] IEA, "Sources of methane emissions, 2017 and 2020," https://www.iea.org/data-and-statistics/charts/sources-of-methane-emissions-2017-and-2020, 2020, licence: CC BY 4.0.

[3] K. Thoning, E. Dlugokencky, X. Lan, and NOAA Global Monitoring Laboratory, "Trends in globally-averaged CH4, N2O, and SF6," 2022. [Online]. Available: https://gml.noaa.gov/ccgg/trends_doi.html

[4] G. Myhre, D. Shindell, F.-M. Bréon, W. Collins, J. Fuglestvedt, J. Huang, D. Koch, J.-F. Lamarque, D. Lee, B. Mendoza, T. Nakajima, A. Robock, G. Stephens, H. Zhang, B. Aamaas, O. Boucher, S. B. Dalsøren, J. S. Daniel, P. Forster, C. Granier, J. Haigh, O. Hodnebrog, J. O. Kaplan, G. Marston, C. J. Nielsen, B. C. O'Neill, G. P. Peters, J. Pongratz, V. Ramaswamy, R. Roth, L. Rotstayn, S. J. Smith, D. Stevenson, J.-P. Vernier, O. Wild, P. Young, D. Jacob, A. R. Ravishankara, and K. Shine, "8 Anthropogenic and Natural Radiative Forcing," Tech. Rep.

[5] M. J. Prather, C. D. Holmes, and J. Hsu, "Reactive greenhouse gas scenarios: Systematic exploration of uncertainties and the role of atmospheric chemistry," *Geophysical Research Letters*, vol. 39, no. 9, p. 2012GL051440, May 2012. [Online]. Available: https://onlinelibrary.wiley.com/doi/10.1029/2012GL051440

[6] C. Swenson and A. Marchant, "Filter incidence narrow-band infrared spectrometer," US Patent US20 220 003 665A1, Jan., 2022. [Online]. Available: https://patents.google.com/patent/US20220003665A1/en?oq=US-2022-0003665-A1

[7] Charles Swenson, Lucas Anderson, Chad Fish, Bruno Mattos, Robert Wright, and Mark Schoeberl, "The Active Cooling for Multispectral Earth Sensors (ACMES) Mission," Portugal, 2022. [Online]. Available: https://az659834.vo.msecnd.net/eventsairwesteuprod/production-atpi-public/c7baeb9d67d4402fa8fa853889369bc8

[8] R. Wright, P. Lucey, L. Flynn, M. Nunes, T. George, S. Gunapala, D. Ting, and S. Rafol, "HYTI: Thermal Hyperspectral Imaging From a Cubesat Platform," in *Small Satellite Conference*, Aug. 2019. [Online]. Available: https://digitalcommons.usu.edu/smallsat/2019/all2019/70

[9] L. Anderson, M. Kirk, B. Mattos, C. Swenson, C. Fish, M. Nunes, and R. Wright, "Active Thermal Control for the Multispectral Earth Sensors (ACMES) Mission," in *Small Satellite Conference*, Aug. 2022. [Online]. Available: https://digitalcommons.usu.edu/smallsat/2022/all2022/169

[10] L. Shibuya Sato, L. Loures, V. Costa, R. Wottrich, A. Jeronymo, H. Júnior, P. Cabral, R. Menezes, M. Oliveira, T. Carvalho, E. Oliveira, D. Vieira, C. Swenson, J. Casas, L. Krause, and J. Costa, "Lessons Learned During Testing Through Commissioning of

the Joint Brazil-US SPORT Mission," *Small Satellite Conference*, Aug. 2023. [Online]. Available: https://digitalcommons.usu.edu/smallsat/2023/all2023/57

[11] C. Wührer, C. Kühl, S. Lucarelli, and M. Bode, "MERLIN: overview of the design status of the lidar Instrument," in *International Conference on Space Optics — ICSO 2018*, vol. 11180. SPIE, Jul. 2019, pp. 839–851. [Online]. Available: https://www.spiedigitallibrary.org/conference-proceedings-of-spie/11180/1118028/MERLIN--overview-of-the-design-status-of-the-lidar/10.1117/12.2535999.full

[12] J. R. Worden, A. J. Turner, A. Bloom, S. S. Kulawik, J. Liu, M. Lee, R. Weidner, K. Bowman, C. Frankenberg, R. Parker, and V. H. Payne, "Quantifying lower tropospheric methane concentrations using GOSAT near-IR and TES thermal IR measurements," *Atmospheric Measurement Techniques*, vol. 8, no. 8, pp. 3433–3445, Aug. 2015. [Online]. Available: https://amt.copernicus.org/articles/8/3433/2015/

[13] R. G. Sellar and G. D. Boreman, "Classification of imaging spectrometers for remote sensing applications," *Optical Engineering*, vol. 44, Jan. 2005. [Online]. Available: https://www.spiedigitallibrary.org/journals/optical-engineering/volume-44/issue-01/013602/Classification-of-imaging-spectrometers-for-remote-sensing-applications/10.1117/1.1813441.full?SSO=1

[14] S. Jongaramrungruang, G. Matheou, A. K. Thorpe, Z.-C. Zeng, and C. Frankenberg, "Remote sensing of methane plumes: instrument tradeoff analysis for detecting and quantifying local sources at global scale," Gases/Remote Sensing/Data Processing and Information Retrieval, preprint, Jul. 2021. [Online]. Available: https://amt.copernicus.org/preprints/amt-2021-205/amt-2021-205.pdf

[15] T. Ehret, A. De Truchis, M. Mazzolini, J.-M. Morel, A. d'Aspremont, T. Lauvaux, R. Duren, D. Cusworth, and G. Facciolo, "Global Tracking and Quantification of Oil and Gas Methane Emissions from Recurrent *Sentinel-2* Imagery," *Environmental Science & Technology*, vol. 56, no. 14, pp. 10 517–10 529, Jul. 2022. [Online]. Available: https://pubs.acs.org/doi/10.1021/acs.est.1c08575

[16] D. J. Varon, D. Jervis, J. McKeever, I. Spence, D. Gains, and D. J. Jacob, "High-frequency monitoring of anomalous methane point sources with multispectral Sentinel-2 satellite observations," *Atmospheric Measurement Techniques*, vol. 14, no. 4, pp. 2771–2785, Apr. 2021, publisher: Copernicus GmbH. [Online]. Available: https://amt.copernicus.org/articles/14/2771/2021/

[17] E. Sánchez-García, J. Gorroño, I. Irakulis-Loitxate, D. J. Varon, and L. Guanter, "Mapping methane plumes at very high spatial resolution with the WorldView-3 satellite," *Atmospheric Measurement Techniques*, vol. 15, no. 6, pp. 1657–1674, Mar. 2022, publisher: Copernicus GmbH. [Online]. Available: https://amt.copernicus.org/articles/15/1657/2022/

[18] "Progress on data and lingering uncertainties – Global Methane Tracker 2024 – Analysis." [Online]. Available: https://www.iea.org/reports/global-methane-tracker-2024/progress-on-data-and-lingering-uncertainties

[19] D. J. Jacob, D. J. Varon, D. H. Cusworth, P. E. Dennison, C. Frankenberg, R. Gautam, L. Guanter, J. Kelley, J. McKeever, L. E. Ott, B. Poulter, Z. Qu, A. K. Thorpe, J. R. Worden, and R. M. Duren, "Quantifying methane emissions from the global scale down to point sources using satellite observations of atmospheric methane," Apr. 2022. [Online]. Available: https://acp.copernicus.org/preprints/acp-2022-246/acp-2022-246.pdf

[20] R. Imasu, T. Matsunaga, M. Nakajima, Y. Yoshida, K. Shiomi, I. Morino, N. Saitoh, Y. Niwa, Y. Someya, Y. Oishi, M. Hashimoto, H. Noda, K. Hikosaka, O. Uchino, S. Maksyutov, H. Takagi, H. Ishida, T. Y. Nakajima, T. Nakajima, and C. Shi, "Greenhouse gases Observing SATellite 2 (GOSAT-2): mission overview," *Progress in Earth and Planetary Science*, vol. 10, no. 1, p. 33, Jul. 2023. [Online]. Available: https://doi.org/10.1186/s40645-023-00562-2

[21] D. Nijkerk, B. v. Venrooy, P. V. Doorn, R. Henselmans, F. Draaisma, and A. Hoogstrate, "The TROPOMI Telescope," in *International Conference on Space Optics — ICSO 2012*, vol. 10564. SPIE, Nov. 2017, pp. 272–278. [Online]. Available: https://www.spiedigitallibrary.org/conference-proceedings-of-spie/10564/105640Z/The-TROPOMI-Telescope/10.1117/12.2309035.full

[22] D. Jervis, J. McKeever, B. O. A. Durak, J. J. Sloan, D. Gains, D. J. Varon, A. Ramier, M. Strupler, and E. Tarrant, "The GHGSat-D imaging spectrometer," *Atmospheric Measurement Techniques*, vol. 14, no. 3, pp. 2127–2140, Mar. 2021. [Online]. Available: https://amt.copernicus.org/articles/14/2127/2021/

[23] S. Cogliati, F. Sarti, L. Chiarantini, M. Cosi, R. Lorusso, E. Lopinto, F. Miglietta, L. Genesio, L. Guanter, A. Damm, S. Pérez-López, D. Scheffler, G. Tagliabue, C. Panigada, U. Rascher, T. P. F. Dowling, C. Giardino, and R. Colombo, "The PRISMA imaging spectroscopy mission: overview and first performance analysis," *Remote Sensing of Environment*, vol. 262, p. 112499, Sep. 2021. [Online]. Available: https://www.sciencedirect.com/science/article/pii/S0034425721002170

[24] L. Guanter, H. Kaufmann, K. Segl, S. Foerster, C. Rogass, S. Chabrillat, T. Kuester, A. Hollstein, G. Rossner, C. Chlebek, C. Straif, S. Fischer, S. Schrader, T. Storch, U. Heiden, A. Mueller, M. Bachmann, H. Mühle, R. Müller, M. Habermeyer, A. Ohndorf, J. Hill, H. Buddenbaum, P. Hostert, S. van der Linden, P. Leitão, A. Rabe, R. Doerffer, H. Krasemann, H. Xi, W. Mauser, T. Hank, M. Locherer, M. Rast, K. Staenz, and B. Sang, "The EnMAP Spaceborne Imaging Spectroscopy Mission for Earth Observation," *Remote Sensing*, vol. 7, no. 7, pp. 8830–8857, Jul. 2015. [Online]. Available: http://www.mdpi.com/2072-4292/7/7/8830

[25] D. H. Cusworth, D. J. Jacob, D. J. Varon, C. Chan Miller, X. Liu, K. Chance, A. K. Thorpe, R. M. Duren, C. E. Miller, D. R. Thompson, C. Frankenberg, L. Guanter, and C. A. Randles, "Potential of next-generation imaging spectrometers to detect and quantify methane point sources from space," *Atmospheric Measurement Techniques*, vol. 12, no. 10, pp. 5655–5668, Oct. 2019. [Online]. Available: https://amt.copernicus.org/articles/12/5655/2019/

[26] T. Matsunaga and H. Tanimoto, “Greenhouse gas observation by TANSO-3 onboard GOSAT-GW,” in *Sensors, Systems, and Next-Generation Satellites XXVI*, vol. 12264. SPIE, Oct. 2022, pp. 86–90. [Online]. Available: https://www.spiedigitallibrary.org/conference-proceedings-of-spie/12264/122640B/Greenhouse-gas-observation-by-TANSO-3-onboard-GOSAT-GW/10.1117/12.2639221.full

[27] R. Rohrschneider, S. Wofsy, J. Franklin, J. Benmergui, J. Soto, and S. Davis, “The MethaneSAT Mission,” in *Small Satellite Conference*, Aug. 2021. [Online]. Available: https://digitalcommons.usu.edu/smallsat/2021/all2021/141

[28] “CO2 Emission Control Technology l Carbon Mapper spectrometer.” [Online]. Available: https://carbonmapper.org/our-mission/technology/

[29] Y. Zhang, R. Gautam, S. Pandey, M. Omara, J. D. Maasakkers, P. Sadavarte, D. Lyon, H. Nesser, M. P. Sulprizio, D. J. Varon, R. Zhang, S. Houweling, D. Zavala-Araiza, R. A. Alvarez, A. Lorente, S. P. Hamburg, I. Aben, and D. J. Jacob, “Quantifying methane emissions from the largest oil-producing basin in the United States from space,” *Science Advances*, vol. 6, no. 17, p. eaaz5120, Apr. 2020. [Online]. Available: https://www.science.org/doi/10.1126/sciadv.aaz5120

[30] L. Shen, D. Zavala-Araiza, R. Gautam, M. Omara, T. Scarpelli, J. Sheng, M. P. Sulprizio, J. Zhuang, Y. Zhang, Z. Qu, X. Lu, S. P. Hamburg, and D. J. Jacob, “Unravelling a large methane emission discrepancy in Mexico using satellite observations,” *Remote Sensing of Environment*, vol. 260, p. 112461, Jul. 2021. [Online]. Available: https://www.sciencedirect.com/science/article/pii/S0034425721001796

[31] M. Nakajima, H. Suto, K. Yotsumoto, K. Shiomi, and T. Hirabayashi, “Fourier transform spectrometer on GOSAT and GOSAT-2,” in *International Conference on Space Optics — ICSO 2014*, vol. 10563. SPIE, Nov. 2017, pp. 1354–1362. [Online]. Available: https://www.spiedigitallibrary.org/conference-proceedings-of-spie/10563/105634O/Fourier-transform-spectrometer-on-GOSAT-and-GOSAT-2/10.1117/12.2304062.full

[32] A. Ludewig, Q. Kleipool, R. Bartstra, R. Landzaat, J. Leloux, E. Loots, P. Meijering, E. van der Plas, N. Rozemeijer, F. Vonk, and P. Veefkind, “In-flight calibration results of the TROPOMI payload on board the Sentinel-5 Precursor satellite,” *Atmospheric Measurement Techniques*, vol. 13, no. 7, pp. 3561–3580, Jul. 2020. [Online]. Available: https://amt.copernicus.org/articles/13/3561/2020/

[33] R. M. van Hees, P. J. J. Tol, S. Cadot, M. Krijger, S. T. Persijn, T. A. van Kempen, R. Snel, I. Aben, and R. M. Hoogeveen, “Determination of the TROPOMI-SWIR instrument spectral response function,” *Atmospheric Measurement Techniques*, vol. 11, no. 7, pp. 3917–3933, Jul. 2018. [Online]. Available: https://amt.copernicus.org/articles/11/3917/2018/

[34] J. Doornink, J. d. Vries, R. Voors, J. Dingjan, B. Ording, N. v. d. Valk, R. Vink, R. Hoogeveen, J. Grant, T. Canas, Q. Kleipool, and P. Veefkind, “The Tropomi instrument: last steps towards final integration and testing,” in *International Conference on Space Optics — ICSO 2014*, vol. 10563. SPIE, Nov. 2017, pp. 1167–1175. [Online].

Available: https://www.spiedigitallibrary.org/conference-proceedings-of-spie/10563/1056342/The-Tropomi-instrument--last-steps-towards-final-integration-and/10.1117/12.2304148.full

[35] J. P. Burrows, M. Weber, M. Buchwitz, V. Rozanov, A. Ladstätter-Weißenmayer, A. Richter, R. DeBeek, R. Hoogen, K. Bramstedt, K.-U. Eichmann, M. Eisinger, and D. Perner, "The Global Ozone Monitoring Experiment (GOME): Mission Concept and First Scientific Results," *Journal of the Atmospheric Sciences*, vol. 56, no. 2, pp. 151–175, Jan. 1999. [Online]. Available: http://journals.ametsoc.org/doi/10.1175/1520-0469(1999)056⟨0151:TGOMEG⟩2.0.CO;2

[36] H. Bovensmann, J. P. Burrows, M. Buchwitz, J. Frerick, S. Noël, V. V. Rozanov, K. V. Chance, and A. P. H. Goede, "SCIAMACHY: Mission Objectives and Measurement Modes," *Journal of the Atmospheric Sciences*, vol. 56, no. 2, pp. 127–150, Jan. 1999, publisher: American Meteorological Society Section: Journal of the Atmospheric Sciences. [Online]. Available: https://journals.ametsoc.org/view/journals/atsc/56/2/1520-0469_1999_056_0127_smoamm_2.0.co_2.xml

[37] M. Dobber, R. Dirksen, P. Levelt, G. van den Oord, R. Voors, Q. Kleipool, G. Jaross, M. Kowalewski, E. Hilsenrath, G. Leppelmeier, Johan de Vries, W. Dierssen, and N. Rozemeijer, "Ozone monitoring instrument calibration," *IEEE Transactions on Geoscience and Remote Sensing*, vol. 44, no. 5, pp. 1209–1238, May 2006. [Online]. Available: http://ieeexplore.ieee.org/document/1624601/

[38] J. J. Sloan, B. Durak, D. Gains, F. Ricci, J. McKeever, J. Lamoire, M. Sdao, V. Latendresse, J. Lavoie, and R. Kruzelecky, "Fabry-Perot interferometer based satellite detection of atmospheric trace gases," US Patent US9 228 897B2, Jan., 2016. [Online]. Available: https://patents.google.com/patent/US9228897B2/en

[39] D. J. Jacob, A. J. Turner, J. D. Maasakkers, J. Sheng, K. Sun, X. Liu, K. Chance, I. Aben, J. McKeever, and C. Frankenberg, "Satellite observations of atmospheric methane and their value for quantifying methane emissions," *Atmospheric Chemistry and Physics*, vol. 16, no. 22, pp. 14 371–14 396, Nov. 2016. [Online]. Available: https://acp.copernicus.org/articles/16/14371/2016/

[40] C. Staebell, K. Sun, J. Samra, J. Franklin, C. Chan Miller, X. Liu, E. Conway, K. Chance, S. Milligan, and S. Wofsy, "Spectral Calibration of the MethaneAIR Instrument," Gases/Remote Sensing/Instruments and Platforms, preprint, Jan. 2021. [Online]. Available: https://amt.copernicus.org/preprints/amt-2020-513/amt-2020-513.pdf

[41] C. L. Weisberg, D. J. Preston, P. Z. Mouroulis, D. W. Wilson, D. R. Ardila, S. R. Zandbergen, C. L. Bradley, and R. O. Green, "Measured efficiency of three diffraction grating designs for the Carbon Plume Mapper (CPM) spectrometer," in *Imaging Spectrometry XXVI: Applications, Sensors, and Processing*, vol. 12688. SPIE, Nov. 2023, pp. 128–135. [Online]. Available: https://www.spiedigitallibrary.org/conference-proceedings-of-spie/12688/126880H/Measured-efficiency-of-three-diffraction-grating-designs-for-the-Carbon/10.1117/12.2692385.full

[42] D. H. Cusworth, R. M. Duren, A. K. Thorpe, W. Olson-Duvall, J. Heckler, J. W. Chapman, M. L. Eastwood, M. C. Helmlinger, R. O. Green, G. P. Asner, P. E. Dennison, and C. E. Miller, "Intermittency of Large Methane Emitters in the Permian Basin," *Environmental Science & Technology Letters*, vol. 8, no. 7, pp. 567–573, Jul. 2021, publisher: American Chemical Society. [Online]. Available: https://doi.org/10.1021/acs.estlett.1c00173

[43] "Argus 2000 IR Spectrometer," Thoth Technology Inc., Ontario, Canada, Owner's Manual OG274001, 2018. [Online]. Available: https://tinyurl.com/3sj5b8zf

[44] S. Love, K. Post, L. Ott, M. Dale, C. Safi, K. Boyd, H. Mohr, C. Ward, M. Caffrey, J. Theiler, B. Foy, M. Hehlen, C. Peterson, R. Hemphill, J. Wren, A. Guthrie, N. Dallmann, P. Stein, A. Meyer, and M. Dubey, "NACHOS, a CubeSat-Based High-Resolution UV-Visible Hyperspectral Imager for Remote Sensing of Trace Gases: System Overview, Science Objectives, and Preliminary Results," in *Small Satellite Conference*, Aug. 2022. [Online]. Available: https://digitalcommons.usu.edu/smallsat/2022/all2022/166

[45] R. G. Sellar and G. D. Boreman, "Comparison of relative signal-to-noise ratios of different classes of imaging spectrometer," *Applied Optics*, vol. 44, no. 9, pp. 1614–1624, Mar. 2005, publisher: Optica Publishing Group. [Online]. Available: https://opg.optica.org/ao/abstract.cfm?uri=ao-44-9-1614

[46] M. A. Kirk, "Developing a Methane Detector for Aerospace Applications," Master's thesis, Utah State University, 2022, publisher: Utah State University. [Online]. Available: https://digitalcommons.usu.edu/etd/8681

[47] S. Beirle, J. Lampel, C. Lerot, H. Sihler, and T. Wagner, "Parameterizing the instrumental spectral response function and its changes by a super-Gaussian and its derivatives," *Atmospheric Measurement Techniques*, vol. 10, no. 2, pp. 581–598, Feb. 2017, publisher: Copernicus GmbH. [Online]. Available: https://amt.copernicus.org/articles/10/581/2017/amt-10-581-2017.html

[48] V. Rozanov, M. Buchwitz, K.-U. Eichmann, R. Beek, and J. Burrows, "SCIATRAN - A new radiative transfer model for geophysical applications in the 240-2400 NM spectral region: The pseudo-spherical version," *Advances in Space Research - ADV SPACE RES*, vol. 29, pp. 1831–1835, Jun. 2002.

[49] L. Mei, V. Rozanov, A. Rozanov, and J. P. Burrows, "SCIATRAN software package (V4.6): update and further development of aerosol, clouds, surface reflectance databases and models," *Geoscientific Model Development*, vol. 16, no. 5, pp. 1511–1536, Mar. 2023, publisher: Copernicus GmbH. [Online]. Available: https://gmd.copernicus.org/articles/16/1511/2023/

[50] John J. Kosovich, "State of Texas—Highlighting low-lying areas derived from USGS digital elevation data: U.S. Geological Survey Scientific Investigations Map 3050, scale 1:700,000," 2008. [Online]. Available: https://pubs.usgs.gov/sim/3050/

[51] B.-M. Sinnhuber, N. Sheode, M. Sinnhuber, M. P. Chipperfield, and W. Feng, "The contribution of anthropogenic bromine emissions to past stratospheric ozone trends: a modelling study," *Atmospheric Chemistry and Physics*, vol. 9, no. 8, pp. 2863–2871, Apr. 2009, publisher: Copernicus GmbH. [Online]. Available: https://acp.copernicus.org/articles/9/2863/2009/

[52] D. R. Bates, "Rayleigh scattering by air," *Planetary and Space Science*, vol. 32, no. 6, pp. 785–790, Jun. 1984. [Online]. Available: https://www.sciencedirect.com/science/article/pii/0032063384901028

[53] K.-N. Liou, *An introduction to atmospheric radiation*, 2nd ed., ser. International geophysics series. Amsterdam Boston Paris [etc.]: Academic press, 2002, no. 84.

[54] U. E. P. Agency, "User's Guide for the Industrial Source Complex (ISC3) Dispersion Models, Volume II - Description of Model Algorithms," Research Triangle Park, North Carolina 27711, Tech. Rep. EPA-454/B-95-003b.

[55] F. Pasquill, *Atmospheric diffusion: the dispersion of windborne material from industrial and other sources*, 2nd ed. Chichester: Horwood [u.a.], 1974.

[56] C. D. Rodgers, *Inverse methods for atmospheric sounding: theory and practice*, repr ed., ser. Series on atmospheric, oceanic and planetary physics. Singapore: World Scientific, 2008, no. 2.

[57] H. Rahman, B. Pinty, and M. M. Verstraete, "Coupled surface-atmosphere reflectance (CSAR) model: 2. Semiempirical surface model usable with NOAA advanced very high resolution radiometer data," *Journal of Geophysical Research: Atmospheres*, vol. 98, no. D11, pp. 20 791–20 801, 1993, _eprint: https://onlinelibrary.wiley.com/doi/pdf/10.1029/93JD02072. [Online]. Available: https://onlinelibrary.wiley.com/doi/abs/10.1029/93JD02072

[58] C. L. Wyatt, *Electro-optical system design: for information processing*, ser. Optical and electro-optical engineering series. New York, NY: McGraw-Hill, 1991.

[59] K. J. Kasunic, *Optical systems engineering.* New York: McGraw-Hill, 2011, oCLC: 824744472.

[60] L. R. Corporation, *TracePro User's Manual - Software for Opto-Mechanical Modeling - Release 6.0*, Nov. 2009.

[61] Z. Zhang, "A flexible new technique for camera calibration," *IEEE Transactions on Pattern Analysis and Machine Intelligence*, vol. 22, no. 11, pp. 1330–1334, Nov. 2000, conference Name: IEEE Transactions on Pattern Analysis and Machine Intelligence. [Online]. Available: https://ieeexplore.ieee.org/document/888718

[62] D. Wunch, G. C. Toon, J.-F. L. Blavier, R. A. Washenfelder, J. Notholt, B. J. Connor, D. W. T. Griffith, V. Sherlock, and P. O. Wennberg, "The Total Carbon Column Observing Network," *Philosophical Transactions of the Royal Society A: Mathematical, Physical and Engineering Sciences*, vol. 369, no. 1943, pp. 2087–2112, May 2011. [Online]. Available: https://royalsocietypublishing.org/doi/10.1098/rsta.2010.0240

[63] C. W. O'Dell, A. Eldering, P. O. Wennberg, D. Crisp, M. R. Gunson, B. Fisher, C. Frankenberg, M. Kiel, H. Lindqvist, L. Mandrake, A. Merrelli, V. Natraj, R. R. Nelson, G. B. Osterman, V. H. Payne, T. E. Taylor, D. Wunch, B. J. Drouin, F. Oyafuso, A. Chang, J. McDuffie, M. Smyth, D. F. Baker, S. Basu, F. Chevallier, S. M. R. Crowell, L. Feng, P. I. Palmer, M. Dubey, O. E. García, D. W. T. Griffith, F. Hase, L. T. Iraci, R. Kivi, I. Morino, J. Notholt, H. Ohyama, C. Petri, C. M. Roehl, M. K. Sha, K. Strong, R. Sussmann, Y. Te, O. Uchino, and V. A. Velazco, "Improved retrievals of carbon dioxide from Orbiting Carbon Observatory-2 with the version 8 ACOS algorithm," *Atmospheric Measurement Techniques*, vol. 11, no. 12, pp. 6539–6576, Dec. 2018, publisher: Copernicus GmbH. [Online]. Available: https://amt.copernicus.org/articles/11/6539/2018/

[64] C. Iwasaki, R. Imasu, A. Bril, T. Yokota, Y. Yoshida, I. Morino, S. Oshchepkov, D. Wunch, D. W. T. Griffith, N. M. Deutscher, R. Kivi, D. Pollard, C. M. Roehl, V. A. Velazco, R. Sussmann, T. Warneke, and J. Notholt, "Validation of GOSAT SWIR XCO_2 and XCH_4 Retrieved by PPDF-S Method and Comparison with Full Physics Method," *Sola*, vol. 13, pp. 168–173, 2017.

[65] P. Hochstaffl, F. Schreier, G. Lichtenberg, and S. Gimeno García, "Validation of Carbon Monoxide Total Column Retrievals from SCIAMACHY Observations with NDACC/TCCON Ground-Based Measurements," *Remote Sensing*, vol. 10, no. 2, p. 223, Feb. 2018, number: 2 Publisher: Multidisciplinary Digital Publishing Institute. [Online]. Available: https://www.mdpi.com/2072-4292/10/2/223

[66] M. K. Sha, B. Langerock, J.-F. L. Blavier, T. Blumenstock, T. Borsdorff, M. Buschmann, A. Dehn, M. De Mazière, N. M. Deutscher, D. G. Feist, O. E. García, D. W. T. Griffith, M. Grutter, J. W. Hannigan, F. Hase, P. Heikkinen, C. Hermans, L. T. Iraci, P. Jeseck, N. Jones, R. Kivi, N. Kumps, J. Landgraf, A. Lorente, E. Mahieu, M. V. Makarova, J. Mellqvist, J.-M. Metzger, I. Morino, T. Nagahama, J. Notholt, H. Ohyama, I. Ortega, M. Palm, C. Petri, D. F. Pollard, M. Rettinger, J. Robinson, S. Roche, C. M. Roehl, A. N. Röhling, C. Rousogenous, M. Schneider, K. Shiomi, D. Smale, W. Stremme, K. Strong, R. Sussmann, Y. Té, O. Uchino, V. A. Velazco, C. Vigouroux, M. Vrekoussis, P. Wang, T. Warneke, T. Wizenberg, D. Wunch, S. Yamanouchi, Y. Yang, and M. Zhou, "Validation of methane and carbon monoxide from Sentinel-5 Precursor using TCCON and NDACC-IRWG stations," *Atmospheric Measurement Techniques*, vol. 14, no. 9, pp. 6249–6304, Sep. 2021, publisher: Copernicus GmbH. [Online]. Available: https://amt.copernicus.org/articles/14/6249/2021/

[67] Instrumental Payload - Sentinel-5P Mission - Sentinel Online. [Online]. Available: https://sentinels.copernicus.eu/web/sentinel/missions/sentinel-5p/instrumental-payload

[68] T. Lauvaux, C. Giron, M. Mazzolini, A. d'Aspremont, R. Duren, D. Cusworth, D. Shindell, and P. Ciais, "Global assessment of oil and gas methane ultra-emitters," *Science*, vol. 375, no. 6580, pp. 557–561, Feb. 2022, publisher: American Association for the Advancement of Science. [Online]. Available: https://www.science.org/doi/10.1126/science.abj4351

[69] "MethaneSAT." [Online]. Available: https://www.methanesat.org/satellite/

[70] E. D. Sherwin, J. S. Rutherford, Y. Chen, S. Aminfard, E. A. Kort, R. B. Jackson, and A. R. Brandt, "Single-blind validation of space-based point-source detection and quantification of onshore methane emissions," *Scientific Reports*, vol. 13, no. 1, p. 3836, Mar. 2023. [Online]. Available: https://www.nature.com/articles/s41598-023-30761-2

[71] D. Labate, M. Ceccherini, A. Cisbani, V. De Cosmo, C. Galeazzi, L. Giunti, M. Melozzi, S. Pieraccini, and M. Stagi, "The PRISMA payload optomechanical design, a high performance instrument for a new hyperspectral mission," *Acta Astronautica - ACTA ASTRONAUT*, vol. 65, pp. 1429–1436, Nov. 2009.

[72] L. Guanter, I. Irakulis-Loitxate, J. Gorroño, E. Sánchez-García, D. H. Cusworth, D. J. Varon, S. Cogliati, and R. Colombo, "Mapping methane point emissions with the PRISMA spaceborne imaging spectrometer," *Remote Sensing of Environment*, vol. 265, p. 112671, Nov. 2021. [Online]. Available: https://linkinghub.elsevier.com/retrieve/pii/S0034425721003916

[73] P. H. Lissberger and W. L. Wilcock, "Properties of All-Dielectric Interference Filters. II. Filters in Parallel Beams of Light Incident Obliquely and in Convergent Beams," *JOSA*, vol. 49, no. 2, pp. 126–130, Feb. 1959, publisher: Optica Publishing Group. [Online]. Available: https://opg.optica.org/josa/abstract.cfm?uri=josa-49-2-126

[74] C. R. Pidgeon and S. D. Smith, "Resolving Power of Multilayer Filters in Nonparallel Light," *JOSA*, vol. 54, no. 12, pp. 1459–1466, Dec. 1964, publisher: Optica Publishing Group. [Online]. Available: https://opg.optica.org/josa/abstract.cfm?uri=josa-54-12-1459

[75] H. A. Macleod, *Thin-film optical filters*, 4th ed., ser. Series in optics and optoelectronics. Boca Raton, FL: CRC Press/Taylor & Francis, 2010, oCLC: ocn176924832.

APPENDICES

APPENDIX A

The effect of varying the angle of incidence

This appendix describes the effect of varying the angle of incidence (AOI) on the performance of all-dielectric single-cavity filters. Since FINIS exploits the interference filter's dependence on the AOI to capture the scene's spectral information, this effect is critical to adequately describing the instrument's spectral response. For our purpose, the main focus of this appendix is to present the analytical expressions that describe the center wavelength shift, bandwidth broadening, and peak transmittance drop that occur for oblique incidence of uncollimated light. The results present here are based on the extensive studies done by Lissberger and Wilcock in [73], Pidgeon and Smith in [74], and consolidated in a book by Macleod [75].

It has been shown that a single layer with an effective refractive index can characterize the effect of oblique incidence [73]. For an ideal single-cavity filter with thickness d and index n, the apparent optical thickness of the thin film at oblique incidence is given by $nd\cos\theta'$, where θ' is the internal angle of incidence. The peak wavelength locations are found when the apparent optical thickness is equal to an integer number m of half-wavelengths:

$$nd\cos\theta' = m\frac{\lambda}{2} \tag{A.1}$$

If considering that λ_0 represents the peak wavelength at normal incidence ($\theta' = 0$), its relationship with the tilted peak wavelength λ simply becomes described by Eq. (A.2).

$$m\frac{\lambda_0}{2} = nd \implies \lambda = \lambda_0 \cos\theta' \tag{A.2}$$

By applying Snell's law, θ' can be written as function of the AOI in the incidence medium with index n_0: $n_0 \sin\theta = n\sin\theta'$. After some trivial algebra, Eq. (A.2) becomes Eq. (A.3). The plot in Fig. A.1 shows the theoretical shift on the CWL $\lambda_0 - \lambda_\theta$ as a function of the AOI, assuming vacuum for the incident medium, 1.87 of effective refractive index n_{eff} and 1672 nm for the center wavelength at normal incidence λ_0.

$$\lambda_\theta = \lambda_0 \sqrt{1 - (\frac{n_0}{n} sin\theta)^2} \tag{A.3}$$

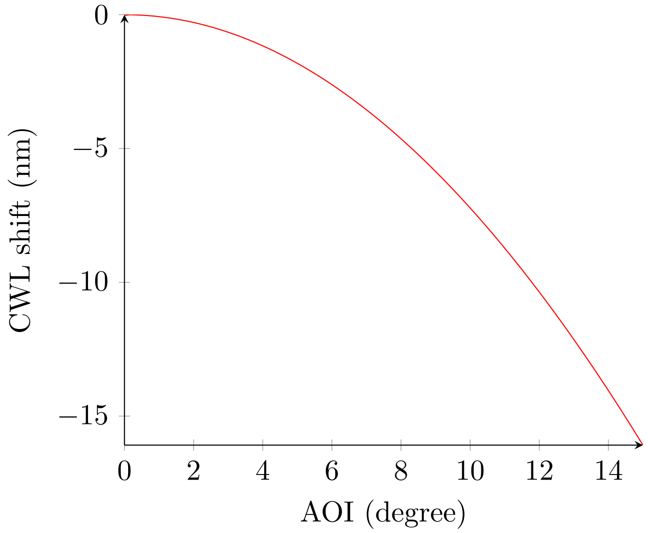

Fig. A.1: Center wavelength shift with the angle of incidence. $\lambda_0 = 1672$ nm, $n_{eff} = 1.87$

In collimated light, all light rays arrive at the filter surface with the same AOI, see Fig. A.2(a). In that case, the peak transmittance and bandwidth remain unchanged, and the only effect of tilting the IF is the shift of the center wavelength towards shorter wavelengths, as described by Eq. (A.3). In many applications, however, including the case of FINIS, the incoming light is not collimated but actually convergent or divergent. In such cases, the performance is given by integrating the transmission curve over the range of AOIs defined by the cone of light. As we shall show, that broadens the bandwidth and reduces the peak transmission.

Let us consider the case shown by Fig. A.2(b). The divergent beam case is analogous. It is simple to see that the range of angle of incidence of all light rays inside the cone becomes $\theta \pm \alpha$. As derived by [75] in terms of wave numbers, the the new peak wavelength can be

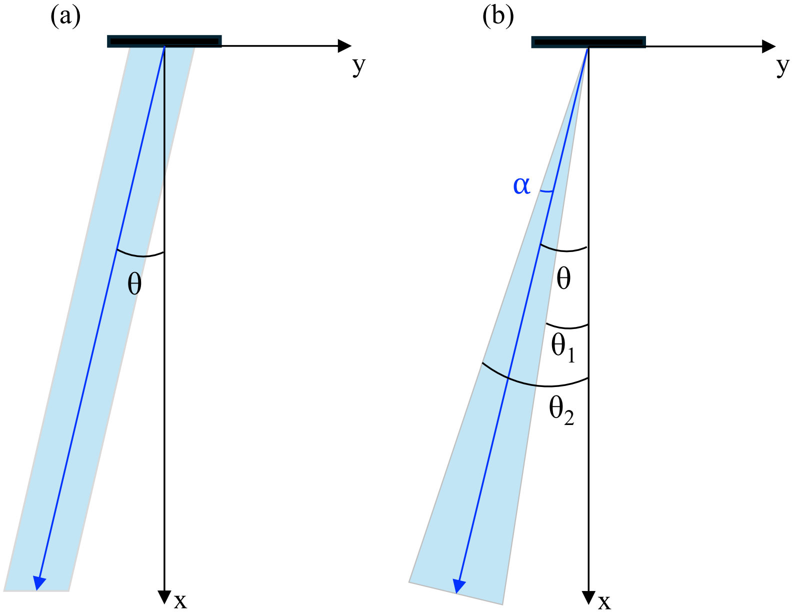

Fig. A.2: (a) Collimated beam with angle of incidence θ. (b) Convergent beam with semi-angle α and angle of incidence of the cone θ.

computed using Eq. (A.4), where θ_1 and θ_2 are the absolute lowest and highest angles of incidence, respectively.

$$\frac{1}{\lambda_{peak}} = \frac{1}{2}(\frac{1}{\lambda_{\theta_2}} + \frac{1}{\lambda_{\theta_1}}) \implies \lambda_{peak} = 2\frac{\lambda_{\theta_1}\lambda_{\theta_2}}{\lambda_{\theta_1} + \lambda_{\theta_2}} \tag{A.4}$$

If $\theta < \alpha$, $\theta_2 = \theta + \alpha$ and $\theta_1 = 0$, so by applying Eq. (A.4), the new center wavelength can be computed using Eq. (A.5).

$$\lambda_{peak} = 2\frac{\lambda_0\lambda_{\theta+\alpha}}{\lambda_0 + \lambda_{\theta+\alpha}} \tag{A.5}$$

Now, if $\theta > \alpha$, the range of angles of incidence goes from $\theta_1 = \theta - \alpha$ to $\theta_2 = \theta + \alpha$, and the new center wavelength can be calculated using Eq. (A.6).

$$\lambda_{peak} = 2\frac{\lambda_{\theta-\alpha}\lambda_{\theta+\alpha}}{\lambda_{\theta-\alpha} + \lambda_{\theta+\alpha}} \tag{A.6}$$

As expected, the effective bandwidth will appear broader, since it results from a convolution of the filter curve with initial bandwidth $\Delta\lambda_0$ with another function with bandwidth given by $\lambda_{\theta_1} - \lambda_{\theta_2}$. As shown by [75], the effective bandwidth, in units of wavelength, can be calculated using Eq. (A.7).

$$\begin{aligned} \Delta\lambda_{new} &= \frac{W}{W_0}\Delta\lambda_0 \\ \text{where } W_0 &= \frac{1}{\lambda_0 - 0.5\Delta\lambda_0} - \frac{1}{\lambda_0 + 0.5\Delta\lambda_0} \\ \text{and } W &= \sqrt{W_0^2 + (\frac{1}{\lambda_{\theta_2}} - \frac{1}{\lambda_{\theta_1}})^2} \end{aligned} \tag{A.7}$$

The peak transmission also falls due to the oblique incidence of a cone of light, and its value is described by Eq. (A.8).

$$\begin{aligned} T_{peak} &= \xi \arctan\frac{1}{\xi} \\ \text{where } \xi &= W_0 \frac{\lambda_{\theta_1}\lambda_{\theta_2}}{\lambda_{\theta_1} - \lambda_{\theta_2}} \end{aligned} \tag{A.8}$$

To illustrate the effect of varying the AOI for uncollimated light, consider a IF with normal-incidence center wavelength at 1672nm, 1.5nm FWHM bandwidth, and 1.87 of effective index. Fig. A.3 presents the calculated transmittance curves for incident collimated light ($\alpha = 0°$) for baseline, and slightly convergent light ($\alpha = 0.25°$ and $\alpha = 0.5°$) subject to different angles of incidence ranging from 0° to 15° in intervals of 3°. Fig. A.4 presents the values of bandwidth and peak transmission for the same set of angles.

Fig. A.5 shows the bandwidth variation applied for the case of FINIS, calculated using Eq. (A.7). The extremely low variation shows that this effect is negligible for FINIS, since the light arrives fairly collimated at the filter surface.

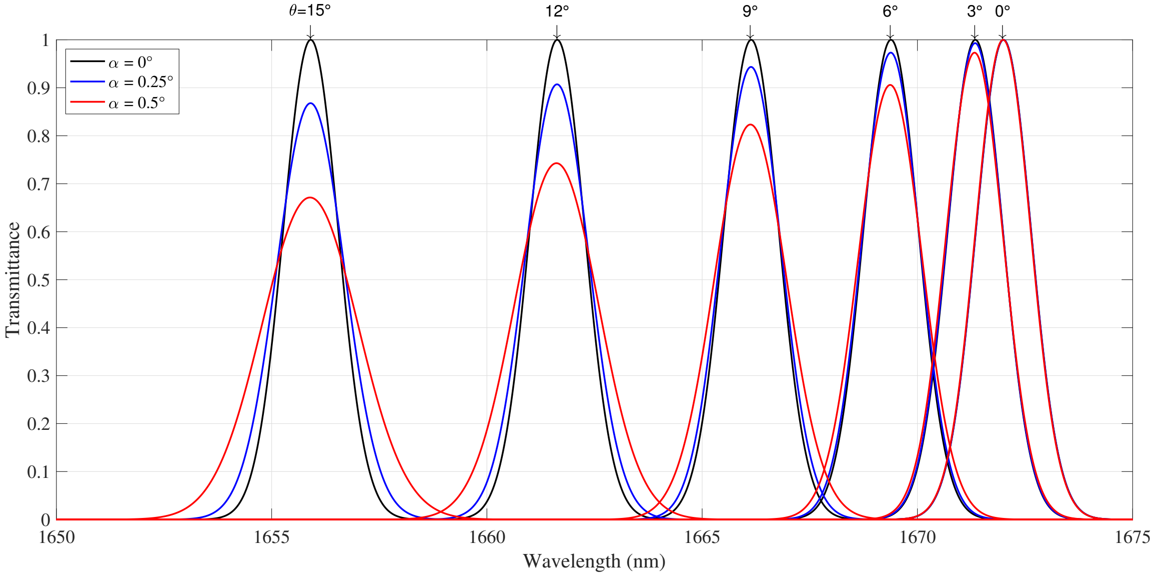

Fig. A.3: IF transmittance curves for difference values of half-FOV α and cone angle of incidence θ

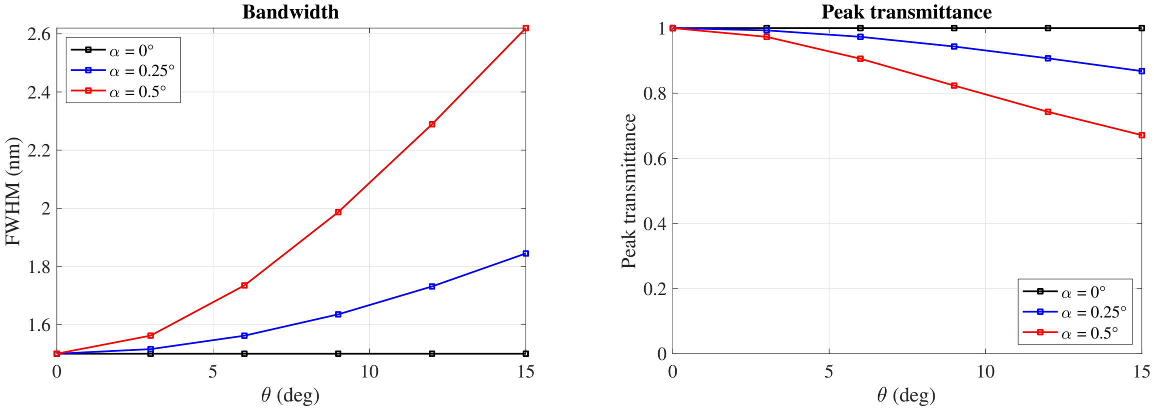

Fig. A.4: Bandwidth broadening and peak transmission decrease as a function of cone of light semi-angle α and incidence angle θ

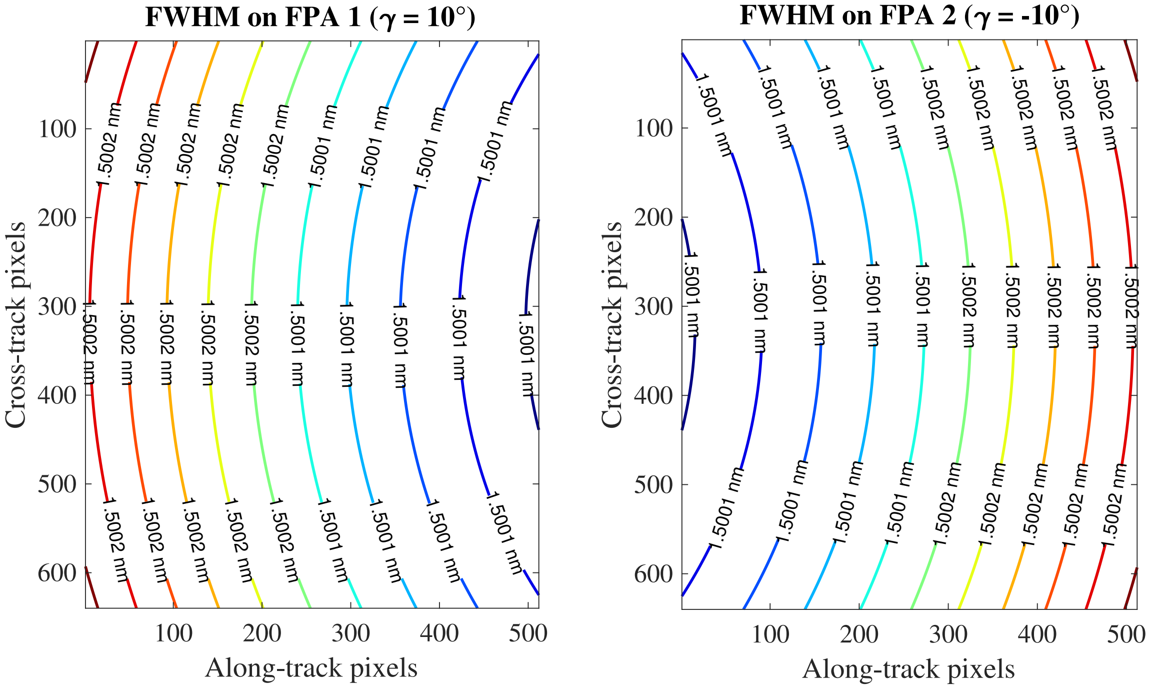

Fig. A.5: Figure of merit of the transmission bandwidth across FPA 1 and FPA 2, where the tilted angles in each optical assembly are set to $\gamma = 10°$ and $\gamma = -10°$, respectively.